



## Durham E-Theses

---

### *Solid-state NMR studies of absorption onto activated carbon*

Thompson, Timothy V.

#### How to cite:

---

Thompson, Timothy V. (1995) *Solid-state NMR studies of absorption onto activated carbon*, Durham theses, Durham University. Available at Durham E-Theses Online: <http://etheses.dur.ac.uk/5228/>

#### Use policy

---

The full-text may be used and/or reproduced, and given to third parties in any format or medium, without prior permission or charge, for personal research or study, educational, or not-for-profit purposes provided that:

- a full bibliographic reference is made to the original source
- a [link](#) is made to the metadata record in Durham E-Theses
- the full-text is not changed in any way

The full-text must not be sold in any format or medium without the formal permission of the copyright holders.

Please consult the [full Durham E-Theses policy](#) for further details.

# Solid-state NMR studies of adsorption onto activated carbon

Timothy V. Thompson B. Sc. (Hons.)

A thesis submitted in partial fulfilment of the requirements for the degree of Doctor of  
Philosophy at the University of Durham.

Department of Chemistry  
University of Durham

1995

The copyright of this thesis rests with the author.  
No quotation from it should be published without  
his prior written consent and information derived  
from it should be acknowledged.



11 DEC 1995

## **Memorandum**

The research in this thesis has been carried out in the Department of Chemistry, University of Durham, between October 1992 and October 1995. Unless otherwise stated, it is the original work of the author. None of the work has been submitted for any other degree.

The copyright lies with the author. No quotation from it may be published without his prior consent and information derived from it should be acknowledged.

## Acknowledgements

There are a few people that I would like to thank for their assistance during my research.

Firstly, my supervisor Professor Robin Harris who has been a great help with interpreting spectra and explaining the theoretical concepts of the NMR experiment. The results from the spectrometer would not have been possible without the help of Dr. Robin Challoner, Dr. David Apperley, Dr. U. Scheler, Nicola Davies, Dr. Alan Kenwright and Barry Say.

From the CBDE at Porton Down I would like to thank Dr. Andrew Trethewey, Colin Pottage and especially Dr. Paul Norman for their samples, knowledge and enthusiasm. I would also like to thank Dr. M. Anderson from UMIST for his help with the sample-sealing technique, and Dr. M. Thomas from Newcastle University for his carbon samples.

The NMR group at Durham have been a great help and I would like to thank Elke, Stefan, Graham, Abdul, Peter, Anna, Steve C, Raouf, Gary, Steve B, Alison and Se-Woung for putting up with me.

## Abstract

This is a study of adsorption on three activated carbon substrates using solid-state NMR. The adsorbates used as probe molecules included a range of phosphates, phosphonates and deuterated water. High-resolution  $^{31}\text{P}$  and  $^2\text{H}$  NMR spectra have been obtained using magic-angle spinning and a single-pulse regime.

The deuterium results include the generation of an adsorption isotherm. The traditional gravimetric analysis and NMR experiments were run concurrently. These results showed that the NMR technique was qualitatively and quantitatively accurate, while the proven adsorption isotherm theory could be applied to the NMR results. The additional information given by the  $^2\text{H}$  NMR results showed evidence of two distinct adsorption sites. Initial adsorption in the micropores gives a peak shifted by 6 ppm to low frequency of the liquid  $^2\text{H}_2\text{O}$  line. This peak was broadened due to restricted motion in the micropores. The second peak was observed only at high relative humidities and was attributed to adsorption on the external surface or in macropores. The chemical shift was similar to that of the pure liquid.

The  $^{31}\text{P}$  NMR results were used to directly observe the adsorption of phosphates with a range of molecular sizes. The NMR data were used to calculate the micropore accessibility for each phosphate. Differences in the adsorption mechanism were recorded, and direct comparison for each carbon gave some structural information.

It was possible to follow competition reactions over time periods of 1 min to 24 hours. A battlefield simulation was studied, with  $^2\text{H}_2\text{O}$  and a phosphate competing for the adsorption sites. The NMR results showed that the phosphate was preferentially adsorbed into the micropores, displacing the  $^2\text{H}_2\text{O}$ . However, the addition of  $^2\text{H}_2\text{O}$  to a carbon saturated with a phosphate enabled more phosphate to be adsorbed into the micropores via a cooperative mechanism.

Measurements of the transverse relaxation for adsorbed molecules suggest that the broad micropore signal consists of some overlapping peaks. The peaks with similar chemical shift are attributed to adsorption in pores with differing dimensions. The natural linewidth involves broadening caused by restricted anisotropic motion within the micropores.

## Abbreviations

$B_0$	The static magnetic field of a spectrometer.
$B_{ring}$	The induced field from a ring current in a static magnetic field.
$\Delta 1/2$	Full peak width at half-height.
$\delta_{31P}$	The chemical shift for resonance of phosphorus nuclei expressed in ppm from the signal from 85% aqueous phosphoric acid.
$\delta_{2H}$	The chemical shift for resonance of deuterium nuclei expressed in ppm from the signal for $^2H_2O$ .
$\gamma$	The gyromagnetic ratio of a nucleus.
MAS	Magic-angle spinning.
$M(t)$	Observed signal intensity at time $t$ .
NMR	Nuclear magnetic resonance.
SA	Shielding anisotropy.
FID	Free induction decay.
PTFE	Polytetrafluoroethylene.
PDMSO	Polydimethylsiloxane.
$\tau$	The delay between radio frequency pulses.
tau	Dephasing time for relaxation experiments.
$T_1$	Spin-lattice relaxation time.
$T_2$	Spin-spin relaxation time.
TMP	Trimethyl phosphate.
TEP	Triethyl phosphate.
DMMP	Dimethyl methylphosphonate.
PP	Cyclohexanyl methyl methyl phosphonate.
$S_{cum}$	Cumulative surface area.
$p/p^\circ$	Partial molar pressure.
$\Delta H_i$	Enthalpy change of immersion.

## Contents

	<b>Page</b>
<b>1 Introduction</b>	<b>1</b>
1.1 Activated carbon	1
1.1.1 Uses of activated carbon	1
1.1.2 Manufacture	3
1.1.3 The activated carbon product	12
1.1.4 Analysis of carbon-oxygen surface groups	13
1.1.5 Porous structure	18
1.1.6 Methods for adsorption analysis	23
1.1.7 Experimental characterisation of adsorption	26
1.1.8 Theoretical treatment of adsorption	34
1.1.9 Active sites in carbons	42
1.1.10 Surface modification	44
1.2 Chemical defence	51
1.3 NMR theory	66
<b>2 Experimental</b>	<b>80</b>
2.1 The NMR spectrometer	80
2.2 Calculation of relaxation times	83
2.3 Samples	86
2.4 Sample sealing	87
<b>3 Deuterium results</b>	<b>96</b>
3.1 Deuterium NMR	96
3.1.1 Loading experiments	97
3.1.2 Adsorption isotherm	104
3.1.3 Substrate evaluation	113

<b>4</b>	<b>Phosphorus results</b>	<b>127</b>
4.1	Phosphorus NMR	127
4.1.1	Method	127
4.1.2	Results	128
4.1.3	Long-term ageing effects	158
4.1.4	Discussion	158
4.1.5	Conclusions	167
<b>5</b>	<b>Competition reactions</b>	<b>168</b>
5.1	Introduction	168
5.2	Results	169
5.2.1	Pre-adsorbed $^2\text{H}_2\text{O}$	170
5.2.2	Pre-adsorbed TEP	179
5.3	Discussion	187
5.4	Conclusions	190
<b>6</b>	<b>Relaxation experiments</b>	<b>191</b>
6.1	Hahn-echo experiments	191
6.2	Experimental method	194
6.3	Results	194
6.4	Discussion	200
6.5	Conclusions	202
<b>7</b>	<b>Conclusions and future work</b>	<b>203</b>

## **Chapter one            Introduction**

### **1.1 Activated carbon**

The activated carbon group of materials includes a wide range of amorphous carbon-based materials which have been treated to achieve a huge degree of porosity and large surface area. They can be produced in granular or powdered form.

#### **1.1.1 Uses of activated carbon**

Activated carbons have been used for centuries for adsorption purposes. The major uses are the removal of colour, odour and taste as well as organic impurities from potable water. There is also a major application in collective air purification in confined areas.

##### **1.1.1.1 Purification of air**

Activated carbons are used as adsorbents purifying air streams for use in inhabited spaces such as hospitals, laboratories and restaurants. The pollution levels are controlled to less than 10 ppm by the use of carbon panel filters. The activated carbon needs to be highly microporous, allowing adsorption at very low concentrations. The carbon in the filters is discarded after use because the regeneration is expensive.

Active carbon is also used to prevent air pollution at source. This includes purification of exhaust air streams from industrial processing and manufacture. The required carbon arrangement needs to cope with the high concentrations of pollutant and must be regenerated to be cost efficient. The regeneration is generally effected by exposure of the carbon to steam, air or non-toxic vapour. The carbon itself has to have a large adsorption capacity, with pore sizes at the larger end of the micropore range.

##### **1.1.1.2 Active carbon in respirators**

Industrial respirators need to cope with molecules of low toxicity and high molecular weight. General active carbons adsorb these molecules very strongly and quickly. Specific carbons can be designed to cope with differing environments and necessities.

Military respirators demand complete protection from extremely toxic vapours, whose molecular weight and concentration can vary considerably. The active carbon needs to be capable of physical adsorption of some gases and chemical adsorption of some other toxins. (Chloropicrin and hydrogen cyanide). The activated carbons that are used have a large range of micro/mesopore sizes to provide efficient adsorption of the varying size and amount of adsorbate molecule. The carbon structure has some transport macropores allowing access to the pore system. For the chemical adsorption of gases the carbon is impregnated with a range of impregnants which are tailored for specific reactivity with target toxins which are not easy to adsorb physically.

#### 1.1.1.3 Air purification in nuclear plants

Activated carbons are used in nuclear plants to prevent the release of radioactively contaminated vapours such as iodine, methyl iodide and various noble gases. Activated carbon beds are also used to decontaminate helium which is used as a protective gas in reactors cooled and moderated by heavy water.

#### 1.1.1.4 Recovery of gasoline, propane, and butane from natural gas

Natural gas contains 3% propane and 5% higher hydrocarbons which can be recovered using activated carbons. About 70% of butane and 98% of pentane can be removed by the carbon acting as a molecular sieve.

#### 1.1.1.5 Alcoholic drinks industry

In the brewing process activated carbon is used to improve the quality of defective beer and also in some cases to change the colour of all the product. Wines and spirits are filtered through activated carbon to remove traces of fusel oil. The production of brandy uses the carbon to remove some aldehydes in the raw distillate, causing the maturing process to be accelerated.

#### 1.1.1.6 Sugar refinement

The sugar industry uses activated carbon to remove colour from the syrup and to improve its processing properties. The carbon removes surface active agents and colloidal substances, thus raising the syrup's surface tension and decreasing its viscosity. This gives quicker crystallisation rates and aids centrifugal separation of the syrup and crystals

#### 1.1.1.7 Medicine

A special type of activated carbon is used to treat ailments of the digestive system, removing bacterial toxins easily as they have a high molecular weight. Activated carbon is also useful in cases of poisoning and is also included in cigarette filters to reduce toxins inhaled by smokers.

#### 1.1.2 Manufacture

The manufacture of active carbons is shown in figure 1.1, which includes two manufacturing steps: the carbonisation of carbonaceous raw materials, then subsequent activation of the carbonised product. (1)

The carbonisation process involves heating any carbon-containing material to temperatures less than 800°C in the absence of oxygen. The properties of the finished product are dependent on the starting carbonaceous material. The carbonisation generally involves heating under a continuous flow of nitrogen gas. The non-carbon elements such as oxygen and hydrogen are eliminated as gaseous by-products. The residual carbon atoms group themselves into sheets of condensed aromatic ring systems with a certain degree of planar structure. The arrangement between these sheet systems is irregular, so the gaps in between them can be filled with tar material which give rise to pores. The pore system makes active carbons excellent adsorbents. The pore system is greatly enhanced during the activation process.

The activation process is an oxidation reaction at elevated temperatures where the oxidising agent is usually steam, carbon dioxide or sometimes air. The carbonisation and activation steps can sometimes be carried out simultaneously using chemical activation elements such as phosphoric acid, zinc chloride and sulphuric acid. These act as dehydrating agents as well, so that the two processes can occur simultaneously.

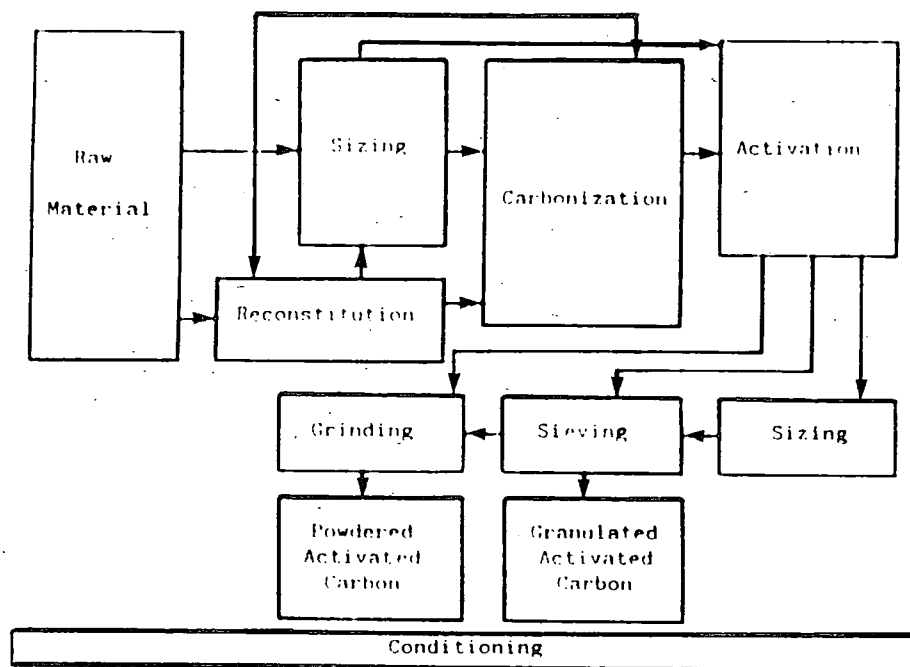


Figure 1.1. Flow chart describing the carbon activation process.

### 1.1.2.1 Raw Materials

Any raw material has to have a high carbon content and few inorganic impurities. Early procedures used young fossil materials like wood and peat. The range of material has spread recently to include fruit stones, (2) nut shells (3) and sawdust. These materials give chars easily which can be quickly activated with reasonably high-quality active carbon products.

Recently more work has been done on types of natural coal. These are cheap and readily available. The following criteria are considered when choosing a raw material:

- a) Potential quality of active carbon product
- b) Volume and cost of raw materials
- c) The ease of material processing.

The raw materials are listed in table 1.1 in order of importance with respect to present world-wide activated carbon production.<sup>(1)</sup>

Material	Total activated tonnes per year
Wood	130 000
Coal	100 000
Lignite	50 000
Coconut Shell	35 000
Peat	35 000
Others	10 000

Table 1.1. Table showing the production of activated carbon world-wide

The activated carbons produced from coal, coconut shells, fruit pits, and other nut shells-with densities greater than wood, have high volatile contents and are used for gaseous adsorption. The granulated carbons are very hard and have large microporous volumes which adsorb gases well.

### 1.1.2.2 Carbonisation

Carbonisation involves the thermal decomposition of material. This eliminates the non-carbon species leaving a fixed carbon mass and a simple pore structure. The process is carried out in rotary kilns or multiple hearth furnaces below 800°C in conjunction with a continuous stream of inert gas. The important parameters that determine the quality of the active carbon product are the rate of heating, the final temperature and the raw material used.

Low heating rates create a higher yield with more stabilised polymeric-type product. However the microporosity was found to be independent of the raw material or the heating rate. The basic pore structure forms by 500°C, but sometimes a higher temperature was used to unblock the pyrolysis products trapped in the pore system.

Variation of the heating rates and carbonisation temperatures has a marked impact on activation (4) and hence the quality of the product. If the temperature of the preparation is lower than the activation temperature then the pyrolytic decomposition continues during the activation process so there is a weight loss which is independent of the activation gas. The oxidative reactivity of the activation gas depends strongly on the rate of heating below 500°C, the amount of time spent around 900°C, and the gas used to activate. Low-temperature carbon blacks gasify much faster in the initial stages of activation.

The carbonisation involves two stages which control the properties of the final product. Initially there is a softening period where temperature control affects the nature of the carbon black produced. The second stage involves hardening and shrinkage, which plays an important role in the development of porosity. Soft raw materials need a very slow softening stage so any gases can escape without causing deformation. The harder raw materials are not too affected by heating rate during the softening process, but a slow hardening process gives a denser and harder product.

### 1.1.2.3 Activation

The activation stage is required to increase the total pore volume and enlarge the individual pore diameters as well as create new porosity. It removes disorganised carbon material, exposing aromatic sheets which interact with the oxidation agent creating a microporous structure. Only in the later stages do existing pores widen and macropores develop by complete burnout of walls between adjacent pores.

This production of the larger macropores results in a reduced total pore volume, so the extent of the burn-off of carbon material is an indication of the degree of activation (5). A predominantly microporous active carbon will be prepared if the burn-off is less than 50%, whereas any burn-off in excess of 75% will cause a predominantly macroporous product. Generally the production will be between 50-75%. This creates active carbon which will exhibit a full range of pore sizes.

The chemistry behind the activation process is not fully understood yet. The carbons which interact with the oxidation agent are thought to be located at the edges of the aromatic sheets or in defect locations and discontinuities. These environments are associated with the unpaired electrons or residual valencies which are rich in potential energy, and are more reactive.

The exact conditions for activation are closely guarded secrets which the manufacturers have optimised. There are two main groups:

- 1) Chemical activation
- 2) Physical activation.

#### 1.1.2.3.1 Chemical Activation.

Chemical activation has mainly been used to prepare active carbons from wood. The starting material is impregnated with the oxidation agent as a concentrated liquid. This makes the raw cellulosic material degrade. The resultant material is extruded and pyrolysed in a rotary kiln (400-600°C) in the absence of air. The product can then be washed to remove the oxidation agent. Then calcination dehydrates the raw material and creates the porous structure.

The most widely used oxidation agents are phosphoric acid, zinc chloride, and sulphuric acid, although potassium sulphide, alkali metal carbonates, calcium chloride and iron chloride have been suggested. (6)

Chemical activation can be carried out at temperatures generally lower than those used in the physical activation process (400-800°C). This means the porous structure tends to be better developed in chemically activated carbons. The pore structure is largely dependent on the degree of oxidant impregnation: The better the impregnation, the larger the pore diameter in the active carbon product.

More recently, Weinerberg and O'Grady (7) prepared active carbons from coal, coke and petroleum coke using chemical activation. They used hydrated potassium hydroxide, and the resultant active carbons exhibited a large microporous volume with a cage-like structure. Nashino et al (8) found that the adsorption capacity of these active carbons was dependent on the grain size of the coal as well as the amount of the chemical oxidant added.

Ehrburger and co-workers(9,10) used KOH and NaOH as chemical oxidants. They found small amounts of alkali reduced the micropore volume, but as the alkali went up (>10%) then the micropore volume increased appreciably. When the KOH was at 70% by weight of coal, the active carbon surface area produced was  $\approx 1600 \text{ m}^2 \text{ g}^{-1}$  and the micropore volume was  $0.687 \text{ cm}^3 \text{ g}^{-1}$ . They showed the micropores widening as the micropore volume increased, giving evidence that carbonisation in the presence of KOH also caused activation of the carbon.

#### 1.1.2.3.2 Physical activation

The physical activation process develops and extends the surface area and produces a porous structure of molecular dimensions. This step is carried out at 800-1100°C in the presence of an oxidising gas such as steam, carbon dioxide or air. The heating is generally done by a coke oven or natural gas, as the activation agent and heat are then introduced simultaneously. However sometimes extra steam is added to control the temperature. The oxygen in the activation agent burns away the more reactive portions of the carbon skeleton in the form of carbon monoxide and carbon

dioxide. The extent of burn-off (gasification) is once again dependent on the gas employed and the activation temperature.

The rate of reaction with steam is retarded by the hydrogen gas product, which is strongly adsorbed on the active centres of the carbon surface, thus retarding activation. The activation by carbon dioxide is also retarded by the production of  $\text{CO}_{(g)}$  and  $\text{H}_2(g)$ , which are quickly adsorbed. The product  $\text{CO}_{(g)}$  hinders either by adsorbing on the active centres or by increasing the rate of backward reaction. Rand and Marsh<sup>(11)</sup> reported that the CO can be added to the activating carbon dioxide to achieve better microporosity in the product. Carbon dioxide activation requires a higher temperature than active carbons produced by steam reactors. In industrial processes flue gas with a small amount of added steam is used so that a combined carbon dioxide/steam activation can take place. It is not possible to control the reaction carefully if the oxygen gas is used as an activation chemical, and the active carbon product is therefore not uniform.

#### 1.1.2.3.3 Mechanism of activation.

The process of carbon activation has two stages. Initially, (when burn-off is less than 10%) the disorganised carbon is burned off preferentially. This unblocks the pores. The second stage involves burning aromatic carbons, producing active sites and wider pores. Reaction with carbon dioxide produces wider pores by external oxidation, than internal activation using steam does.

Kalback et al <sup>(12)</sup> found pure graphitised carbon would preferentially burn off single aromatic sheets with a preferred orientation. This was followed by the burning away of the walls of the layer planes, producing larger pores. Marsh and Rand <sup>(13)</sup> found that activation with  $\text{CO}_2$  created access to pores that were previously unreachable, as well as widening the original pores.

Mc Enancy and Dovaston (14) studied a range of microporous carbons at several activation temperatures using nitrogen adsorption and mercury porosimetry. These results showed that the mesopores and macropores were predominant at lower activation temperatures. However, the activation temperatures of 1500-1700 K converted open porosity to a closed-pore system.

Tomkow et al (15) compared the porosity developed by using water vapour, carbon dioxide and oxygen for two brown coals. The three activation gases all produced predominantly micropores at low temperature burn-off. At higher burn-offs the differences became more pronounced. Steam produced a well-developed pore system with a large pore-size distribution.

Carbon dioxide tended to just produce micropores, accounting for 73% of the pore volume and 90% of the surface area. This is very different from the steam carbons, as shown in table 1.2.

Activation method	Steam	CO <sub>2</sub>
Micropore volume (%)	33	73
Micropore area (%)	63	90
Total pore volume (cm <sup>3</sup> g <sup>-1</sup> )	0.83	0.49

Table 1.2. Table showing the pore distribution for different activation processes.

This means that the CO<sub>2</sub> activation produced a more uniform porosity. The two processes can be used for different applications depending on the individual requirements.

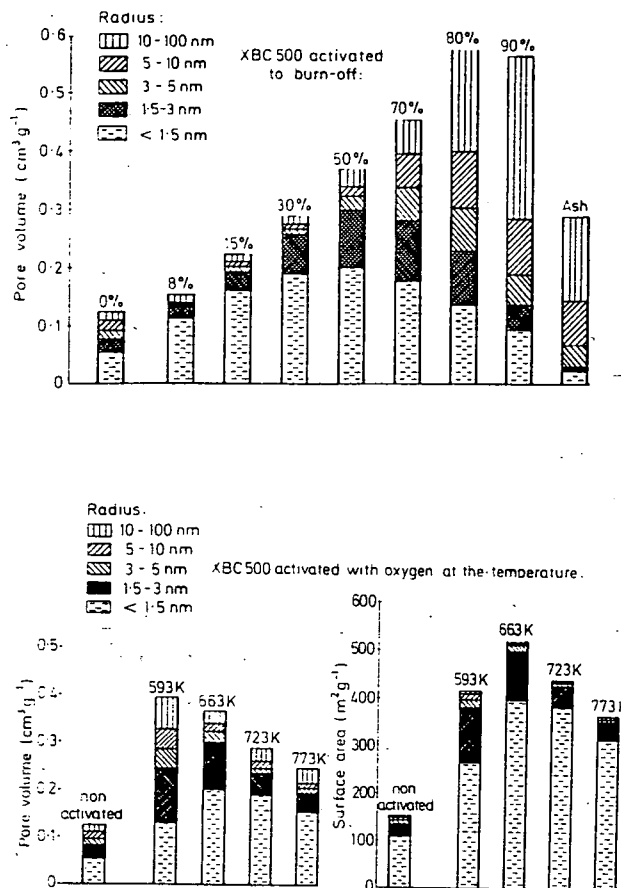


Figure 1.2. Trends in the pore size distribution according to the activation process [Tomkow et al (15)]

Activation with oxygen had a very different behaviour: A strong microporous structure develops at very low temperatures but does not increase with elevated temperatures. The total volume is only  $0.27 \text{ cm}^3 \text{ g}^{-1}$  at 25% burn-off, which then dropped off slightly at 70% burn-off. This behaviour is similar to that caused by steam but in that case the pore volume decrease is compensated by an increased macroporosity which is not found for oxygen as shown in figure 1.2.

This proved that the micropores were being burnt out to meso- and macropores when steam was used as the activation gas. This infers that, for oxygen, the activation only occurs in the initial part of the process. In the later stages the micropores are blocked by the surface oxygen structures forming at the entrances, restricting further expansion inside the pore.

#### 1.1.2.3.4 The activation model

Caron (16) deduced that during the initial stages of the activation process, the peripheral and more-accessible single aromatic sheets are burnt off, producing mainly micropores. The formation of these micropores is limited by the availability of accessible sheets and continues to decrease. As the burn-off continues, the larger sheets start burning out at the walls between the micropores. This produces meso and macropores, so the total surface area drops off dramatically.

This shows that the most important factor determining the different qualities in the carbons is the level of burn-off. This means that manipulation of the length of activation allows selective product properties for differing applications.

#### 1.1.3 The activated carbon product

Active carbons are produced by activating the randomly orientated aromatic sheets in the carbon black. This produces a pore system and a chemical structure on the surface. The random ordering of the sheets causes a variation in the arrangement of the electron clouds in the carbon skeleton and creates unpaired electrons and unused valencies. These obviously affect the adsorption behaviour.

There are also appreciable amounts of oxygen and hydrogen still present in the activated carbons. They are generally associated with the starting carbonaceous material and become part of the chemical structure because of incomplete carbonization. They are sometimes chemically bonded to the surface during the activation process. The hetero atoms can be bonded to the edges of the aromatic sheets to form surface groups, or bonded to the centre of the sheets to form heterocyclic ring systems.

This means that the active carbons will adsorb oxygen at temperatures of 400-500°C very well.(17) There is also a measurable amount of chemically bonded hydrogen.(18,19) Active carbons have an acid-base character developed as a result of the surface oxides.

#### 1.1.3.1 Acidic carbons

Acidic carbons adsorb appreciable amounts of bases but very small amounts of acids. These carbons are generally obtained by activation in oxygen (200-700 °C). The acidic groups have been postulated as lactones, ketones, quinones, anhydrides and ethereal structures. However none of these are conclusively proved or account for the amount of oxygen present.

#### 1.1.3.2 Basic carbons

Basic carbons arise from the surface oxide groups with a basic character. The exact nature of the groups is not known and so far has not been studied in any great depth. The same types of techniques used for acidic groups can be applied to help with these as well. There will not be any further discussion of this category as such carbons lie out of the scope of this project.

#### 1.1.4 Analysis of carbon-oxygen surface groups

Carbon-oxygen surface structures are the most important influences on the surface characteristics. There has been a lot of work done to elucidate these structures, but their exact nature is not yet known. Several techniques have been used but they seem to give conflicting results. The future use of FTIR, ESCA and NMR should help to elucidate the problem. Active carbons have an acid-base character developed as a result of the surface oxides.

##### 1.1.4.1 Thermal desorption

Thermal desorption studies by Trembley<sup>(20)</sup> et al. and by Matsumoto and co-workers<sup>(21)</sup> gave evidence of two types of surface chemical structure, as shown in figure 1.3. One structural type evolves CO<sub>2</sub> on decomposition and the other category evolves CO<sub>(g)</sub>. The CO<sub>2</sub> evolution starts at 300°C and could be from carboxylic or lactonic functions. The other chemical structures, evolving CO<sub>(g)</sub> at temperatures in excess of 500°C, could be postulated as phenols and quinones.

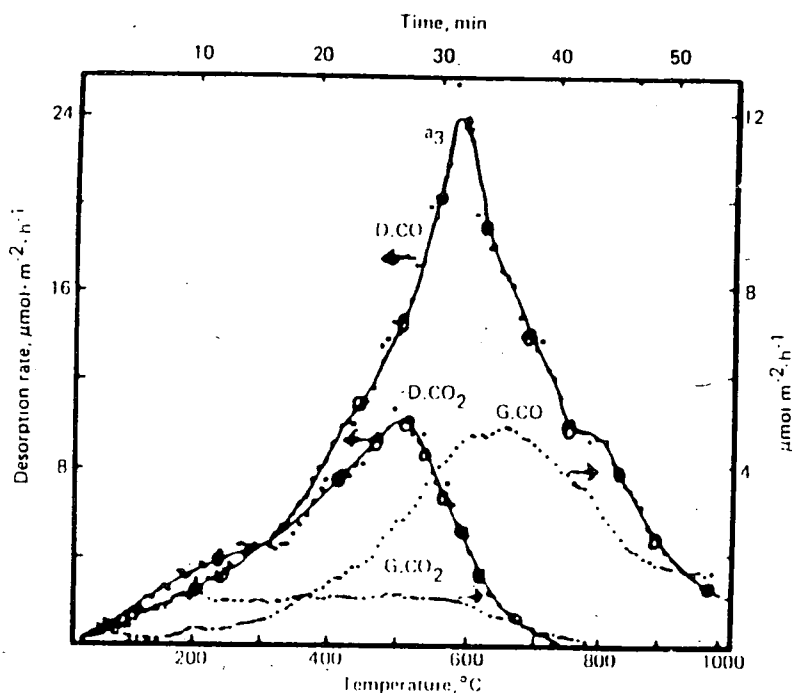


Figure 1.3. Description of the chemisorbed oxygen from oxidised diamond (D) and graphite (G) as a function of temperature. [Matsumato and Setaka (21)]

There is also evidence from Barton et al. (22) to show two types of acidic group evolving CO<sub>2</sub>, and hence there are two separate linear rates of desorption, as seen in figure 1.4.

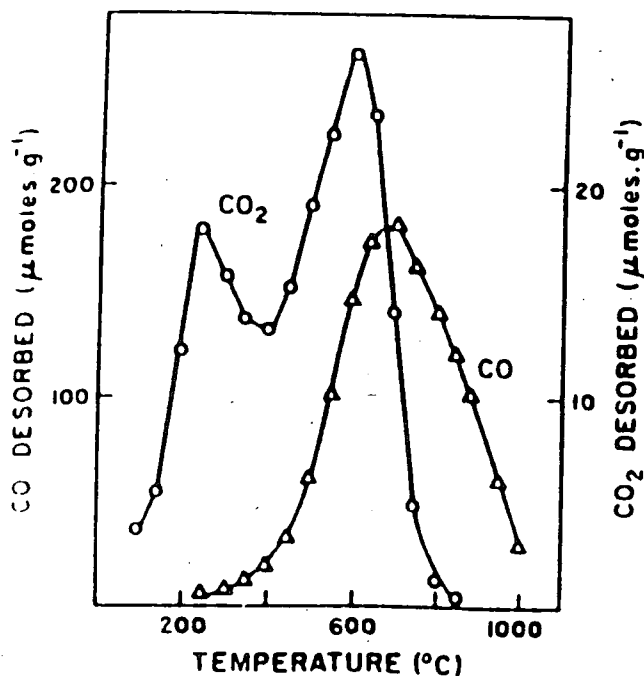


Figure 1.4. Desorption of CO<sub>2</sub> and CO from Spheron-6 as a function of degassing temperature. [Barton et al. (22)]

### 1.1.4.2 Polarography

Hallam and Drushel<sup>(23)</sup> used polarography to identify quinone groups present in carbon blacks, whose presence had been suggested by IR measurements. They postulated the presence of three main types of quinone and hydroquinone groups shown in figure 1.5.

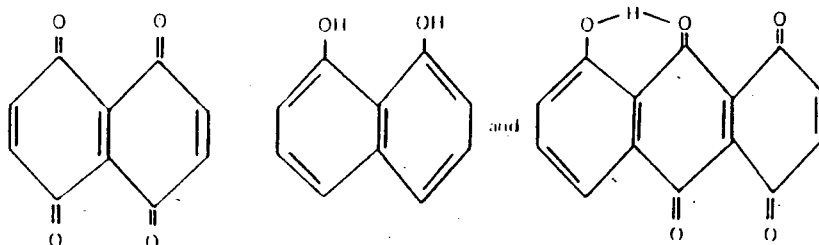


Figure 1.5. Proposed structures for quinone and hydroquinone groups in carbon blacks. [Hallum and Drushel<sup>(23)</sup>]

### 1.1.4.3 Infrared spectroscopy

Infrared spectroscopy is a very important tool used to distinguish groups within an active carbon. The problem with IR is that the carbon is black and adsorbs most of the radiation, so thin sample slices have to be used. This means that initially only coals could be studied as they could be finely divided. This problem was solved by using halide pellets in which ground carbonaceous materials were evenly distributed. The advent of FTIR<sup>(24)</sup> helped to improve the sensitivity of the infra red experiment, along with photoacoustic infra red<sup>(25)</sup> experiments.

Hallum and Drushel<sup>(23)</sup> first reported the IR spectrum of a carbon black with a high oxygen content using a mull of Nujol. A band at  $1600\text{ cm}^{-1}$  was attributed to either condensed ring systems or to hydrogen-bonded conjugated carbonyl groups. Garten and Weiss<sup>(26)</sup> found two bands  $1705$  and  $1600\text{ cm}^{-1}$  for sugar charcoals. The band at  $1600\text{ cm}^{-1}$  was attributed to carboxylate ion formation from  $\beta$ -lactone groups. The band at  $1705\text{ cm}^{-1}$  disappeared when treated with NaOH, which was attributed to  $\alpha$ -lactone groups. However this is a matter of dispute.

Ishizaki and Marti<sup>(27)</sup> examined Filtrasorb, which is a commercially available activated carbon, before and after neutralisation. The spectrum before neutralisation is shown below in figure 1.6, it has five bands at; 1760-1710  $\text{cm}^{-1}$ , 1670-1520  $\text{cm}^{-1}$ , 1480-1340  $\text{cm}^{-1}$ , 1300-1230  $\text{cm}^{-1}$  and 1180-1100  $\text{cm}^{-1}$ . Comparisons with the neutralised system showed the nature of the acidic structures. The spectrum showed a shift of the 1760-1710  $\text{cm}^{-1}$  band corresponding to the tautomeric structures. The 1670-1500 $\text{cm}^{-1}$  region was the result of several overlapping features, which are attributed to quinonic and carboxylate structures. They remained after neutralisation and treatment with acid, as shown in figure 1.6.

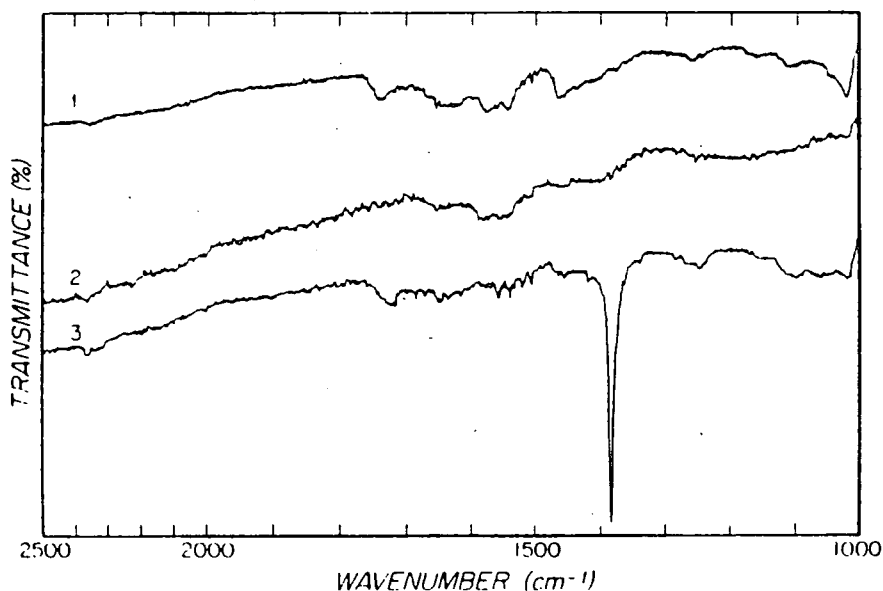


Figure 1.6. Direct transmission IR spectra of 1) Filtrasorb 200. 2) Filtrasorb 200 with NaOH. 3) Filtrasorb 200 with HCl. [Ishizaki and Marti (27)]

When treated with acid the adsorption in the 1670-1500  $\text{cm}^{-1}$ -region decreased and a peak at 1380-1385 $\text{cm}^{-1}$  developed. This was explained as the development of carbonate structures, caused by chemisorbed  $\text{CO}_2$  on semiquinone structures. The 1480-1340  $\text{cm}^{-1}$  region is the OH bending area, the 1465  $\text{cm}^{-1}$  peak reduces when treated with base and is evidence of phenolic groups.

#### 1.1.4.4 FTIR

The use of the interferometer instead of gratings and slits along with internally calibrated computer systems to add up all the interferograms means that FTIR is considerably superior to conventional IR. O'Reilly and Gasler<sup>(28)</sup> applied FTIR to some carbon black samples but the spectrum picks up some broad adsorption features. Some attempts at Lorentzian fitting gave interesting results but the authors declared the statistical results inaccurate. There was some evidence to suggest some C-C stretches, and the nature of these would seem to suggest aromatic ring stretches.

Van Driel<sup>(29)</sup> compared an activated carbon before and after activation to try and assess which oxide groups were introduced. He obtained a difference spectrum shown in figure 1.7, by subtracting the unoxidised from the oxidised spectrum. This shows peaks at  $1735\text{ cm}^{-1}$  and  $1585\text{ cm}^{-1}$  being enhanced on oxidation whereas the peak at  $1463\text{ cm}^{-1}$  completely disappears. The peak at  $1735\text{ cm}^{-1}$  was assigned as an  $\gamma$ -lactone structure.

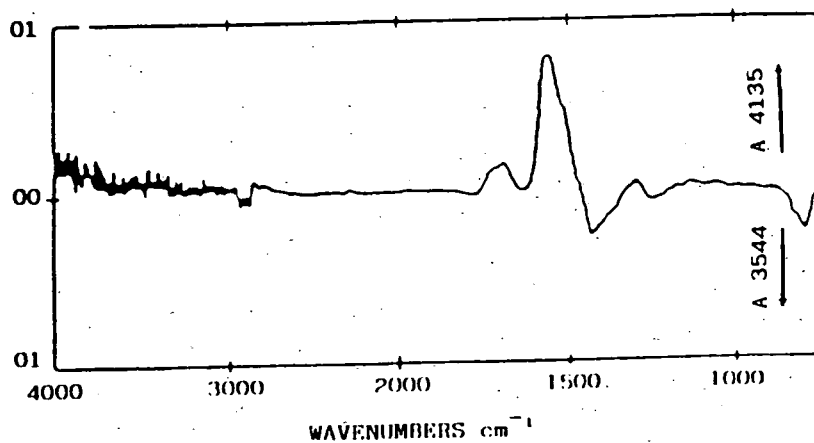


Figure 1.7. A difference FTIR spectrum of oxidised and unoxidised activated carbon. [Van Driel (29)]

Dauben and Epstein<sup>(30)</sup> interpreted some Fourier transform infrared photothermal beam deflection (IR-PDS) results which suggested the presence of cyclic anhydrides. They thought that these structures were formed by the oxidation of the edge carbons and they were not seen at higher temperatures as the poly aromatic carbon network annealed and enlarged.

#### 1.1.4.5 PES

Photo electron spectroscopy uses X-rays to probe the top 15-20 Å of the surface yielding information about the electron binding energies. Essentially this entails the evaluation of the C1s and O1s energy levels which are affected by the local environment. Potentially the technique is very useful to differentiate between the positions and nature of surface oxide groups. However as yet there has been little work on activated carbon systems. Thomas et al<sup>(31)</sup> found evidence for at least two types of oxygen, but further analysis with deconvolution has shown four types of oxygen containing groups to be present. The technique does need some more experimentation on activated carbon systems, but it should prove a very useful tool for determining the identity of oxide groups.

#### 1.1.5 Porous structure

The classical basic definition of pore sizes defines micropores with entrances <2nm in width, mesopore entrances between 2 nm and 50 nm and macropores having entrances in excess of 50 nm. Active carbons have a large adsorption capacity 0.6-0.8 cm<sup>3</sup> g<sup>-1</sup>, the majority of this is created by the micropores. There is also the possibility of mesopores and macropores: the definition of these being dependent not only on the size of the pore entrance, but also on their adsorption behaviour. The most striking property occurs with mesopores (2nm < r > 50nm), where the adsorbate condenses in a liquid like state and forms a meniscus. This behaviour creates a hysteresis loop in the adsorption- desorption profile because it is harder to desorb the adsorbate from this state.

Solano et al<sup>(32)</sup> discovered that active carbons exhibit low pressure hysteresis: this was ascribed to the trapping of adsorbate after the inelastic distortion of some micropores. Stoekli et al<sup>(33)</sup> found the reverse when the accessibility of the micropore system increased at low pressures after several adsorption - desorption cycles.

The actual three-dimensional structure of the active carbon can only be postulated from tunnelling electron microscopy (T.E.M.)<sup>(34)</sup> observations. There is a limiting structure model proposed by Oberlin et al<sup>(35)</sup> who looked at typical unactivated carbon materials. It is generally assumed that the micropores are slit shaped gaps produced by distortion of the aromatic sheets. Figure 1.8 shows a schematic representation of the activated carbons porous system.



Figure 1.8. A schematic representation of the microporous structure within activated carbons<sup>(1)</sup>.

Figure 1.9 shows four TEM micrographs of the activated carbon gradually focussing in more detail. The first one (A) shows several granules, the next one (B) just shows one granule, and the scales are shown. The third picture (C) is a closer view of the surface, showing some of the texture. The final micrograph (D) is the limit of the TEM experiment and shows the texture very well, it highlights the entrance to a round hole, which is larger than a micropore.

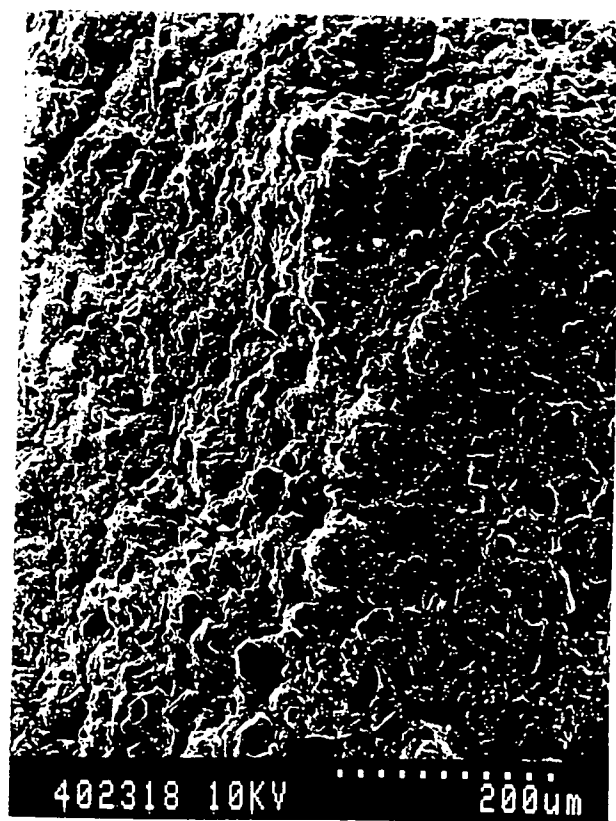
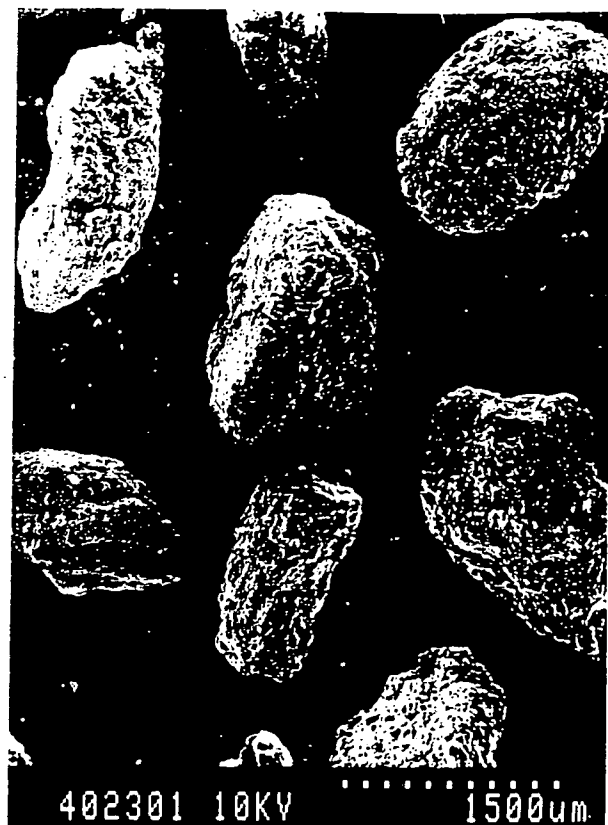
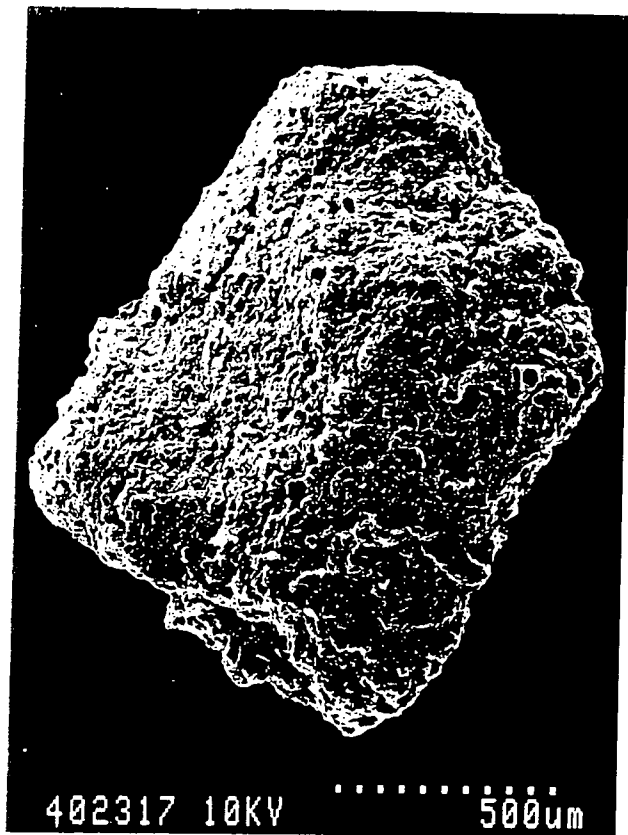


Figure 1.9. Four TEM micrographs of the BPL activated carbon.

### 1.1.5.1 Micropores

The microporous surface ( $S_{mi}$ ) is represented as the walls of the slits, and has the area of several hundred square metres per gram of solid. The surface is related to the volume ( $V$ ) and accessible width ( $l$ ) in equation 1.1. by

$$S_{mi} \text{ (m}^2\text{g}^{-1}\text{)} = 2.10 V^3 \text{ (m}^3\text{g}^{-1}\text{)} \div l \text{ (m)}$$

Equation 1.1.

For micropores  $l$  is small so the area associated with them is much larger than for meso and macropores. The external surface area  $S_e$  includes the walls of the mesopores and macropores as well as the discontinuities of the aromatic sheets. The  $S_e$  values for active carbons are generally very small, with 10-200 ( $\text{m}^2 \text{g}^{-1}$ ). The main difference between  $S_{mi}$  and  $S_e$  is that the adsorption energy value can be twice as high for micropores as compared to the open surface. (36)

This enhancement is due to the overlapping of adsorption forces from the opposite walls in the micropores, this decreases rapidly as the gap between the walls increases. Calculations show that for slit pores with twice the width of the adsorbed molecule then the adsorption force is 1.2 times greater than that of an open surface graphite. This means that the micropores will obviously fill before the molecules adsorb onto the open surface. This is known as Dubinin's theory of volume filling for micropores. (TVFM).

The actual mechanism of adsorption is also different in the micropores compared to the open surface. In the micropores the adsorption corresponds to the filling of volume, whereas for larger pores there is a gradual multilayer formation process. This means that the adsorption of vapours by active carbons is composed of two separate contributions.

- 1) The filling of the microporous volume
- 2) Multilayer build up on the external surface

The microporous volume can be analysed separately from the external surface by using benzene as the adsorbate.<sup>(37)</sup> The microporous volume fills preferentially and can be saturated at room temperature. The additional filling adsorption of nitrogen at 77.78 K gives the value of  $S_e$ . See figure 1.10.

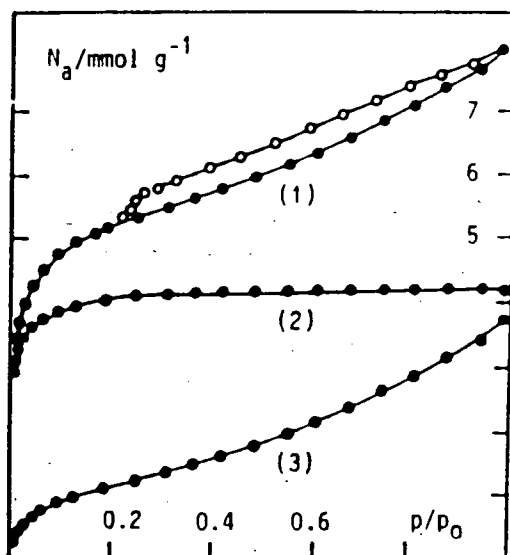


Figure 1.10. The calculated contributions to the overall adsorption isotherm of benzene by carbon A-35 at 293K. 1) Adsorption from micropores. 2) Adsorption from external surface. 3) Adsorption from mesopores. [Bansal et al (1)]

The true surface area of the micropores can be obtained from the adsorption of helium, the small angle scattering of X rays<sup>(38)</sup>, the adsorption of water under certain circumstances<sup>(39)</sup>, or from the distribution curve of the microporosity derived from experiments with molecular probes of known dimensions<sup>(40)</sup>.

### 1.1.5.2 Mesopores, macropores and the external surface

Meso and macroporosity can be assessed by using mercury porosimetry, which is based on the penetration of mercury into the pores under external pressure. Mercury is a non-wetting liquid and will fill circular pores of radii  $>r_p$ , where  $r_p$  is given by equation 1.2.

$$r_p \text{ (nm)} = 7300 \div P(\text{atm})$$

Equation 1.2.

This means that at room pressure the mercury will fill pores with radii greater than 7.3  $\mu\text{m}$ . The limit is  $\approx 2000$  atms, resulting in a pore size lower limit of just 2.0 nm, and hence covering the majority of the meso and macropore range. In reality it does not cover the range  $<3.8$  nm, which often has some contribution to the external surface. However plots of  $S_{cum}$  against  $r_p$  often give a linear representation from 4-15 nm, so the total area down to 2 nm can be extrapolated. The results for  $S_e$  are in good correlation to the results determined from hysteresis loop calculations.

### 1.1.6 Methods for adsorption analysis

Historically adsorption characteristics of various adsorbates have been studied using adsorption isotherms. The adsorption isotherms were first fully classified into five main groups by Bruner, Derning, Derning and Teller<sup>(41)</sup>, and are referred to as the B.D.D.T. classification. The five classes are shown in figure 1.11 along with a composite step isotherm.

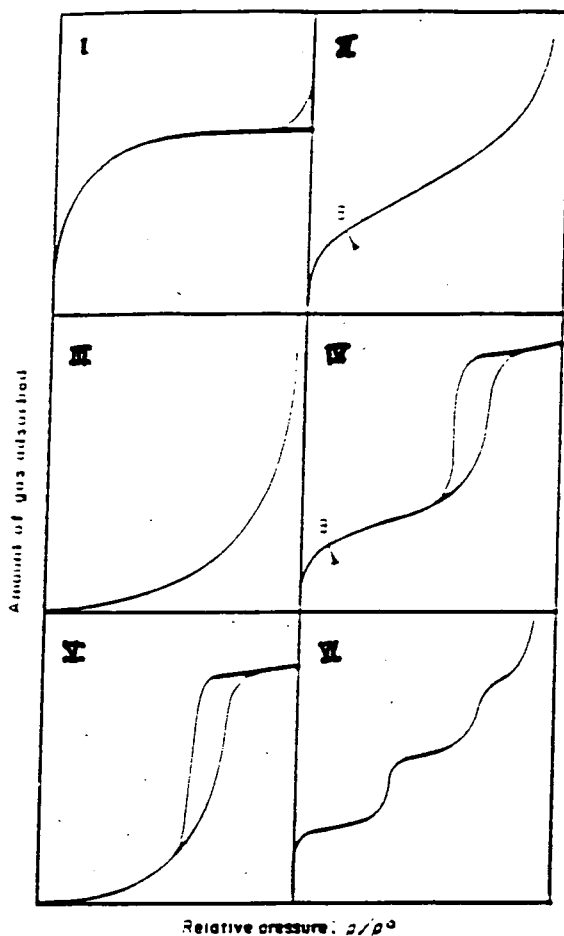


Figure 1.11. The B.D.D.T classification of adsorption isotherm types 1-5.

#### 1.1.6.1 Gravimetric adsorption analysis

The adsorption of gases can be determined volumetrically or gravimetrically<sup>(42)</sup>. Usually the large adsorption capacity of activated carbons means that gravimetric methods are used. The increase in the mass of adsorbent is measured as it comes into contact with the adsorbate. It is possible to measure the mass changes to an accuracy of  $\pm 0.1\text{mg}$ , which in the case of nitrogen gas at 78 K is  $\pm 0.3\text{ m}^2$ , which is small when compared to Se values for typical carbons. The adsorption of  $\text{N}_2(\text{g})$  has become a standard characterisation measurement for micropores, labelled a BET adsorption area for a monolayer adsorption of  $\text{N}_2(\text{g})$  at standard temperature and pressure. A plot of the adsorbate vapour mass uptake against  $p/p^\circ$  of the vapour is generated, for adsorption and desorption, in the isotherm.

### 1.1.6.2 Immersion calorimetry

Immersion calorimetry is undertaken using the Tian-Calvert type calorimeter, the apparatus is shown in figure 1.12.

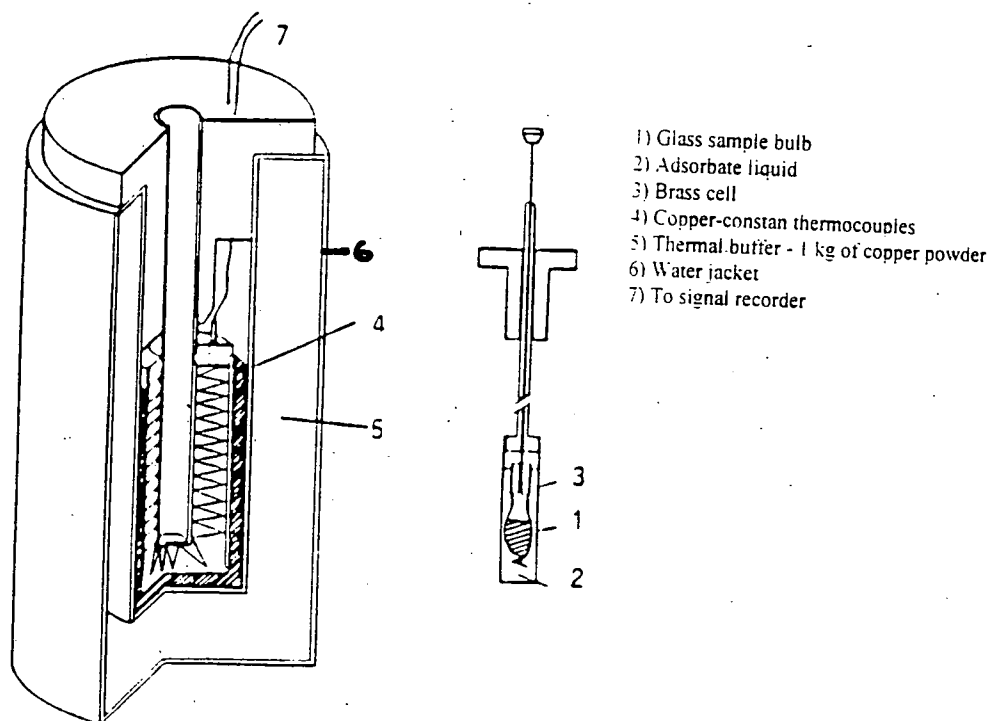


Figure 1.12. Schematic diagram of the Tian-Calvert immersion calorimeter used for active carbons.

This calorimeter is set up to measure enthalpies 2-50 J. The reproducibility is  $\pm 1\%$ , so the technique is very useful for accurate enthalpy determination for immersion in water or organic liquids.

Stoekli et al<sup>(43)</sup> found that the amount of primary adsorption sites is related to the enthalpy of immersion of active carbons in water. These uniform hydrophilic sites are probably of the carbonyl type as they yield  $\text{CO (g)}$  upon desorption. Other types of sites were treated similarly and the total enthalpy was a sum of the individual contributions. Potentially the adsorption branch of the water isotherm can be calculated by using enthalpies of immersion

### 1.1.7 Experimental characterisation of adsorption by activated carbons

The experimental results fall into three sections: consisting of the three types of adsorption isotherm that are measured, a series of results from the immersion calorimetry and some molecular probe work.

#### 1.1.7.1 Gravimetrically determined adsorption isotherms

The physical adsorption of gases by active carbons is described by the Dubinin theory<sup>(39)</sup> which has been developed gradually since 1947. This simple equation covers a range of adsorbate gases but noticeably does not describe the water adsorption isotherm. The state of the adsorbate in the micropores is still open to discussion but a reasonable approximation describes it as a condensed adsorbate at the same temperature and pressure.

Dubinin's theory does describe the adsorption isotherm for non polar molecules such as cyclohexane shown in figure 1.13. The adsorption can be described taking into account purely dispersive forces.

The interaction of water with active carbons does not follow Dubinin's theory and a separate equation has to be developed to describe the adsorption isotherm that is measured and shown in figure 1.14. The adsorption of water is dependent on both the chemical and physical characteristics of the active carbon. This means that any adsorbed amount at a specific relative pressure of 0.6 atms used by Dubinin<sup>(39)</sup> does not necessarily represent a monolayer water capacity adsorbed on the micropore walls. Consequently Dubinin's equations are not applicable.

The third type of adsorption isotherm that has been measured is the adsorption of polar organic vapours, these are typified by the adsorption of methanol shown in figure 1.15.

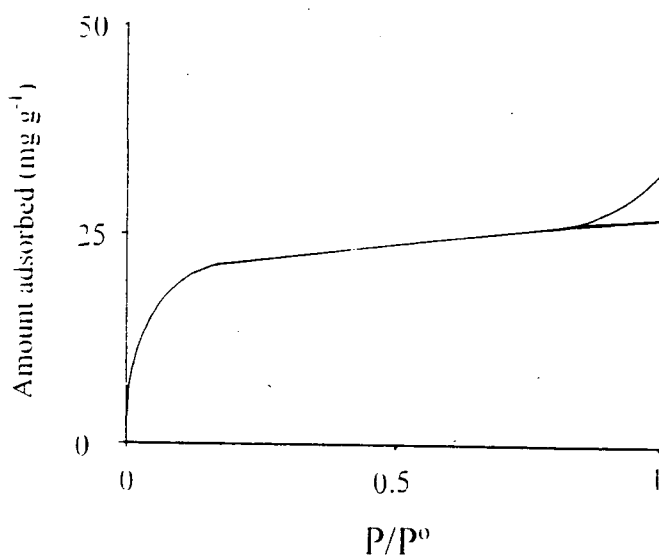


Figure 1.13. Dynamic cyclohexane adsorption isotherm.

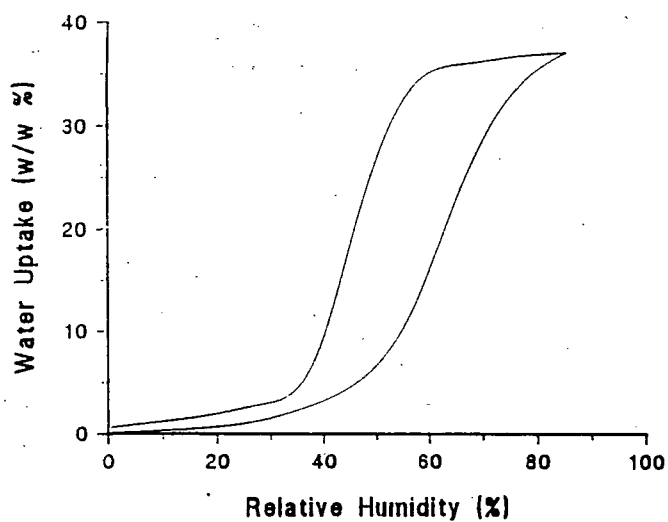


Figure 1.14. Dynamic water adsorption isotherm for BPL at 22°C at 1 l min<sup>-1</sup> flow rate. (C. Pottage C.B.D.E.)

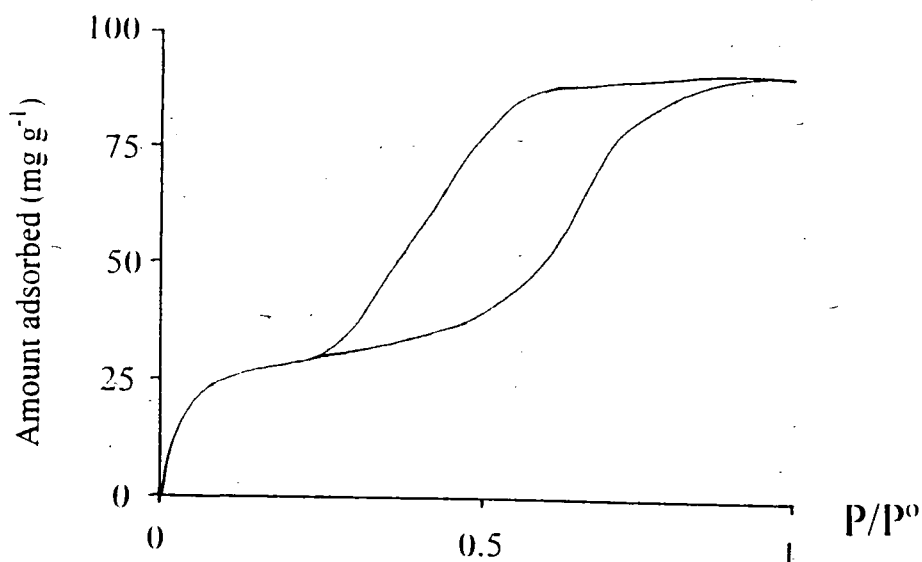


Figure 1.15. Dynamic methanol adsorption isotherm

### 1.1.7.2 Immersion calorimetry

When a solid is brought into contact with a non-reacting liquid, a thermal effect is produced which is termed the heat of adsorption. This thermal effect is from the net integral heat of adsorption in forming an adsorption layer at saturated vapour pressure, plus the heat of wetting of this film. Activated carbons which are highly microporous create thermal effects of wetting the external surface and filling the microporous volume which are easily measured.

For activated carbons the heat of immersion for different liquids varies so the heat of immersion can not be just related to the surface area, but is actually a measure of the accessibility of the surface for a given liquid. The heat of immersion depends on the chemical structure of the carbon surface as well as the nature of the adsorbent. This means that the results can be used to analyse surface polarity, site heterogeneity, hydrophobicity and other surface properties<sup>(44)</sup>. The thermal energetics are high for specific interactions between water and surface oxygen groups on the activated carbons and so it has been suggested that these groups could be analysed using immersion calorimetry<sup>(45)</sup>.

Barton and co-workers<sup>(46-48)</sup> looked at the average polarity of the surface of graphite covered with surface oxide groups. Immersion calorimetry of a series of butyl derivatives with differing dipole moments was carried out. When using n-hexane the surface oxide groups had very little effect on the heat of immersion. However the butyl derivatives varied greatly when the surface oxide groups were present, suggesting that for the molecules with a dipole moment there was an interaction with the electrostatic field at the surface caused by the oxide groups.

This trend for increased immersion heats with greater amounts of surface oxygen was also found in the activated carbon Spheron-6 <sup>(47)</sup> when studying polar molecules such as water and methanol.

Maggs and Robins (49) examined the relationship between surface area and the heat of immersion for several commercial activated carbons and carbon cloths using liquids of varying molecular dimensions. The accessible area as a function of the molecular diameter of the liquid decreased as the molecule increased in size for all the carbons and cloths as shown in figure 1.16.

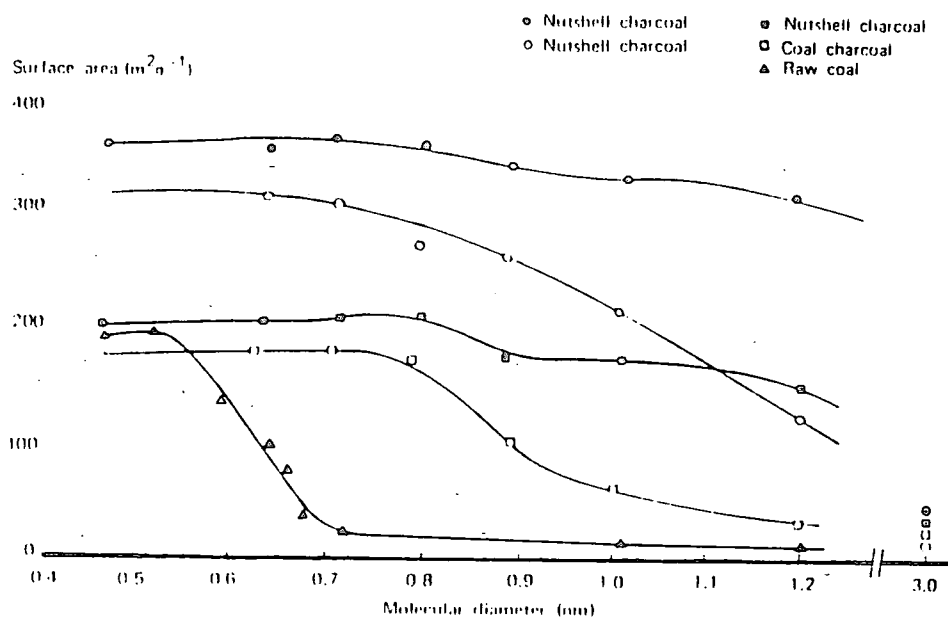


Figure 1.16. The accessible surface area as a function of the molecular dimensions of the wetting liquid for granular charcoals [Maggs and Robbins (49)]

The shape of the plots shows a considerably different porous structure in the various carbons, the highly activated carbons showing a more open structure. When these were compared to the BET nitrogen areas it could be seen that only part of the total area was accessible to even the smallest molecules. The inferred conclusion was that the BET monolayer capacity is actually a pore volume capacity. When the carbons were activated with CO<sub>2</sub> at elevated temperatures, then the areas accessible to all the molecules increased considerably with the degree of activation. Nearly all the BET area was available to benzene at 80% burnoff.

Atkins et al<sup>(50)</sup> measured heats of immersion for charcoal cloth with mainly narrow pores and a commercial activated carbon with a large range of micropores (1-2 nm) using several organic liquids. They found a large variation in  $\Delta H_i$  values, indicating once again that  $\Delta H_i$  is a measure of accessibility not surface area. Since the concept of BET surface area is unrealistic for microporous carbons, they suggest that the representation of  $\Delta H$  per unit surface area is invalid, and so the values of  $\Delta H$  per unit weight of carbon ( $\text{Jg}^{-1}$ ) should be quoted. This notation is used in the following discussion.

Zettlemoyer et al<sup>(51)</sup> determined the heat of immersion of a polymer based carbon, carbosieve-s, with a narrow micropore size distribution (0.5nm), using water, methanol and 2-propanol. They compared  $\Delta H_i$  with pre-coverage of the surface with the immersion liquid.

The immersion heats decreased to a plateau at 20% micropore filling followed by a decrease after 80% filling when using water. There were two plateaus after 25% and 80% for methanol, and when using 2-propanol there was a sharp decrease followed by a plateau. The differential heats of adsorption ( $q_d$ ) were calculated from the slopes of the heats of adsorption plots and drawn against surface coverage. These showed a rapid fall from  $180 \text{ kJmol}^{-1}$  at  $1 \text{ mg g}^{-1}$  adsorption to  $82 \text{ kJ mol}^{-1}$  at  $2 \text{ mg g}^{-1}$  adsorption for water.

In the case of methanol there was also a sharp fall, and the adsorbate approached liquid-like properties at 30% micropore filling. The heats of adsorption for 2-propanol were very different with two maxima occurring at 40% and 90% pore volume filling as shown in figure 1.17.

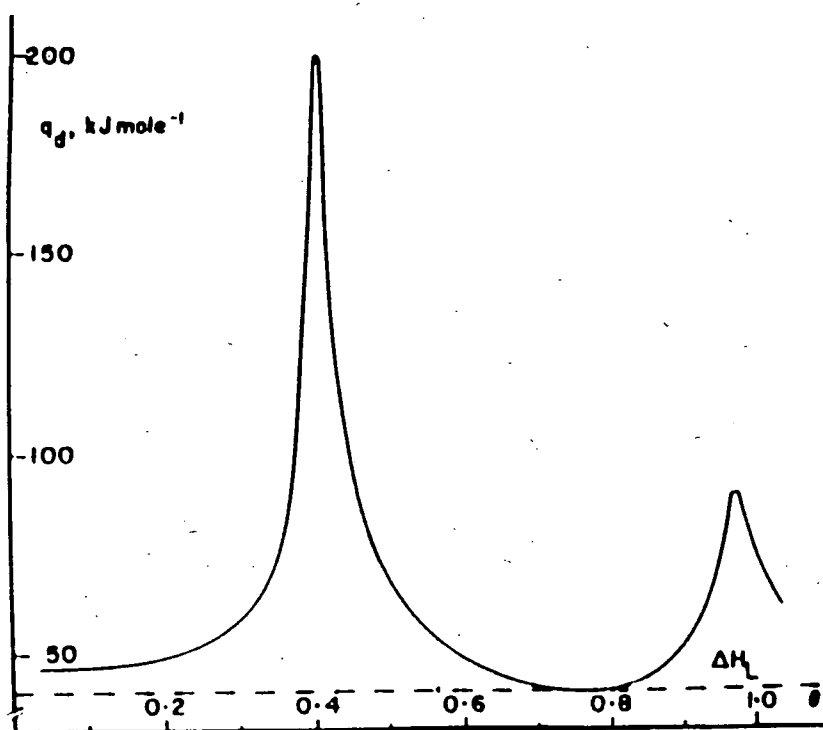


Figure 1.17. The differential heat of adsorption of 2-propanol on carbosieve at 25°C [Zettlemoyer et al (51) ]

The large fall in the heat of adsorption at low coverages was attributed to surface heterogeneity with adsorption occurring at the acid group sites. The difference between methanol and propanol was caused by differing molecular diameters. The theory to explain this is extended a little later on, but the two maxima are interesting in the light of NMR results I have recorded on phosphate adsorption on activated carbons.

Barton et al (52) measured the  $\Delta H_i$  for water and cyclohexane for adsorption onto a BPL carbon oxidised to various degrees with Nitric acid. The results showed that the major influence on  $\Delta H_i$  was the number of surface oxide groups when adsorbing water. They found no numerical relationship between the two but  $\Delta H_i$  increased upto a certain concentration of oxide sites and then no further increase was

observed for additional oxide groups. The results suggested that a concentration of 6 mmol g<sup>-1</sup> of oxide groups was ideal. If the oxide groups were more prolific then they did not encourage any extra adsorption via hydrogen bonding. The data are presented in figure 1.18.

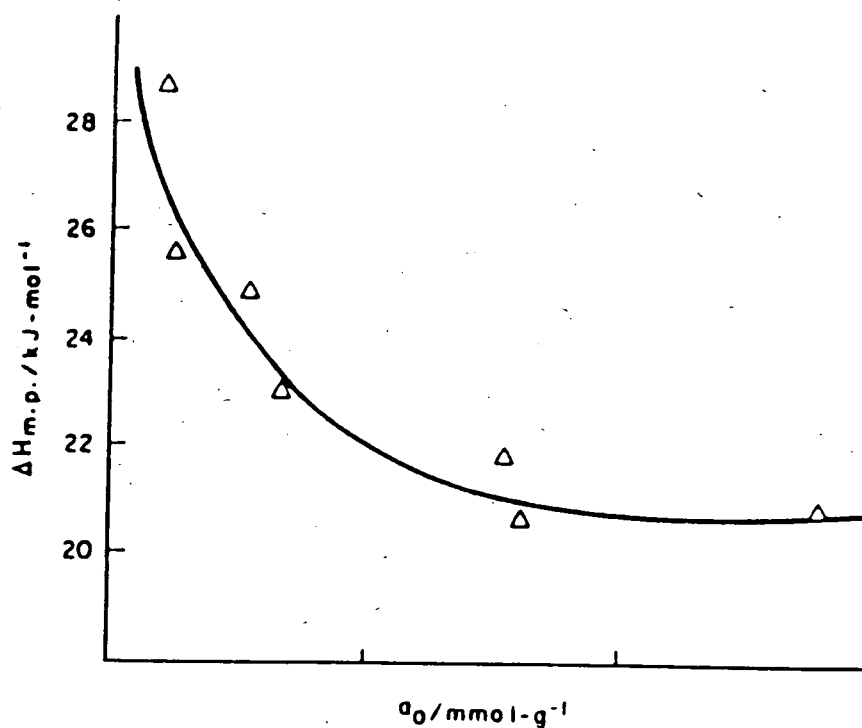


Figure 1.18. The variation of the heat of adsorption in water with the concentration of hydrophilic adsorption centres  $a_0$ . [Barton et al (52)]

The results were different when using cyclohexane, with the molar enthalpy of interaction decreasing rapidly initially, and then falling slowly above the threshold value of 6 mmol g<sup>-1</sup> of surface oxide sites, where the hydrophilic nature is increased. This means that the cyclohexane was affected by the pore filling creating the enthalpy change whereas the water had a major enthalpy change, associated with the surface oxide concentration. The pore filling process had a comparatively small effect in the case of the water adsorption.

### 1.1.7.3 Molecular probes

Research has been undertaken to find pore size distribution and molecular sieve behaviour of activated carbons using organic probe molecules. Dacey and Thomas<sup>(53)</sup> studied the adsorption of various organic molecules onto Saran charcoal. The carbon adsorbed straight chain molecules like n-pentane, and flat molecules such as benzene very rapidly, whereas neopentane was adsorbed more slowly. This was attributed to the presence of slit shaped pores in the carbon.

Rozwadowski and Wojsz<sup>(54)</sup> found that the amount of isooctane ( $r = 0.68\text{nm}$ ) and  $\alpha$  - pinene ( $r = 0.8\text{nm}$ ) which could be adsorbed was much less than benzene and other smaller molecules. The carbons therefore had a number of pores inaccessible to the larger molecules. When compared to  $\text{N}_2$  data only 13% and 7% of the total area was accessible to isooctane and  $\alpha$ -pinene. The area calculated by organic molecules is therefore not of any great relevance to the total volume if the carbon is highly microporous. The micropores for the steam-activated carbons were enlarged, and accepted more of the large adsorbates.

The uptake of butane, isobutane and neopentane according to Walker<sup>(55)</sup>, is dependent on the molecular dimensions of the adsorbate and the temperature of carbonisation. With high carbonisation temperatures ( $>1500\text{ K}$ ) the micropores shrink and the adsorption of neopentane is almost negligible. The adsorption of benzene and cyclohexane is ten times greater than neopentane.

Bansal and co<sup>(56-60)</sup> looked at molecular sieves made from polymer carbons interacting with several organic vapours. He found that adsorption was determined by:

- 1) The carbon pore size.
- 2) The size and shape of the adsorbate molecules.
- 3) The chemical nature of the carbon surface.

### 1.1.8 Theoretical treatment of adsorption by activated carbons

To describe the shape of the adsorption isotherms that were shown in section 1.7.1, several theories have been developed. An activated carbon has a very complicated surface. It has a porous structure which relates to its adsorption capacity and a chemical structure which determines how it interacts with polar and non-polar adsorbates. It has active sites such as edges, dislocations and discontinuities which react with other heteroatoms.

This means that the adsorption behaviour of an activated carbon cannot be analysed by surface area and pore size distribution alone. It also means that any model for adsorption of active carbon adsorbents of a complicated nature is very difficult to devise.

The model has to look at the chemical and porous structure of the carbon. The nature and amount of surface chemical structures, surface area, pore size distribution as well as the chemical/physical properties of the adsorbate all have to be considered. The activated carbon has to be characterised with respect to the number and nature of the chemical structures on the surface, the polarity of the surface, pore size distribution, micropore volume and surface area. This characterisation has been attempted by analysing the adsorption isotherms, calorimetry and molecular probe results.

#### 1.1.8.1 Adsorption of non-polar organic vapours

The adsorption of non-polar organic vapours is purely physical involving short range repulsive interactions and dispersion/attraction forces. The dispersive forces are an increase in the energy of adsorption in the micropores due to the superposition of the adsorption potentials of opposite pore walls. The isotherms are explained by Dubinin's theory of volume filling of micropores (TVFM)<sup>(61)</sup>. The characteristic energy  $E^0$  increases from 8.5-35 kJ mol<sup>-1</sup> for benzene depending on the micropore structure. This explains the very fast rise in the adsorption isotherm at low  $P/P^0$  shown in figure 1.13.

For non polar molecules the adsorption patterns were generally BDDT type 1 with 90-95% of adsorption at pressures  $P/P^0 < 0.2$ . This means the carbons were very microporous with the pores being only a few molecular diameters in width.

### 1.1.8.2 Adsorption of water vapours

There has been a lot of work on the adsorption of water vapour, trying to give reasons for the shape of the adsorption isotherm and its hysteresis as shown in figure 1.14.

There are a few ambiguities which have been raised in the experimental results and these are still under discussion. The role of associated oxygen and capillary condensation in the adsorption process are not fully understood as yet.

Dubinin et al<sup>(62-64)</sup> have the view that the active sites and their oxygen groups act as primary adsorption centres, which the water molecules can be bound to at low pressure. These adsorbed water molecules then act as secondary adsorption sites, where the water is adsorbed by hydrogen bonding. As the relative pressure builds up then two-dimensional islands of water are generated. These islands eventually join up to form a continuous film or monolayer over part of the carbon's surface. Hysteresis arises from the fact that while adsorption occurs through cluster formation, desorption comes from a continuous layer in non porous carbons and from menisci in porous carbons. Obviously the forces on adsorption only apply to the active sites, and are smaller than the ones for the whole layer on desorption, so the desorption forces are inherently greater and the requisite pressures higher.

Conversely Puri and workers<sup>(65,66)</sup> looked at a range of carbons with differing oxygen content and found that the  $\text{CO}_2(\text{g})$  forming sites, when evacuated, were the sites which adsorbed water. They found that if any of the  $\text{CO}_2(\text{g})$  evolving sites were present, then the adsorption/desorption loop would not meet at zero. This suggested that the water was bound to the sites and couldn't be removed on desorption. The amount of water was one mole of water per mole oxide site. The rest of the oxygen combined to the carbon had little effect on the adsorption or hysteresis. When the  $\text{CO}_2(\text{g})$  evolving sites were increased then the hysteresis increased and conversely when reduced the hysteresis was less pronounced. Their conclusion was that capillary condensation doesn't play a part in the adsorption of water.

Barton et al (52) found that the adsorption of water vapours onto BPL - active carbon was affected more by hydrophilic centres than pore volume. They found that 1.6 mols of water were adsorbed per acid group.

Youssef<sup>(67-69)</sup> found that carbon activated using  $ZnCl_2$  followed by  $HNO_3$  actually fixed oxygen deep into the micropores, so then hysteresis was pronounced. The carbon held more water on desorption compared to other samples. They also found that  $N_2(g)$  BET values differed from  $CO_2(g)$  ones suggesting that for  $H_2O(g)$  adsorption the monolayer represents the number of reacting groups rather than the number of adsorbed molecules required to form a monolayer.

The opposing view from Wiig and Juhola<sup>(70,71)</sup> suggests that condensation of water in the capillaries is the dominant process. They say that even the filling of the micropores occurs by capillary condensation. They suggest that physical/chemical adsorption becomes significant if the carbon is highly microporous with hydrophilic groups at the surface, and this is the reason that the desorption curve doesn't lower the adsorption part.

Kiselev and co<sup>(72-74)</sup> looked at porous and non-porous carbons with varying oxygen content. They found adsorption depended on degree of oxidation as well as porosity. The more hydrophobic the surface was, the more important the capillary condensation became. The suggestion was that the steep rise in the isotherm was caused not by islands merging, but from capillary condensation which also caused hysteresis. Kiselev said that initial adsorption was in the most constricted portions of the pores with the largest adsorption potential. The thickness of the adsorbed layer increases with pressure until a continuous layer is formed and capillary condensation occurs. The process extends to larger portions of the pores as the pressure increases. Hysteresis occurs because desorption occurs in wide parts of the pore body, compared to the adsorption which occurs at the narrower pore neck.

Bansal et al.<sup>(75)</sup> observed adsorption of water vapour onto polymer based carbons with different porosities and oxidised them to vary the oxygen content. They found that the shape of the isotherm varied with the carbon type, indicating the adsorption mechanism varied with the differing porosities. Carbons with differing pore structures but similar oxygen content showed similar results at low pressures, but differed significantly at higher pressures. This suggests that oxygen sites are important initially and pore structure important at higher pressures. They also found that increasing the oxygen content increased water uptake when  $p/p^0 < 0.5$  (low P) continuously. However when  $p/p^0 > 0.5$  there was no increase, carbons with no associated oxygen took up virtually no water when  $p/p^0 > 0.5$  as shown in figure 1.19.

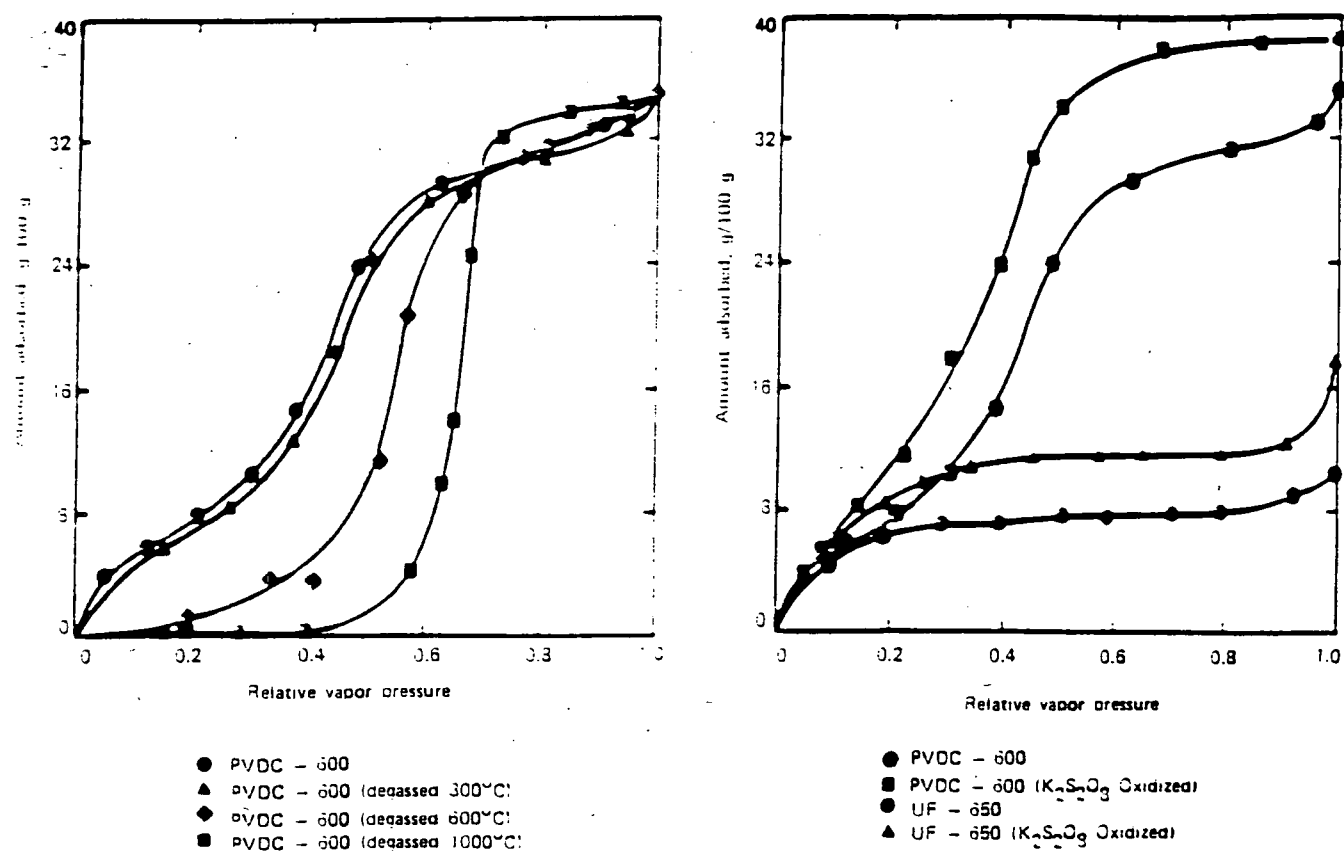


Figure 1.19. Water vapour adsorption isotherms on polyvinylidene chloride (PVDC) and urea formaldehyde (UF) based carbons, before and after outgassing and oxidation. [Bansal et al (75)]

When Saran charcoal was degassed at  $1000^{\circ}\text{C}$  or activated in steam at  $850^{\circ}\text{C}$ , the adsorption of water vapour at lower pressures decreased, but at higher pressures the adsorption increased as shown in figure 1.20.

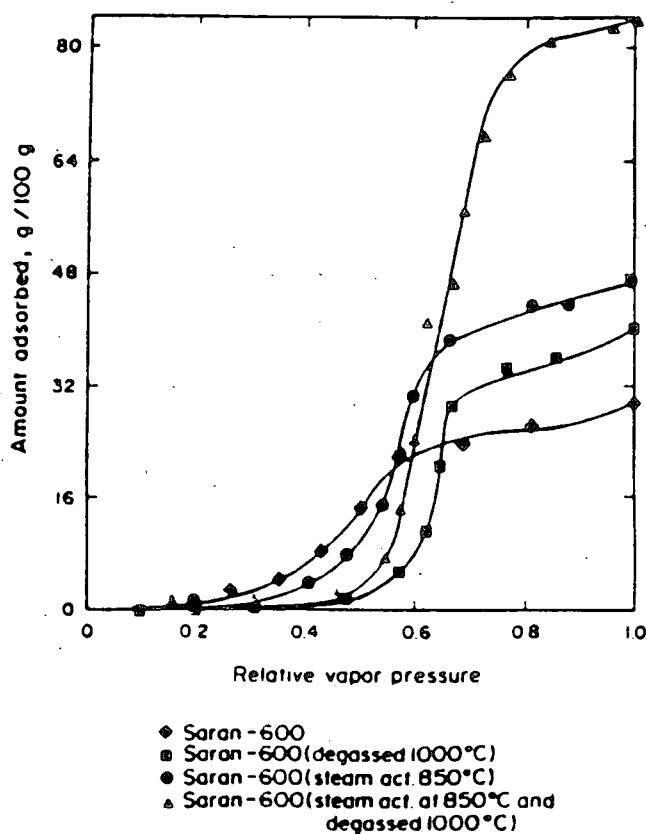


Figure 1.20. Water vapour adsorption isotherms on outgassed and steam activated Saran carbon. [Bansal et al (75)]

The decrease in adsorption at lower pressures was caused by a reduction in combined oxygen as the sample was degassed. The increase at higher pressures was due to the widening of the pores by the activation process. This was further supported by an increase in  $\text{H}_2\text{O}$  adsorption when the activated sample was degassed at  $1000^{\circ}\text{C}$ . The widening of the pores was evident on pore size distribution curves.

The conclusions were that at low pressures the adsorption process is dominated by surface oxygen groups attached to single carbon atoms forming on the wall of micropores. However as the carbon becomes more hydrophobic the porosity dominates and capillary condensation becomes more significant. The hysteresis is still present when all the combined oxygen was removed at  $1000^{\circ}\text{C}$  outgassing, confirming the capillary condensation was present as shown in figure 1.21.

The most recent theories of H. Liu et al<sup>(76)</sup> attempt to describe the hysteresis in terms of two effects. The molecular packing effects in the potential wells associated with narrow pores means that it is easier to adsorb the water than to desorb it. The interconnectivity of the pore structure also creates some hysteresis, where at high relative pressures the adsorbed molecules create a larger diffusion coefficient through the pores as they block them up. This means that it is easier for the adsorbate to adsorb into clear paths than to desorb from the blocked passages.

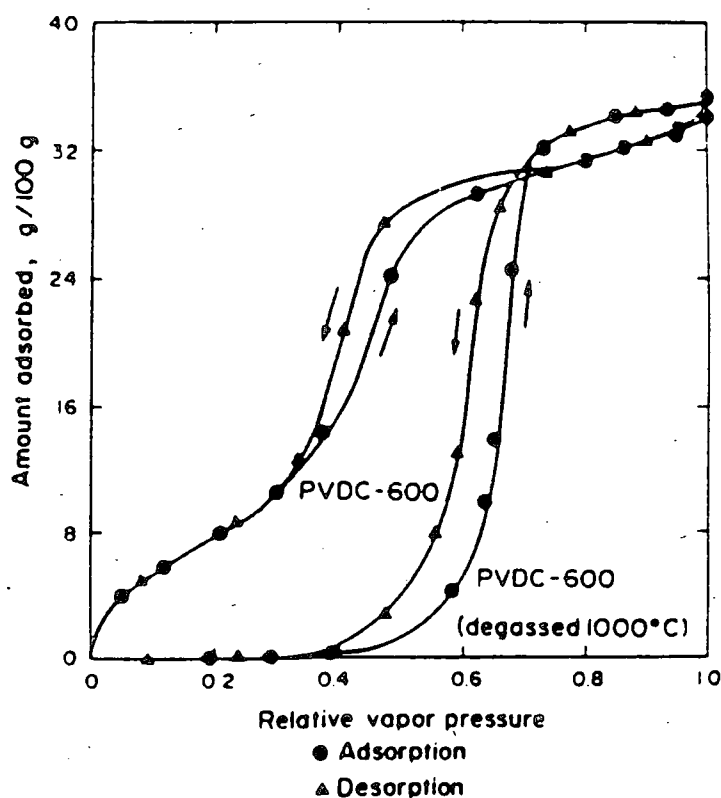


Figure 1.21. Water vapour adsorption-desorption isotherms for (PVDC) carbon, before and after outgassing at  $1000^{\circ}\text{C}$ . [Bansal et al (75)]

### 1.1.8.3 Adsorption of polar organic vapours

The theory describing the adsorption of polar vapours has to describe the isotherm in figure 1.15. The best description of adsorption onto microporous carbons is given by the Polanyi-Dubinin potential theory.<sup>(77-78)</sup> However this is better when the adsorption energy is not too heterogeneous, and the state properties of the adsorbate are very similar to the liquid phase. For polar molecules the two states are different so the theory needs to be adapted for accurate interpretation.

Rozwadowski and co.<sup>(54,79)</sup> looked at the adsorption of aliphatic alcohols and amines on active carbons. They compared the state of the adsorbate and the pure liquid and worked out the share relevant to dispersive adsorbate-adsorbent reactions.

Polar adsorbates such as methanol and ethanol followed the Dubinin-Polyani theory of volume filling of micropores at high pressures. There were however deviations at lower pressures suggesting two mechanisms of adsorption. These differences were attributed to the pure liquid. If this was taken into account, the theoretical curves were closer to experimental values. The wetting ratio  $W/W_0$  is dependent on the amount of the adsorbate. The degree of association depends on the amount of adsorbate and these  $P^0$  values were used for calculating adsorption work  $A$  in the Dubinin-Polyani equation given in equation 1.3.

$$\theta = (W/W_0 \{A / \beta \epsilon_0\}^2)$$

Equation 1.3.

where :

$$A = RT \ln (P^0/p)$$

Equation 1.4.

$A$  depends on temperature and on the amount of liquid adsorbed. The fugacity ( $f^*$ ) of the saturated vapour at a given stage of adsorption is given in equation 1.5. as

$$f^* = \nu P^0$$

Where  $\nu$  = activity coefficient dependent on the degree of pore filling

Equation 1.5.

The activity coefficients for some alcohols and amines were calculated and vary from unity by some degree. Any value deviating from one indicates the properties of the adsorbate are different from the liquid phase. Values below unity show strong association of the adsorbate, this was especially noticeably in amines. Alcohols only gave values less than unity when at low coverage.

The workers found that at large percentage coverage the  $\Delta S^*$  values for the adsorbate and pure liquid were very similar, and the adsorbate can be approximated to the liquid state.

Rozwadowski and Wojsz<sup>(54)</sup> concluded that the adsorption of polar molecules on microporous carbons involves the chemisorption or strong specific adsorption at low pressures, the energy of these interactions being much greater than the dispersive interactions. The positive  $\Delta S^*$  and  $\Delta H^*$  values in mid/high pressure ranges indicate strong association of the amine molecules adsorbed compare to bulk properties. The theory of adsorption at high pressures is according to the theory of pore filling. They suggest that the shape of the experimental isotherm is a result of two overlapping and opposing interactions; adsorbate-adsorbent and adsorbate-adsorbate interactions. This is affected by the nature of the adsorbate and the nature of the carbon surface.

Adsorption of polar molecules such as methanol and ethanol was influenced by surface oxide groups. The adsorption of these alcohols and benzene decreased as the amount of oxygen groups decreased, whereas the adsorption of other molecules increased with gradual elimination of acidic oxygen groups.

Stoekli et al<sup>(80)</sup> also found that successive adsorption-desorption cycles actually mutated the surface; when large molecules such as trimethyl phosphate were used, the average pore size after three adsorption-desorption cycles was increased considerably, and the heterogeneity was increased.

The benzene adsorption seems to be influenced by surface oxygen groups which yield  $\text{CO}_{(g)}$ , the theory behind this is that the  $\pi$  electron system interacts with the partially positive charge on a carboxyl carbon in quinonic oxygen in the micropores. Benzene complexed with these sites requires high energy to diffuse out and so hysteresis is observed.

### 1.1.9 Active sites in carbons available for adsorption

Active carbons have a structure with aromatic sheets with condensed ring systems stacked in non-polar layers. The sheets have limited dimensions so obviously there is a significant amount of edges. There are also defects, dislocations and discontinuities. The carbon atoms have unpaired electrons and residual valency with an associated higher potential, these are termed active sites. A lot of research has been aimed at characterising these sites and how they chemisorb oxygen. Initially Rideal and Wright<sup>(81)</sup> found that there were different active sites when they used oxygen gas on active carbon surfaces. They suggested three types of site which each behaved differently at various oxygen pressures. Puri and Bansal<sup>(82)</sup> looked at sugar and coconut carbons at various oxygen temperatures, and analysed the production of  $\text{H}_2(g)$  as an elimination product. They found the  $\text{H}_2(g)$  was eliminated in a number of steps as  $\text{O}_2(g)$  temp went up, they concluded that the chemisorbed  $\text{H}_2(g)$  originally on the carbon was bonded in a range of different sites. Various workers in the field were finding that there was definitely more than one type of chemisorbed oxygen on the activated carbon. Hart et al<sup>(83)</sup> found that there were two types of adsorption at  $300^\circ\text{C}$ , on activated graphon, one fast and one slower. The faster adsorption had an activation energy of  $7.4 \text{ kcal mol}^{-1}$ , and the maximum amount of oxygen chemisorbed on these sites was 2.6% of the total BET surface area.

Bansal et al<sup>(84-86)</sup> characterised ultraclean surfaces of graphon by looking at the chemisorption of oxygen at low temperatures. ( $70^\circ\text{C}$ - $160^\circ\text{C}$ ). The graphon sample was cleaned in a vacuum of  $10^{-9}$  torr in a stainless steel system shown in figure 1.22.

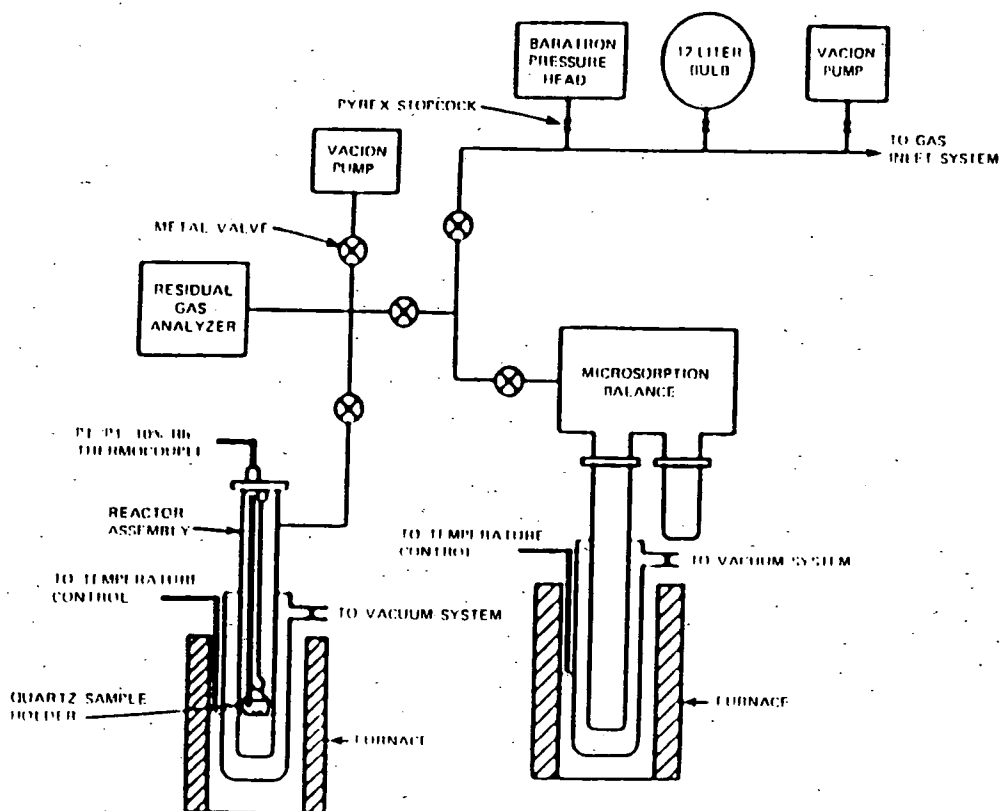


Figure 1.22. Schematic of ultraclean vacuum system for the study of oxygen chemisorption. [Bansal et al (85)]

The apparatus includes a gas inlet system, a vacuum assembly and an adsorption unit with a residual gas analyser and a microdesorption balance.

The results of input energy ( $q$ ) against log time showed linear regions. The low pressures had only one linear region, but as the pressure increased then the amount of linear regions increased upto 683 mtorr, and then dropped off. This was explained as the same chemisorption process occurring at a range of different sites. The activation energies of adsorption from Arrhenius plots were found to be independent of surface coverage for any one group of sites. The  $E_a$  for each site was however different and in total, five different sites were discovered with  $E_a$  from 3.1-12.4 kcal mol<sup>-1</sup>.

The existence of these different types of site has been attributed to the geometry of the carbon atoms at the surface. The activated complex forming between the gas atoms and the C-C surface will have varying potential energy depending on the C-C spacing. This will give a variation in the corresponding activation energy of chemisorption. Some of the theoretical  $E_a$  values were calculated by Sherman and Eyring<sup>(87)</sup> using likely C-C spacings and agree with experimental values well. These were terminating faces and gaps between edge carbons with adjacent basal planes.

Puri et al<sup>(88-90)</sup> gave evidence for completely different sites termed unsaturated sites. The sites could be determined by reacting  $\text{Br}_2$  and KBr solution. The number of sites was related to combined oxygen coming off as  $\text{CO}_2(\text{g})$ , one mole of unsaturated site being created by chemisorption of two moles of oxygen evolved as  $\text{CO}_2(\text{g})$ .

#### 1.10 Surface modification

Activated carbons invariably have appreciable quantities of adsorbed oxygen chemisorbed to the surface. All microcrystalline carbons have associated hydrogen chemically bonded at the edges of the graphitic planes. The carbons can fix heteroatoms (S, N, Cl, Br,) into the surface as stable structures, they can also adsorb certain molecules such as phenols, amines and cationic species.

X ray diffraction shows that the adsorption occurs at the edges or corners of aromatic sheets, at defects within the sheets or within the aromatic sheets as heterocyclic compounds.

##### 1.1.10.1 Impregnation of the active carbon

Impregnation of the active carbon is often associated with dispersion of small metal and metal oxide particles on the surface, providing excellent catalytic activity. The primary role of the carbon is to favour the highly dispersed metal phase by physically separating the metal crystallites over the extended surface area of the support. The impregnation of metals prior to activation also modifies the gasification properties and pore structure of the final activated product. This enables the activated carbon to a certain extent to be designed and produced with particular properties.

Activated carbons which have been impregnated with potassium iodide<sup>(91)</sup> and amines<sup>(92)</sup> have been used by the nuclear industry for the retention of radioactive iodine compounds from coolant airstreams.

Impregnation with pyridine and picoline has been used to keep ASC Whetlerites from degrading in the presence of moisture<sup>(93)</sup>. Activated carbons impregnated with  $\text{Cu}^{2+}$ ,  $\text{Ag}^+$ ,  $\text{Cr}^{\text{VI}}$ ,  $\text{NH}_4^+$  and  $\text{CO}_3^{2-}$  were found to be very efficient in the chemisorption of arsine, hydrogen cyanide, cyanogen chloride, chloroform and phosgene. These are used for military respirators as explained in a later chapter.

#### 1.1.10.1.1 The impregnation process.

The metal ions can be added to the carbon prior to the activation process and are dispersed within the activated carbon that is produced. Baker and Pozionek<sup>(94)</sup> also used a rotary evaporator on activated carbons to impregnate the volatile species and non volatile impregnants were adsorbed from alcohol solutions. The level of impregnation can then be determined by using a weight difference method.

#### 1.1.10.2 Modification of the carbons by halogenation

The treatment of activated carbons with halogens has been studied by several people trying to modify the surface character. The halogen can be introduced by physical adsorption<sup>(95)</sup> and chemically via addition to active sites<sup>(96)</sup>, exchange with chemisorbed hydrogen<sup>(97)</sup> and surface oxidation.<sup>(98)</sup>

The halogens are fixed to the surface in the form of carbon-halogen surface compounds and are thermally very stable. Reyerson and co.<sup>(99)</sup> found that appreciable quantities of chlorine and bromine from the gas phase were fixed irreversibly to the surface. The adsorption characteristics of chlorine containing activated carbons according to Alekseevskii and Likharev<sup>(100)</sup>, were better than many commercially available carbons. For this reason the M.O.D. are interested in studying adsorption onto a carbon which has been treated with chlorine gas. The chlorine gas is adsorbed well into the microporous structure and is therefore irreversibly bound.

## References

- 1) R. C. Bansal, J. B. Donnet and F. Stoekli, *Active carbon*, Marcel Dekker, New York, 1988.
- 2) M. Iley, H. Marsh and R. J. Reinoso, *Carbon*, 1973, **11**, 633.
- 3) R. J. Reinoso and J. Gonzalez, *Carbon*, 1984, **22**, 13.
- 4) D. M. Mackay and P. V. Roberts, *Carbon*, 1982, **20**, 95.
- 5) M. M. Dubbinin and E.D. Zaverina, *Dokl Akad. Nauk. SSSR.*, 1949, **65**, 295.
- 6) M. Smisek and S. Cerny in *Active carbon*, Elsevier, Amsterdam, 1970.
- 7) A. N. Weinerberg and T.M. O'Grady, *U.S. Patent 4,082,694*, Apr. 4, 1978.
- 8) H. Nishino, H. Kubo and H. Ichukawa, *U.S. Patent 2,764,561*, Oct. 9, 1973.
- 9) P. Ehrburger, A Addoun, F. Addoun and J. B. Donnet, *Submitted for presentation at FUNCAT COGAS conference*.
- 10) F. Kraehenbuehl, H. F. Stoekli, P. Ehrburger and A Addoun, *Carbon*, 1986, **24**, 112.
- 11) B. Rand and H. Marsh, *Carbon*, 1971, **9**, 79.
- 12) W.M. Kalbach, L. F. Brown and R. E. Wert, *Carbon*, 1970, **8**, 117.
- 13) H. Marsh and B. Raand, *Carbon*, 1971, **9**, 47.
- 14) B. McEnancy and N. Dovaston, *Carbon*, 1975, **13**, 515.
- 15) K. Tomkow, T. Siemieniewska, F. Czechowski and A. Gankowska, *Fuel*, 1977, **56**, 121.
- 16) J. Caron. *Private communication*. 1985.
- 17) J. Zawadzki, *Carbon*, 1981, **19**, 19.
- 18) B. R. Puri and R. C. Bansal, *Carbon*, 1964, **1**, 451.
- 19) R. C. Bansal, T. L. Dhami and S. Parkash, *Carbon*, 1977, **15**, 157.
- 20) G. Trembley, F. J. Vastola and P. L. Walker, *Carbon*, 1978, **16**, 35.
- 21) S. Matsumoto and N. Seteka, *Carbon*, 1979, **17**, 303.
- 22) S. S. Barton, D. J. Gillespie and B. H. Harrison, *Carbon*, 1973, **11**, 649.
- 23) J. V. Hallum and H. V. Drushell *J. Phys. Chem.*, 1958, **62**, 110.

- 24) M. Starsinic, R. L. Taylor and P. L. Walker, *Carbon.*, 1983, **21**, 69.
- 25) Y. H. Pao, in *Optoacoustic spectroscopy and detection*, Academic press, New York, 1977.
- 26) V. A. Garten and D. E. Weiss, *Rev. Pure. Appl. Chem.*, 1957, **7**, 69.
- 27) G. Ishizaki and I. Marti, *Carbon.*, 1981, **19**, 409.
- 28) J. M. O'Reilly and R. A. Mosher, *Carbon.*, 1983, **23**, 47.
- 29) J. Van Driel in *Activated Carbon a fascinating material*, eds. A. Capelle and F. De. Vooyo, Norit N. V., Netherlands. 1983, p. 40.
- 30) W. G. Dauben and W. W. Epstein, *J. Org. Chem.*, 1959, **24**, 1595.
- 31) J. M. Thomas, E. L. Evans, M. Barber and P. Swift, *3rd conf. Ind. Carbon Graphite. London, Soc. Chem. Ind.* 1971, 411.
- 32) L. A. Solano, R. J. Reinoso, M.J. Martinez and L. J. D. Gonzalez, *Adsorp. Sci. Technol.*, 1984, **1**, 317.
- 33) H. F. Stoekli, A. Perrt and P. Mena, *Carbon.*, 1980, **18**, 443.
- 34) H. Marsh, D. Crawford, T. M. O'Grady and A. Weinenberg, *Carbon.*, 1982, **20**, 419.
- 35) A. Oberlin, M. Villey and A Combaz, *Carbon.*, 1980, **18**, 347.
- 36) D. H. Everett and J. C. Powl, *J. Chem. Soc. Faraday trans. I.* 1976, 619.
- 37) S. J. Gregg and K. S. W. Sing in *Adsorption, surface area and porosity.*, Academic press, London. 1982.
- 38) A. Janosi and H. F. Stoekli, *Carbon.*, 1979, **17**, 465.
- 39) M. M. Dubinin, *Carbon.*, 1986, **24**, 355.
- 40) F. Kraehenbuehl, H. F. Stoekli, A. Addoun, P. Ehrburger and J. B. Donnet, *Carbon.*, 1986, **24**, 483.
- 41) S. J. Gregg, *Adsorption, surface area and porosity*, ed. S. J. Gregg and K. S. W. Sing. Academic press, London, 1967.
- 42) H. F. Stoekli and F. F. Kraehenbuehl, *Carbon.*, 1984, **22**, 297.
- 43) H. F. Stoekli, F. F. Kraehenbuehl and D. Morel, *Carbon.*, 1983, **21**, 589.
- 44) J. W. Whalen, *J. Phys. Chem.*, 1961, **65**, 1676.

- 45) H. F. Stoekli and F. F. Kraehenbuehl, *Carbon*, 1982, **19**, 353.
- 46) S. S. Barton, G. L. Boulton and B. H. Harrison, *Carbon*, 1972, **10**, 391.
- 47) S. S. Barton and B. H. Harrison, *Carbon*, 1972, **10**, 745.
- 48) S. S. Barton and B. H. Harrison, *Carbon*, 1975, **13**, 47.
- 49) F. A. P. Maggs and G. A. Robbins in *Characterisation of porous solids*, eds. S. J. Gregg, K. S. W. Sing and A. Capon, Soc. of Chem. Ind., 1979, p. 50.
- 50) D. Atkins, A. I. McLeod, K. S. W. Sing and A. Capon, *Carbon*, 1982, **20**, 339.
- 51) A. C. Zettlemoyer, P. Pendleton and F. J. Micale in *Adsorption from solution*, eds. R. H. Ottewill, C. H. Rochester and A. L. Smith, Academic press, New York, 1983, p. 113.
- 52) S. S. Barton, M. J. B. Evans, J. Holland and J. E. Koresh, *Carbon*, 1984, **22**, 265.
- 53) J. R. Dacey and D. G. Thomas, *Trans. Faraday Soc.*, 1954, **50**, 740.
- 54) M. Rozwadowski and R. Wojsz, *Chem. Papers.*, 1975, **29**, 660.
- 55) P. L. Walker, Jr, L. G. Austin and S. P. Nandi in *Chemistry and physics of carbon*, Vol. 2, ed. P. L. Walker, Jr, Marcel Dekker, New York, 1966, p. 257.
- 56) R. C. Bansal and T. L. Dhami, *Carbon*, 1980, **18**, 137.
- 57) R. C. Bansal and T. L. Dhami, *Carbon*, 1980, **18**, 297.
- 58) R. C. Bansal and T. L. Dhami, *Indian J. Tech.*, 1985, **23**, 92.
- 59) R. C. Bansal and T. L. Dhami in *First Indian conf. Carbon*, December 1982, Proc. Indian Carbon Soc. Publ.
- 60) R. C. Bansal, S. Parkash and T. L. Dhami, *Indian J. Chem.*, 1980, **19A**, 1116.
- 61) M. M. Dubinin in *Progress in surface and Membrane Science*, Vol. 9, ed. D. A. Cadenhead, Academic press, New York, 1975, pp. 1-70.
- 62) M. M. Dubinin, E. D. Zaverina, and V. V. Serpinski, *J. Phys. Chem. Soc.*, 1955, 1760.
- 63) M. M. Dubinin, *Carbon*, 1980, **18**, 355.
- 64) M. M. Dubinin and V. V. Serpinski, *Carbon*, 1981, **19**, 402.
- 65) B. R. Puri, K. Murari and D. D. Singh, *J. Phys. Chem.*, 1961, **37**, 65.
- 66) B. R. Puri, *Carbon*, 1966, **4**, 391.

- 67) A. M. Youssef, *Carbon.*, 1975, 13, 449.
- 68) A. M. Youssef, *Carbon.*, 1974, 12, 443
- 69) A. M. Youssef, T. M. Ghazy and T. El. Nabarawy, *Carbon.*, 1982, 20, 113.
- 70) E. O. Wiig and A. J. Juhola, *J. Am. Chem. Soc.*, 1949, 71, 561.
- 71) A. J. Juhola and E. O. Wiig, *J. Am. Chem. Soc.*, 1949, 71, 2069.
- 72) A. V. Kiselev and N. V. Kovalena, *Zh. Fiz. Khim.*, 1956, 30, 2775.
- 73) N. N. Avgul, D. M. Dzhigit, A. V. Kiselev and K. D. Scherbakova, *Dokl. Akad. Nauk. SSSR.*, 1953, 105, 92.
- 74) N. N. Avgul, D. M. Dzhigit, A. V. Kiselev and K. D. Scherbakova, *Dokl. Akad. Nauk. SSSR.*, 1955, 101, 285.
- 75) R. C. Bansal, T. L. Dhami and S. Parkash, *Carbon.*, 1978, 16, 389.
- 76) H. Liu, L. Zhang and N.A. Seaton, *Langmuir.*, 1993, 9, 2576.
- 77) M. M. Dubinin in *Chemistry and Physics of Carbon*, Vol. 2, ed. P.L. Walker. Jr, Marcel Dekker, New York, 1966, pp. 1-70.
- 78) M. M. Dubinin, *Zh. Fiz. Khim.*, 1965, 39, 1305.
- 79) M. Rozwadowski, J. Siedlowksi and R. Wojsz, *Carbon.*, 1979, 17, 411.
- 80) H. F. Stoekli, A. Perret and P. Mena, *Carbon.*, 1980, 18, 443.
- 81) E. K. Rideal and M. W. Wright, *J. Am. Chem. Soc.*, 1925, 1347.
- 82) B. R. Puri, S. L. Malhotra and R. C. Bansal, *J. Indian Chem. Soc.*, 1963, 40, 179.
- 83) P. J. Hart, F. J. Vastola and P. L. Walker. Jr, *Carbon.*, 1967, 5, 363.
- 84) R. C. Bansal, F. J. Vastola and P. L. Walker. Jr, *J. Colloid Interface Sci.*, 1970, 32, 187.
- 85) P. L. Walker. Jr, R. C. Bansal and F. J. Vastola in *The structure and chemistry of solid surfaces*, Wiley, 1969, p81.
- 86) R. C. Bansal, F. J. Vastola and P. L. Walker. Jr, *Carbon.*, 1971, 9, 185.
- 87) A. Sherman and H. Eyring, *J. Am. Chem. Soc.*, 1932, 54, 2661.
- 88) B. R. Puri, N. K. Sandle and O. P. Mahajan, *J. Chem. Soc.*, London, 1963, 4880.
- 89) B. R. Puri and R. C. Bansal, *Carbon.*, 1966, 3, 523.
- 90) R. C. Bansal, T. L. Dhami and S. Parkash, *Carbon.*, 1980, 18, 395.

- 91) B. H. M. Billings, J. B. Docherty and M. J. Bervan, *Carbon.*, 1984, **22**, 83.
- 92) D. A. Collins, L. R. Taylor and R. Taylor, in *Proc. 9th AEC Air Cleaning Conf.* CONF. 660904 Vol 1 1957, p. 59.
- 93) R. J. Grabenstetter and F. E. Blace, in *Summary of Technical Report of Div. No. 10 NDRC Military problems with aerosol and Nonresistant Gases, Vol 1* , PB 158505, 1964, Chapter 4.
- 94) J. A. Baker and E. J. Poziomek, *Carbon.*, 1974, **12**, 45.
- 95) D. L. Ghandi S. K. Sharma, A. Kumar and B. R. Puri, *Indian J. Chem.*, 1938, **13**, 1317.
- 96) B. R. Puri, O. P. Mahajan and D. D. Singh, *J. Indian Chem. Soc.* 1961, **38**, 943.
- 97) B. R. Puri and R. C. Bansal, *Carbon.*, 1966, **3**, 533.
- 98) R. C. Bansal, T. L. Dharmi nd S. Parkash, *Carbon.*, 1980, **18**, 395.
- 99) L. H. Reyersonand A. W. Wishart, *J. Phys Chem.*, 1938, **42**, 679.
- 100) L. A. Alekeevskii and N. A. Likharev, *J. Gen. Chem. (USSR)*, 1942, **12**, 306.

## 1.2 Chemical defence

The concept of applying choking fumes as an offensive weapon has been around for centuries. In 428 B.C. the Spartans burnt wood saturated with pitch and sulphur to drive out the Alterions defending the city of Plateau.

The first Hague convention in 1899 had considered the serious increase of the chemical warfare (CW) threat. Twenty five nations met and acknowledged that the new nitro-cellulose and nitro-glycerine propellants produced the potential of "asphyxiating or deleterious gases" being introduced to battle by means of high velocity shells. By then no such weapons had actually been made but all twenty five nations agreed to ban them, with the notable exception of the US

A major turning point in chemical warfare history was on the 22nd of April 1915 at Ypres when the Germans introduced chlorine as an offensive weapon. Scheele had discovered chlorine gas in 1774 and the Germans decided to use it in a large scale chemical attack. This was possible because the Germans had built up on the Rhine a huge chemical dyestuffs industry by 1913 and this output was converted in wartime to synthesis of explosives and later to poison gases.

At Ypres the Germans released 168 tonnes of chlorine along a four mile front. The gas was carried by a light prevailing wind towards the allied trenches. The dense chlorine gas resembled a low greenish mist which travelled over to the soldiers, who had no protection against CW weapons. The Germans also bombarded the lines with shells containing lachrymators over the three-day attack. Precise figures are difficult to calculate but some 15,000 casualties were reported with 5,000 dying during or soon after the attacks.

The gas was discharged by batteries of twenty tubes placed every 40m along the fighting front. When the wind was light and in the correct direction the gas was simply discharged and allowed to drift towards the enemy. The Germans provided the first CW protection, which consisted of a cotton pad which was dipped into a sodium carbonate and thiosulphate solution to counter the effects of the chlorine as soldiers breathed through the pad.

The effects of chlorine are dependent on the length of exposure and quantity of gas taken into the respiratory system. At high concentrations victims experience feelings of suffocation, struggle on the ground momentarily and die. The corpses show contorted figures, lips fringed with blood and foam from their bursting lungs. The exposure causes an agonising death. Lower concentrations cause a burning of the throat, creating difficulty in breathing and constant coughing. These symptoms are followed by death in two days. The chlorine causes secretion of huge quantities of a frothy fluid in the airsacs in the lungs. The fluid builds up and the lack of oxygen causes weakness, fatigue and lassitude. When tilted forward patients can produce over a litre of the frothy green liquid. The lowest concentrations of chlorine caused bronchitis in the majority of cases. Headaches and debility would last up to several weeks but patients lasting 36 hours would generally recover to some extent.

During the period 1915-1917 there were several novel types of CW used in the battlefield. The pattern developed with new offensive weapons necessitating the development of more refined and effective defensive equipment allowing soldiers to remain operative in CW conditions. The simultaneous use of lachrymators with chlorine meant that the temporary cotton pads were no longer adequate defensive mechanisms. The pads were replaced by a flannel veil fitted with eye pieces. The veil had sodium carbonate and thiosulphate impregnated, along with glycerol to prevent the cloth drying out and losing its protective features.

The next development in the offensive arena was phosgene( $\text{COCl}_2$ ), which the Germans had discovered. Phosgene is several times more poisonous than chlorine and new defensive measures were developed to cope with this new threat. The anti-chlorine solution was changed to include sodium phenolate, and the Russians found that hexamethylene tetramine was very effective against phosgene so the P.H. (phenolate-hexamine) helmet came into service. The flannel hood or veil shown in figure 1.2.1 had a beak-like protuberance which was a primitive exhalation valve. The Germans then increased the use of lachrymators, attacking the veil at the eye pieces. This meant that the allied forces introduced primitive gas masks or respirators, developed by the British to protect against phosgene, chlorine and lachrymators. The air intake was purified



Figure 1.2.1. Flannel veil introduced in 1915.

by passage through a canister containing activated charcoal to remove lachrymators from the air stream, soda lime to remove chlorine and phosgene, and some potassium permanganate. The face piece consisted of layers of muslin impregnated with sodium zincate and hexamethylene tetramine along with goggles for the eyes. This is shown in figure 1.2.2.

By the spring of 1917 the defensive methods developed by the British, despite being cumbersome and awkward, had massively reduced CW casualties and coped with the continually improving German technology in offensive CW weapons.

In July of 1917 the Germans developed the next generation of CW Biphénylchloroarsine was introduced. This sternuator was basically a cough-inducing agent similar to modern C.S. gas. Sternuators are solids with negligible solubility. They were vaporised by an explosive charge and the heat formed tiny particles which readily penetrated standard mask filters. The induced coughing and potential vomiting forced soldiers to remove their masks making them vulnerable to other agents. The British simultaneously developed a sternuator called Adamsite which was used during the war, and in more modern times as a riot control agent. To combat sternuators the masks needed to incorporate a particulate filter but this seriously restricted air flow and hampered breathing.

Mustard gas was also developed at this point and was initially used on July 12<sup>th</sup> 1917 near Ypres. This was a totally new genre of chemical agent. The oily liquid has a very low volatility. Mustard gas  $[(\text{ClCH}_2\text{CH}_2)_2\text{S}]$  is adsorbed through the skin as well as the respiratory system, causing death at low exposures. Mustard gas is categorised as a blister agent. It was very difficult to provide protection because it penetrates both leather and rubber. The effects of mustard gas are varied, depending on the level of exposure. A slight irritation of the nose occurs and the smell of garlic or mustard is noticed at high concentration, but there are no immediate deleterious effects. Exposure to the vapour affects the eyes initially, and, if unprotected, effective blindness occurs. Extreme exposure causes false membranes to develop on the tongue and trachea, and sometimes the lung tissue disintegrates completely.

Lower levels of exposure to mustard causes nausea, the skin being irritated and inflamed, with blister formation at the sites of the splashing liquid. High concentrations of vapour can also cause blistering, especially in armpits and body crevices of the pelvic region. The white blood cell count in humans drops so low that the body is a culture medium ripe for bacterial attack. Affected persons present a picture of absolute misery, with headache, intense depression, insuperable lassitude and fatigue, with extensive body wastage. There was no adequate protection against mustard gas during world war one and it became known as the "king of war gases".

The first-generation chemical defence respirator system from WW1 moved on from the initial veil to a layered muslin mask with a separate box filter. The filter had a separate activated carbon section, and wool-asbestos particulate filter as shown in figure 1.2.2. The next protective innovation was the "light-type" rubber mask, coming into service at the beginning of the second world war. There were 100 million light-type rubber helmets produced with an individual canister containing carbon and a particulate filter attached directly to the mask by 1942. The masks were light weight, allowed some spoken communication via a speech diaphragm and had specially designed separate thin-sided spectacles available for soldiers with imperfect sight.

The advent of the second world war nerve agents such as Tabun, Sarin, Soman and even the VX agents did not necessitate any great improvement in the masks. Nerve agents are generally liquids at room temperature but have a large range of volatility. The b.p. of Sarin is  $151^{\circ}\text{C}$ , but VX agents have a b.p. above  $250^{\circ}\text{C}$ , and are persistent skin hazards. These VX agents will cause death in a 70kg male if a dose in excess of 2mg is adsorbed through the skin. The nerve agent is distributed via the blood throughout the tissues, where it blocks the enzyme acetylcholinesterase. The enzyme controls nerve impulses, and when these are inhibited muscular coordination is lost, causing patients to die from respiratory failure. Nerve agents were the first CW agents known to interact with a specific biochemical target. Development moves on with new chemical and biological offensive threats. Protective devices to combat the non-volatile liquids have evolved into whole body suits (NBC suits) made of impregnated carbon cloth to stop adsorption of nerve agents through the skin.



Figure 1.2.2. Muslin mask with a carbon box filter.

Since the second world war there have been several developments in protective equipment. The conflict in Korea in 1952 saw the rubber masks with the eye pieces permanently crimped into position instead of being screwed in the mask.

In 1966 the S6 gas mask shown in figure 1.2.3. was brought into service. There was a rubber mask available in four sizes, with an air-bag seal which moved with the facial contours. The lenses were made of glass. Prescription ones were available eventually. The air flow was guided round the nose and this helped to eliminate misting up of the lenses. The filter canister was screwed on either the left or right hand side with a small mounting. The main disadvantages were that the rubber was susceptible to attack from ozone and sweat and perished quickly making it impermeable. The lenses were also very large and no use for optically-sighted weapons.

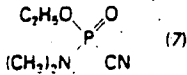
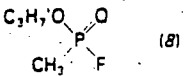
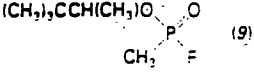
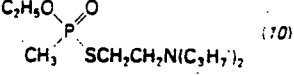
The S8 mask was developed but never used. The mask was made with a butyl rubber which was much more resistant to degradation but there was no air-bag seal as the rubber was not very flexible. The eye pieces were very much smaller and could be used for optically-sighted hardware, but they severely reduced the soldier's field of vision.

In 1985 the present S10 respirator was brought into service. The main body was made from chlorobutyl rubber with a single reflex flap seal. The rubber is fairly malleable and has excellent agent repellence. There is a single cast main body with five holes. The two eye-holes are filled with easily fitted polycarbonate lenses which are large and designed with a view to making optical sighting easy, but also to retaining a large field of vision. Corrective lenses are available and interchangeable easily, so logistics are considerably improved. There are two side-holes; one for the respirator canister and one for either a speech amplifier or a second canister. The central hole houses a one-way valve for exhaust gases and includes a speech horn to aid communication. The mask is shown in figure 1.2.4. For comparison, figure 1.2.5. shows the range of respirators developed by the MOD at Porton Down since 1915. The S10 mask has a drinking tube so that fluids can be taken in without damaging the integrity of the system. The mask has a hard rubber ridge round the outside to give a good seal when used in conjunction with a NBC protective suit.



Figure 1.2.3. The S6 respirator with a filter canister introduced in 1966.

Table 1.2.1. gives a brief résumé of the chemical threats developed up to the end of world war two. There is information on their structure, actions, b.p. and activity.

Code	Common name	Chemical structure	Boiling point/°C	Vapour pressure / mmHg	LC <sub>50</sub> / mg min m <sup>-3</sup>	LD <sub>50</sub> mg/kg	EC <sub>50</sub> / mg min m <sup>-3</sup>
<b>Blood agents</b>							
AC	Hydrogen cyanide	HCN (7)	26	638 (20°C)	1000 (1 min) 2000 (10 min)	1.0	>3000 (60 min)
CK	Cyanogen chloride	CNCl (2)	13	1000 (20°C)	11000 (10 min)	—	50
<b>Choking agents</b>							
CG	Phosgene	COCl <sub>2</sub> (3)	8	1406 (25°C)	3200	—	120
<b>Blister agents</b>							
H	Mustard agent	(ClCH <sub>2</sub> CH <sub>2</sub> ) <sub>2</sub> S (4)	217	0.072 (20°C)	1500	0.2	100
L	Lewisite	ClCH=CHAsCl <sub>2</sub> (5)	190	0.40 (20°C)	1200	0.5	20
HN-3	Nitrogen mustard	(ClCH <sub>2</sub> CH <sub>2</sub> ) <sub>2</sub> N (6) (Decomposes)	256	0.007 (20°C)	Slightly lower toxicity than sulphur mustard Hydrochloride (usual form) more aggressive than free base		
<b>Nerve agents</b>							
GA	Tabun	 (7)	240	0.035 (20°C)	150	0.08	100
GB	Sarin	 (8)	147	2.1 (20°C)	—	—	55
GD	Soman	 (9)	210	0.34 (20°C)	100 70	0.025 0.01	15 25
VX	—	 (10)	320	0.0004 (20°C)	50 (Aerosol droplets)	0.007	5

**Footnotes**

LC<sub>50</sub>: The product of concentration (C) of a gas and the duration (t) of exposure which will kill 50 per cent of the exposed population.

LD<sub>50</sub>: The dose of a chemical that will kill 50 per cent of the population.

EC<sub>50</sub>: The product of the concentration (C) of a gas and the duration (t) of exposure that will produce an effect in 50 per cent of the exposed population.

Table 1.2.1. Chemical warfare agents used in the period 1915-1945.

Attached to the respirator masks are filter canisters through which the airstream is drawn and purified during inhalation. Present British S10 respirator canisters consist of two elements (see figure 1.2.6):

1. A high-efficiency particulate filter consisting of coated glass fibres
2. A high efficiency vapour-adsorption layer of impregnated active carbon. The carbon bed is downstream of the particulate filter, so that any vapour from trapped particles is picked up by the carbon.

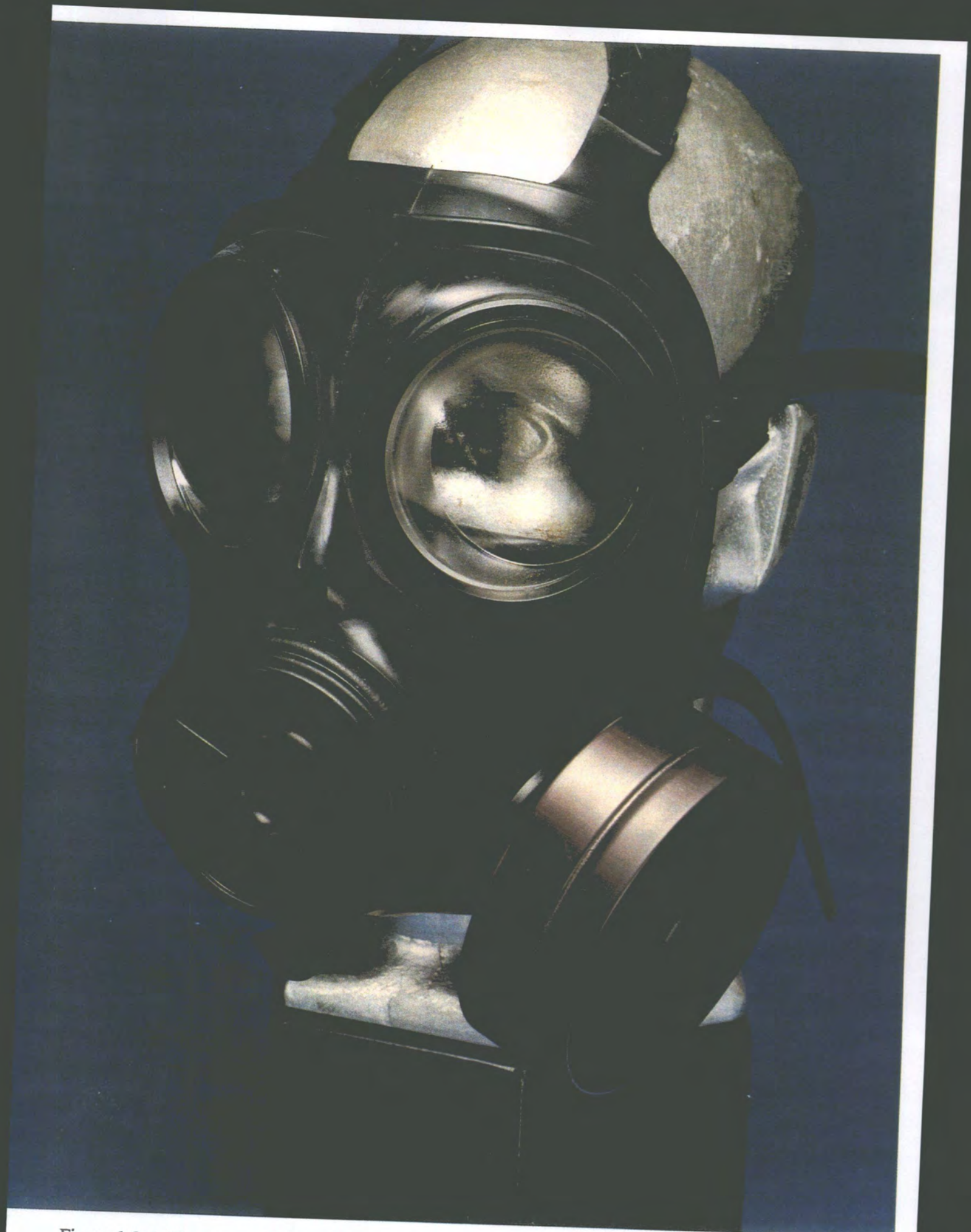


Figure 1.2.4. The current S10 respirator.



Figure 1.2.5. The respirator development at Porton Down from 1915 onwards.



Figure 1.2.6. A section through a filter canister.

The S6 respirator had the canister design shown in figure 1.2.7, with the airstream passing through a resin/wool particulate filter before the activated carbon bed.

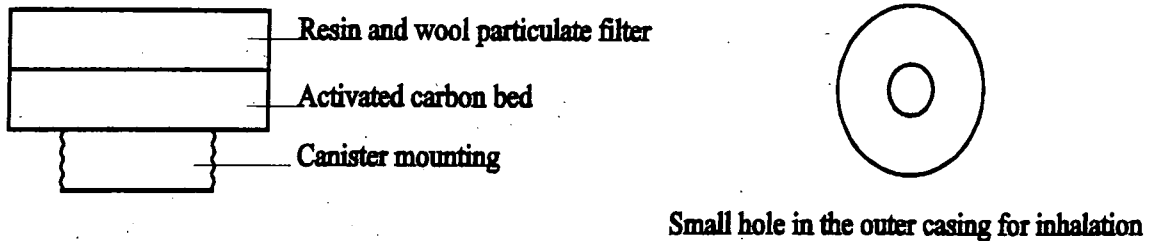
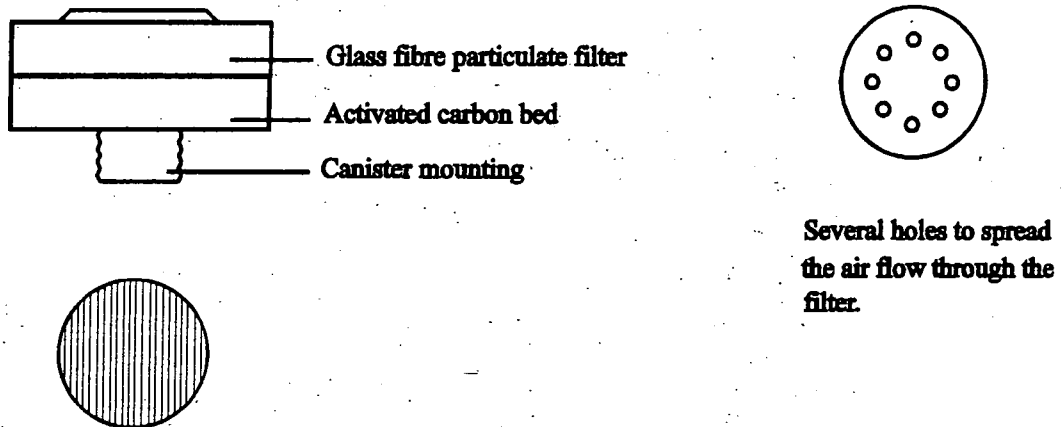


Figure 1.2.7. Section through the S6 respirator filter canister.

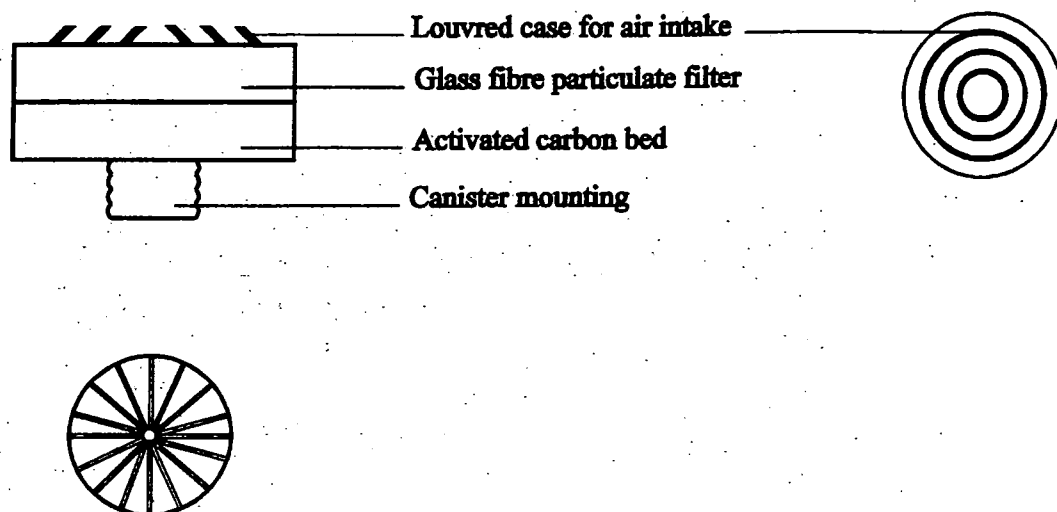
The next respirator canister, shown in figure 1.2.8., had a linearly-pleated glass fibre particulate filter and a 27mm carbon bed. The canister had a multi-hole front to help with air-flow intake through all the carbon.



Lineally pleated glass fibre filter

Figure 1.2.8. Section through the S8 respirator filter canister

The present S10 respirator has a glass fibre/cloth particulate filter pleated radially to decrease resistance to air flow. The carbon bed is only 23mm deep but snow-storm filled for maximum adsorption and hence protection. The case is louvred to help with air intake and exposure of all the carbon as shown in figure 1.2.9.



**Radially pleated glass fibre filter**

Figure 1.2.9. Section through the S10 respirator filter canister.

For a given gas-solid system the quantity of gas adsorbed is dependent on pressure and temperature as well as the surface properties of the adsorbent. Solids of a non-porous or macroporous nature show a direct relationship between amount adsorbed and surface area. Microporous and mesoporous solids have an adsorption dependence on pore-filling mechanisms, especially for micropores at low relative pressures, where the gas-solid interactions are enhanced in the constricted pores.

For respiratory protection the micropore adsorption is vital and requires very fast adsorption as the gaseous dwell time on the activated carbon is quite short. The pore structure must be readily accessible so the macropore transport channels are very important, leading easily to the micropores for efficient adsorption kinetics. The micropores physisorb various gases on the surface including water vapour. However some agent gases are only weakly physisorbed at ambient temperatures. In these cases activated carbon alone is not sufficient protection, so the carbons are impregnated with various chemicals which provide chemisorption sites for target agent molecules. Table 1.2.2. gives a brief outline of the impregnants and their purposes.

Chemical	Approx % by weight	Target toxin
Copper	7%	HCN
Chromium trioxide	5%	HCN
Triethylenediamine(TEDA)	1%	CICN, PIII to PV
Silver	<0.1%	Phosgene

Table 1.2.2. Target agents for the impregnants added to the activated carbon.

Clearly understanding of the physiochemical nature of adsorption by activated carbons, encompassing both structural and dynamic aspects, is vital for CW defense, yet currently only a few studies have addressed such issues with any substantial success. NMR, being isotope-specific and giving excellent discrimination between chemical species, is an ideal tool for probing surface species (although signal intensity can be a problem). The object of the present project was to use solid-state NMR to advance understanding of the adsorption process in activated carbon. It is hoped that this will contribute to the next generation of advances in respiratory protection against chemical agents.

### 1.3. NMR theory

The NMR experiment gives information about the chemical environment of a nucleus. The spectrum gives a specific chemical shift and an observed linewidth which can be used to provide information about this environment. This work uses adsorbate molecules to probe the activated carbon substrate. The NMR data can provide information about the environment of the adsorbate molecule and hence provide details about the carbon substrate.

#### 1.3.1. Factors affecting linewidths

The solid-state NMR line is broadened by either homogeneous interactions, that affect the whole band in the same manner, or inhomogeneous interactions, that arise from several overlapping factors. The linewidth of a static spectrum is influenced by shielding anisotropy (SA), dipolar interactions, and in some cases quadrupolar interactions. These interactions are orientation dependent and broaden the observed line. In solid samples the molecules are held rigidly, with only restricted motion possible. The molecules can have any orientation and this causes a broadening of the observed line.

#### Dipolar interactions

Nuclei with magnetic moments produce small localised magnetic fields at other magnetic sites. The resonance frequency depends on the local field at the site of the resonating nucleus, and the local field varies throughout the sample due to the different spin and spatial orientations of neighbouring nuclei. The local field typically varies over a range of several mT. There will be a significant spread in the resonance frequencies resulting in a linewidth broader by several orders of magnitude than the typical line from a liquid sample. The broadening effect caused by these dipole-dipole interactions is termed dipolar broadening and can be of the order of tens of kilohertz. Homonuclear coupling is a homogeneous, and heteronuclear coupling is an inhomogeneous, broadening effect.

In liquid samples, the molecules typically execute rapid and random rotation so the dipole-dipole interaction has no time-averaged effect on resonance frequencies. This means that the line is not broadened by dipolar interactions for liquids, so linewidths of tenths of Hz can be observed.

#### Shielding anisotropy

Shielding anisotropy also broadens the line in the NMR of solid samples. The chemical shift in an NMR adsorption line is the displacement of the resonance frequency due to a local field produced by a variation in the electron orbits in the strong external magnetic field necessary for the NMR experiment. In general the chemical shift is a tensor rather than a scalar, since the chemical shift depends on the orientation of the molecule with respect to the external field. In a polycrystalline sample, molecular orientation will vary from crystallite to crystallite, giving a continuous spread in the shifted lines. This spread of chemical shifts provides an extra source of inhomogeneous broadening in the solid-state and gives linewidths in the kilohertz range. In a liquid sample, the rapid random rotation of the molecules averages the molecular orientation to a single value so the nuclei resonate at only a single frequency. The observed line is therefore not broadened, and at the average chemical shift for liquids.

#### Quadrupolar interactions

When a quadrupolar nucleus is placed in a magnetic field the Zeeman and quadrupolar energy terms need to be considered. If the Zeeman term is dominant then the magnetic field rather than the electric field determines the direction of quantization. The energy levels are essentially those of NMR perturbed by quadrupolar effects. For a single crystal containing nuclei with only one direction, the spectrum will consist of  $2I$  lines split by  $0.75(3\cos^2\theta-1)/(2I-1)$ , where  $I$  is the nuclear spin and  $\theta$  is the angle between the external magnetic field and the molecular axis. In a powder all values of  $\theta$  are possible and a powder pattern results. For spin-1 nuclei, the powder pattern takes the same shape as that arising from dipolar interactions. This is termed a Pake doublet. In solid systems the quadrupolar effects are generally larger than dipolar effects

because of the large quadrupolar coupling constant ( $\chi$ ) magnitudes. Quadrupolar broadening is inhomogeneous and can give solid linewidths of several tens of megahertz.

In a liquid sample, the rapid-random rotation of the molecules averages the quadrupolar energy by randomly varying  $\theta$ . Consequently only a single NMR adsorption is observed. However in most cases the averaging is not efficient enough to give a sharp line, though for deuterium the observed linewidths can still be less than a hertz. The observed line is therefore not broadened, and at the average chemical shift for liquids.

Unpaired electrons can cause inhomogeneous broadening in the static case with the electrons not relaxing. The activated carbon substrate does contain some unpaired electrons at edge-dislocations, which act as primary adsorption sites. However the small amount of these sites means that they probably would not significantly affect the bulk linewidth of the adsorbate.

#### Motional narrowing

The linewidth for intermediate systems can lie between the liquid and rigid solid scenarios. These intermediate linewidths are attributed to broad solid lines narrowed, to a certain extent, by molecular motion.

Molecules which have rapid anisotropic motion, for example along a molecular axis, often exhibit linewidths in the hundreds of hertz range. The dipolar coupling is orientation dependent and the anisotropic motion causes the broad solid linewidth to scale according to the value of  $\theta$  (The angle between the applied magnetic field and the axis of motion). The value of  $\theta$  depends on the orientation of rotation axis compared to the external magnetic field, and scales the linewidth by  $(3\cos^2\theta-1)$ . The linewidth is then comprised of residual static dipolar interactions.

If the molecular motion is only moderately fast isotropic motion then the dipolar interaction is not completely averaged, causing the linewidth to increase from liquid values. The quadrupolar broadening can similarly affect the linewidth, if the motion is not sufficient to average the quadrupolar energy.

The intermediate linewidth could also be attributed to a distribution of chemical shifts. If the nuclei are in a range of environments with similar isotropic chemical shifts, then the lines overlap, causing a broad line to be observed.

#### 1.3.1.1. Magic-angle spinning (MAS)

The magic-angle spinning experiment<sup>(1)</sup> is used in solid-state NMR to remove the effect of shielding anisotropy. The experiment involves rotating the solid sample in a specially designed rotor. The rotor is spun about an axis at  $54.7^\circ$  to the applied magnetic field  $B_0$ . The induced motion along this axis averages the orientation dependence of the shielding anisotropy given by  $(3\cos^2\theta - 1)$ , to zero. MAS can only fully average the chemical shift anisotropy to zero if the spinning rate is greater than the width of the powder pattern. Homogeneous broadening effects require spinning speeds 5 times the interaction to fully narrow the lines. Inhomogeneous interactions break up into spinning side-bands at modest spinning speeds. MAS is therefore often not capable of averaging the dipolar or quadrupolar interactions because the broadening can be several tens of kHz and the sample can not be spun that fast. The MAS experiment also averages the bulk magnetic susceptibility to zero<sup>(2,3)</sup> because it also has an orientation dependence of  $(3\cos^2\theta - 1)$ .

The MAS experiment will reduce the linewidth for solid samples by averaging the shielding anisotropy to zero. However Suwelack et al <sup>(4)</sup> found that MAS will not readily remove all the linewidth observed for molecules with considerable molecular motion. Figure 3.1.1 shows the linewidth as a function of correlation time for isotropic molecular motion and a symmetric axial shielding tensor, the relative effect of two MAS spinning rates are shown.

The increased linewidth observed for systems with intermediate motion compared to liquids, arises because of the time dependency of the MAS experiment. When the molecular motion and MAS have similar frequencies the time-dependent effects are convoluted, producing sum and difference frequencies. When this difference frequency is close to zero then the interaction contributes to the relaxation process and hence the linewidth increases.

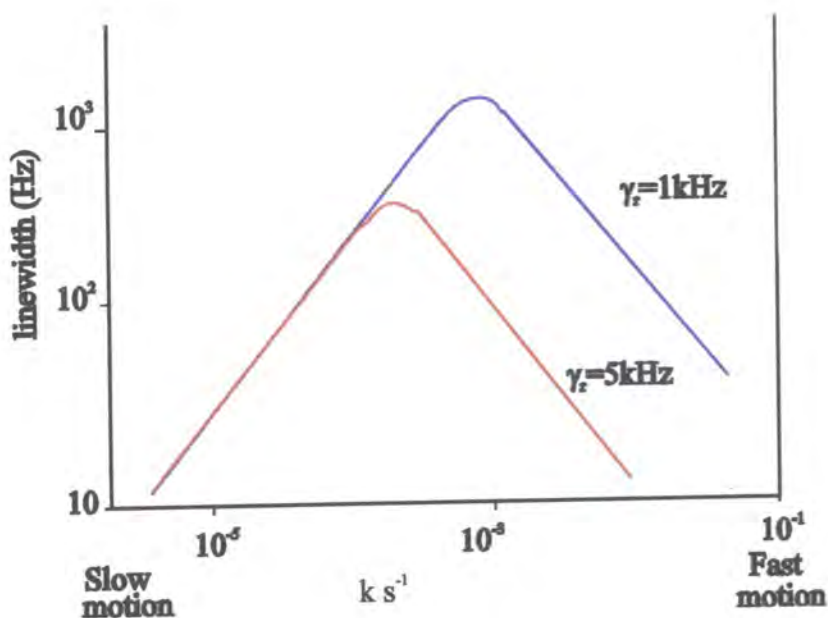


Figure 3.1.1. The effect of MAS on linewidth, for varying rates of molecular motion.

Clearly in systems with intermediate motion, MAS does not completely remove the line-broadening effect of shielding anisotropy. MAS will readily narrow cases with rapid anisotropic molecular motion broadened by residual static dipolar interactions, but will not easily narrow systems with insufficient motion.

#### 1.3.1.2. Decoupling

One experimental technique used to remove the dipolar coupling interactions between the observed nucleus and protons is termed high power proton-decoupling. In solid-state NMR the broadening caused by dipolar coupling of protons can be removed by decoupling. Decoupling involves rapid transitions between the  $\alpha$  and  $\beta$  states of the proton. The observed nucleus sees an average of the two states and the splitting of the observed line collapses. The rf power input has to be very large to stir up the proton spins in the broad-line proton NMR signal.

The high power proton-decoupling experiment will reduce the linewidth for solid samples by averaging the dipolar coupling to zero. However Rothwell et al (5) found that decoupling will not remove all the line-width observed for molecules with motion between the solid and liquid state. Figure 3.1.2 shows the linewidth as a

function of correlation time for isotropic molecular motion and dipolar coupling ( $r_{\text{CH}}=0.11 \text{ nm}$ ), the relative effect of two decoupling powers are shown.

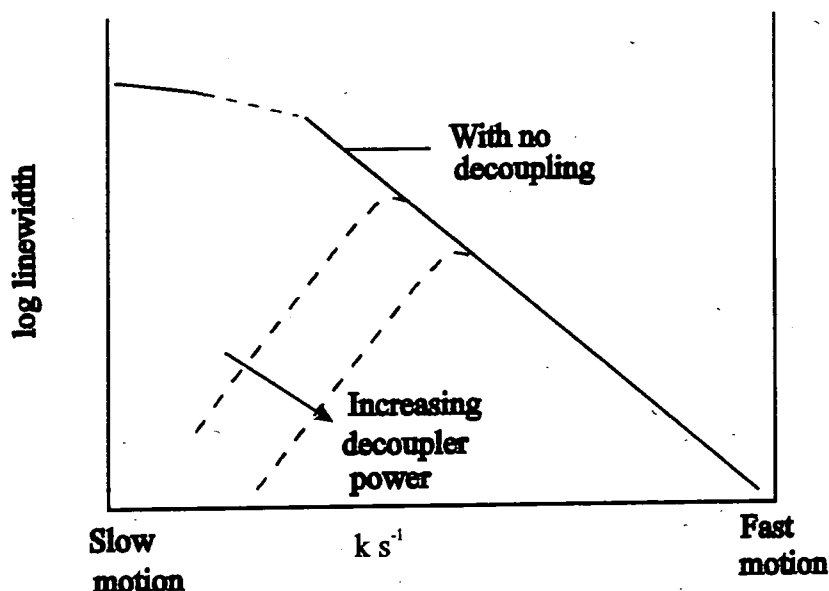


Figure 3.1.2. The effect of high-power proton decoupling on linewidth for varying decoupling powers.

Clearly in systems with intermediate motion, decoupling does not completely remove the line-broadening effect of dipolar interactions. The increased linewidth observed for systems with intermediate motion compared to liquids, arises because of the time dependency of the decoupling (expressed as  $\gamma B_1/2\pi$ ). When the molecular motion and decoupling have similar frequencies the time-dependent effects are convoluted, producing sum and difference frequencies. When the difference frequency is close to zero then the heteronuclear dipole interaction contributes to the relaxation process and increases the linewidth.

### 1.3.1.3. Variable temperature experiments

Molecular motion in the intermediate regime can be changed by variation of the sample temperature. If the temperature is reduced then the motion is slowed down, making the sample more like a solid. This may reduce the observed linewidth for experiments with MAS and high power proton-decoupling. If the temperature is raised then the molecular motion is increased, and the sample behaves more like a liquid, with an associated reduction in linewidth. These reductions in linewidth can only be

introduced if the variation in temperature is sufficient to dramatically change the molecular motion. Figures 3.1.1/2 show that the linewidth has a motion dependency, where either increased or reduced motion may lower the observed linewidth.

#### 1.3.1.4. Adsorbent-adsorbate systems

The activated carbon systems with adsorbate molecules are intermediate between rigid solids and liquids. The observed linewidths are around 180 Hz for the  $^2\text{H}$  NMR of  $^2\text{H}_2\text{O}$  and 250-300 Hz for the  $^{31}\text{P}$  NMR of phosphates. High-resolution spectra were obtained using a MAS speeds of 3-4 kHz and a single-pulse regime.

Figure 3.1.3 shows the  $^2\text{H}$  NMR of 10% w/w  $^2\text{H}_2\text{O}$  adsorbed onto SC2 carbon. The initial spectrum (A) is static and proton decoupled, and (B) is static but not decoupled. Spectrum (C) is spun at 3.5 kHz with no decoupling and (D) is spun at 3.5 kHz and decoupled. The static spectrum has a linewidth of 340 Hz, which does not vary significantly when the protons are decoupled. The MAS at 3.5 kHz reduces the linewidth to 180 Hz and once again proton decoupling does not affect the linewidth.

The static linewidth for the activated carbon-adsorbate systems is of an intermediate character. This may arise from many possible origins, for instance dipolar interactions involving adsorbate molecules with rapid anisotropic motion, moderately fast isotropic motion or intermolecular interactions with surface protons even with isotropic motion of the adsorbate near the activated carbon substrate. Such dipolar interactions are not completely averaged by this motion so the residual interactions broaden the line. Figure 3.1.4 shows how the molecular motion cannot remove the dipolar coupling when the molecule is associated with the surface, since the averaging effect over all distances retains H,H interactions.

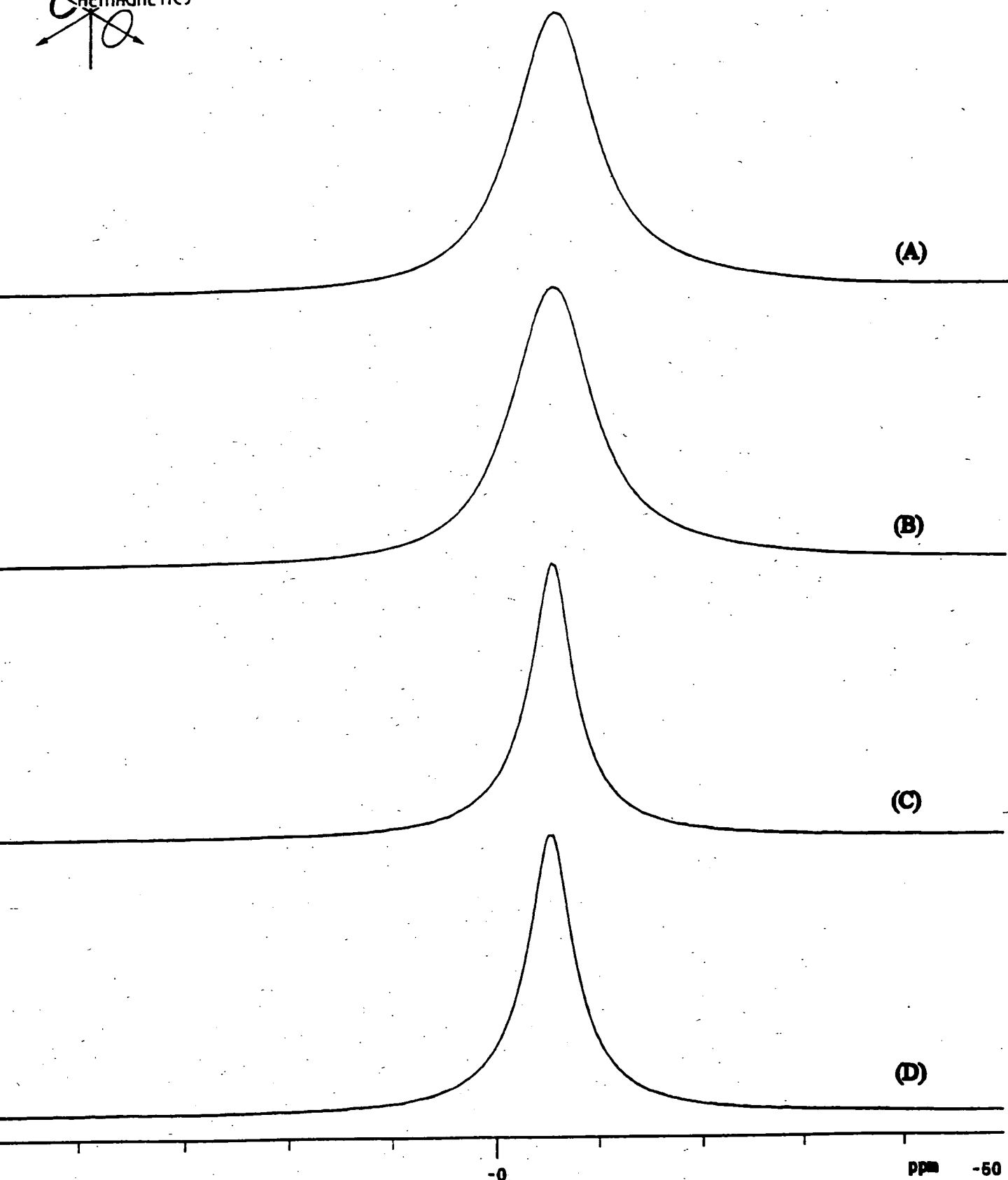


Figure 3.1.3 shows the  $^2\text{H}$  NMR of 10% w/w  $^2\text{H}_2\text{O}$  adsorbed onto SC2 carbon. The initial spectrum (A) is static and proton decoupled, (B) is static but not decoupled. Spectrum (C) is spun at 3.5 kHz with no decoupling, and (D) is spun at 3.5 kHz and decoupled.

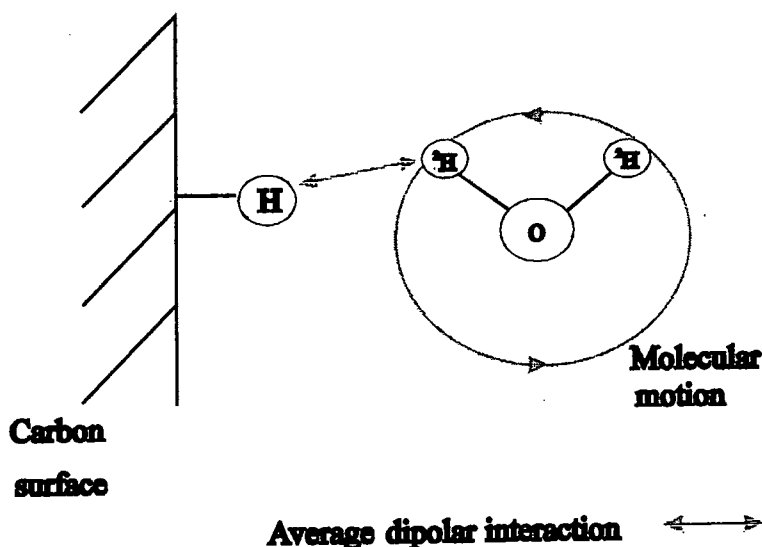


Figure 3.1.4. Schematic diagram showing the average dipolar interaction between the adsorbate and carbon surface.

The dipolar interaction can only be completely removed by translation of the adsorbate molecule away from the surface. However, rapid isotropic motion will average intramolecular dipolar interactions even for adsorbed molecules.

The adsorbate molecules have motion in between solids and liquids. However variable temperature experiments have failed to change the molecular motion sufficiently enough to reduce the observed linewidths any further than the MAS experiments at ambient temperature.

The NMR experiment can distinguish between some interactions to help explain the origin of the observed linewidth in the adsorbate systems. A dispersion of chemical shifts definitely causes an inhomogeneous broadening, and can be differentiated from homogeneous broadening by looking at the natural linewidth value derived from T2 experiments, as explained in chapter 6. Residual static interactions can be removed using MAS although motion can complicate the broadening. Figure 3.1.3 clearly shows that MAS does narrow the line so some residual static interactions are present in the system. Heteronuclear dipolar interactions can be removed by decoupling and are affected by MAS, but figure 3.1.3 shows that decoupling has little effect on the peak width. This shows that heteronuclear broadening is not a major broadening effect for the adsorbate systems. Homonuclear dipole interactions can also

be discounted because the phosphorus interactions would be small because the internuclear distance is large. The deuterium nuclei have small homonuclear coupling constants ( $D$ ), because they are proportional to the square of the gyromagnetic ratio ( $\gamma^2$ ). This is a very small value for the deuterium nucleus.

### 1.3.2. Influences on chemical shifts

The chemical shifts observed in NMR experiments are directly related to the shielding effect of the electrons around the observed nucleus. This enables the chemical shift to be used to provide information about the environment of the adsorbate molecule. If several environments are very similar then the chemical shifts will also be similar, and the lines can overlap. This overlap also causes the observed linewidth to increase. Adsorbates in pores with similar dimensions will have a distribution of shifts, with the peaks overlapping. The observed chemical shift in this case will be a weighted average arising from a distribution of similar environments. The rotational motion of an adsorbed molecule at a surface will not eliminate the effect of the surface on the isotropic shift of the adsorbate.

The activated carbon substrate consists of layers of graphitic sheets folded back on each other to provide an extensive surface area for adsorption. The graphitic sheets have a delocalised  $\pi$ -electron cloud and associated ring currents. It is possible to use the chemical shift data from the adsorbates to infer the distance of the adsorbate from the graphite plane.

The effect of an external magnetic field on these ring currents can be modelled by looking at benzene<sup>(6)</sup>. When the magnetic field is applied the ring currents produce an induced magnetic dipole moment. Outside the benzene ring this reinforces the external field ( $B_0$ ) and inside the ring it opposes the field. As a simple model, the benzene ring can be treated as a ring of six electrons, which precess about the ring when a magnetic field is applied perpendicular to the plane of the molecule. The ring is like a circular wire of radius  $r$  (the C-C bond length 1.40 Å) with an electron current flowing around it. The induced dipole moment giving rise to ( $B_{\text{ring}}$ ) can therefore be

calculated. The magnetic susceptibility is highly anisotropic, since there is no free electron current if  $B_0$  lies in the plane of the ring.

If we use equation 3.1.1<sup>(7)</sup> then the shielding constant can be calculated by;

$$-\Delta\delta = B_{\text{ring}}(1-3\cos^2\theta)/R^3$$

Equation 3.1.1.

where  $R$  is the distance from the ring and  $\Delta\delta$  is the change in chemical shift induced by the ring current.

Equation 3.1.1 gives a ring current effect on the chemical shift, of 1.75 ppm for the proton attached to a carbon atom in a benzene ring. This uses a C-H bond length of 1.09 Å for the calculation. The observed chemical shift for the proton when moving from cyclohexa-1,3-diene to benzene is 1.4 ppm, so the equation is reasonably valid. The equation has also been used to look at 1,4-polymethylene benzenes<sup>(8)</sup>, where the methylene protons in the bridge do show the expected shift to low frequency. Values of 3-4 ppm have been reported.

Equation 3.1.1 has been applied to the activated carbon systems to see if the large chemical shift to low frequency can be explained using ring current effects. The graphite is assumed to behave as single benzene rings with the water molecule sat at the centre of the ring of  $\pi$ -electron density.

Figure 1.3.5 shows a simple model of the adsorption of  $^2\text{H}_2\text{O}$  onto the activated carbon surface. The ring currents are shown and the induced magnetic dipole moment.

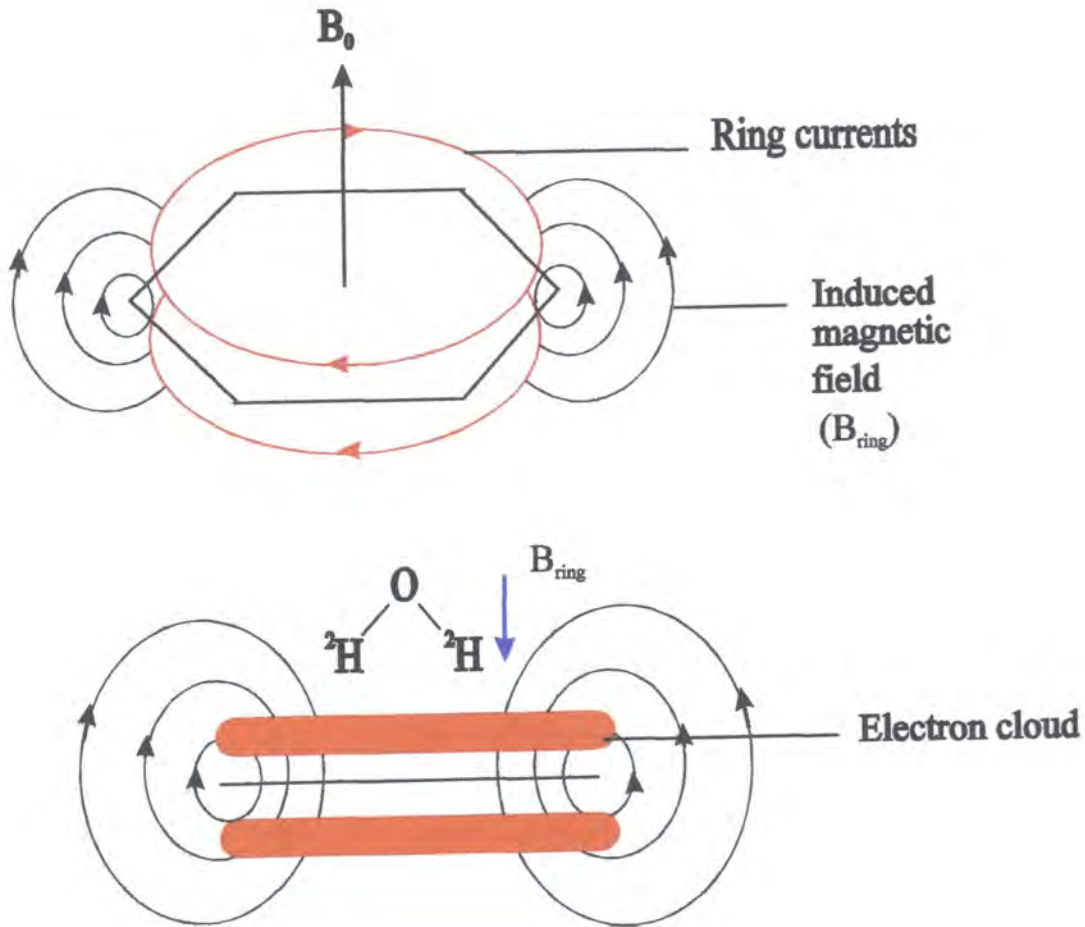


Figure 3.1.5. Schematic diagram showing the effect of induced ring currents in a magnetic field on adsorbed molecules.

The model is very simplified but can be applied to the activated carbon substrate if the graphite plane is assumed to be regular. Equation 3.1.1 gives a value of 1.65 Å for the distance between the plane of the  $\pi$ -electron cloud and the  $^2\text{H}$  nuclei in adsorbed water, if a standard chemical shift value of -6 ppm is inserted. The model calculation assumed that the water molecule sits between two walls of a slit-shaped pore, with shielding effected by both surfaces. The model is not very accurate with many assumptions, but does show that the observed chemical shift of -6 ppm could be caused by ring current affects. These arise from the adsorption onto graphitic surfaces within slit-shaped pores.

### 3.1.3 The effect of paramagnetics<sup>(9)</sup>

The activated carbon substrate contains several paramagnetic impurities. The paramagnetic centres affect the relaxation properties of the adsorbate, which means that the observed T1 and T2 values are not directly comparable to the adsorbate's motion. Zeolite systems with paramagnetic centres have been studied by Thangaraj and Ganapathy (10). They have observed non-exponential decay of the longitudinal magnetisation which can be explained by theory. The transverse magnetisation is broadened homogeneously by coupling to paramagnetic centres, and inhomogeneously due to the bulk susceptibility of the material.

If an adsorbate is directly associated with a paramagnetic centre then the chemical shift can vary markedly (observed <sup>1</sup>H shifts cover some 200 ppm). This contact interaction involves transfer of unpaired electron density, causing either positive or negative shifts, depending on the electron distribution. In the activated carbon systems there are not very many paramagnetic sites available for direct contact with the adsorbate, so no major changes in the observed isotropic shifts are observed.

## References

- 1) R. K. Harris, in *Nuclear magnetic resonance spectroscopy*, Wiley, New York, 1987, p145.
- 2) S. Hayashi, M. Yanagisawa and K. Hayimuzu, *Anal. Sci.* 1991, **7**, 955.
- 3) A. N. Garroway, *J. Mag. Reson.* 1982, **49**, 168.
- 4) H. Suwelack, K. Rothwell and J. S. Waugh, *J. Chem. Phys.* 1980, **73**, 2559.
- 5) K. Rothwell and J. S. Waugh, *J. Chem. Phys.* 1981, **74**, 2721.
- 6) A. Carrington and A. D. McLachlan, in *Introduction to magnetic resonance*, Harper, New York, 1980, p60.
- 7) R. J. Abraham, J. Fisher and P. Loftus, in *Introduction to NMR*, Wiley, New York, 1988, p19.
- 8) J. S. Waugh and R. W. Fessenden, *J. Am. Chem. Soc.* 1957, **79**, 846.
- 9) D. R. Eaton and W. D. Phillips, *Advan. Mag. Reson.*, 1965, **103**, 1.
- 10) A. Thangaraj and S. Ganapathy, *Indian J. of Chem.* 1990, **29A**, 1080.

## Chapter two            Experimental

### 2.1 The NMR spectrometer

The NMR analyses were all carried out using a Chemagnetics CMX200 spectrometer. The spectrometer used an Oxford instruments wide-bore (89.5 mm) superconducting magnet with a magnetic field strength of 4.7 T. This gives resonance frequencies of 200.13, 81.02 and 30.72 MHz for  $^1\text{H}$ ,  $^{31}\text{P}$  and  $^2\text{H}$  nuclei respectively.

The CMX200 is a three-channel spectrometer; these are equivalent and capable of irradiation over all possible frequencies. Digital pulse generation and phasing make many sophisticated experiments viable. The system was controlled by a Sun workstation interface, and the experimentalist used the CMXW software package for acquisition, file-storage, automation and plotting. Transmitter power levels could be set manually by dials on the spectrometer, through the keyboard or within a pulse programme. More efficient operation was possible via the implementation of macros - for setting tuning conditions, running variable-parameter and time-delay experiments and contiguous plotting.

A Chemagnetics "HX" dual-channel double-bearing probe was used for acquisition over the whole frequency range for the experiments. Tuning to a particular nucleus required insertion of the suitable capacitor in the probe. The probe used 7.5 mm Zirconia pencil rotors which had a sample capacity of ca. 500 mg. The sample was packed between a PTFE end-cap and spacer; the bottom of the rotor then had a fluted Kel-F drive tip inserted. Spinning rates of up to 6 kHz were obtainable, but high-resolution spectra required only 3 kHz so this speed was generally used for the experiments. The experiments sometimes required a sealed system. A technique for producing sealed glass ampoule-inserts for the pencil rotors, capable of spinning at 3 kHz, was developed and is described later in the chapter.

### 2.1.1. The optimisation procedure

Prior to acquisition of spectra several tuning procedures need to be followed to optimise and standardise the performance of the spectrometer. The experimentalist must set the magic-angle, optimise shimming coils, set the  $90^\circ$  pulse and reference the chemical shift for the observed nucleus.

The orientation of the rotor relative to the magnetic field was set to the magic-angle using either of two methods. It is possible to maximise the rotational echoes in the  $^{79}\text{Br}$  FID of solid KBr. The shape of the  $\text{NO}_3$  peak in the  $^{15}\text{N}$  spectrum of a  $\text{NH}_4\text{NO}_3$  sample (20% enriched) was also used to set the angle. Small deviations from the magic-angle do not affect the spectra in the experiments reported herein, so the angle was not set prior to each spectrometer session.

Shimming involves the fine adjustment of coils within the magnet to achieve a homogeneous magnetic field. Setting the shims from scratch is a very lengthy process described in the literature.<sup>(1)</sup> When this had been carried out for the "HX" probe then the values were stored in the computer in the shims file. For each experiment session it was then only necessary to recall the file and perform small adjustments. The small adjustments were optimised by maximising the  $^1\text{H}$  FID for PDMSO.

In an experiment using a simple pulse sequence the optimum signal intensity is observed when the pulse induces a  $90^\circ$  nutation of the sample's bulk magnetisation. This means that the  $90^\circ$  pulse duration needs to be determined to obtain good signal to noise ratios. This can be achieved by obtaining the null point corresponding to a  $180^\circ$  pulse. It was necessary to be careful because the carbon samples, used in the experiments, had a large bulk conductivity caused by the graphitic sheets within the sample. This meant that the  $90^\circ$  pulse duration was longer than the reference sample so the  $90^\circ$  pulse had to be reset on the test sample after the reference sample was run. The sample's conductivity sometimes made the RF circuit hard to tune and match but a smaller sample mass in an insert or the addition of flowers of sulphur to the sample negates this problem.

The experiments performed on these samples are all basic pulse sequences. The state of the adsorbate is between gas and liquid so cross-polarisation from the proton nuclei is not possible. The rapid molecular motion of the adsorbate means that the Hartmann-Hahn matching condition cannot be achieved. This molecular motion also causes the heteronuclear dipole interactions between the  $^{31}\text{P}$  or  $^2\text{H}$  nuclei, with protons within the sample to be averaged out. Decoupled experiments therefore exhibit similar line-widths as those observed using the single pulse regime.

The phosphorus spectra were referenced to an external sample of brushite ( $\text{CaPO}_4 \cdot \text{H}_2\text{O}$ ) at a chemical shift of 1.2 ppm. The deuterium spectra were referenced with respect to a sealed sample of  $^2\text{H}_2\text{O}$  (99.99% enriched from Aldrich) at a chemical shift of 0 ppm. The quoted chemical shifts in this thesis are given to an accuracy of  $\pm 0.1$  ppm.

### 2.1.2. Acquiring the spectra

The nuclei studied in the experiments are  $^{31}\text{P}$  and  $^2\text{H}$  nuclei present in the adsorbates as probe molecules. Table 2.1.1. lists the relevant spectroscopic data for these nuclei.

Nucleus	Spin, I	Natural abundance %	Sample abundance %	Gyromagnetic ratio, $\gamma$ $10^7 \text{ rad T}^{-1} \text{ s}^{-1}$	Relative receptivity to $^1\text{H}$
$^1\text{H}$	1/2	99.98	99.985	26.7519	1
$^{31}\text{P}$	1/2	100	100	10.841	0.0665
$^2\text{H}$	1	0.015	99.99	4.1066	$9.6 \times 10^{-3}$

Table 2.1.1. Spin properties of the nuclei studied in this work.

acquire the data. The single pulse with no decoupling experiments used the '1pulse' programme. The time-delay experiments also used the 1pulse programme in conjunction with the Delay macro purpose written by the experimentalist. The  $T_1$  relaxation time was determined by inversion recovery using the 'tlir' pulse-programme. The  $T_2$  experiments were performed using two pulse programmes, 'Fullecho' and 'Hahnecho'. These were purpose-written by the experimentalist to achieve and observe a Hahn-echo sequence.

Some spectral parameters are listed for each spectrum in this thesis, especially pulse delay time, number of acquisitions and time-delay between experiments, as these were liable to vary between spectra. The more typical parameters such as the spinning speed of 3 kHz are given here. The dwell time and number of points acquired for each spectrum were chosen to provide reasonable spectral widths and acquisition times.

## 2.2. Calculation of relaxation times

This work contains experiments that determine  $T_1$  and  $T_2$  values for activated carbon systems with adsorbates. The spin-lattice relaxation times have been determined using the inversion-recovery sequence. The spin-spin relaxation times were determined using the Hahn-echo pulse sequence. Each relaxation experiment uses the one-pulse sequence and the delay time  $\tau$  is varied using a macro collecting FID's for each time value. Spectra are then obtained using constant apodization, fourier-transformation, baseline-correction and phasing. Peak picking can then provide lists of signal intensity relative to the changing time parameter. This provides a series of data points from which the relaxation time can be calculated.

SPSS for MS windows version 6.0 has been used for all fitting procedures. The program uses the Levenberg-Marquardt estimation minimising the squared residuals with no constraints. The data calculated from the analysis give a value for the relaxation time and asymptotic 95% confidence limits for the error margins. The equations used for the calculations are given in equations 2.2.1. and 2.2.2.

### Inversion recovery

$$M_z(t) - M_\infty = [M_z(0) - M_\infty] \exp(-\tau/T_1)$$

Equation 2.2.1.

Hahn-echo

$$M_y(t) = M_y(0) \exp(-\tau/T_2)$$

Equation 2.2.2.

Figure 2.2.1. shows the inversion-recovery experiment for a typical  $^{31}\text{P}$ - and  $^2\text{H}$ -containing adsorbate on activated carbon. The presence of paramagnetics means that precise values for  $T_1$  are not intrinsic. To ensure that complete relaxation occurs between pulses a pulse delay of at least  $5T_1$  is required. The inversion-recovery sequence gave values of  $^{31}\text{P}$   $T_1 = 60 \pm 4$  ms and a  $^2\text{H}$   $T_1$  value of  $210 \pm 24$  ms. This means that recycle delays of 2 s ensure complete relaxation between pulses for experiments observing either nucleus.

### 2.3. Samples

The samples of carbon were all provided by the MOD at Porton Down. The adsorbates were all obtained from Aldrich.

#### 2.3.1. Carbon substrates

The substrate samples are all activated carbons that are of interest to the MOD for use in the respirator canister filtration system. The MOD provided samples of fully activated carbons coded as BPL, SC2 and ASZM. Some experiments have been carried out on the unactivated BPL and SC2 carbons and partially activated derivatives prepared by Dr. M. Thomas at Newcastle university.

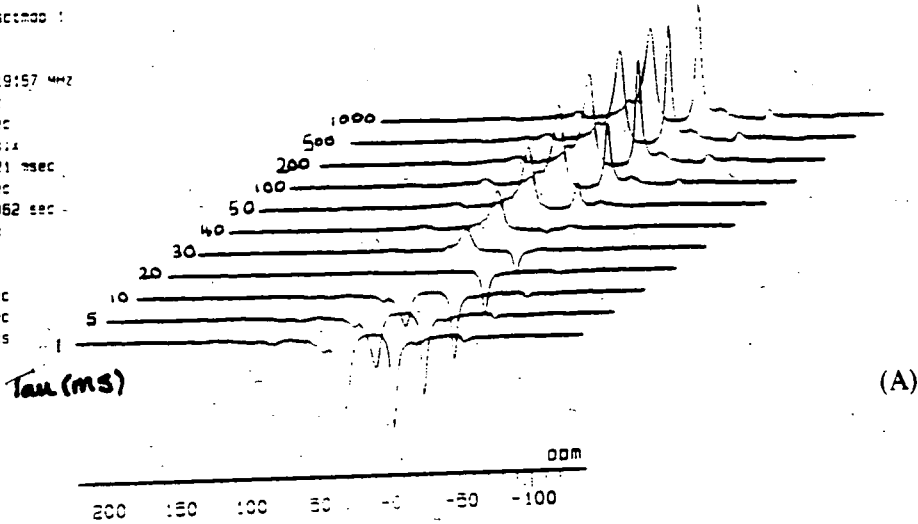
The carbon samples are all provided in the granular form used in the respirator canisters. Table 2.3.1. provides further information about the activated carbon samples.

# T1 Relaxation by inversion recovery



## Durnam CMX200H-NMR System

Durnam Initial Settings  
 T1 by inversion recovery using compensated pulse - Durnam  
 pprn=t1r  
 cpr=0.1asc200 :  
 cfn=junk  
 cfd=11  
 sf1=81.019157 MHz  
 sw=50 KHZ  
 ad=15 usec  
 al=255 colx  
 adm=3.121 msec  
 dw=20 usec  
 ext=2.0062 sec  
 p=157 deg  
 pd=2 sec  
 pw=8 usec  
 rd=15 usec  
 tau=1 msec  
 ac=64 scns

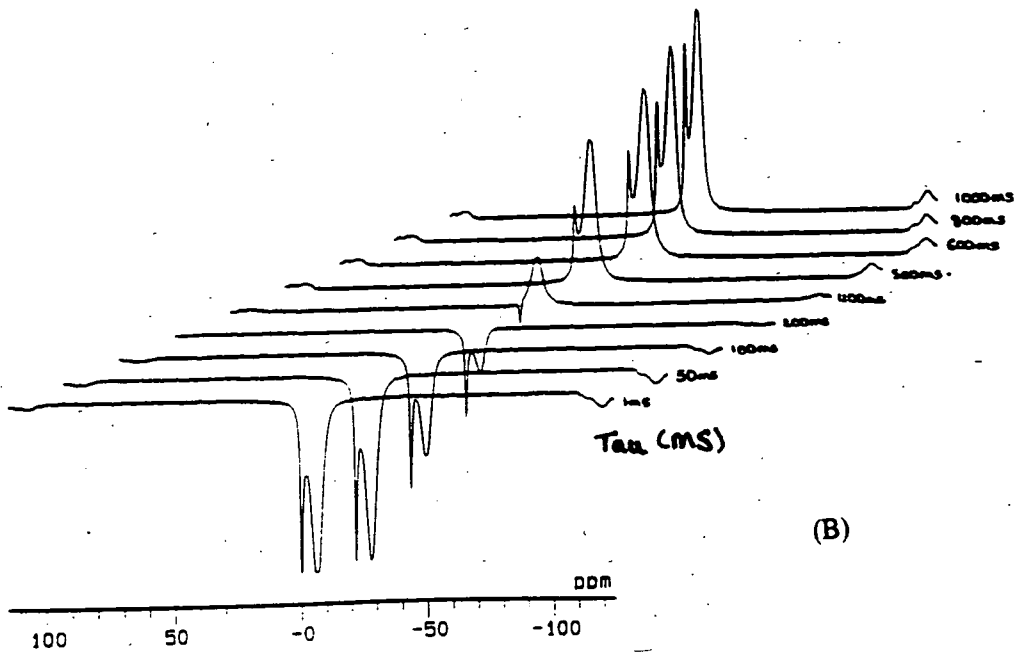


(A)



## Durnam CMX200H-NMR System

Durnam Initial Settings  
 T1 by inversion recovery using compensated pulse  
 pprn=t1r  
 cpr=200p1dd2ot1  
 cfn=junk0  
 cfd=0  
 sf1=30.7 MHz  
 sw=25 KHZ  
 ad=15 usec  
 al=1k colx  
 adm=40.961 msec  
 dw=40 usec  
 ext=5.042 sec  
 p=157 deg  
 pd=5 sec  
 pw=9 usec  
 rd=15 usec  
 tau=1 msec  
 ac=8 scns



(B)

Figure 2.2.1. Stacked spectra of the inversion recovery experiment for (A) a typical  $^{31}\text{P}$  and (B) a  $^1\text{H}$  containing adsorbate, adsorbed onto activated carbon.

Sample	Carbon origin	Total pore volume (ml g <sup>-1</sup> )	Micropore volume (ml g <sup>-1</sup> )	Mesopore volume (ml g <sup>-1</sup> )	Impregnants
SC2	Coconut shells	0.57	0.34	0.13	None
BPL	Coal	0.65	0.22	0.18	None
ASZM	Coal	0.41	0.15	0.04	Cu, Ag, Mo, Zn

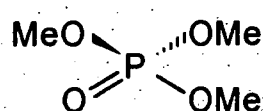
Table 2.3.1. Table listing the typical characteristics of the activated carbons.

### 2.3.2. The adsorbates

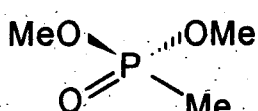
The following adsorbates were obtained from Aldrich for use as probe molecules for adsorption by the activated carbons.

#### 2.3.2.1. <sup>31</sup>P containing adsorbates

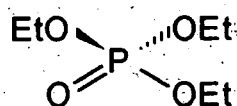
Triethyl phosphate (TEP), Trimethyl phosphate (TMP), Dimethyl methyl phosphonate (DMMP) and Cyclohexyl methyl methyl phosphonate (PP)



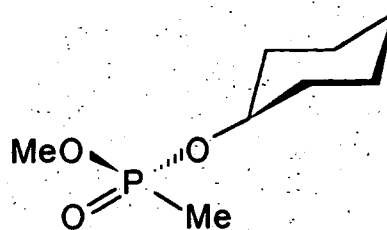
**TMP**



**DMMP**



**TEP**



**PP**

#### 2.3.2.2. <sup>2</sup>H containing adsorbates

<sup>2</sup>H<sub>2</sub>O 99.99% enriched

## 2.4. Sample sealing

To study adsorbent-adsorbate systems it is necessary to create sealed systems with controlled adsorption. The system has to be small enough to fit into a MAS rotor and have sufficient symmetry to spin at 3-4 kHz. The following section describes how this can be achieved using small glass ampoules. The ampoules are inserted into CMX 7.5 mm MAS rotors after adsorption. There are six major steps to make the ampoule containing a sealed system.

### 2.4.1. Preparation

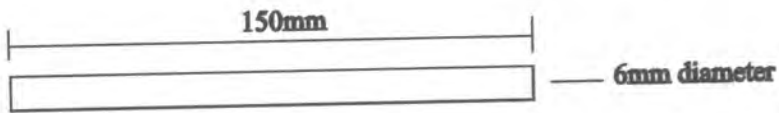
Initially a fifteen centimetre length of 6mm diameter of thin walled glass tube was cut, as shown in figure 2.4.1.(A). A section of wider diameter glass was then joined on so the tube can be attached to the vacuum line, as shown in figure 2.4.1.(B).

Both ends of the glass tube were then placed on the glass lathe and rotated at an intermediate speed. Two constrictions were made at one and four centimetres from the narrow end as shown in figure 2.4.1.(C). These were produced by heating at the appropriate position, then, when the glass glowed red, one end of the tube was pulled out half centimetre. The constrictions should be approximately 1 mm in diameter.

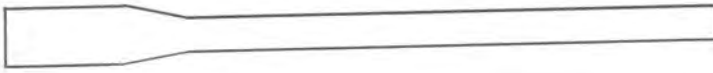
The final preparation stage involved sealing the end of the tube and is shown in figure 2.4.1.(D). The large end of the tube was held in the lathe and rotated quickly. The narrow end of the tube was then heated until it glowed red and was sealed off. At this point a carbon block was applied to the seal to flatten it as much as possible. If necessary a heated glass rod was used to remove any excess glass. The base needs to be flat so that it packs easily into the rotor and the ampoule spins better if the excess weight of superfluous glass is removed. The remaining tube has to be strong enough to withstand the vacuum pressure.

## PREPARATION

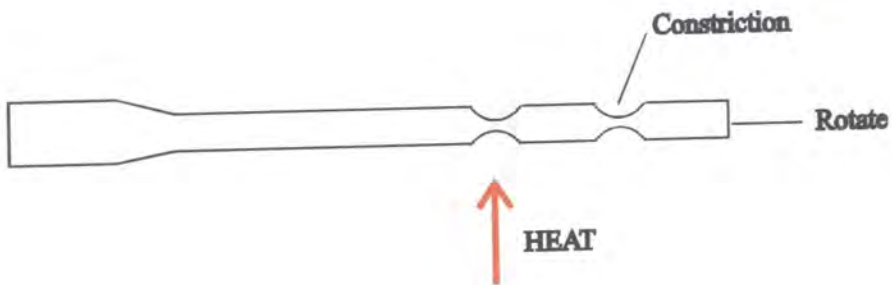
### A) Glass rod



### B) Vacuum line adapter



### C) Constrictions



### D) Sample seal

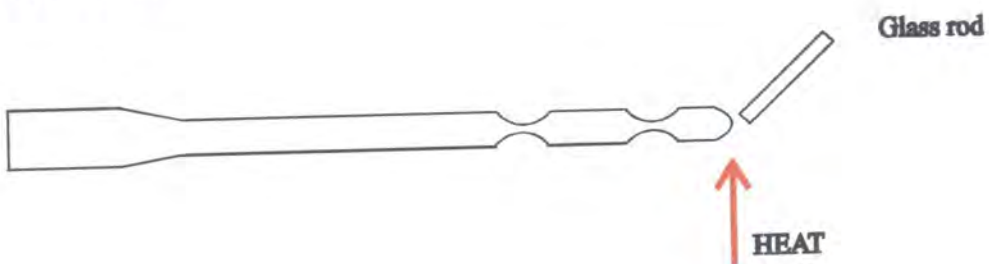


Figure 2.4.1 Schematic diagram of the preparation process.

#### 2.4.2. Sample addition

The sample was then placed into the bottom of the glass tube. The sample has to be added to the tube using a spatula. The granules have to be poked through the constrictions using a thin copper wire. The process can be quite time consuming if the constrictions are narrow. The sample should fill a maximum of 70 % of the lower compartment of the sample tube.

The final addition to the tube was a peice of glass wool which was placed at the top of the four centimetre constriction. The glass wool prevents any of the sample being sucked away when the tube is evacuated.

#### 2.4.3. Vacuum techniques

The glass tube was placed onto a vacuum line as shown in figure 2.4.2. The taps to the sample and the adsorbate were initially closed and the rest of the system pumped down. Slowly the tap to the sample tube was opened so that the tube was evacuated and the sample did not suck out of the tube. If necessary it is possible at this point to leave the system to dehydrate at 400°C for 24 hours. Heating is carried out using a sand oven or metal block heater and is especially useful for zeolite systems.

The next stage was a freeze-pump-thaw cycle which was repeated five times to remove any adsorbed gases. The tube was initially held in liquid nitrogen, pumped down and then allowed to thaw to room temperature. The sample was then frozen at liquid nitrogen temperature once again and the tap to the adsorbate opened for the first time. The system was allowed to equilibrate for one hour before the tap was shut off again.

It is possible to measure the adsorption quantitatively using this system. Initially the volume of the vacuum line has to be measured, then the initial and final pressure within the system noted from the Pirani gauge. The moles actually adsorbed can then easily be calculated using the gas laws.

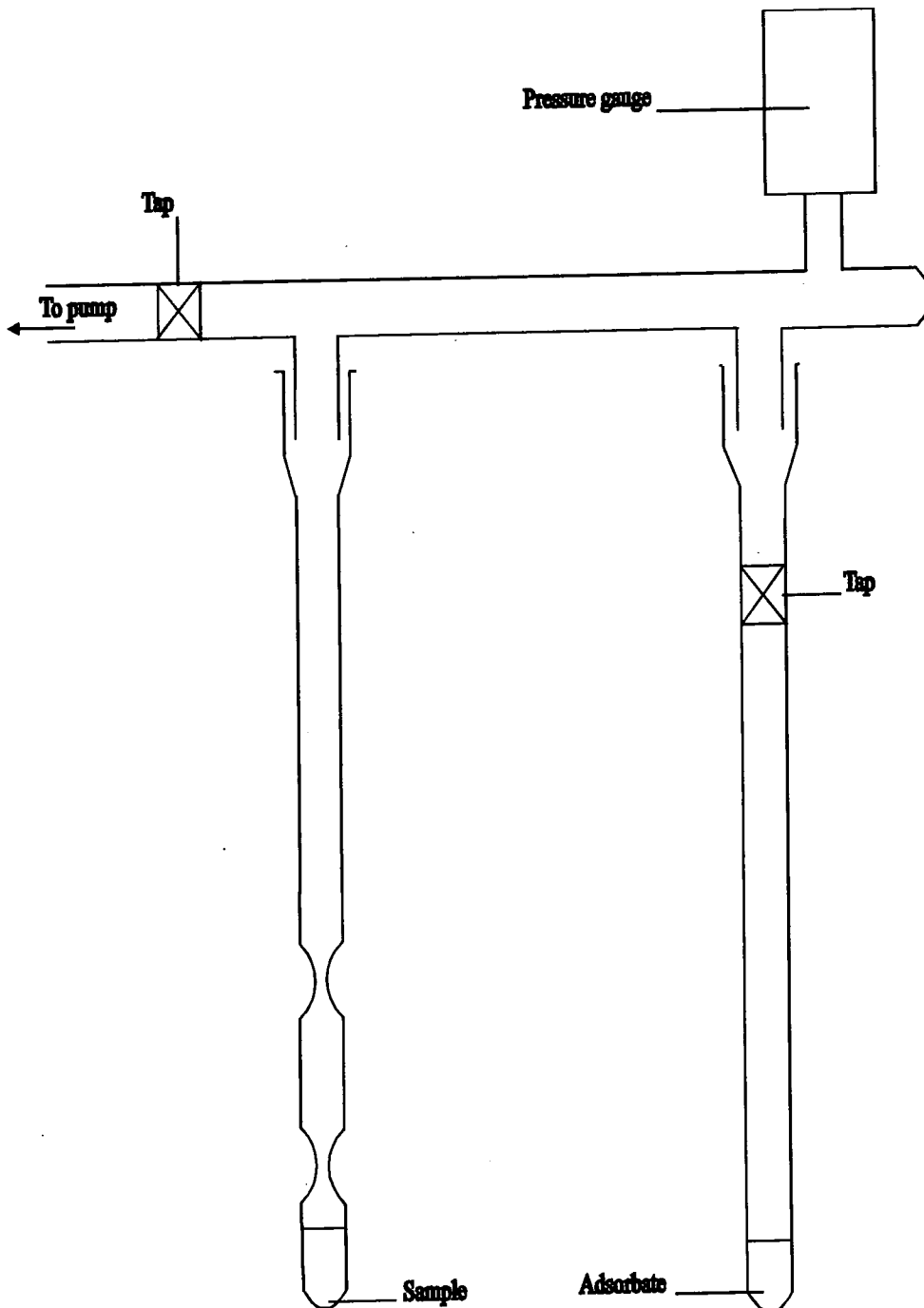


Figure 2.4.2. Schematic diagram of the vacuum line assembly.

#### 2.4.4. Rough sealing

After the adsorption had been carried out, the tap to the vacuum pump was closed. The top constriction was then heated, while the tube was on the vacuum line, using a hand torch with a small, strong blue flame. When the glass glowed red, the tube was pulled down using a pair of tweezers to seal it off, as shown in figure 2.4.3.

The seal is only rough, but it is important to pull down vertically so the tube will fit onto the lathe. The remaining ampoule remains under reduced pressure and contains a sealed system.

#### ROUGH SEAL

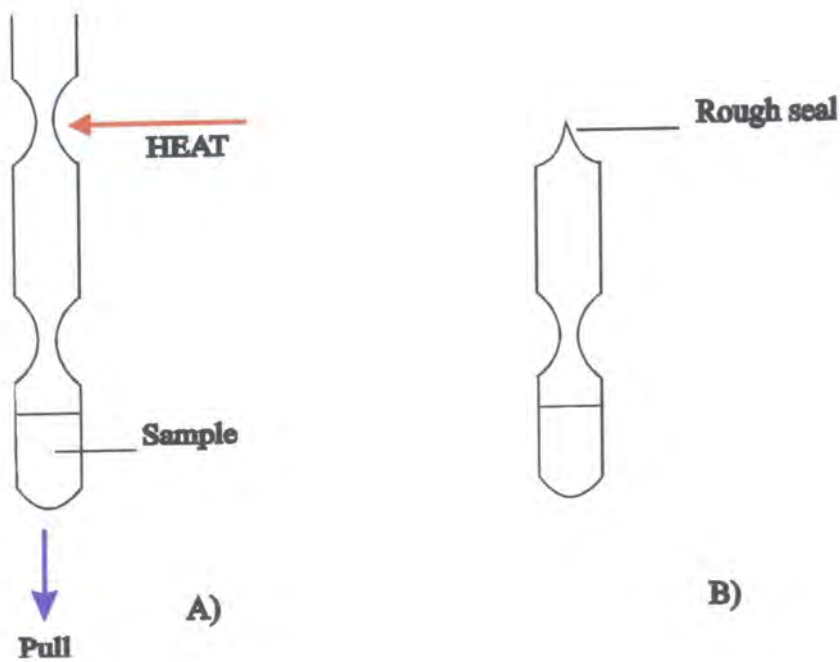


Figure 2.4.3. Schematic diagram showing the rough sealing process.

#### 2.4.5. Accurate seal

The accurate seal was achieved using a pair of specially designed brass holders as shown in figure 2.4.4. The five-centimetre rough ampoule was placed in the stock so that the constriction at one centimetre just showed, then the head was screwed on to hold it in place.

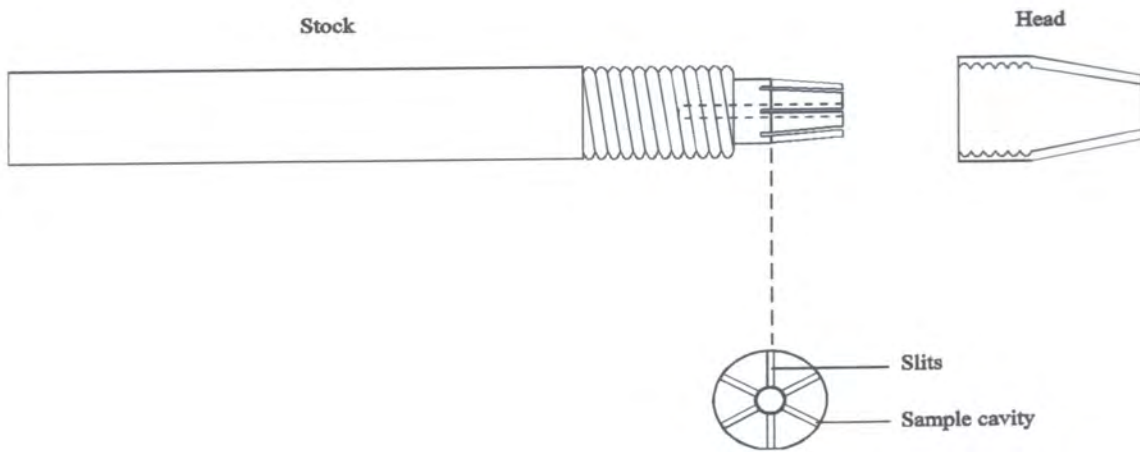


Figure 2.4.4. Diagram showing the specially designed brass holder.

The one stock with the ampoule was then placed into liquid nitrogen so that the liquid level covered the sample as shown in figure 2.4.5.

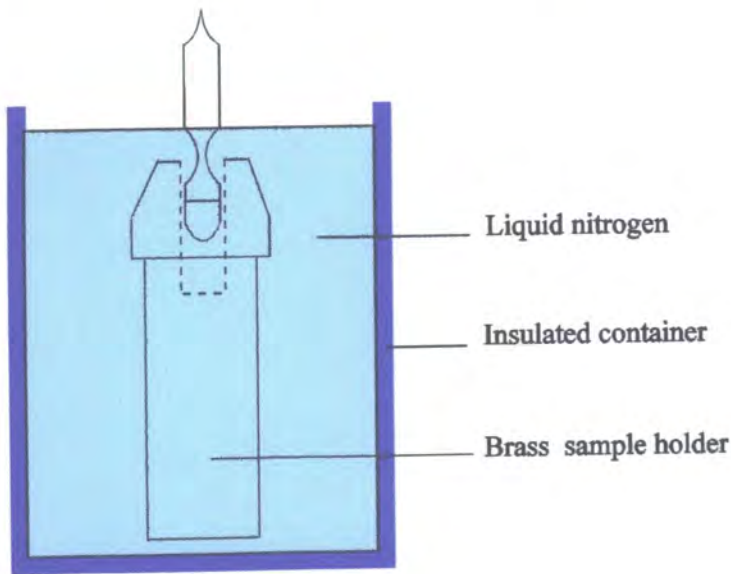


Figure 2.4.5. Diagram of the cooling process.

The frozen stock was then placed onto the lathe and the other end of the glass placed into a stock at room temperature. The glass was then rotated very quickly as shown in Figure 2.4.6. The constriction was then heated until red and the brass holders pulled apart. The seal was once again neatened using a glass rod.

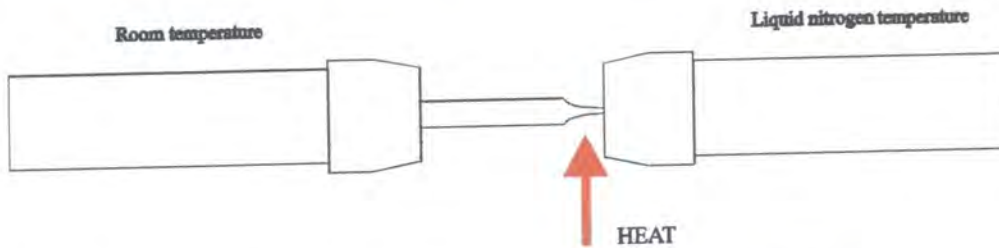


Figure 2.4.6. Diagram showing the lathe setup for the accurate seal.

The sample does not heat up significantly because the brass has a much larger thermal conductivity and specific heat capacity than the glass ampoule. When the brass holder has returned to room temperature, the glass ampoule was removed by placing tweezers in the slits under the ampoule. Figure 2.4.7. shows the position of the ampoule when it has been sealed and the shape when it has been extracted from the holder.

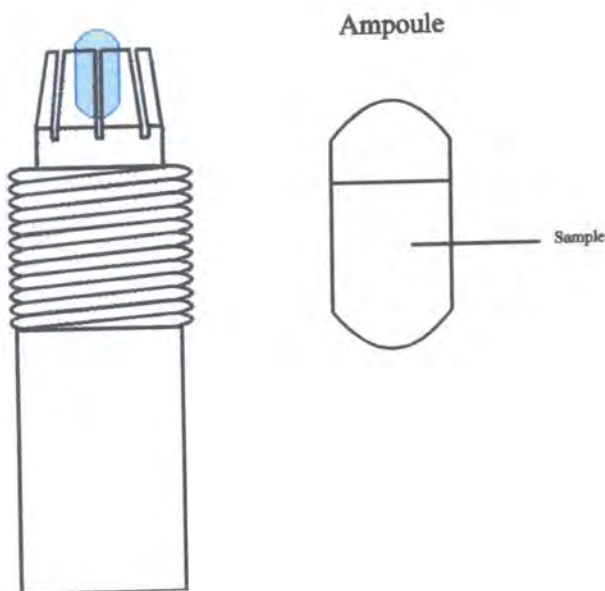


Figure 2.4.7. Diagram of the sealed ampoule in the stock.

#### 2.4.6. Packing the rotor

The rotor has to be packed very carefully so the ampoule can spin at the very fast rates that MAS requires. The glass tube is selected very carefully so that it fits neatly into the rotor. The Chemagnetics 7.5 mm pencil rotor is extremely stable on the spinning axis and the design makes ampoules easy to accommodate. The rotor opens at both ends so that the ampoule is easy to remove, and the stability means that even ampoules with slight imperfections in symmetry will spin.

The rotor has to be packed as shown in figure 2.4.8. The drive tip and spacer are placed in the bottom of the rotor and then some packing powder is added. The packing powder has to be fine and show no NMR signal for the nuclei studied. In my experiments I use flowers of sulfur or sodium chloride. The ampoule is then bedded on the powder and the top filled with more packing powder. The end cap is then inserted tightly and the rotor spun at upto 4 kHz.

## CMX 7mm MAS sample rotor

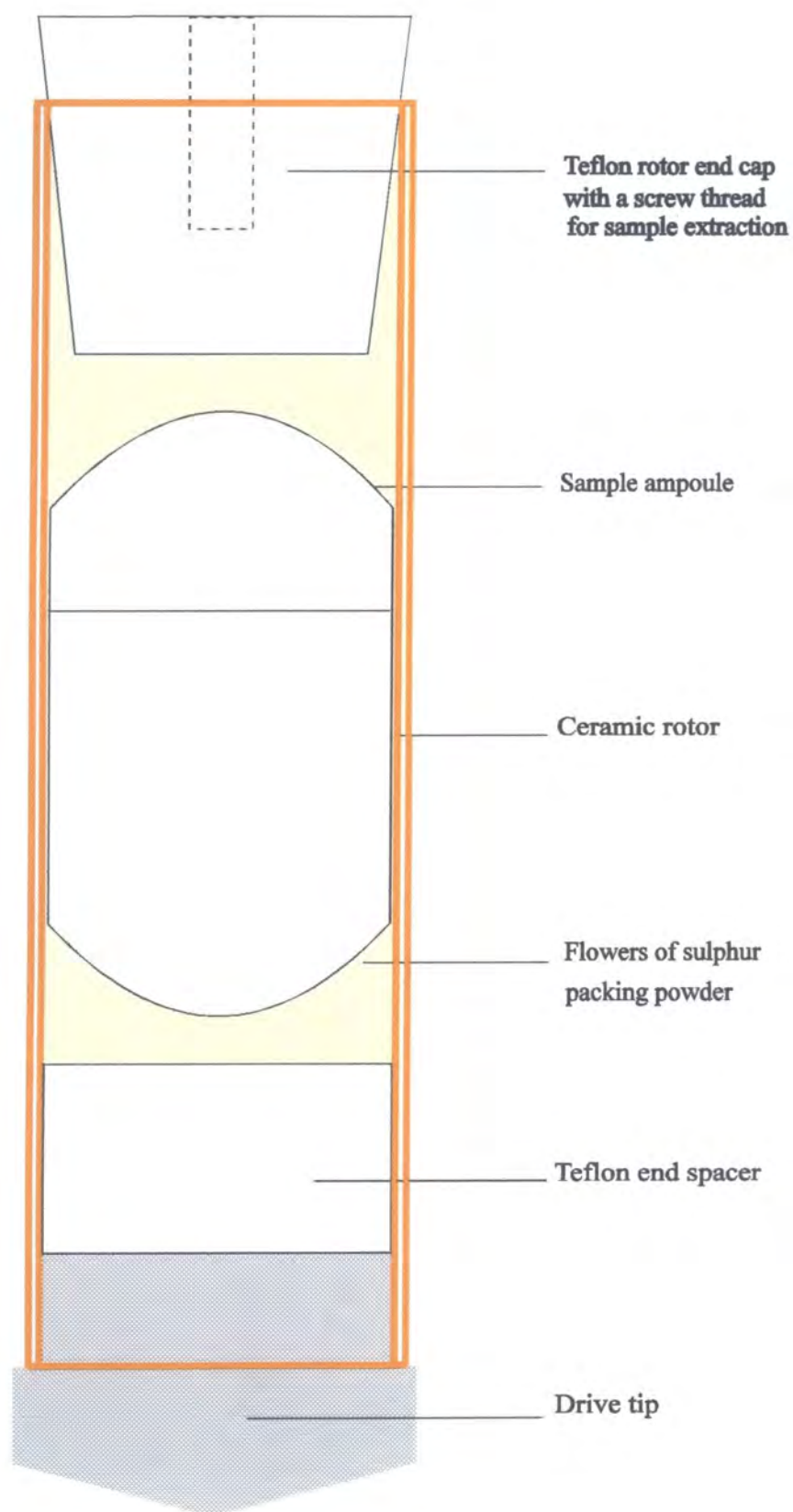


Figure 2.4.8. Diagram of the pencil rotor packed with the ampoule.

## Chapter 3      Deuterium results

### 3.1 Deuterium NMR

The first section of results will concentrate on deuterium NMR. The adsorption of water onto activated carbons has been an area of considerable interest producing many theories explaining the adsorption process. This seemed an ideal place to start an NMR investigation because the results could be compared to those obtained by other methods of analysis explained in the introduction.

There are several advantages in using  $^2\text{H}$  NMR instead of the more usual proton NMR. Solid-state NMR of protons is awkward because the signals tend to be very broad and there is only a small shift range so the signals overlap. This makes the peak assignment difficult. There are also protons in the substrate and in the small percentage of water that the granules have when taken from the sample bottle. These background signals make it difficult to distinguish peaks from the adsorbate probe molecules.

To overcome these difficulties I used 99.99% isotopically enriched  $^2\text{H}_2\text{O}$  as the adsorbate. The deuterium NMR signals for adsorbed molecules are quite narrow compared to those observed in proton NMR spectra, reducing the overlap of peaks with similar chemical shifts. The peaks are narrower because the  $^2\text{H}, ^2\text{H}$  dipolar interaction is smaller than the  $^1\text{H}, ^1\text{H}$  interaction, this is because the dipolar interaction is proportional to the square of the gyro-magnetic ratio ( $\gamma^2$ ). The large abundance of the  $^2\text{H}$  nuclei means that the experiments are very fast to obtain good signal intensity even at low loadings (typically 4-36 mins). The other advantage was that  $^2\text{H}$  nuclei do not occur naturally, so any  $^2\text{H}$  NMR signal must be from the adsorbate molecules. Deuterium nuclei are quadrupolar and susceptible to quadrupolar broadening effects. However in the adsorbed state the molecular motion is fast, and when coupled with MAS the broadening is removed.

The results from the  $^2\text{H}$  NMR fall into three sections. The first part is a systematic loading experiment using one type of activated carbon substrate and analysing the spectrum with various loadings of liquid  $^2\text{H}_2\text{O}$ . The second set of results produced an adsorption isotherm. This was a simultaneous gravimetric and NMR experiment to compare the NMR data with those conventionally accepted by carbon chemists. The final section compares several activated carbon types, to see how NMR spectra of samples with similar loadings of adsorbate could give information about the pore structure of the carbon substrate.

### 3.1.1 Loading experiments

The loading experiments were all carried out on the BPL dry carbon which contained less than 2% w/w of water. Samples were produced with loadings from 5%-50% w/w of  $^2\text{H}_2\text{O}$ . The samples were prepared by adding a known mass of liquid  $^2\text{H}_2\text{O}$  by pipette to the carbon sample and then allowing them to equilibrate for one hour in a sealed sample bottle.

These samples were then analysed by deuterium NMR on the CMX200 using the 7.5 mm pencil rotor MAS probe, which holds approximately 500 mg of sample. High-resolution spectra were obtained using spinning speeds of 3.0 kHz and a single-pulse regime with no proton decoupling. In this experiment a recycle delay of 2 s was used and 256 acquisitions taken for each sample. This meant the acquisition time for each spectrum was 9 minutes. The spectra were recorded under identical conditions in absolute intensity mode to allow direct comparison.

The spectra recorded for 5-20% w/w loading of  $^2\text{H}_2\text{O}$  are shown in figure 3.1.1. The spectra are shown on the same expansion, with a single peak around -8 ppm, compared to the reference sample of liquid  $^2\text{H}_2\text{O}$  at 0 ppm. As the loading increases the area under the peak gets larger. This shows that the NMR experiment is quantitative, so the amount of  $^2\text{H}_2\text{O}$  present in a sample could be calculated by comparison with a reference sample. The spectra recorded for 25-35% w/w loading of  $^2\text{H}_2\text{O}$  are shown in figure 3.1.2. These spectra are also shown on the same expansion. The spectra show

the same pattern, with the peak around -8 ppm gradually increasing in area as the load increases. The spectra recorded for 40-50% w/w loading of  $^2\text{H}_2\text{O}$  are shown in figure 3.1.3. These spectra are all on the same expansion so that they can be compared directly. When the loading reaches 40% w/w the peak at -8 ppm reaches a maximum intensity and a second narrower peak at 0 ppm develops. As the load increases the second peak becomes larger but the broader peak at -8.0 ppm remains with the same area.

The chemical shift and linewidth data for each sample are given in table 3.1.1. An accurate analysis of the chemical shift data gives an interesting result. As the load increases then the chemical shift moves to high frequency. The broad peak at 5% w/w is at -8.8 ppm, but at 50% loading the broad peak is at -6.7 ppm.

Sample loading	$\delta_{2\text{H}}$ Peak 1 (ppm)	$\delta_{2\text{H}}$ Peak 2 (ppm)	$\Delta_{1/2}$ Peak 1 (Hz)
Pure $^2\text{H}_2\text{O}$ liquid		0	6
5% w/w $^2\text{H}_2\text{O}$	-8.8		166
10% w/w $^2\text{H}_2\text{O}$	-8.5		130
15% w/w $^2\text{H}_2\text{O}$	-8.3		117
20% w/w $^2\text{H}_2\text{O}$	-8.0		117
25% w/w $^2\text{H}_2\text{O}$	-8.0		113
30% w/w $^2\text{H}_2\text{O}$	-7.9		113
35% w/w $^2\text{H}_2\text{O}$	-7.7		119
40% w/w $^2\text{H}_2\text{O}$	-7.2	0	131
45% w/w $^2\text{H}_2\text{O}$	-7.0	0	153
50% w/w $^2\text{H}_2\text{O}$	-6.7	0	165

Table 3.1.1 Chemical shift and peak width data for the  $^2\text{H}_2\text{O}$  loading experiment.



### Durham CMX200H-NMR System

D2O loading expts onto BPL dry carbon 5-20% w/w  
single pulse Bloch Decay

ppfn=1pulse  
cdir=bp1dd20  
cfn=250494sp.5  
cfd=0  
sf1=30.702 MHz  
sw=20 KHz  
ad=15 usec  
al=1k cplx  
aqt=51.201 msec  
dw=50 usec  
extm=2.0512 sec  
p=157 deg  
pd=2 sec  
pw=6 usec  
rd=15 usec  
ac=256 scns

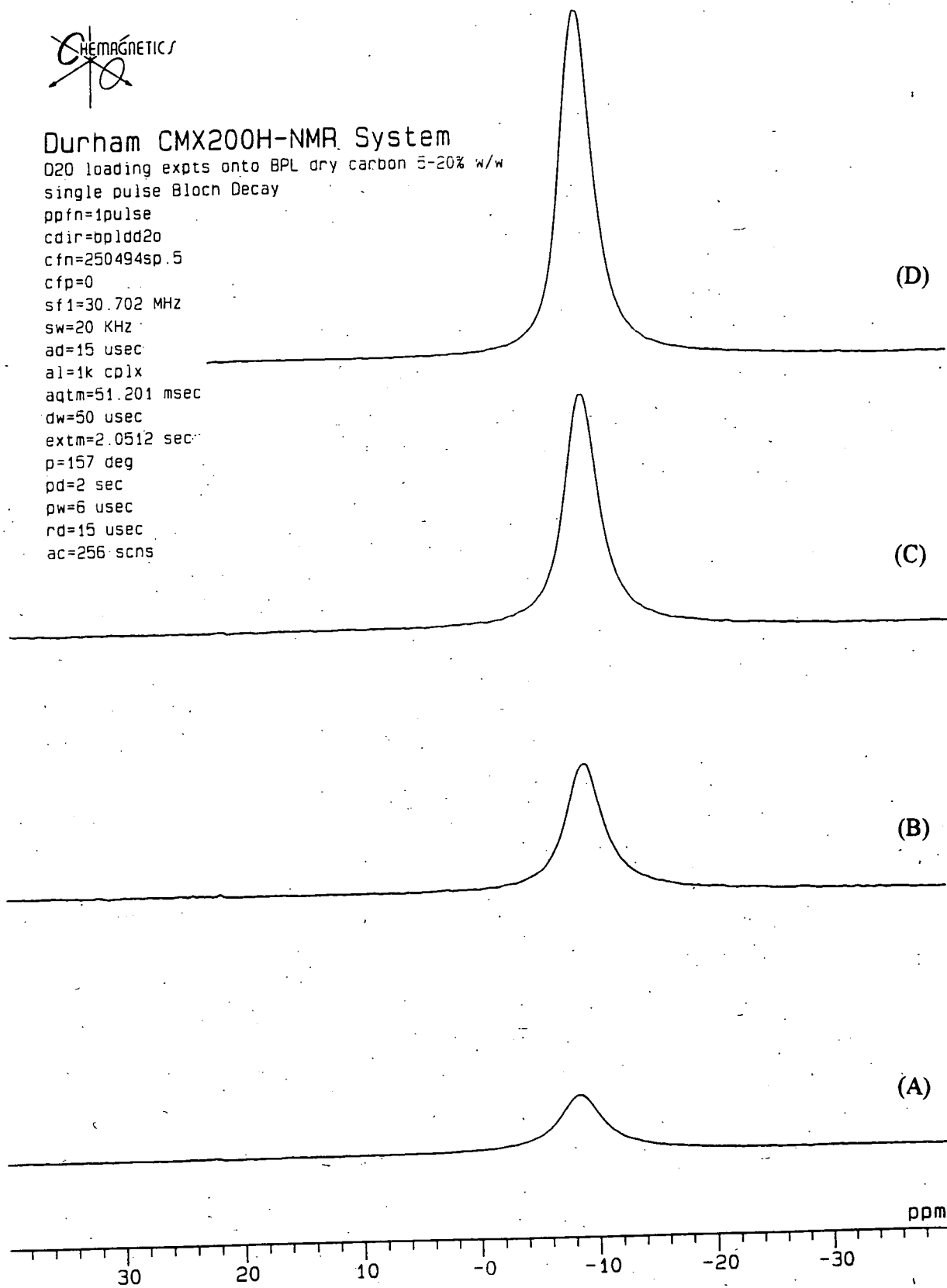


Figure 3.1.1.  $^2\text{H}$  NMR spectra of BPL activated carbon with; (A) 5% w/w  $^2\text{H}_2\text{O}$ , (B) 10% w/w  $^2\text{H}_2\text{O}$ , (C) 15% w/w  $^2\text{H}_2\text{O}$  and (D) 20% w/w  $^2\text{H}_2\text{O}$ .



### Durham CMX200H-NMR System

D2O loading expts onto BPL dry carbon 25-35% w/w  
single pulse Bloch Decay  
ppfn=1pulse  
cdir=bpldd2o  
cfn=250494sp.8  
cfp=0  
sf1=30.702 MHz  
sw=20 KHz  
ad=15 usec  
al=1k cplx  
aqtm=51.201 msec  
dw=50 usec  
extm=2.0512 sec  
p=157 deg  
pd=2 sec  
pw=6 usec  
rd=15 usec  
ac=256 scns

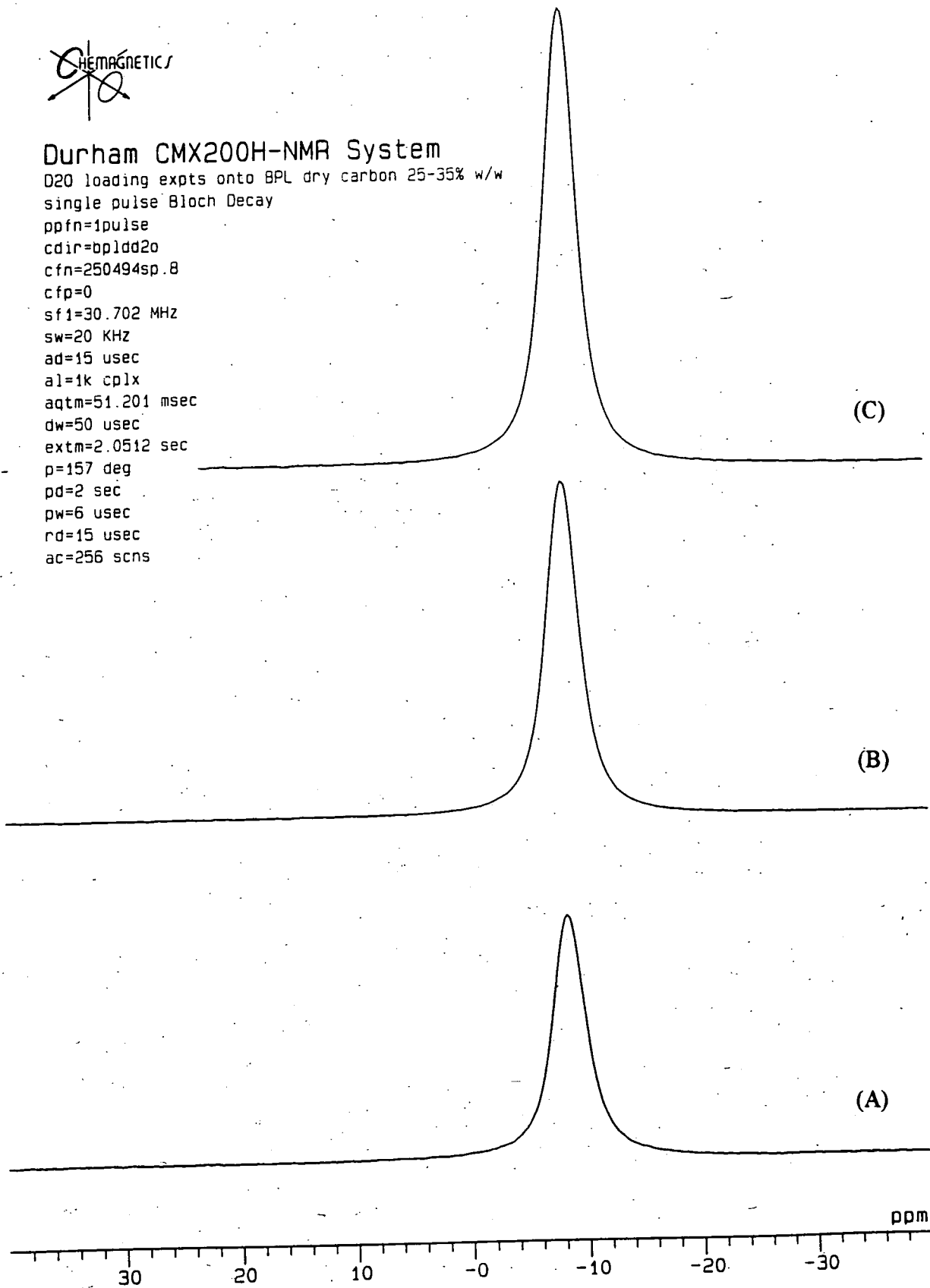


Figure 3.1.2.  $^2\text{H}$  NMR spectra of BPL activated carbon with; (A) 25% w/w  $^2\text{H}_2\text{O}$ ,  
(B) 30% w/w  $^2\text{H}_2\text{O}$  and (C) 35% w/w  $^2\text{H}_2\text{O}$ .



### Durham CMX200H-NMR System

50% D2O on BPL dry at 3.5 kHz

single pulse Bloch Decay

ppfn=1pulse

cdir=2dbp1dd2o

cfm=240494sp.12

cfp=2

sf1=30.702 MHz

sw=20 KHz

ad=15 usec

al=1k cplx

aqtm=51.201 msec

dw=50 usec

extm=2.0512 sec

p=157 deg

pd=2 sec

pw=6 usec

rd=15 usec

ac=256 scns

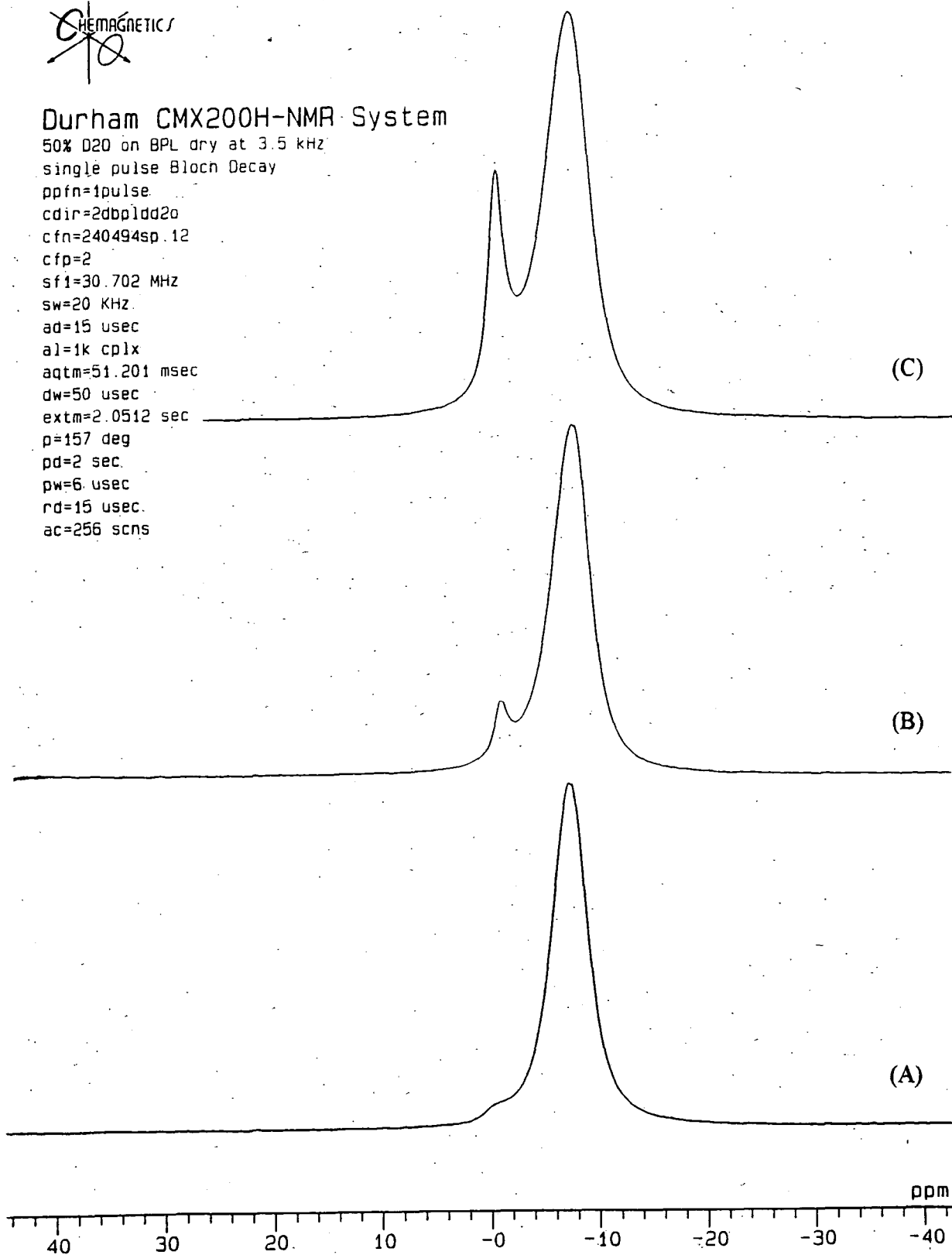


Figure 3.1.3.  $^2\text{H}$  NMR spectra of BPL activated carbon with; (A) 40% w/w  $^2\text{H}_2\text{O}$ ,  
(B) 45% w/w  $^2\text{H}_2\text{O}$  and (C) 50% w/w  $^2\text{H}_2\text{O}$ .



The comparison of the linewidths gives some extra information about the adsorbed molecules. The peak at -8 ppm has a half-height width ( $\Delta_{1/2}$ ) of 100-165 Hz compared to the pure liquid  $^2\text{H}_2\text{O}$  at 0 ppm which is only 6 Hz wide. The broad peak also changes width as the  $^2\text{H}_2\text{O}$  load increases. At 5% loading the  $\Delta_{1/2}$  is 166 Hz, as the load increases to 30% the  $\Delta_{1/2}$  falls to 113 Hz. The  $\Delta_{1/2}$  then rises to 165 Hz as the load reaches 50% w/w.

### 3.1.1.1 Discussion

The adsorption of water by activated carbon occurs on the high surface area provided by the pore-system, and is believed to occur in two stages. Initially, adsorption occurs on active surface sites. These sites may be impurities such as ash or oxygen functional groups resulting from the activation process. It is proposed that these will act as the primary sites for water adsorption and are occupied at low relative water vapour pressure (usually at  $p/p_0 < 0.4$ , or 40% RH in this case). The NMR data support this supposition. The broad peak at  $\sim -8$  ppm is attributed to  $^2\text{H}_2\text{O}$  molecules physisorbed by the activated carbon. The large linewidth (100-160 Hz) arises because the motion of the  $^2\text{H}_2\text{O}$  molecules is restricted when they are adsorbed. (see the  $T_2$  information presented later). In fact, the deuterium spectrum shows spinning sidebands which are indicative of a relatively rigidly bound adsorbate. In addition to providing evidence for the strong binding of the deuterium oxide initially adsorbed by the activated carbon, the substantial chemical shift of the deuterium signal (relative to free  $^2\text{H}_2\text{O}$ ) is indicative of the adsorbate being held within the pore structure of the carbon; the adsorbate being held between the graphitic sheets in the pores could result in its being extensively shielded by the delocalised  $\pi$ -electron clouds.

After this primary adsorption has occurred, further adsorption is thought to occur through hydrogen bonding, with the primary sites acting as centres for water clusters to form and spread across the surface as the relative pressure increases. The NMR data also support this hypothesis. Table 3.1.1 shows that the linewidth of the -8 ppm peak decreases steadily until the load is 30% w/w. This would result if the

adsorbed deuterium oxide was gradually becoming more like "liquid"  $^2\text{H}_2\text{O}$ . At about 30% w/w, the film of adsorbate merges within the micropores; this corresponds to the steep pore filling region of the isotherm. At this point, the linewidth would be expected to remain constant as the adsorbate is essentially like "liquid"  $^2\text{H}_2\text{O}$ . It should however be noted that the chemical shift at this point is still -8 ppm, indicating that the process is occurring within the shielded bulk of the carbon material, probably in the micro/meso pore region. When these micropores are full then the water adsorbs in larger pores, these sites experience less shielding so the broad peak is shifted to higher frequency and the overlap of peaks increases the observed line width.

At loadings of 40% w/w of deuterium oxide and greater, the carbon is effectively saturated. Significantly, the NMR data demonstrate a new phenomenon at this point. A sharp  $^2\text{H}_2\text{O}$  signal appears which has a chemical shift of approximately 0 ppm. Clearly, this arises because the deuterium oxide associated with this peak is in a substantially different environment to the material adsorbed at lower loadings. As the peak is sharp, it is indicative of "liquid" like  $^2\text{H}_2\text{O}$ , and its chemical shift shows that the nuclei are not heavily shielded. It is likely that this peak corresponds to  $^2\text{H}_2\text{O}$  adsorbed on the surface or in macropores close to the surface.

### 3.1.2 Adsorption isotherm

NMR data on the adsorption of  $\text{H}_2\text{O}$  onto activated carbon have been reported (1,2). All of the reported experiments have concentrated on the NMR aspects of the system, and have not attempted to relate the adsorption studies to the characteristic adsorption isotherm of the material studied. Following the loading experiments using liquid  $^2\text{H}_2\text{O}$  discussed above, it was decided to remedy this lack of information by detailed adsorption isotherm studies. Since the site of adsorption on the porous material is determined by the partial pressure of vapour above the adsorbate (water adsorption on BPL carbon is type V by the B.D.D.T. classification), the present studies have compared NMR data with a gravimetrically determined deuterium oxide isotherm obtained for BPL carbons exposed to deuterium oxide vapour in the partial pressure range  $p/p_0 = 0$  to  $0.8$  (linearly equivalent to relative humidity 0-80%).

The data obtained have demonstrated that NMR results are directly comparable to those from more classical methods of determining adsorption equilibria, with the added advantage that some meaningful dynamic data can be extracted from NMR. The NMR data are analysed with respect to the integral area under the peaks, the chemical shift and observed line widths. This allows the NMR data to be verified as well as provide information about the state of the directly observable adsorbed molecules in the pore structure.

#### 3.1.2.1 Materials

The  $^2\text{H}_2\text{O}$  used in the experiment was supplied by Aldrich with 99.99% isotopic enrichment. The activated carbon (BPL) was supplied by Chemiviron Carbon. The "unaged" sample was used as supplied (water content  $<2\%$  w/w), whereas the "aged" sample was obtained by exposing a sample of unaged carbon to a flowing humid airstream (80% RH,  $22^\circ\text{C}$ ) for a period of about one year. When supplied, the BPL carbon typically had a BET surface area of  $1200 \text{ m}^2 \text{ g}^{-1}$  and a micropore volume of  $0.53 \text{ cm}^3 \text{ g}^{-1}$  at STP.

### 3.1.2.2 Gravimetric method for the adsorption isotherm

The procedures for measuring a water adsorption isotherm with this equipment have been described fully elsewhere<sup>(3)</sup>. Isotherms were taken during both adsorption and desorption cycles in order to obtain the characteristic hysteresis of the type V behaviour. The sample humidifying equipment consisted of three parts, as described below. The heat exchanger, reservoir and sample tubes were maintained at 22 °C in a constant temperature cabinet. These are shown in figure 3.1.4

{i} A humid air generator: compressed air of dewpoint less than minus 20°C was filtered by passing it through a dry carbon bed prior to being split into two streams. One stream was passed through a Dreschel bottle containing  $^2\text{H}_2\text{O}$  held at 35°C, prior to recombination with the second dry air stream. The combined streams were then passed through a heat exchanger maintained at 22°C prior to flowing into the reservoir.

{ii} A humid air reservoir: This consisted of a perspex container of approximately 8 litre capacity. The RH of the air in the reservoir was monitored by means of a cooled-mirror dew-point meter and maintained at the desired value by balancing the dry/humid airflow from the generator with needle valves.

{iii} Sample tubes: The carbon samples were contained in four beds of approximately 2 cm diameter, and initially 2.3 cm depth (approximately 4 g. of carbon per bed). Air was drawn through each bed from the reservoir; the flow through each bed was maintained at 1.2 l min<sup>-1</sup> and controlled by independent needle valves and rotameters. The exhaust air was drawn through a diaphragm pump, then to a series of condensers where excess  $^2\text{H}_2\text{O}$  was recovered.

The samples were weighed at hourly intervals until no further weight change occurred (equilibrium was defined as a change of less than 0.1% in observed weight); this was typically of the order of 4-6 hours. The RH of the flowing air was then adjusted to the required new value, and the whole process repeated in order to build up the required isotherm. Deuterium oxide isotherms were measured for both the aged and unaged samples of carbon.

### 3.1.2.3 NMR method for the adsorption isotherm

At each point of the isotherm determined gravimetrically, aliquots of 0.8 g of carbon samples were transferred to hermetically sealed vials for NMR analysis. The sample bed was then re-weighed and the process repeated for the next value of RH.

The sealed samples were analysed by solid-state NMR spectroscopy. Samples were typically analysed within 2 days of their being sealed for the NMR experiments, which were carried out on a Chemagnetics CMX 200 MAS spectrometer ( $^2\text{H}$  resonance at 30.721 MHz). High-resolution spectra were obtained using spinning speeds of 4.0 kHz and a single-pulse regime with no proton decoupling. The MAS probe uses 7.5 mm pencil rotors, which contain the sealed ampoules. The ampoules have a sample capacity of approximately 300 mg. The spin-lattice relaxation time ( $T_1$ ) was measured via the inversion-recovery method on a sample with 20% w/w  $^2\text{H}_2\text{O}$  adsorbed onto the new BPL carbon. These measurements gave a value of 200 ms so in all cases a recycle delay of 2 s was used to ensure complete relaxation between pulses. The acquisition time for the spectra was 20 ms. The number of transients that were required varied from 128 to 1024 depending on the  $^2\text{H}_2\text{O}$  loading, and thus each spectrum took between 4 and 35 minutes to run.

The sample mass was measured by a difference method, subtracting the mass of the ampoule (ca 0.5 g) from the mass of the ampoule and the sample (0.8 g) prior to the NMR analysis. The experiments were carried out under the same conditions for each sample so as to achieve the quantitative analysis.

The deuterium spectra were referenced (immediately prior to each sample spectrum) to an external sample of bulk  $^2\text{H}_2\text{O}$  liquid set at 0 ppm, which had a linewidth of 6 Hz. The  $90^\circ$  pulse duration was then calibrated using a standard sample of 40% w/w  $^2\text{H}_2\text{O}$  adsorbed onto the unaged BPL carbon kept in a sealed glass ampoule. The area under the peak for the standard sample was measured using the absolute intensity mode, then the test sample was compared to this integration, taking into account the sample mass.

### 3.1.2.4 Results

The results for the aged and unaged carbon samples are presented in tables 3.1.2 and 3.1.3 respectively. These give a measure of the  $^2\text{H}_2\text{O}$  uptake, expressed as a w/w% of the sample for both gravimetric- and NMR-determined adsorption at different values of RH.

RH(%)	Gravimetric	NMR		
	$^2\text{H}_2\text{O}$ (w/w%)	$^2\text{H}_2\text{O}$ (w/w%)	Peak width (Hz)	Number of peaks
20	0.65	0.5	828	1
30	1.05	1.0	284	1
40	3.4	3.4	171	1
55	8.3	8.3	129	1
70	24.5	19.8	136	1
80	35.1	34.1	141	2
85	38.2	38.2	144	2
80	38	37.7	133	2
70	36.8	33.6	131	2
60	33.9	29.8	136	1
50	20.2	18.7	140	1
40	5.6	5.2	140	1
30	2.7	2.8	332	1
20	1.2	1.0	645	1
10	0.4	0.5	1065	1

Table 3.1.2 Gravimetric and NMR data for  $^2\text{H}_2\text{O}$  adsorption onto the "unaged" BPL sample

RH(%)	Gravimetric		NMR	
	$^2\text{H}_2\text{O}$ (w/w%)	$^2\text{H}_2\text{O}$ (w/w%)	Width (Hz)	Number of peaks
20	1.7	1.9	531	1
30	3	3.3	544	1
40	7.3	6.4	181	1
55	23	22	141	1
70	36.5	33.5	131	1
80	39.6	40.2	134	2
85	40.5	40.5	128	2
80	39.4	40.2	133	2
70	38.3	37.5	141	2
60	35.9	33.4	123	1
50	30.2	27.1	136	1
40	12.1	12	140	1
30	5.2	5	454	1
20	2.6	2.8	845	1
10	1.2	1.0	1224	1

Table 3.1.3. Gravimetric and NMR data for  $^2\text{H}_2\text{O}$  adsorption onto the “aged” BPL sample

The adsorption data given in tables 3.1.2 and 3.1.3 are shown graphically in figures 3.1.5 and 3.1.6 as the characteristic deuterium oxide adsorption isotherm. The NMR data are shown as a solid line, the gravimetric data as a dotted line, while the peak widths, tabulated in tables 3.1.2 and 3.1.3, are shown as dashed lines in respect of the right hand ordinate of the figures. The adsorption branch of the isotherm is shown with circles as markers, the desorption branch with triangles. The results show good correlation between the NMR and gravimetric values. The adsorption isotherms have the same shape, and the characteristic hysteresis is clearly defined for the NMR data as well as by the gravimetric analysis.

As discussed briefly in section 3.1.1 the NMR results give further information which is not available directly from the traditional methods. Figure 3.1.7 shows the NMR spectra from the aged BPL with a low load, a medium load and finally a saturated load of  $^2\text{H}_2\text{O}$ . Initially a broad peak develops at 6 ppm to low frequency of the bulk  $^2\text{H}_2\text{O}$  peak. This broad peak builds up to a maximum area as the RH

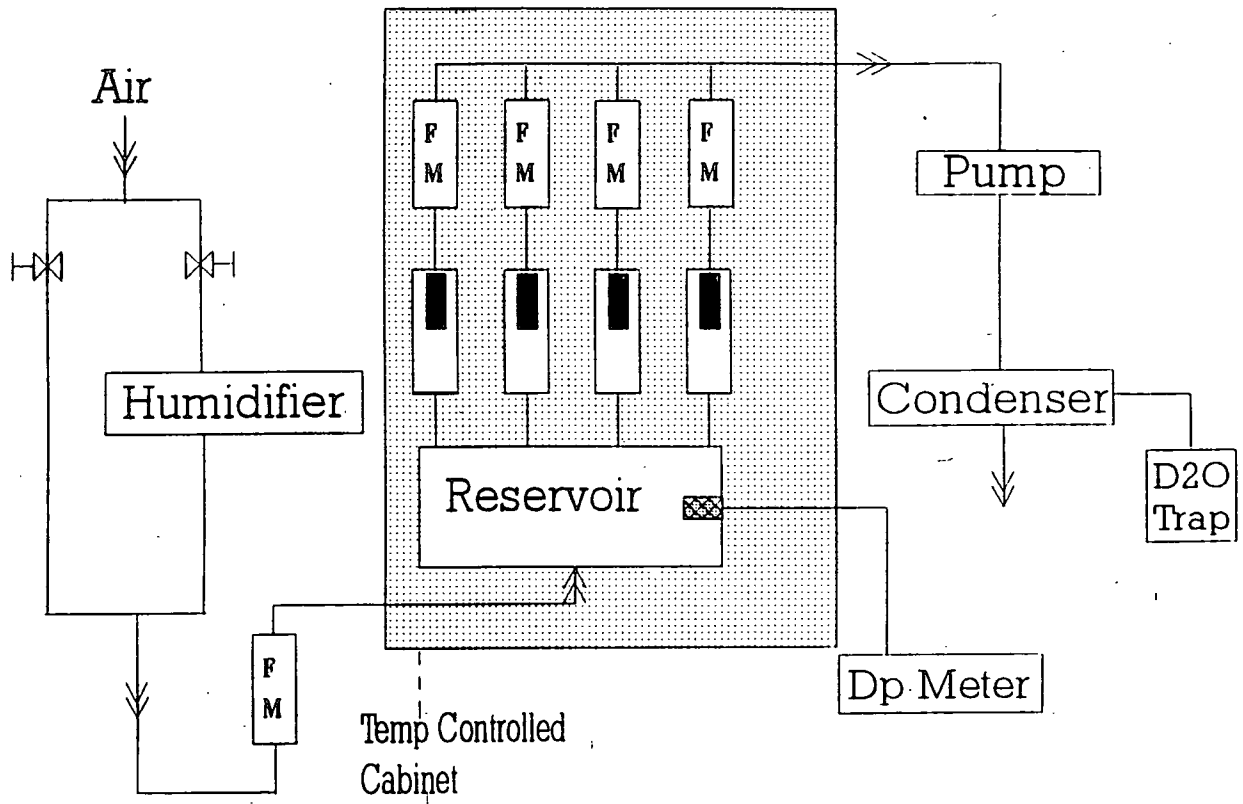


Figure 3.1.4. Schematic diagram of the water adsorption apparatus.  
 FM = Flow meter Dp = Dew point

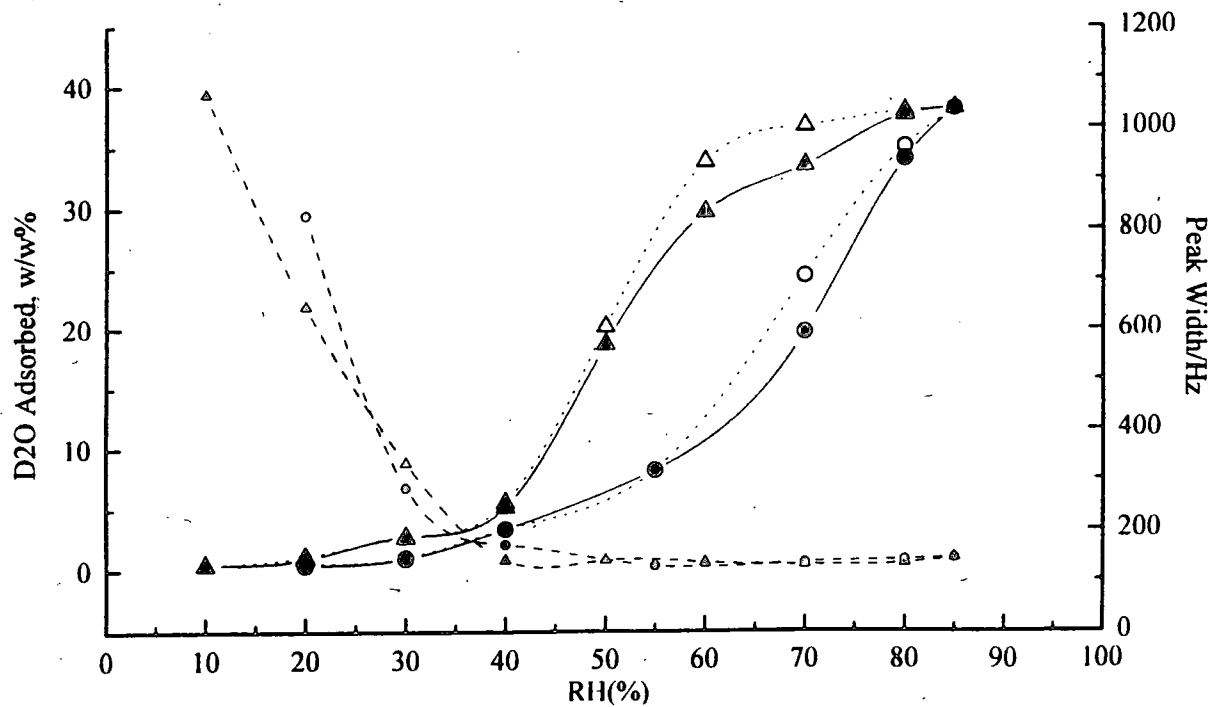


Figure 3.1.5. Adsorption of deuterium oxide on unaged BPL carbon: solid line shows NMR data, dotted line shows gravimetric data, dashed line shows peakwidth; circle shows adsorption branch, triangle shows desorption branch

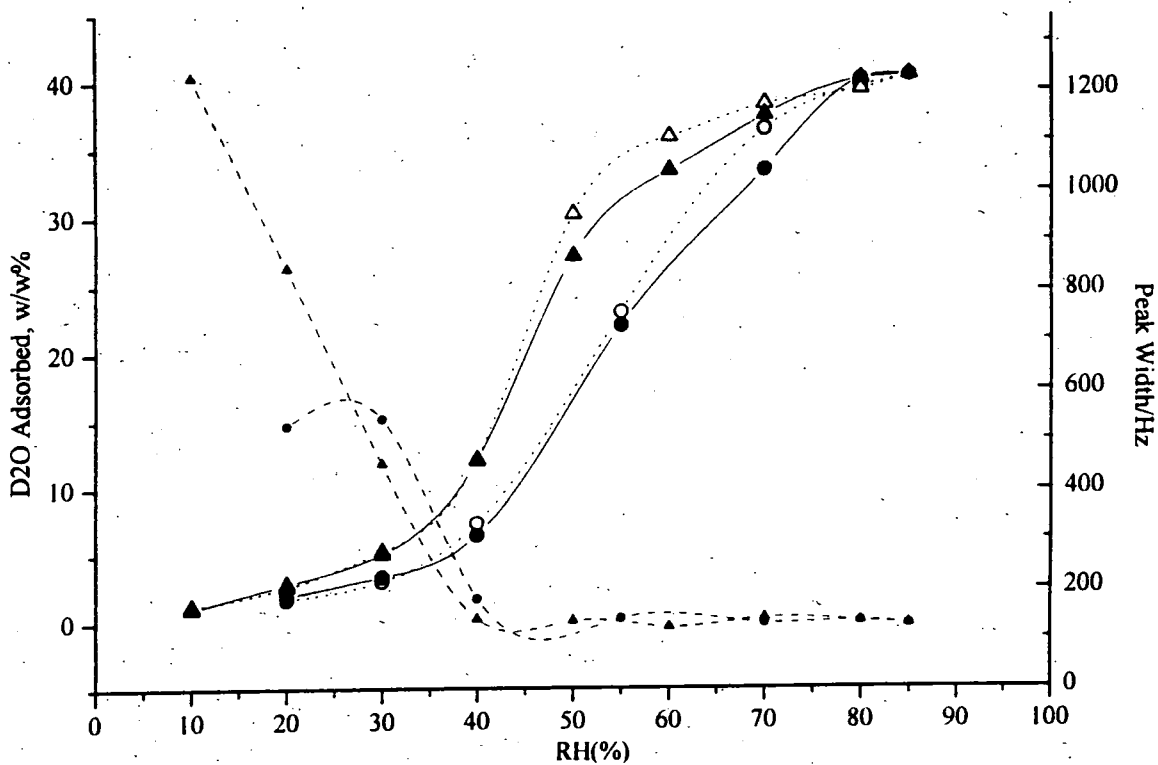


Figure 3.1.6. Adsorption of deuterium oxide on aged BPL carbon: solid line shows NMR data, dotted line shows gravimetric data, dashed line shows peakwidth; circle shows adsorption branch, triangle shows desorption branch

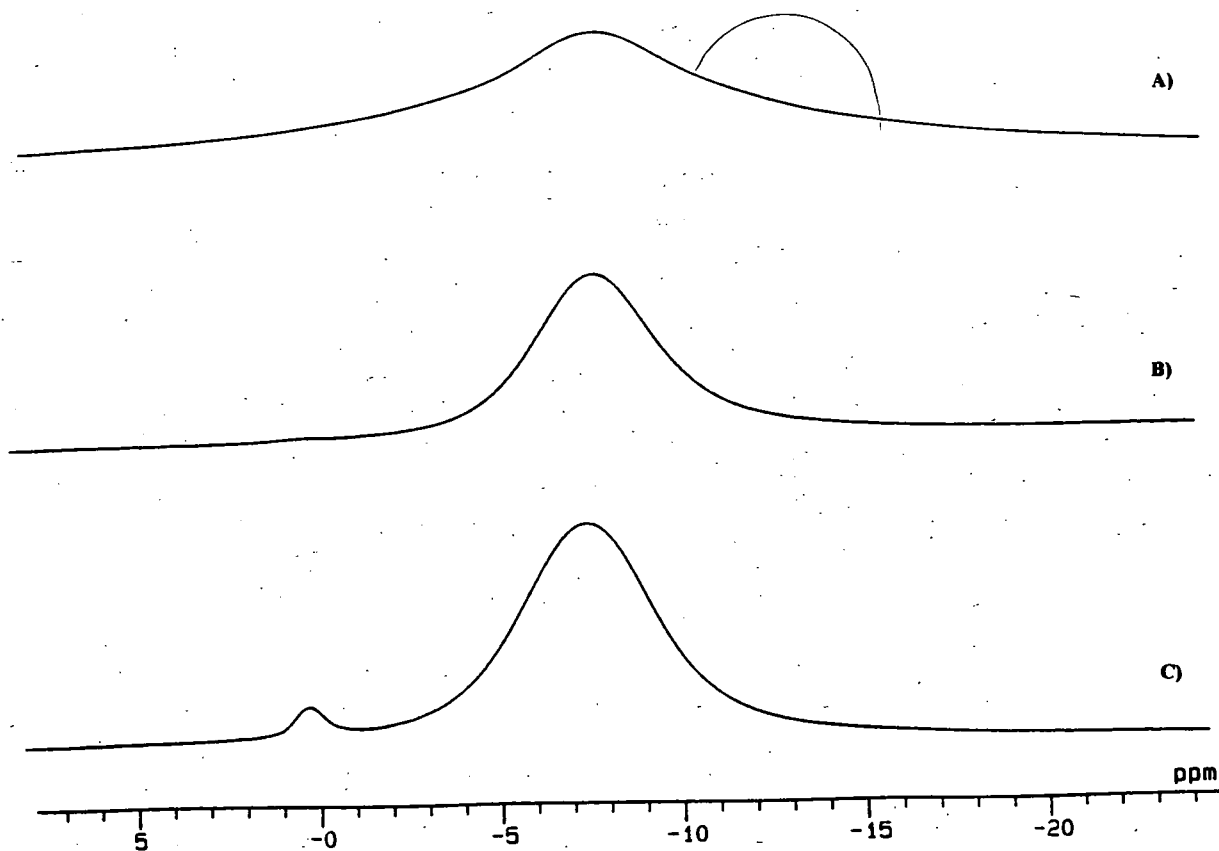


Figure 3.1.7. Deuterium spectra of; A) Aged BPL with 30% RH  $^2\text{H}_2\text{O}$ , B) Aged BPL with 60% RH  $^2\text{H}_2\text{O}$  and C) Aged BPL with 85% RH  $^2\text{H}_2\text{O}$

increases, and then a second narrow peak appears at approximately the same shift as the  $^2\text{H}_2\text{O}$  reference sample. The second peak develops at 80% RH (with an ~35% w/w loading of  $^2\text{H}_2\text{O}$  on the BPL carbon) on the adsorption branch of the adsorption cycle. On the desorption branch, the second peak ceases to be visible when the relative humidity drops below 70%.

The broad peak has a width of 600-1000 Hz when the  $^2\text{H}_2\text{O}$  loading is less than 3% w/w. However when the loading is greater than 5% the line width is reduced, to 130-140 Hz. These widths are recorded in tables 3.1.2 and 3.1.3, as is the number of peaks observed at a given RH, and are shown in figures 3.1.5 and 3.1.6 in relation to the deuterium isotherm.

#### 3.1.2.5 Discussion

The data derived from the two types of experiment are in good agreement, the isotherms derived from both NMR and gravimetric experiments being very comparable, particularly in the lower RH region of the plots shown in figures 3.1.5 and 3.1.6. The deviations between the NMR and gravimetric data are more apparent at higher RH values and it would be expected that loss of adsorbate would be greater at the higher loadings and for the NMR experiments which were carried out approximately two days after the gravimetric experiments. Figures 3.1.5 and 3.1.6 show this.

The adsorption isotherms that were created from the NMR data clearly show the characteristic hysteresis in the adsorption/desorption branches of the isotherm. This indicates that it is harder for the water to be removed than it is to be adsorbed; the origins of this are thought to lie in differences in the shape of the menisci of liquid adsorbed in the micropores during adsorption and desorption cycles. The NMR data also show well the characteristic difference between the isotherms for unaged and aged carbon which has been reported previously. The isotherm for aged carbon is much tighter and shifted to the left compared with the isotherm for unaged carbon; this is in keeping with the surface of the aged carbon becoming more hydrophilic as a result of chemisorption of very small quantities of deuterium oxide on the carbon surface.

Duplication of these changes in the shapes and positions of the two isotherms was taken as good evidence that the data obtained by NMR experiments had valid physical significance in terms of the adsorption of deuterium oxide into the pore structure of an activated carbon.

Clearly integration of the  $^2\text{H}$  NMR spectra gives meaningful results that compare to gravimetric results. The chemical shift and line width data for the isotherm adsorption experiment follow the same pattern as the  $^2\text{H}_2\text{O}$  loading data in the previous section. The gaseous adsorption of  $^2\text{H}_2\text{O}$  also shows a broad peak initially, at -6 ppm for the BPL carbon, at loadings below 35% w/w of  $^2\text{H}_2\text{O}$ . Above this threshold a second (narrow) peak develops at 0 ppm, as the broad peak reaches a maximum area. Once again the broad peak is attributed to  $^2\text{H}_2\text{O}$  adsorbed in micropores, and the narrow peak to  $^2\text{H}_2\text{O}$  in macropores or on the external surface.

Interestingly, the narrow peak demonstrates its own hysteresis. On the desorption branch of the isotherm, initial weight loss does not appear to be associated with this second peak at 0 ppm. The peak remains until the relative pressure of deuterium oxide vapour is reduced to below 70%RH. The implication of this observation is that although the deuterium oxide associated with this peak is the last to be adsorbed, it is not the first to be desorbed. Gravimetric analysis can not distinguish between the two environments, so this two-stage hysteresis had not been discovered previously.

### 3.1.6 Conclusions

The experiments described above have been used to demonstrate that NMR techniques can successfully be applied to isotherm adsorption studies on activated carbons. Clearly more information can be obtained from such experiments, and future studies using NMR to investigate alternate adsorbates and carbons of different pore structure would be useful.

### 3.1.3 Substrate evaluation

This section describes a study of a range of carbon substrates. The samples have either 10% or 40% loadings of  $^2\text{H}_2\text{O}$ , and the  $^2\text{H}$  NMR spectra are compared to see any differences. The variations in the probe molecules' environments can then be related to the structure of the carbon substrates.

#### 3.1.3.1 Materials

The activated carbon samples used in this experiment were all prepared by Dr. M. Thomas at Newcastle university. The nutshell samples started with a base un-activated carbon denoted as 0% burn-off. This carbon was activated under controlled conditions of steam and carbon dioxide - this provided samples at 20%, 30% and 51% weight burn-off. The BPL carbon samples came from a coal base and the un-activated carbon was again termed 0% burn-off. Newcastle provided samples with 22% and 30% burn-off from the same activation process used for the nutshell carbons.

Once again the adsorbate used was 99.99%-enriched  $^2\text{H}_2\text{O}$  from Aldrich. The samples that were not evacuated were prepared by addition of a known mass of the adsorbate by pipette. The samples were then allowed to equilibrate for one hour before NMR analysis. The evacuated samples were produced using the sealed ampoule technique outlined in chapter two. The carbon was treated to three freeze-pump-thaw sequences and then a known mass of liquid  $^2\text{H}_2\text{O}$  was adsorbed after vacuum transfer of the adsorbate. The sample was then sealed under vacuum and analysed by NMR.

#### 3.1.3.2 NMR method

The  $^2\text{H}$  NMR spectra were run on the CMX200 spectrometer using the 7.5 mm pencil rotor MAS probe. A single-pulse regime with no decoupling was applied. In this experiment the 10%  $^2\text{H}_2\text{O}$  samples used 296 transients and the 40%  $^2\text{H}_2\text{O}$  samples used 64 transients. The sealed samples have a smaller sample mass, so 2048 transients were used. The recycle delay was 2 s to allow complete relaxation between pulses, so experimentation time was 2-70 minutes.

### 3.1.3.3 Results

Spectra from the nutshell carbon samples with 10% w/w  $^2\text{H}_2\text{O}$  loading are shown in figure 3.1.8. The percentage burn-off for each sample is indicated on the figure. An accurate evaluation of the chemical shifts is given in table 3.1.4.

Burn-off	$^2\text{H}_2\text{O}$ load	$\delta_{2\text{H}}$ Peak 1	$\Delta_{1/2}$ Peak 1	$\delta_{2\text{H}}$ Peak 2
0%	10%	-3.0 ppm	350 Hz	0 ppm
20%	10%	-9.5 ppm	293 Hz	0 ppm
30%	10%	-7.9 ppm	200 Hz	0 ppm
51%	10%	-6.3 ppm	149 Hz	

Table 3.1.4. Chemical shift and peak width data for 10%  $^2\text{H}_2\text{O}$  on the nutshell carbons.

The spectra in figure 3.1.8 show that the 0% burn-off (unactivated) carbon has a small broad peak at -3.0 ppm and a dominating large narrow peak at 0 ppm. The carbon with just 20% weight burn-off shows a large broad peak (293 Hz) centred at -9.5 ppm. There is evidence of a small narrow peak at 0 ppm beginning to develop. The 30% burn-off carbon has a broad peak (200 Hz wide) at -7.9 ppm, and a very small peak at 0 ppm. Finally the 51% burn-off sample shows just the broad peak at -6.3 ppm and only 149 Hz wide. This group of results shows a trend of the chemical shift moving to higher frequency as the burn-off increases, for the activated samples. The observed linewidth decreases as the burn-off increases. There is a similar amount of  $^2\text{H}_2\text{O}$  adsorbed for each sample so the area under each spectrum is constant.

The spectra from the experiment using 40% w/w  $^2\text{H}_2\text{O}$  adsorbed onto the nutshell carbon samples are shown in figure 3.1.9. The NMR data are given in table 3.1.5.



### Durham CMX200H-NMR System

Nutshell with 51% burnoff with 10% D2O

single pulse Bloch Decay

ppfn=1pulse

cdir=Newc1

cfn=nut51010.sp1

cfp=2

sf1=30.72201 MHz

sw=50 KHZ

ad=15 usec

al=1k cplx

aqtm=20.481 msec

dw=20 usec

extm=1.0205 sec

p=157 deg

pd=1 sec

pw=6 usec

rd=15 usec

ac=296 scns

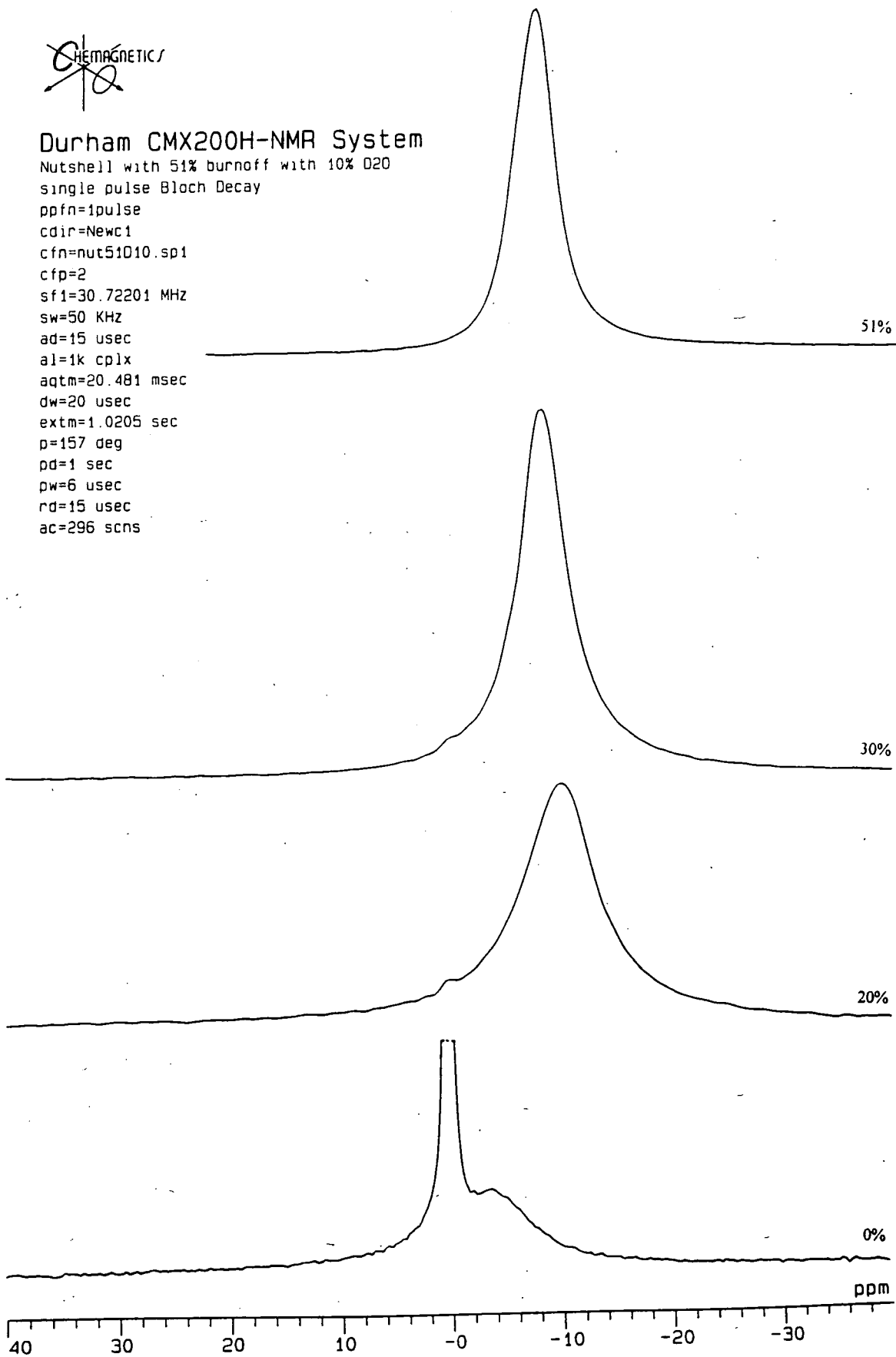


Figure 3.1.8. The nutshell carbon with various indicated burn-offs and a 10% w/w loading of  $D_2O$ .

Burn-off	$^2\text{H}_2\text{O}$ load	$\delta_{2\text{H}}$ Peak 1	$\Delta_{1/2}$ Peak 1	$\delta_{2\text{H}}$ Peak 2
0%	40%	-3.0 ppm	410 Hz	0 ppm
20%	40%	-9.0 ppm	186 Hz	0 ppm
30%	40%	-7.9 ppm	162 Hz	0 ppm
51%	40%	-7.2 ppm	157 Hz	0 ppm

Table 3.1.5. Chemical shift and peak width data for 40%  $^2\text{H}_2\text{O}$  on the nutshell carbons.

These spectra show the carbon samples when the pores are effectively saturated with 40% w/w  $^2\text{H}_2\text{O}$ . The unactivated nutshell carbon exhibits a major narrow peak (7.5 Hz) at 0 ppm, which is similar to that for pure  $^2\text{H}_2\text{O}$  spectrum. The 20% burn-off carbon shows a large narrow peak (34 Hz) at 0 ppm and a small broad peak (186 Hz) at -9.0 ppm. The 30% burn-off carbon has a dominating narrow peak (35 Hz) at 0 ppm and a smaller broad peak (162 Hz) at -7.9 ppm. Finally the 51% burn-off carbon has a small narrow peak at 0 ppm and a major broad peak (157 Hz) at -7.2 ppm. Once again the chemical shift for the adsorbed  $^2\text{H}_2\text{O}$  moves to higher frequency as the burn-off increases from 20% to 51% on the activated carbons. The observed linewidth decreased as the burn-off increases. The unactivated samples seem to have a very large narrow peak and very little adsorbate in the environment contributing to the broad peak.

The coal based BPL carbons were analysed in a similar manner with the un-activated carbon substrate termed 0% burn-off, and samples with 22% and 30% weight burnt off in the activation stage also tested. Figure 3.1.10 shows  $^2\text{H}$  NMR spectra of these samples with a 10% w/w loading of  $^2\text{H}_2\text{O}$ . The NMR data are given in table 3.1.6.



### Durham CMX200H-NMR System

Nutshell with 51% burnoff and 40% D2O

single pulse Bloch Decay

ppfn=1pulse

cdir=Newc1

cfn=Nut51040.sp1

cfp=2

sf1=30.72201 MHz

sw=50 KHz

ad=15 usec

al=8k cplx

aqtm=163.84 msec

dw=20 usec

extm=2.1639 sec

p=157 deg

pd=2 sec

pw=5.5 usec

rd=15 usec

ac=64 scns

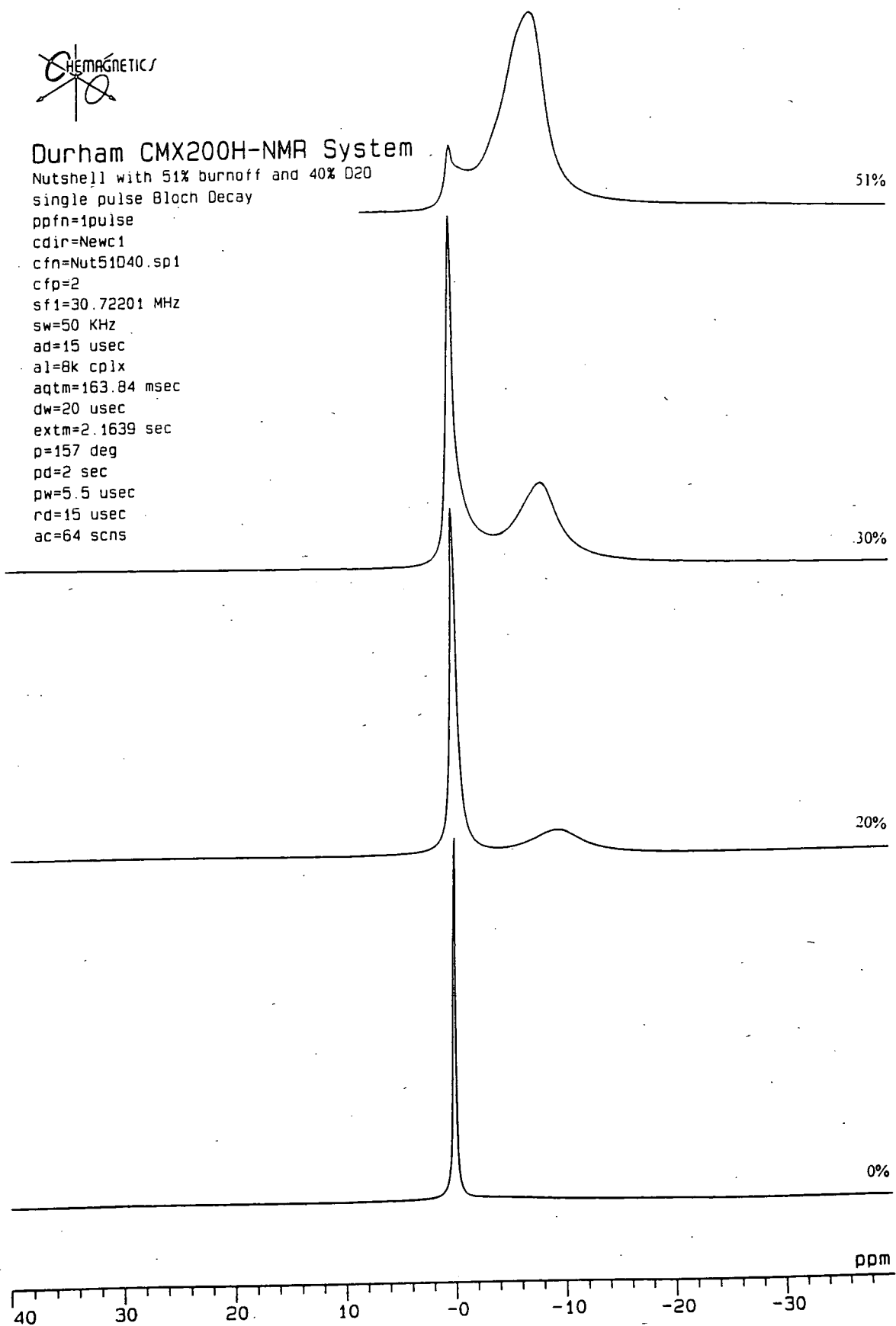


Figure 3.1.9. The nutshell carbon with various indicated burn-offs and a 40% w/w loading of  $^2\text{H}_2\text{O}$ .

Burn-off	$^2\text{H}_2\text{O}$ load	$\delta_{2\text{H}}$ Peak 1	$\Delta_{1/2}$ Peak 1	$\delta_{2\text{H}}$ Peak 2
0%	10%	0 ppm	400 Hz	0 ppm
22%	10%	-8.0 ppm	230 Hz	
30%	10%	-7.7 ppm	227 Hz	

Table 3.1.6. Chemical shift and peak width data for 10%  $^2\text{H}_2\text{O}$  on the BPL carbons.

The 10% w/w  $^2\text{H}_2\text{O}$  NMR spectra show that the unactivated BPL sample has a very small broad peak (400 Hz) at ca. 0 ppm and also a large narrow peak (7.5 Hz) superimposed at 0 ppm. The sample with 22% weight burn-off shows a large broad peak at -8.0 ppm, which has a full width at half-height of 230 Hz. The 30% burn-off BPL carbon shows a broad peak (227 Hz) at -7.7 ppm. The data show that the chemical shift again moves to high frequency as the burn-off increases from 22% to 30%. The observed linewidth does not seem to vary significantly. The un-activated carbon has adsorbed the  $^2\text{H}_2\text{O}$  predominantly in the site associated with the narrow peak at 0 ppm.

Figure 3.1.11 shows  $^2\text{H}$  NMR spectra of these BPL samples saturated with a 40% w/w loading of  $^2\text{H}_2\text{O}$  to fill all the pores. The NMR data are given in table 3.1.7.

Burn-off	$^2\text{H}_2\text{O}$ load	$\delta_{2\text{H}}$ Peak 1	$\Delta_{1/2}$ Peak 1	$\delta_{2\text{H}}$ Peak 2
0%	40%	0 ppm	400 Hz	0 ppm
22%	40%	-7.7 ppm	218 Hz	0 ppm
30%	40%	-7.0 ppm	220 Hz	0 ppm

Table 3.1.7. Chemical shift and peak width data for 40%  $^2\text{H}_2\text{O}$  on the BPL carbons.



### Durham CMX200H-NMR System

BPL with 30% burnoff with 10% D2O

single pulse Bloch Decay

ppfn=1pulse

cdir=Newc2

cfn=8p130010.sp1

cfp=2

sf1=30.72201 MHz

sw=50 KHz

ad=15 usec

al=1k cplx

aqtm=20.481 msec

dw=20 usec

extm=1.0205 sec

p=157 deg

pd=1 sec

pw=6 usec

rd=15 usec

ac=296 scns

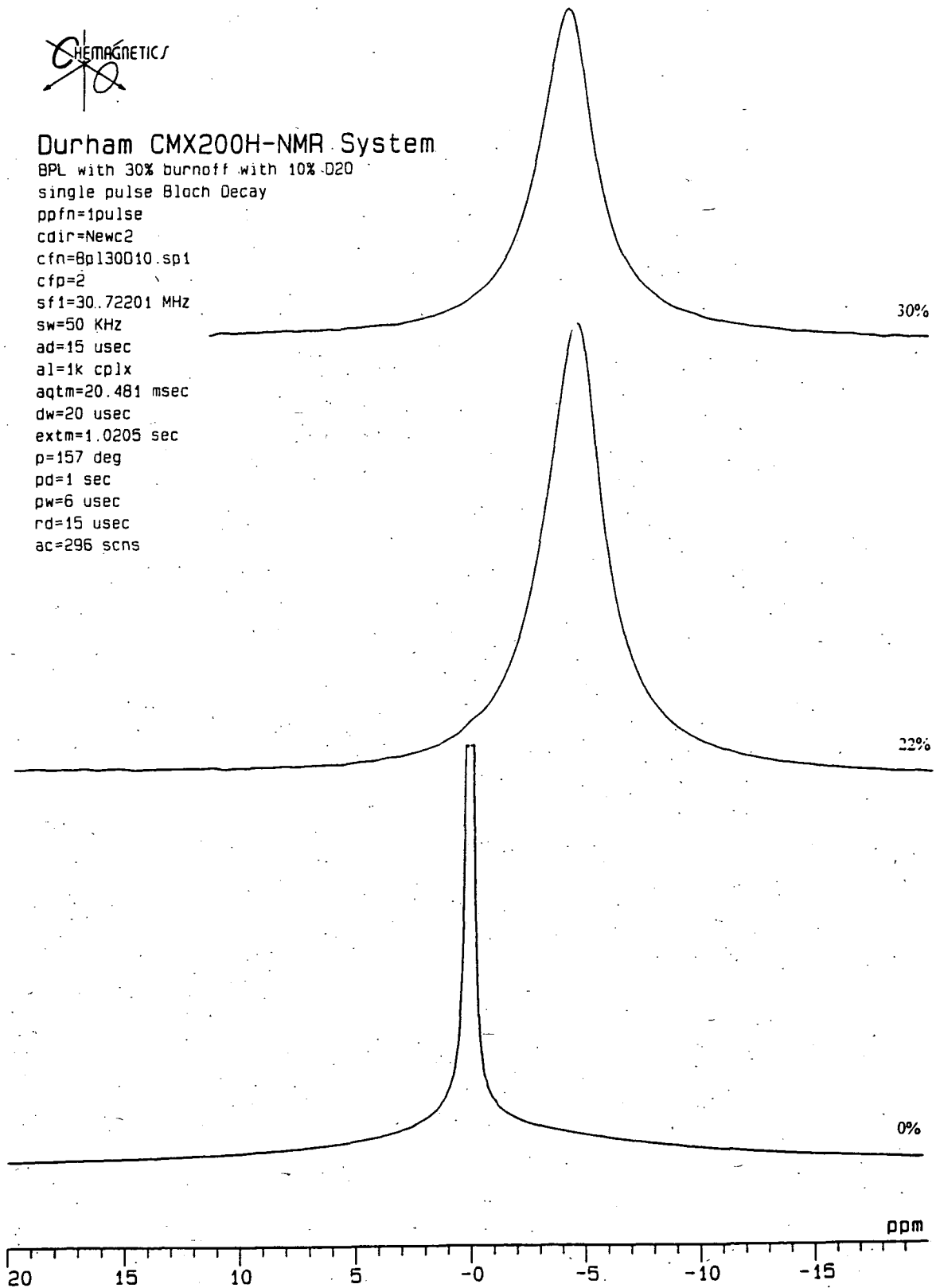


Figure 3.1.10. The coal BPL carbon with various indicated burn-offs and a 10% w/w loading of  $^2\text{H}_2\text{O}$ .



### Durham CMX200H-NMR System

BPL with 30% burnoff and 40% D2O

single pulse Bloch Decay

ppfn=1pulse

cdir=Newc2

cfn=Bp130040.sp1

cfp=2

sf1=30.72201 MHz

sw=50 KHz

ad=15 usec

al=8k cplx

aqtm=163.84 msec

dw=20 usec

extm=2.1639 sec

p=157 deg

pd=2 sec

pw=5.5 usec

rd=15 usec

ac=64 scns

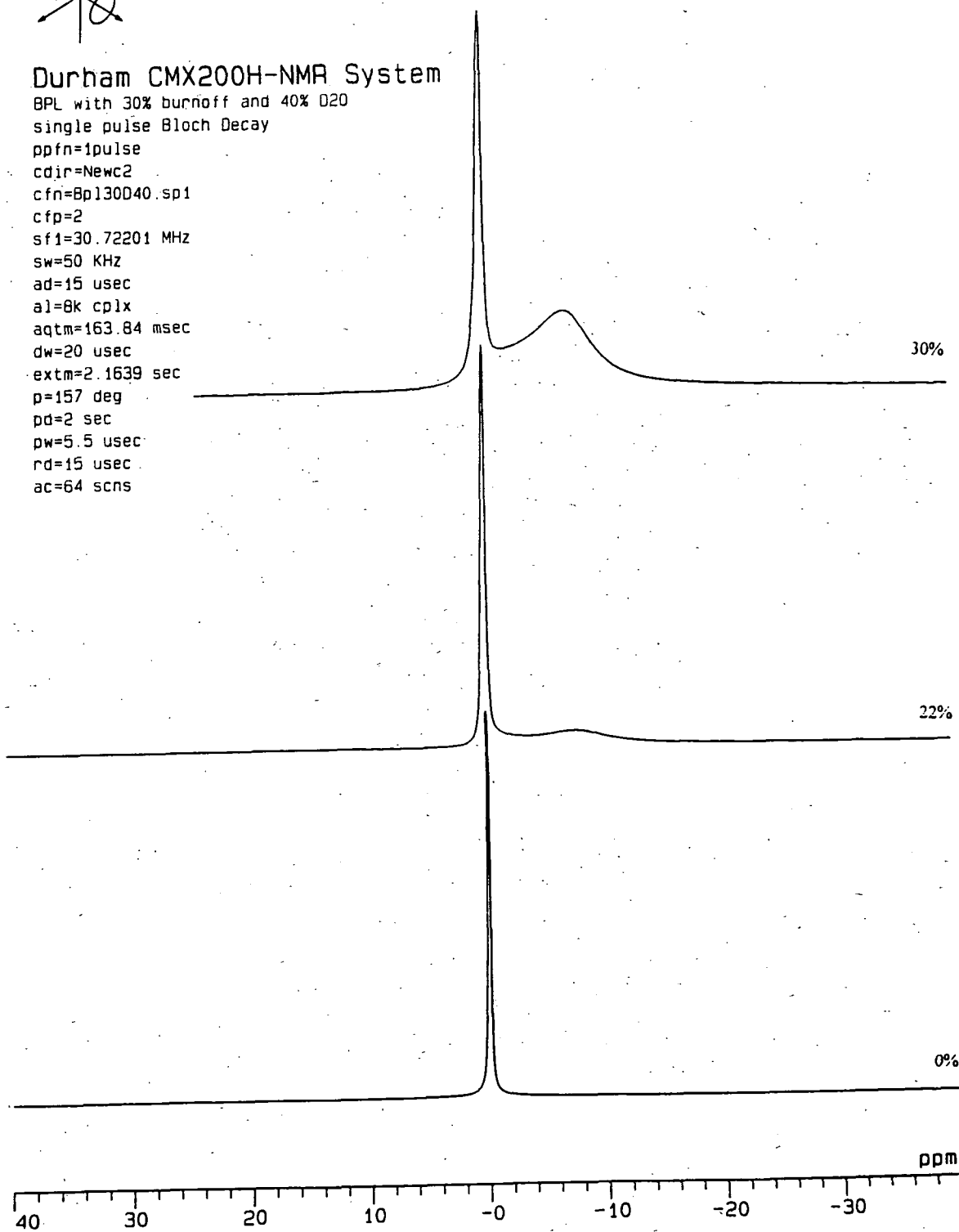


Figure 3.1.11. The coal BPL carbon with various indicated burn-offs and a 40% w/w loading of  $^2\text{H}_2\text{O}$

The 40% w/w  $^2\text{H}_2\text{O}$  NMR spectra show that the unactivated BPL sample has a very small broad peak (400 Hz) at ca. 0 ppm but on this scale it cannot be seen. There is once again a large narrow peak (7.5 Hz) superimposed at 0 ppm. The sample with 22% weight burn-off shows a large broad peak at -7.7 ppm, which has a full width at half-height of 218 Hz. The spectrum has a narrow peak (54 Hz) at 0 ppm that develops as the broad peak is full. The 30% burn-off BPL carbon shows a broad peak (220 Hz) at -7.0 ppm and also exhibits the narrow peak (50 Hz) at 0 ppm for this saturated loading. The data show that the chemical shift again moves to high frequency as the burn-off increases from 22% to 30%. The observed linewidth does not seem to vary significantly. The unactivated carbon has adsorbed the  $^2\text{H}_2\text{O}$  predominantly in the site associated with the narrow peak at 0 ppm.

The un-activated carbon does not seem to adsorb very much  $^2\text{H}_2\text{O}$  in the broad peak. It was postulated that this occurred because the pore entrances were very small before activation and these were blocked by oxygen adsorbed from the atmosphere. To see if this was the case some samples were prepared under vacuum so the pore entrances were free. Figure 3.1.12 shows the unactivated nutshell carbon with evacuation and without. The evacuated sample has 10% and 40% loads of  $^2\text{H}_2\text{O}$ . The sample without evacuation and a 40%  $^2\text{H}_2\text{O}$  loading is also shown for comparison.

The spectra show that the un-activated evacuated samples do have more  $^2\text{H}_2\text{O}$  adsorbed in the environment related to the broad peak than the normally prepared sample. The evacuated samples show several overlapping peaks from -3.0 to -8.0 ppm. There is still some  $^2\text{H}_2\text{O}$  adsorbed in the narrow peak at 0 ppm.

Figure 3.1.13 shows the spectra of 30% burn-off activated carbon with 40%  $^2\text{H}_2\text{O}$  adsorbed. The first sample was prepared with the evacuation process for comparison with the normal preparation technique. The spectra show that there is no qualitative difference between evacuated and non-evacuated activated samples. There is a broad peak at -8.0 ppm and a larger narrow peak at 0 ppm for both samples.



### Durham CMX200H-NMR System

0% burn off Nutshell with 40% O2O added with evacuation.

single pulse Bloch Decay

ppfn=1pulse

cdir=newc4

cfn=tim

cfp=0

sf1=30.72201 MHz

sw=50 KHz

ad=15 usec

al=1k cplx

aqtm=20.481 msec

dw=20 usec

extm=520.54 msec

p=157. deg

pd=500 msec

pw=5.5 usec

rd=35 usec

ac=2048 scns

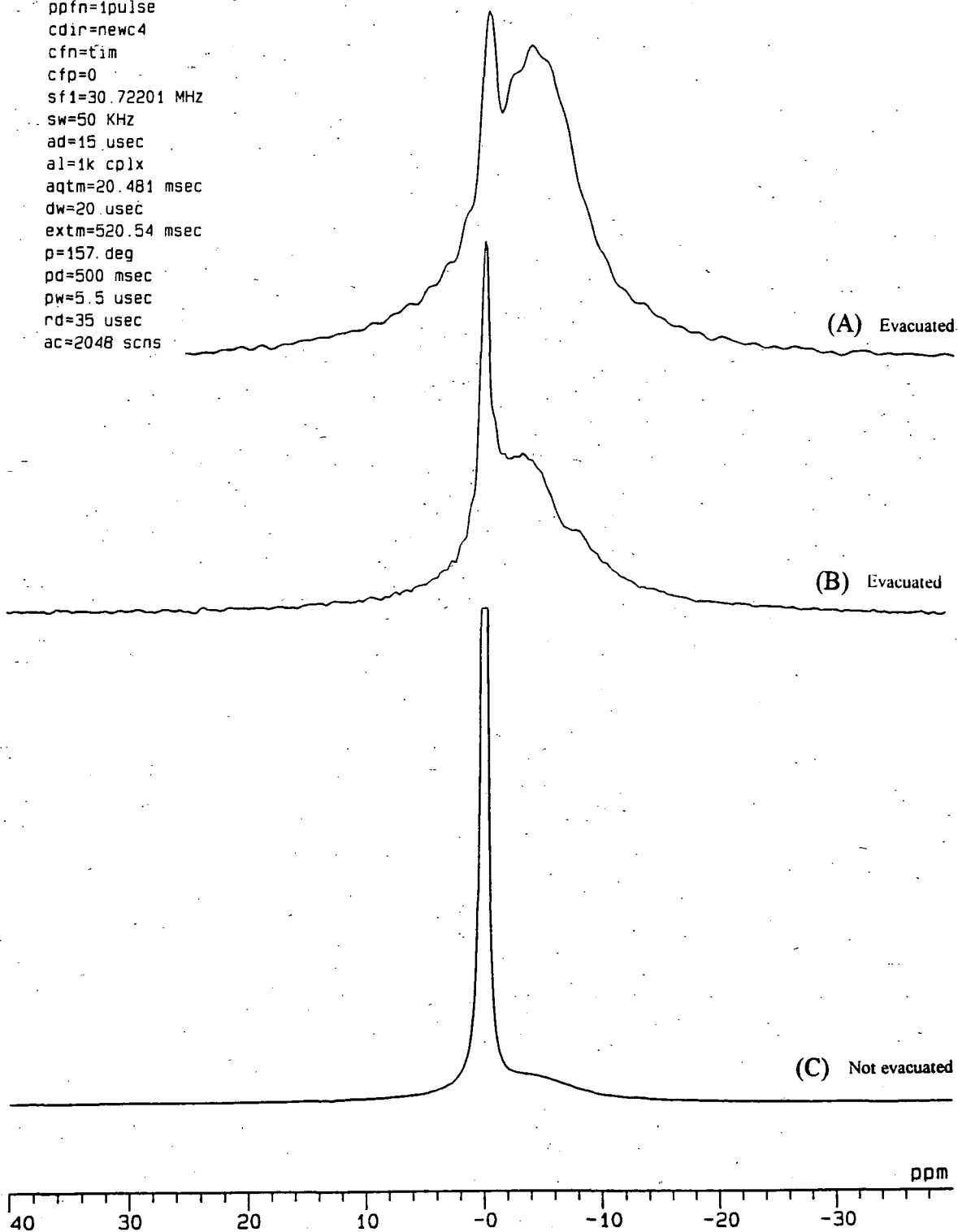


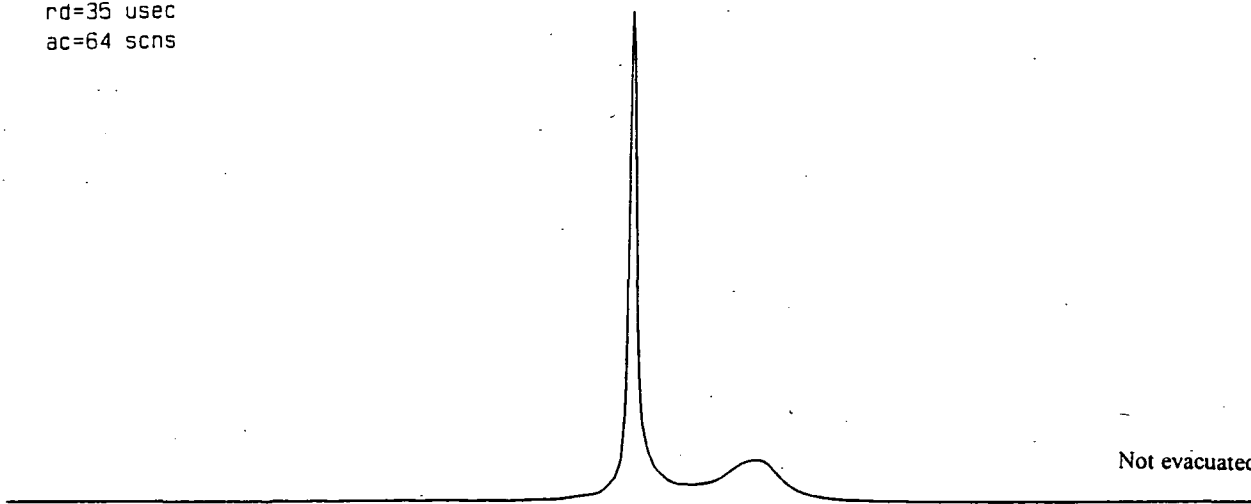
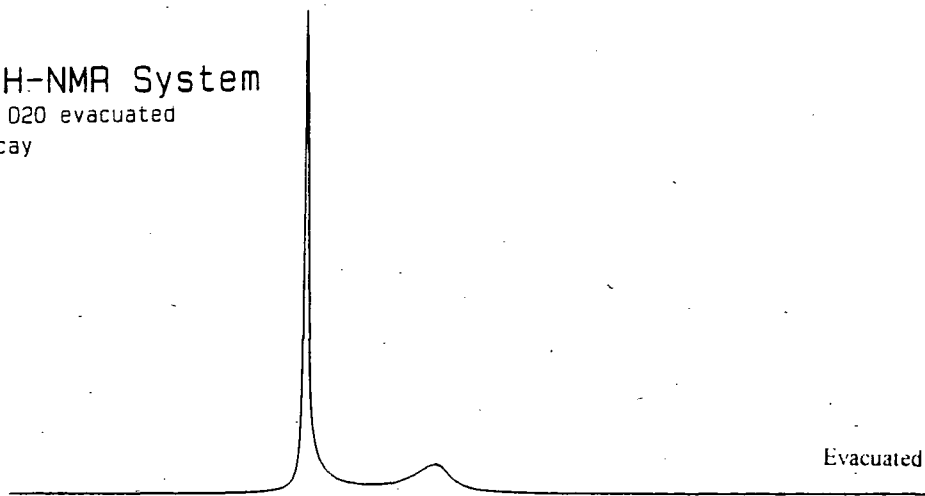
Figure 3.1.12. A comparison of the unactivated nutshell carbon with (A) Evacuation and 40%  $^2\text{H}_2\text{O}$ , (B) Evacuation and 10%  $^2\text{H}_2\text{O}$  and (C) No evacuation and 40%  $^2\text{H}_2\text{O}$ .



### Durham CMX200H-NMR System

30% Nutshell with 40% D2O evacuated  
single pulse Bloch Decay

ppfn=1pulse  
cdir=newc3  
cfn=Nut30d40.sp2  
cfp=2  
sf1=30.72201 MHz  
sw=50 KHz  
ad=15 usec  
al=16k cplx  
aqtm=327.68 msec  
dw=20 usec  
extm=1.3277 sec  
p=157 deg  
pd=1 sec  
pw=5.5 usec  
rd=35 usec  
ac=64 scns



ppm

30

20

10

-0

-10

-20

-30

-40

Figure 3.1.13. The 30% burn-off nutshell carbon with 40% w/w  $^2\text{H}_2\text{O}$  with and without evacuation prior to adsorption.

### 3.1.3.4 Discussion

Carbon chemists suggest that the unactivated samples have a small pore system with very small entrances. At low percentage burn-offs the carbon sample is activated creating small micropores over a small size range. Increasing the burn-off percentage increases the amount of micropores and also the size range that they exhibit. At very high percentage burn-offs the walls of the micropores are burnt out to form large micropores and mesopores within the carbon structure. This is explained in the introduction chapter on activated carbon theory. The object of this section is to correlate the accepted carbon theory with the  $^2\text{H}$  NMR results obtained by directly observing the adsorbed water molecules.

The nutshell and BPL carbon results show that as the burn-off increases above 20% the chemical shift of the broad peak moves to higher frequency. This is consistent with the concept of the pores becoming larger and the consequent reduction in  $^2\text{H}$  shielding for the adsorbed  $^2\text{H}_2\text{O}$  molecules. The pattern is followed for 10% and 40%  $^2\text{H}_2\text{O}$  loads, providing very consistent results. This suggests that for the nutshell carbons the small micropores have a  $\delta_{2\text{H}}$  of -9.5 ppm. The larger micropores give average chemical shifts of between -8.0 and -6.3 ppm depending on the amount of burn-off.

Analysis of the 40% loading of  $^2\text{H}_2\text{O}$  yields further interesting results. A comparison of the relative intensities of the broad and narrow peaks for the activated samples gives information about the total micropore volume available. For nutshell carbons the 20% burn-off creates micropores with a narrow pore-size range. The micropore volume is not as large as for the 30% burn-off carbon, which has more pores and a wider pore-size range. The  $^2\text{H}$  NMR results show a corresponding increased peak area for the peak at -8.0 ppm assigned to  $^2\text{H}_2\text{O}$  adsorbed in the micropores. Each sample has a similar amount of  $^2\text{H}_2\text{O}$  adsorbed so the carbon with 51% burn-off has a further increase in the broad peak with a correspondingly reduced narrow peak. The BPL samples follow the same pattern with the 30% burn-off sample showing a large shielded peak compared to the 22% sample.

The data for the full width at half-height are more difficult to draw conclusions from. The observed linewidths have two competing factors. As the pore size increases the molecules experience less restricted motion, so the natural linewidth will decrease. However

the pore-size range increases as the pores get larger and this means that the broad peak consists of more overlapping lines, especially on the high frequency side, which increases the observed linewidth. The nutshell carbons show a decrease in linewidth, suggesting that the motional narrowing is the dominant effect. The NMR data suggest that the pore distribution is small even for the higher burn-off samples, with larger pores as the activation is increased but reasonably even increase across the sample. Conversely the BPL samples have no decrease in the line-width with the motional narrowing balanced by the extra peaks caused by a larger pore-size distribution.

The evacuation of the unactivated samples had a very pronounced affect on the  $^2\text{H}$  NMR spectra. The evacuation was expected to clear the pore entrances which are very small. This makes the internal pore structure more easily available to the  $^2\text{H}_2\text{O}$  molecules. The NMR data agree with this theory, showing a much larger broad (shielded) peak associated with  $^2\text{H}_2\text{O}$  adsorbed in the pore structure. The unactivated carbons have a poorly defined pore structure, so the shielded peak is very broad, consisting of several overlapping peaks from -3.0 to -8.0 ppm.

The evacuation of the activated sample shows no difference to the normal preparation. This shows that the activation process increases the pore entrance size as well as the uniformity of the pore structure.

### 3.1.3.5 Conclusions

The  $^2\text{H}$  NMR analysis of various well-defined carbons using  $^2\text{H}_2\text{O}$  as the adsorbate probe molecule can provide a lot of information about the carbon structure. The chemical shift can be directly related to the size of the micropores, with shifts to higher frequency as the pores increase in size. Comparison of the peak areas can give information comparing total accessible micropore volume for activated carbon samples. Observed linewidths are more complicated to analyse but some information can be inferred about the adsorbed molecules mobility. Finally unactivated carbons need to be treated very carefully because the accessible pores are reduced when the small pore entrances are blocked. Activated carbons have larger pore entrances so the evacuation of these samples is not necessary.

## References

- 1) I. Yu and M. Lee, *J. Magn. Reson. Ser. A*, 1994, **109**, 41.
- 2) K. Overloop and L. van Gervan, *J Magn. Reson.*, 1992, **100**, 303.
- 3) L. B. Adams, C. R. Hall, R. J. Holmes and R. A. Newton, *Carbon*, 1988, **26**, 451.

### 4.1 Phosphorus NMR

The second section of results concentrates on phosphorus NMR. The adsorption of phosphates onto activated carbons has been an area of considerable interest. The phosphates are used as nerve agent simulants to investigate how nerve agents would interact with the activated carbon. The simulants are similar in shape, size and content, but contain no P-F bond.

There are several advantages in using  $^{31}\text{P}$  NMR to study the adsorption of these molecules. Solid-state NMR of phosphorus is straightforward because the  $^{31}\text{P}$  nucleus is 100% abundant and there is a large shift range, so the signals do not overlap. This makes the peak assignment quite easy. There are no phosphorus nuclei in the substrate, so there are no background signals to make it difficult to distinguish peaks from the adsorbate probe molecules. The 100% abundance of the  $^{31}\text{P}$  nuclei means that the experiments are very fast to obtain even at low loadings (typically 2 min). In the adsorbed state the molecular motion is fast, and when coupled with MAS the SA line-broadening is removed so the lines are quite narrow.

The results from the  $^{31}\text{P}$  NMR fall into an experimental framework with three variables. The first part is a systematic phosphate loading experiment using 10%-60% w/w loads with 10% w/w increments. The second variable used was the four differing types of phosphate, trimethyl phosphate (TMP), triethyl phosphate (TEP), dimethyl methyl phosphonate (DMMP) and cyclohexyl methyl methyl phosphonate (PP). The third changeable part of the experiment was the type of activated carbon substrate, with three different carbons analysed. The three carbon types used were SC2, ASZM and the BPL.

#### 4.1.1. Method

The loading experiments were all carried out on the dry carbon which contained less than 2% w/w of water. Samples were produced with loadings from 10%-60% w/w of each phosphate on all three carbon substrates. The samples were

prepared by adding a known mass of liquid phosphate by pipette to the carbon sample. The samples were then allowed to equilibrate for one hour in a sealed sample bottle. The sample was then transferred to the MAS rotor and the mass of the sample and rotor noted. The sample mass was then calculated using a difference method. The empty rotor weighed 5.107 g.

These samples were then analysed by phosphorus NMR on the CMX200 using the 7.5 mm pencil rotor MAS probe, which holds approximately 500 mg of sample. High-resolution spectra were obtained using spinning speeds of 3.0 kHz and a single-pulse regime with no proton decoupling. In this experiment a recycle delay of 1 s was used and 128 acquisitions taken for each sample. This means the acquisition time for each spectrum was 2 minutes. The spectra were recorded under identical conditions in absolute intensity mode to allow direct comparison. The spectra were all run over a 48 hour period so the experimental set-up was consistent. The peaks were integrated using the integration package provided with CMXW. The results were then normalised taking into account the sample mass in the rotor. The final data are presented in the following section. The results of the integration, chemical shift and observed linewidth are shown for each sample.

#### 4.1.2. Results

The normalised integration, chemical shift and linewidth data for the loading of the four phosphates onto the SC2 carbon are given in table 4.1. The corresponding data for the ASZM and BPL carbon substrates are given in table 4.2. and 4.3. respectively. The vast amount of results and the complex interactions between the experimental variables mean that the discussion has to refer back to these tables during the whole chapter. The first part concentrates on the effect of the adsorption onto the carbon for the four adsorbates. The second section looks at the loading characteristics for a standard system. This is followed by the one major anomalous result in the loading experiments. The final part looks at the carbon substrates and how each one interacts with the different phosphates.

## SC2 carbon

Phosphate	Load	Integral Broad	Integral narrow	$\delta$ Broad	$\Delta_{1/2}$ Broad (Hz)
TEP	10	10		-7.9	272
	20	20		-8.3	316
	30	28	2	-8.4	300
	40	34	6	-8.4	320
	50	34	16	-8.4	320
	60	34	26	-8.4	330
TMP	10	10		-5.0	220
	20	20		-5.3	250
	30	30		-5.2	263
	40	38	2	-5.2	245
	50	48	2	-5.2	245
	60	50	10	-5.1	250
DMMP	10	10		26.3	
	20	20		26.0	
	30	30		26.0	
	40	40		26.3	
	50	50		26.3	
	60	50	10	26.3	
P.P	10	7	3	24.4	
	20	15	5	24.5	
	30	24	6	24.4	
	40	26	14	24.3	
	50	32	18	24.3	
	60	34	26	24.3	

Table 4.1. Table of the  $^{31}\text{P}$  NMR data for the phosphate loading onto the SC2 carbon. The PP areas are time dependent so average values are given.

## ASZM carbon

Phosphate	Load	Integral Broad	Integral Narrow	$\delta$ Broad	$\Delta_{1/2}$ Broad (Hz)
TEP	10	10		-6.9	330
	20	20		-6.2	310
	30	28	2	-6.0	350
	40	30	10	-6.0	350
	50	32	18	-6.0	350
	60	32	28	-6.0	350
TMP	10	10		-3.6	260
	20	20		-3.6	240
	30	29	1	-3.6	283
	40	38	5	-3.5	290
	50	38	12	-3.4	275
	60	38	22	-3.4	275
DMMP	10	10		28.5	
	20	20		26.7	
	30	30		26.3	
	40	34	6	27.3	
	50	35	15	27.3	
	60	35	25	27.3	
P.P	10	8	2	25.8	
	20	12	8	24.7	
	30	16	14	25.8	
	40	18	22	26.1	
	50	18	32	26.4	
	60	18	42	26.6	

Table 4.2. Table of the  $^{31}\text{P}$  NMR data for the phosphate loading onto the ASZM carbon. The PP areas are time dependent so average values are given.

## BPL carbon

Phosphate	Load	Int Broad	Int Narrow	$\delta$ Broad	$\Delta 1/2$ Broad (Hz)
TEP	10	10		-7.3	275
	20	20		-7.1	280
	30	30		-7.0	300
	40	40		-7.0	300
	50	49	1	-6.9	320
	60	50	10	-6.9	360
TMP	10	10		-4.3	260
	20	20		-4.1	275
	30	30		-4.1	308
	40	40		-4.0	313
	50	50		-4.0	356
	60	54	6	-4.0	360
DMMP	10	10		26.9	
	20	20		26.6	
	30	30		26.6	
	40	40		26.9	
	50	46	4	27.1	
	60	46	14	27.1	
P.P	10	10		25.5	
	20	20		24.5	
	30	30		25.1	
	40	33	7	25.3	
	50	33	17	25.3	
	60	33	27	25.7	

Table 4.3. Table of the  $^{31}\text{P}$  NMR data for the phosphate loading onto the BPL carbon. The PP areas are time dependent so average values are given.

#### 4.1.2.1. Phosphate adsorption

The initial section of the results concentrates on the phosphates and how they are affected as they are adsorbed onto the activated carbons. Figure 4.1 shows the NMR spectra of four liquid adsorbates prior to adsorption. The spectra are shown on the same scale to enable easy comparison. All the precise chemical shift data are listed in table 4.5. The NMR spectra consist of narrow lines with distinct chemical shifts. The spectrum for the TMP has a small impurity but this does not affect the adsorption results as it is a very small percentage.

Figure 4.2 shows the same adsorbates but they have a 10% w/w loading adsorbed onto the SC2 carbon. The spectra are once again easy to compare as they are all on the same scale. Each peak shows a distinct broadening as they are adsorbed onto the activated carbon. The chemical shift also moves a long way to low frequency (7-8 ppm) in each case. The PP adsorbate is interesting because even at a 10% loading there are two peaks in the  $^{31}\text{P}$  NMR spectrum. The broad peak is shifted to low frequency but the narrower one appears close to the chemical shift for pure liquid PP.

Figure 4.3 shows the 60% w/w loads of the same phosphates on the three carbon samples tested. The  $^{31}\text{P}$  NMR spectra again show a broad peak shifted to low frequency by 7-8 ppm for each phosphate. The 60% w/w load also show a distinct extra narrow peak close to the pure liquid shift of each phosphate. The PP adsorbate shows two narrow peaks as well as a broad one. This is discussed later in the anomalous loading result section.

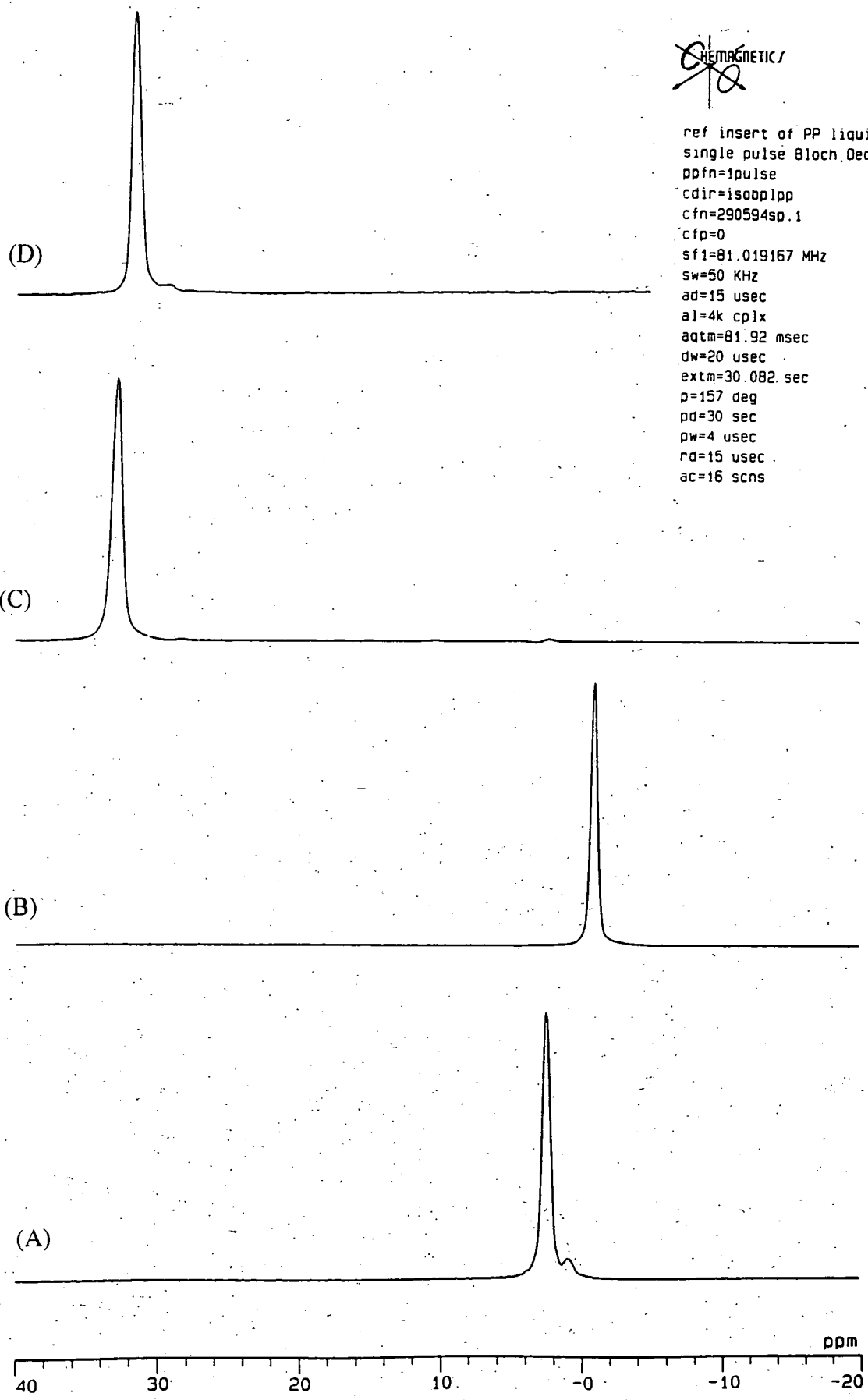


Figure 4.1.  $^{31}\text{P}$  NMR spectra of the pure liquid adsorbates used in the loading experiment. (A) TMP, (B) TEP, (C) DMMP and (D) PP.



10% PP on SC2 at 3.5 khz  
single pulse Bloch Decay  
ppfn=1pulse  
cdir=isosc2pp  
cfn=300594sp.1  
cfp=0  
sf1=81.019167 MHz  
sw=50 KHz  
ad=15 usec  
al=512 cplx  
aqt=10.241 msec  
dw=20 usec  
extm=1.0103 sec  
p=157 deg  
pd=1 sec  
pw=4 usec  
rd=15 usec  
ac=128 scns

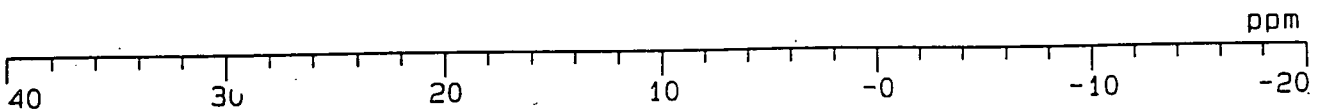
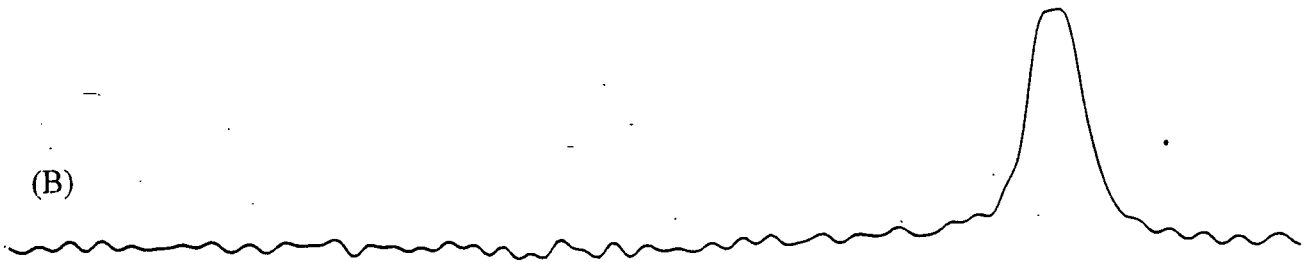
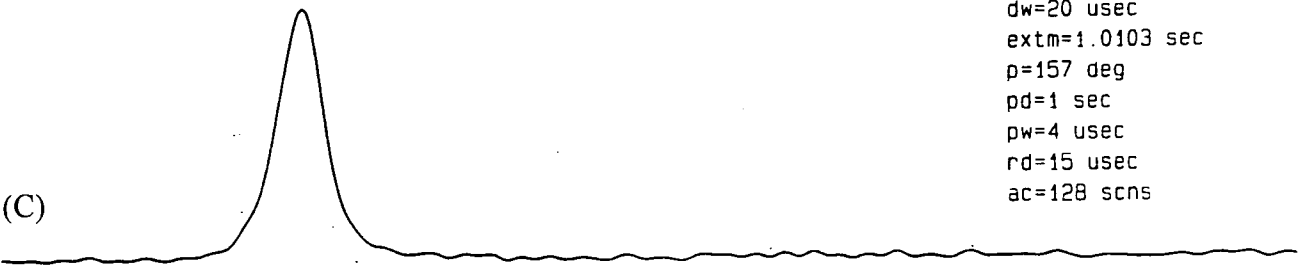


Figure 4.2.  $^{31}\text{P}$  NMR spectra of the SC2 carbon with a 10% w/w load of (A) TMP, (B) TEP, (C) DMMP and (D) PP.



60% PP on SC2  
single pulse Bloch Decay  
ppfn=1pulse  
cdir=isosc2pp  
cfn=300594sp.6  
cfp=0  
sf1=81.019167 MHz  
sw=50 KHz  
ad=15 usec  
al=512 cplx  
aqt=10.241 msec  
dw=20 usec  
extm=5.0103 sec  
p=157 deg  
pd=5 sec  
pw=4 usec  
rd=15 usec  
ac=128 scns

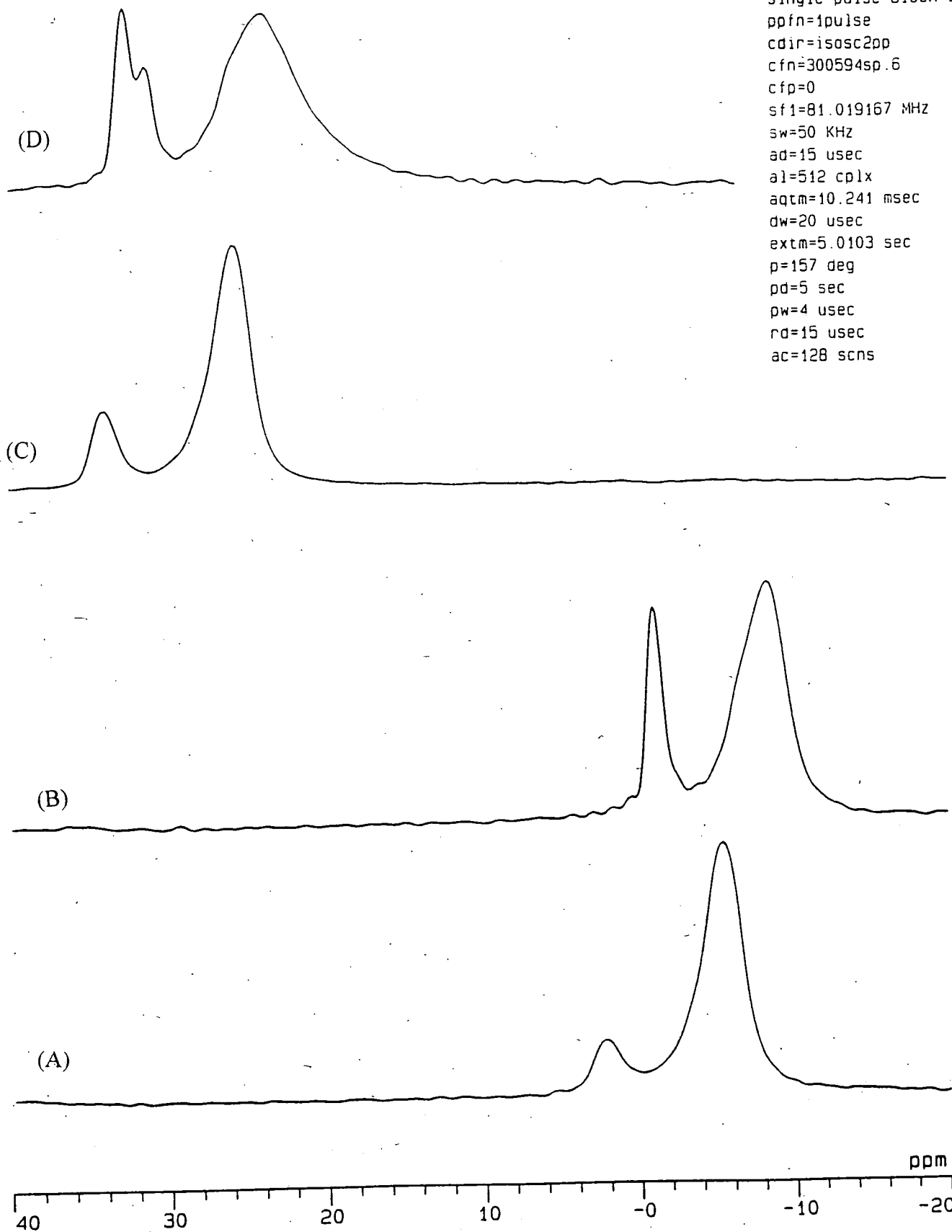


Figure 4.3.  $^{31}\text{P}$  NMR spectra of the SC2 carbon with a 60% w/w load of (A) TMP, (B) TEP, (C) DMMP and (D) PP.

#### 4.1.2.2. Systematic loading

The second part of the results looks at the typical loading profile of a phosphate onto a carbon substrate to see if there is a similar pattern to the  $^2\text{H}_2\text{O}$  loading. Figure 4.4 shows the  $^{31}\text{P}$  NMR spectra of 10-30% loading of TMP on the SC2 carbon. Figure 4.5 shows the  $^{31}\text{P}$  NMR spectra of 40-60% loading of the TMP onto SC2 carbon. The spectra are all on the same scale so the changes associated with the incremental increase in load can be observed.

The results show that initial adsorption gives rise to the broad peak shifted to low frequency. The increase in load indicates this broad peak increases in area until a maximum size is reached. At this point a second, narrower peak, which is close to the pure adsorbate shift, develops. The narrow peak is a second adsorbate environment, which then grows as the adsorbate load increases. This is a typical loading profile, but the total maximum area of the broad peak and the advent of the second peak vary depending on the phosphate and the carbon type.

Figure 4.6 shows the broad peak integral as a function of phosphate loading for the four phosphates on the SC2 carbon.

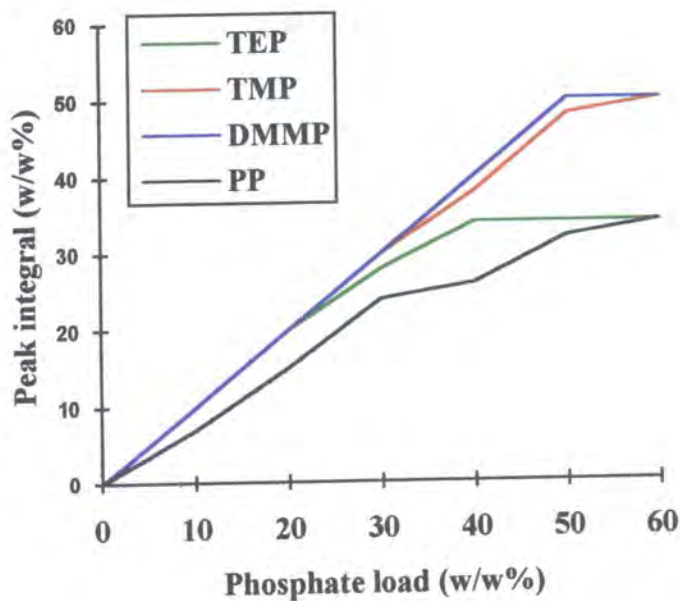


Figure 4.6. Graph of the broad peak integral against load for the SC2 carbon.



### Durham CMX200H-NMR System

30% TMP on SC2 at 3.6 kHz  
single pulse Bloch Decay

ppfn=1pulse  
cdir=isobplpp  
cfn=300594sp.3  
cfn=0  
sf1=81.019167 MHz  
sw=50 KHz  
ad=15 usec  
al=512 cplx  
aqtm=10.241 msec  
dw=20 usec  
extm=1.0103 sec  
p=157 deg  
pd=1 sec  
pw=4 usec  
rd=15 usec  
ac=128 scns

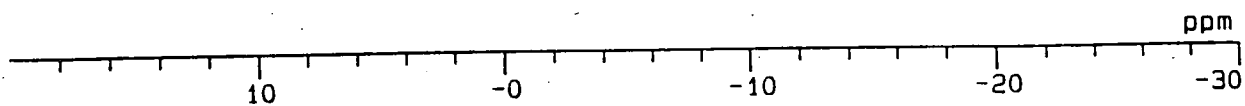
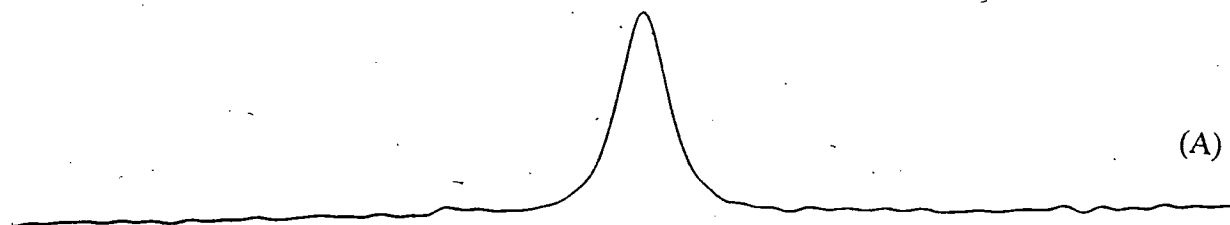
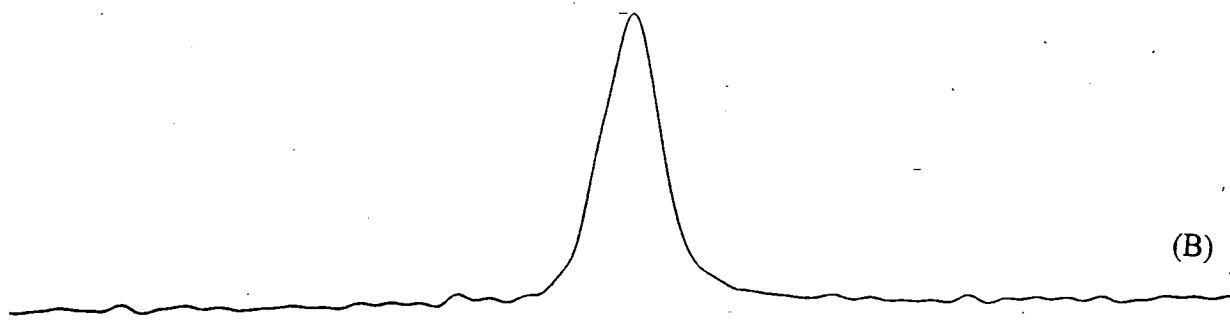
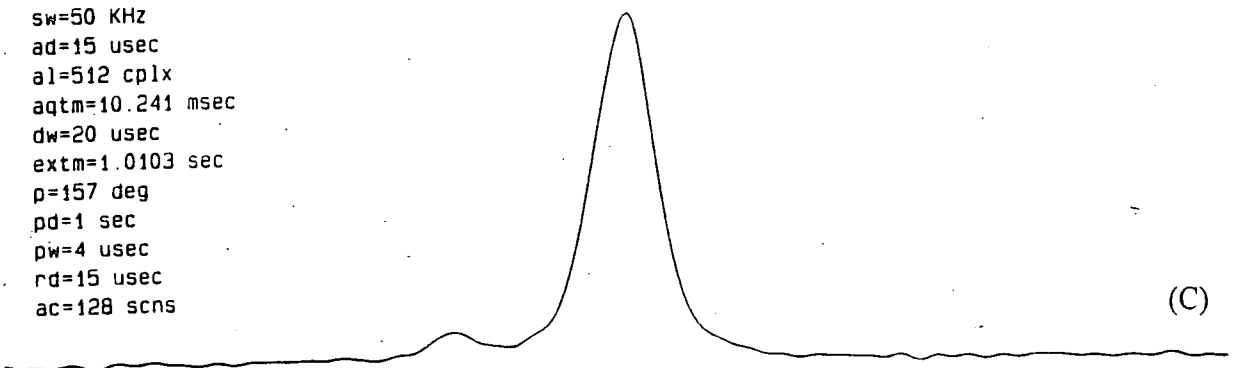


Figure 4.4.  $^{31}\text{P}$  NMR spectra of the SC2 carbon loading experiment with TMP, spectrum (A) 10% w/w (B) 20% w/w and (C) 30% w/w load.



### Durham CMX200H-NMR System

60% tmp on sc2 at 3.5 khz

single pulse Bloch Decay

ppfn=1pulse

cdir=isobolpp

cfn=300594sp.6

cfp=0

sf1=81.019167 MHz

sw=50 KHZ

ad=15 usec

al=512 cplx

aqtm=10.241 msec

dw=20 usec

extm=1.0103 sec

p=157 deg

pd=1 sec

pw=4 usec

rd=15 usec

ac=128 scns

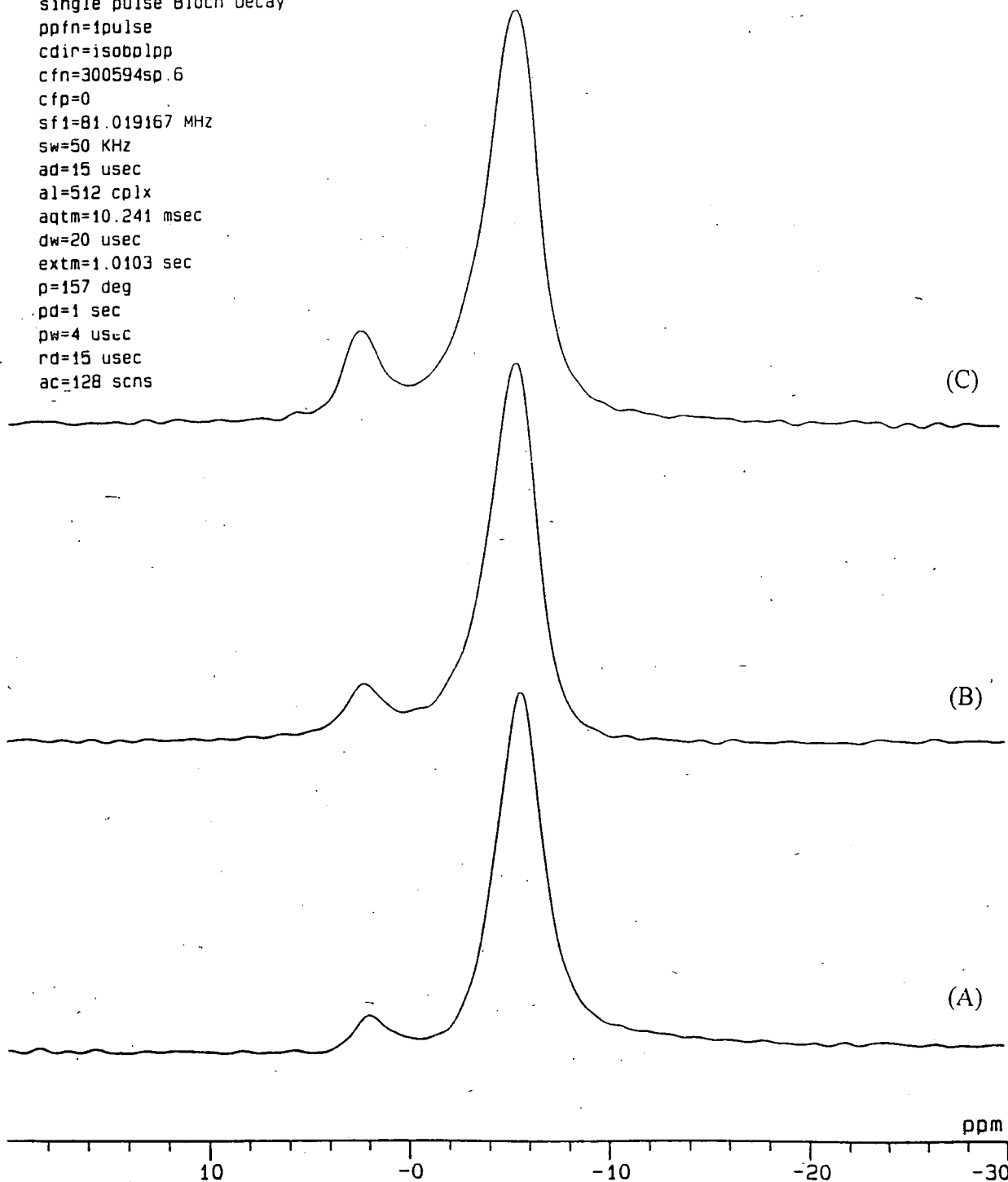


Figure 4.5.  $^{31}\text{P}$  NMR spectra of the SC2 carbon loading experiment with TMP. spectrum (A) 40% w/w (B) 50% w/w and (C) 60% w/w load.

The graph of the broad peak integral against load for the four phosphates is shown in figure 4.7 for the ASZM carbon and figure 4.8 for the BPL carbon.

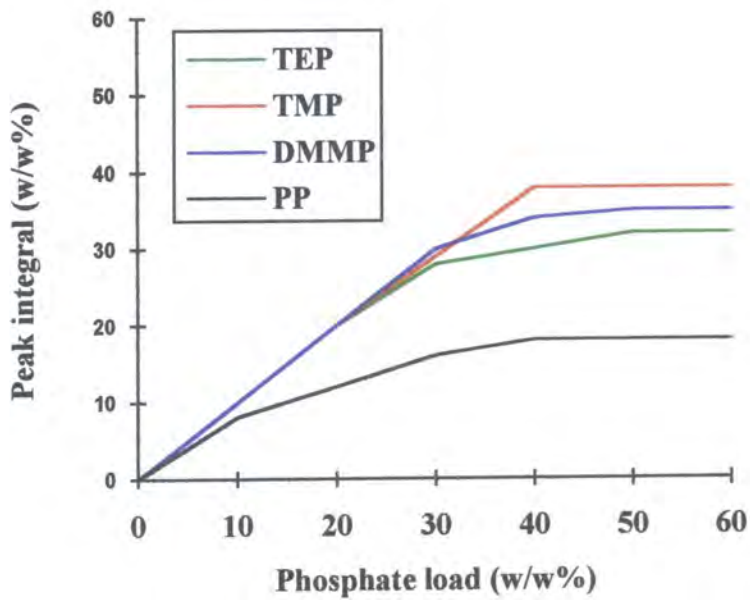


Figure 4.7. Graph of the broad peak integral against load for the ASZM carbon.

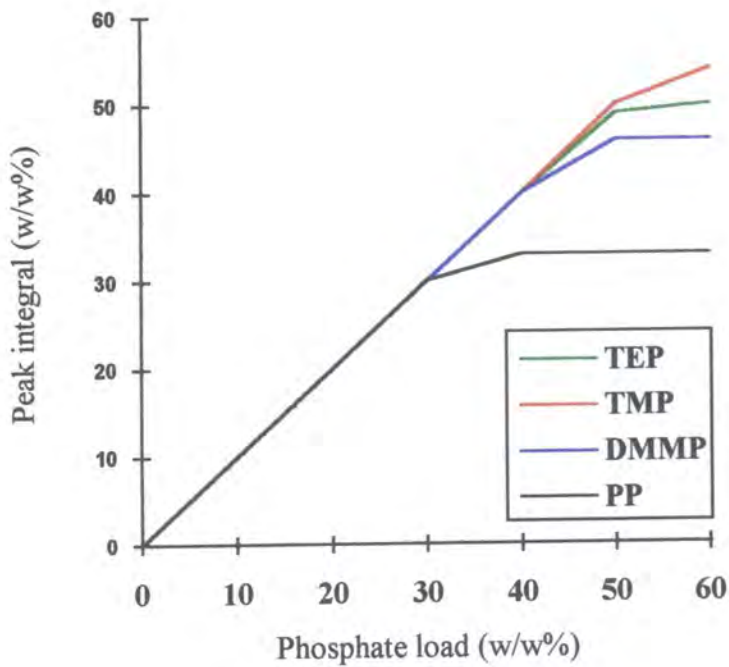


Figure 4.8. Graph of the broad peak integral against load for the BPL carbon.

The results taken from the broad peak integration data show that the TMP and TEP loading characteristics are similar for each type of carbon, with the broad peak developing, then reaching a maximum area at loads greater than 40% w/w. The TMP molecule seems to consistently give a larger maximum peak area than the larger TEP molecule. The DMMP loading for the ASZM and BPL carbon follows a similar pattern, but the SC2 carbon seems to prefer the DMMP adsorbate, so the broad peak has a large maximum area. The PP loading is different for the SC2 carbon, with a strange shape that will be discussed in the next section. The ASZM and BPL carbon have a similar pattern with the broad peak only able to have a small area, showing saturation at low loads. The broad peak does get larger even when the narrow peak appears for the PP adsorbate.

Table 4.4 shows the maximum integration area for the broad peak for each phosphate adsorbed on the three carbon types. The data are all derived from the NMR experiment.

	TEP (w/w%)	TMP (w/w%)	DMMP (w/w%)	PP (w/w%)
SC2	34	50	50	34
ASZM	32	38	35	18
BPL	50	54	46	33

Table 4.4. The maximum adsorption for the broad peak calculated from the integration area.

The next section of results looks at the area of the narrow peak as it develops for each adsorbate on the carbons. The graphs show how the narrow peak develops with load, it is possible to use linear regression to determine the maximum broad peak area from these results. When the narrow peak adsorbs all the additional phosphate in the loading experiment, then the plot of narrow peak area against phosphate load becomes a straight line where  $x = y$ . The line can be extrapolated back to the point where the narrow peak area is zero. The loading value at this point is the maximum

load that the broad peak can adsorb. The two narrow lines for the PP adsorbed onto SC2 are added together in the area calculation.

Figure 4.9 shows the corresponding advent of the narrow peak as a function of load for the four phosphates on the SC2 carbon. Figure 4.10 shows the corresponding advent of the narrow peak as a function of load for the four phosphates on the ASZM carbon.

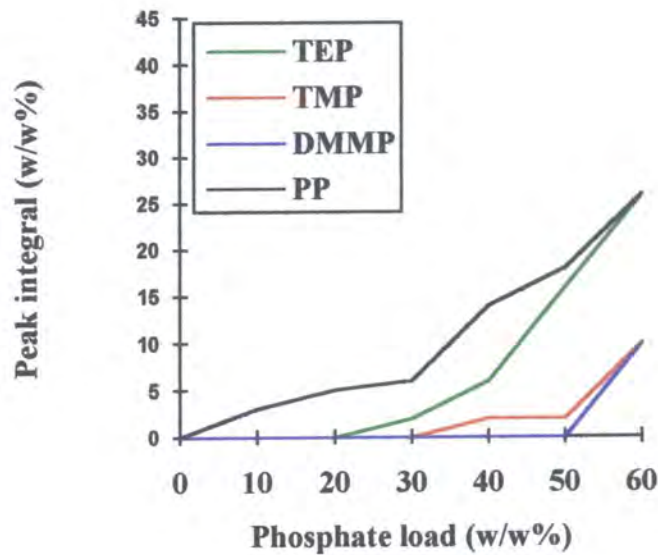


Figure 4.9. Graph of the narrow peak integration versus load for the SC2 carbon.

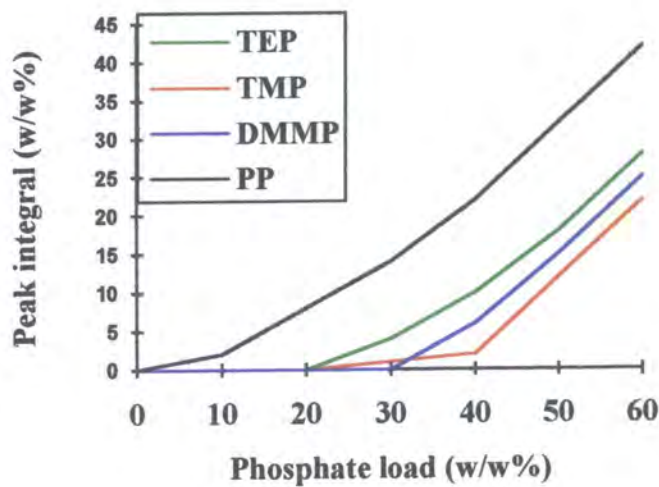


Figure 4.10. Graph of the narrow peak integration versus load for the ASZM carbon.

Figure 4.11 shows the area of the narrow peak as a function of the phosphate load for the BPL carbon substrate.

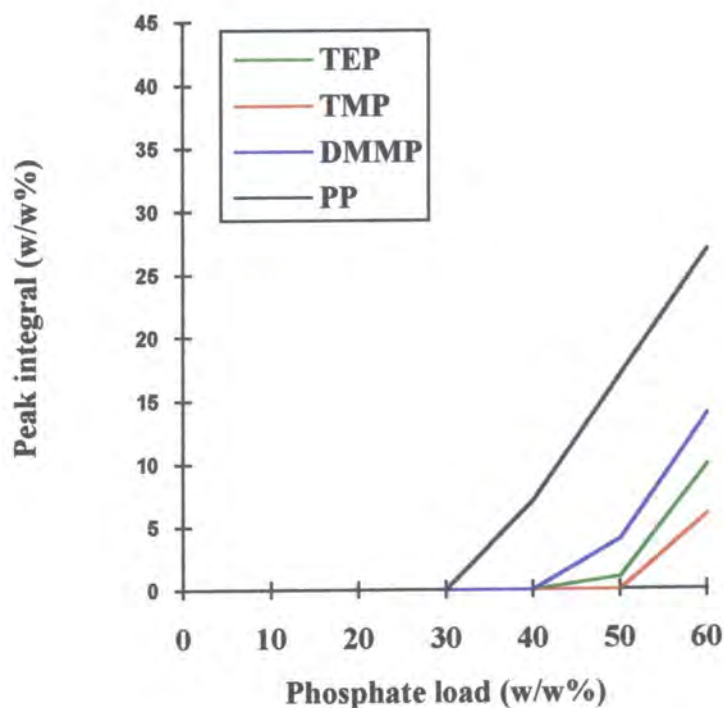


Figure 4.11. Graph of the narrow peak integration versus load for the BPL carbon.

The results for the narrow peak show that the narrow peak develops as the broad peak reaches the limiting area. There is no clear-cut off point, however, especially for the SC2 carbon where the narrow peak seems to occur before the environment associated with the broad one totally fills up.

#### 4.1.2.3. Anomalous loading pattern

The loading pattern observed was noticeably different for the PP loaded onto SC2 carbon granules. Figure 4.12 shows the  $^{31}\text{P}$  NMR spectra of 10-30% loading of PP on the SC2 carbon. Figure 4.13 shows the  $^{31}\text{P}$  NMR spectra of 40-60% loading of the PP onto SC2 carbon. The spectra are all on the same scale so the changes associated with the incremental increase in load can be observed. The broad peak shifted to low frequency is observed initially, as expected, with a low loading of PP.



### Durham CMX200H-NMR System

30% PP on SC2 at 3.5 khz

single pulse Bloch Decay

ppfn=1pulse

cdir=isosc2pp

cfn=300594sp.3

cfp=0

sf1=81.019167 MHz

sw=50 KHz

ad=15 usec

al=512 cplx

aqtm=10.241 msec

dw=20 usec

extm=1.0103 sec

p=157 deg

pd=1 sec

pw=4 usec

rd=15 usec

ac=128 scns

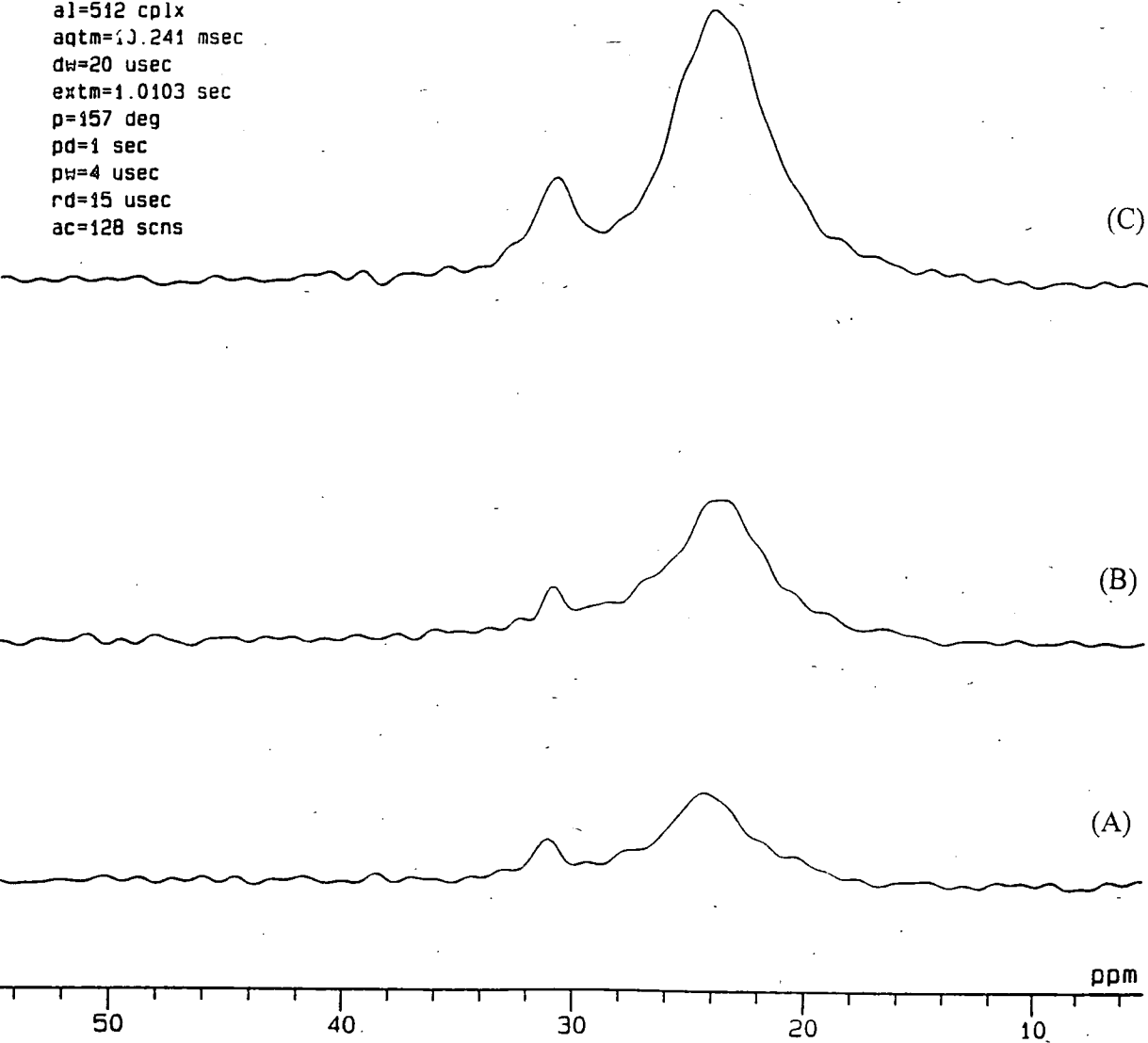


Figure 4.12.  $^{31}\text{P}$  NMR spectra of the SC2 carbon loading experiment with PP, spectrum (A) 10% w/w (B) 20% w/w and (C) 30% w/w load.



### Durham CMX200H-NMR System

60% PP on SC2 at 3.5 khgz

single pulse Bloch Decay

ppfn=1pulse

cdir=isusc2pp

cfn=300594sp.6

cfp=0

sf1=81.019167 MHz

sw=50 KHZ

ad=15 usec

al=512 cpix

aqtm=10.241 msec

dw=20 usec

extm=5.0103 sec

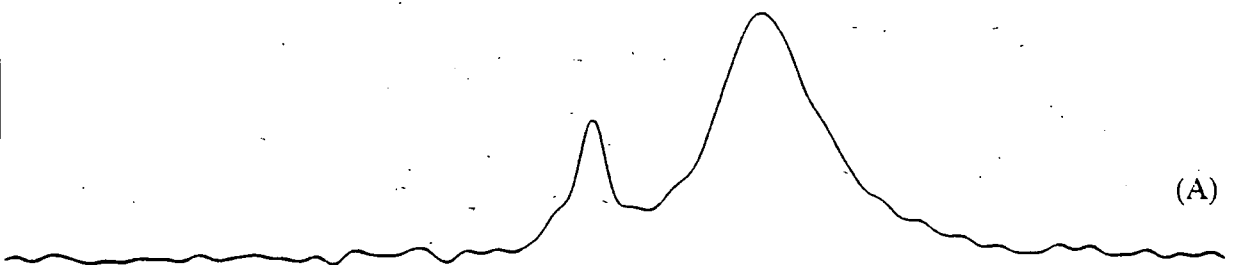
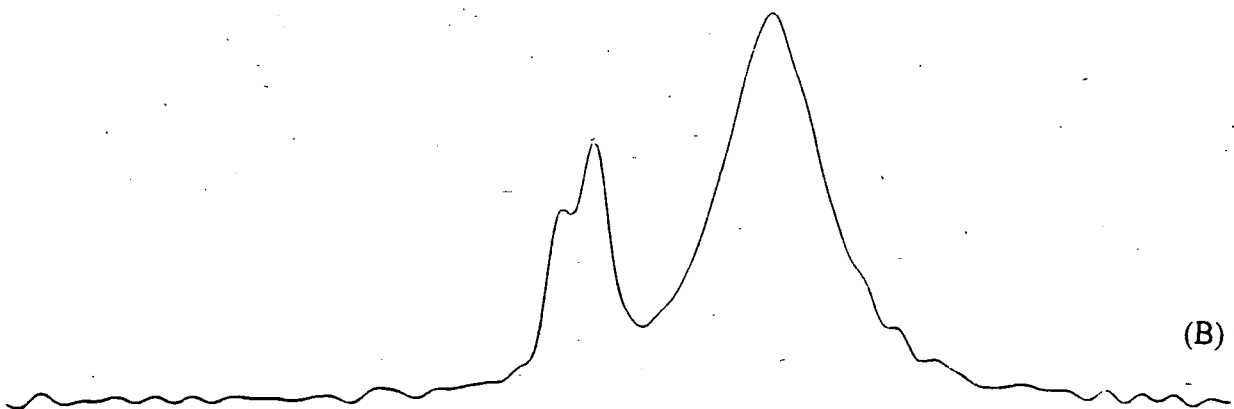
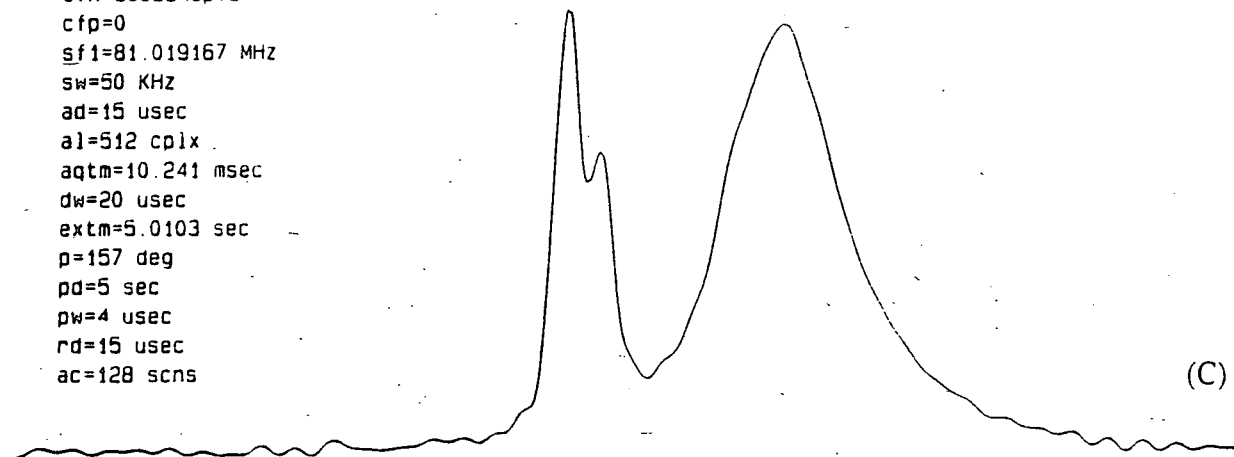
p=157 deg

pd=5 sec

pw=4 usec

rd=15 usec

ac=128 scns



ppm

Figure 4.13.  $^{31}\text{P}$  NMR spectra of the SC2 carbon loading experiment with P.P. spectrum (A) 40% w/w (B) 50% w/w and (C) 60% w/w load.

When the load increases then a narrow peak develops at 31.7 ppm. This peak then appears to fill up, and at 50% and 60% w/w loads of PP a second narrow peak is observed. The second narrow peak, at 32.8 ppm, then builds up as the load increases. The increase in load also adds some extra width to the high-frequency side of the broad peak.

The chemical shift results for the narrow peak are given in table 4.5. The chemical shift of the pure liquid adsorbate prior to adsorption is given for comparison with the adsorbed phosphates.

Chemical shift of the narrow peak (ppm)				
	TMP	TEP	DMMP	PP
Liquid	2.69	-0.70	32.9	31.7
SC2	2.45	-0.90	34.15	32.8, 31.5
ASZM	2.50	-0.75	33.2	31.90
BPL	2.50	-0.75	34.2	32.4

Table 4.5. Table of the chemical shift of the narrow line for the four phosphates.

The results show that the carbons have shifted the TEP and TMP lines slightly to lower frequency compared to the pure liquid. The DMMP and PP phosphates are shifted slightly to higher frequency than the pure liquid except for the SC2 carbon. The first narrow line for the SC2 carbon with PP adsorbed moves marginally to lower frequency and the second line is at higher frequency than the pure liquid. All the lines are slightly broader (130%) for the adsorbed spectra than the pure liquid.

#### 4.1.2.4. Analysis of the carbon types

This section analysed the NMR data for chemical shift and line width for each carbon substrate to see if the adsorption mechanism for the phosphates could be elucidated. Figure 4.14 shows the linewidth and chemical shift for increments of TEP and TMP loaded onto SC2 carbon.

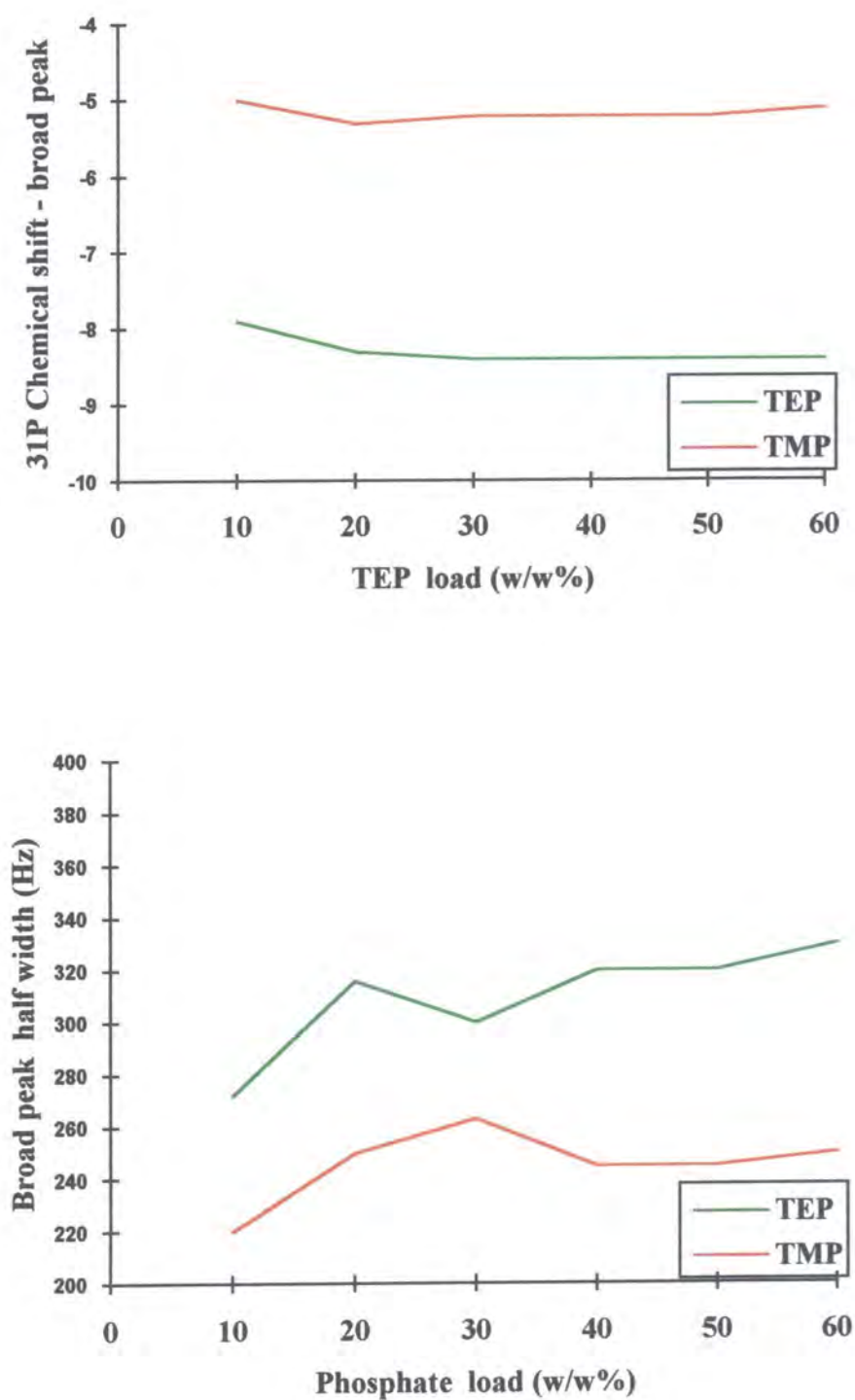


Figure 4.14. Plots of chemical shift and half-height linewidth for the broad peak of TEP and TMP adsorbed onto the SC2 carbon.

The results show that the linewidth of the broad peak initially increases with increased load and then falls as the narrow peak becomes evident. The linewidth then gradually increases again as the load increases. The chemical shift of the broad peaks moves to lower frequency as the load increases. The major change is between 10 and 20% w/w for each phosphate adsorbed onto SC2 carbon.

Figure 4.15 shows the linewidth and chemical shift for increments of TEP and TMP loaded onto ASZM carbon.

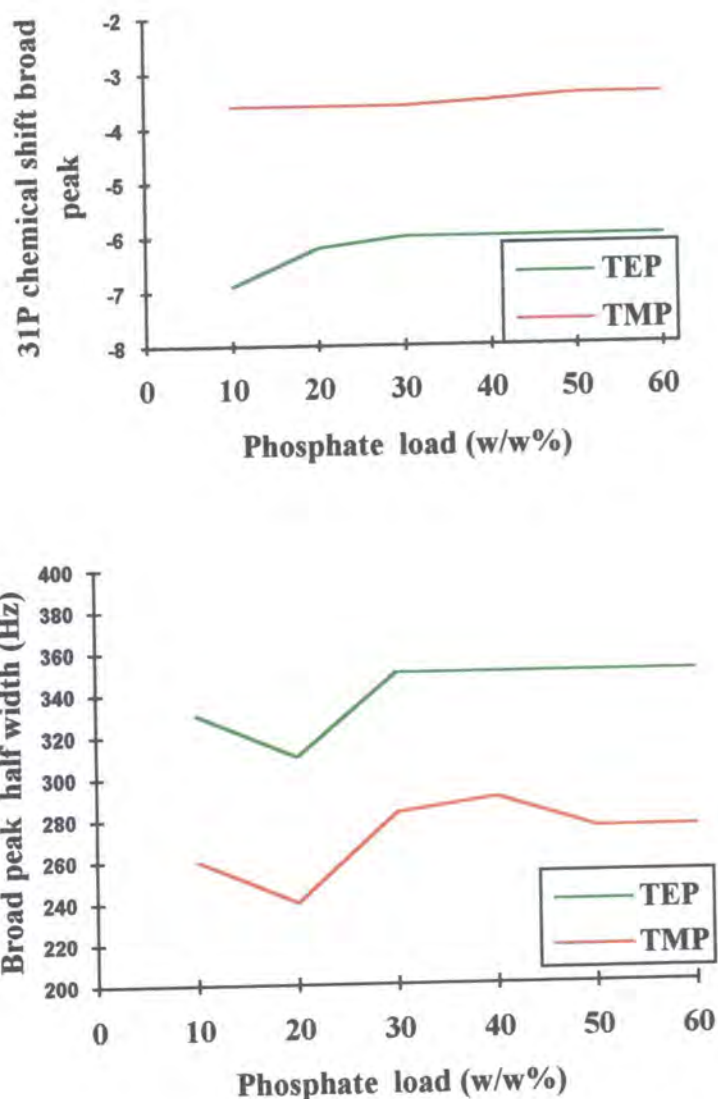


Figure 4.15. Plots of chemical shift and half-height linewidth for the broad peak of TEP and TMP adsorbed onto the ASZM carbon.

The results show that the linewidth of the broad peak initially decreases with increased load and then increases as the narrow peak becomes evident. The chemical shift of the broad peak moves to higher frequency as the load increases. The major change is between 10% and 20% w/w for the TEP adsorbed onto ASZM carbon.

Figure 4.16 shows the linewidth and chemical shift for increments TEP and TMP loaded onto BPL carbon.

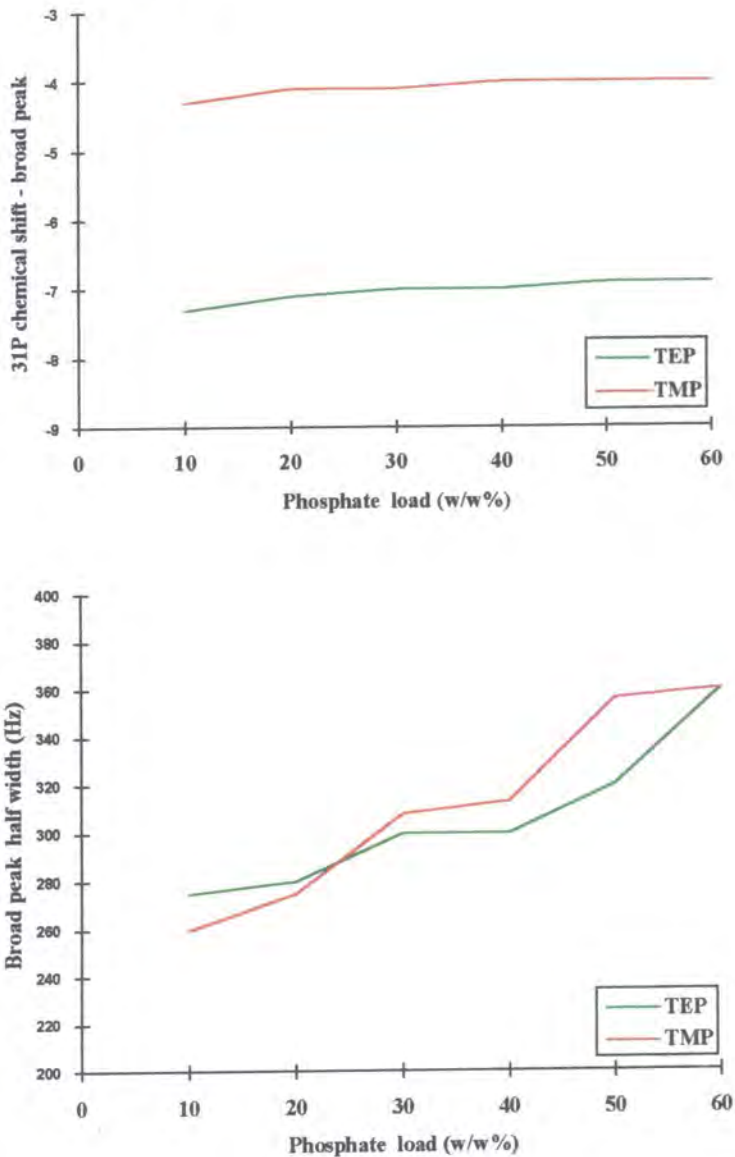


Figure 4.16. Plots of chemical shift and half-height linewidth for the broad peak of TEP and TMP adsorbed onto the BPL carbon.

The results show that the linewidth of the broad peak increases consistently with increased load. The chemical shift of the broad peak moves slightly to higher frequency as the load increases.

The pattern for the chemical shift of the broad peak as a function of phosphate load for the DMMP and PP is different for the carbon substrates. Figure 4.17 shows the chemical shift of the broad peak for DMMP and PP on the SC2 carbon.

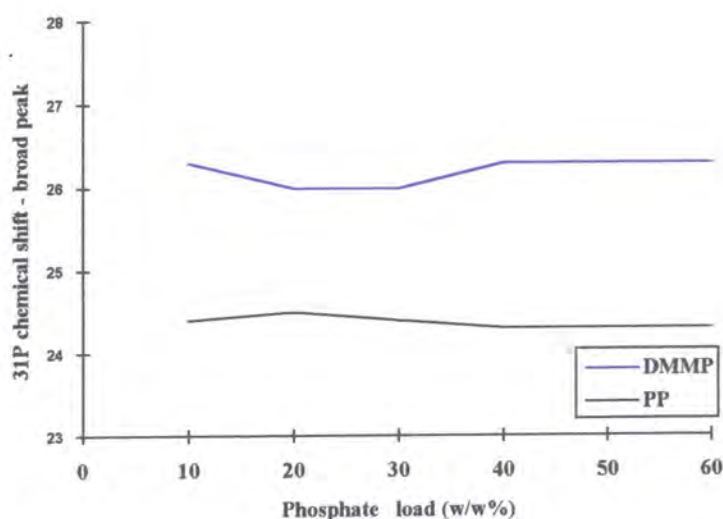


Figure 4.17. Plot of chemical shift for the broad peak of DMMP and PP adsorbed onto the SC2 carbon.

The results show that the chemical shift of the PP broad peaks moves slightly to lower frequency as the load increases. The chemical shift of the DMMP broad peaks moves slightly to lower frequency as the load reaches 30% w/w and then increases slightly.

Figure 4.18 shows the chemical shift of the broad peak for DMMP and PP on the ASZM carbon.

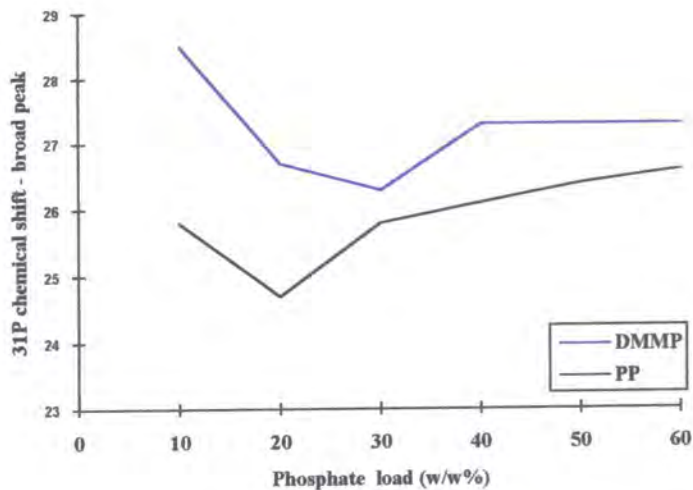


Figure 4.18. Plot of chemical shift for the broad peak of DMMP and PP adsorbed onto the ASZM carbon.

The results show that the chemical shifts of the DMMP and PP broad peaks initially move to lower frequency as the loads increase. They then move to higher frequency as the load further increases.

Figure 4.19 shows the chemical shift of the broad peak for DMMP and PP on the BPL carbon.

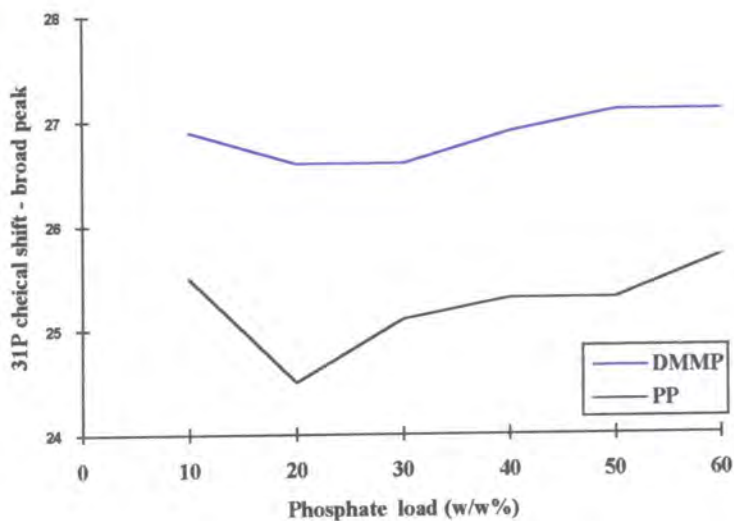


Figure 4.19. Plot of chemical shift for the broad peak of DMMP and PP adsorbed onto the BPL carbon.

The results show that the chemical shift of the DMMP and PP broad peaks initially move to lower frequency as the load increases. They then move to higher

frequency as the load further increases. This is similar to the behaviour on the ASZM carbon.

#### 4.1.2.5. Investigation of the carbon substrates

This section looks at the results for each phosphate on the three carbon types. Figure 4.20 shows the spectra of 60% w/w loads of TEP and TMP on the three carbon substrates. Figure 4.21 shows the 60% w/w loads of DMMP and PP on the three carbon types. These spectra are on similar scales and show how the saturated carbon types compare for different phosphates.

The TMP and TEP spectra are quite similar in their appearance when the carbons are saturated. The ASZM and BPL carbons have a broad peak at a similar chemical shift and half-width. The broad peak for the SC2 carbon is narrower and shifted to lower frequency. The narrow peak is similar in position and width for all three carbons.

The spectra for DMMP and PP are different. The broad peak position for the BPL and ASZM is similar but the BPL peak is broader. The SC2 carbon once again has a narrower peak shifted to low frequency. The narrow peak for the ASZM carbon seems to be shifted to low frequency compared to the BPL carbon for both adsorbates. The SC2 carbon has a narrow peak similar to the BPL carbon for the DMMP carbon. The PP adsorbate gives two narrow peaks with one similar to the BPL and one similar to the ASZM carbon.

Comparison of the peak integral and chemical shift for the incremental loading experiment allows the comparison of the carbon substrates. Figure 4.22 shows the broad peak integration and chemical shift data for incremental loads of TEP adsorbed onto the three carbon substrates. Figure 4.23 shows the broad peak integration and chemical shift data for incremental loads of TMP adsorbed onto the three carbon substrates. Figure 4.24 and 4.25 show the broad peak integration and chemical shift data for incremental loads of DMMP and PP respectively, adsorbed onto the three carbon substrates.

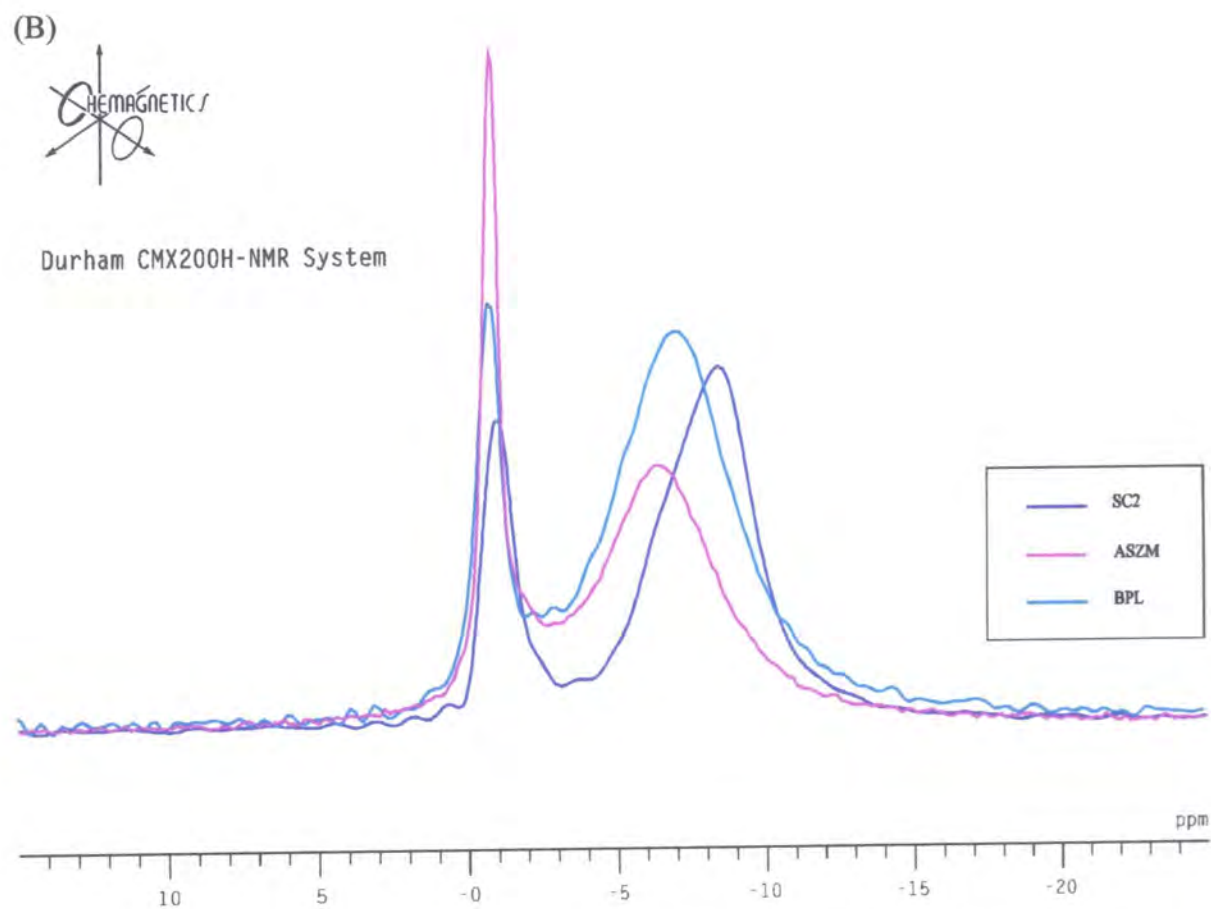
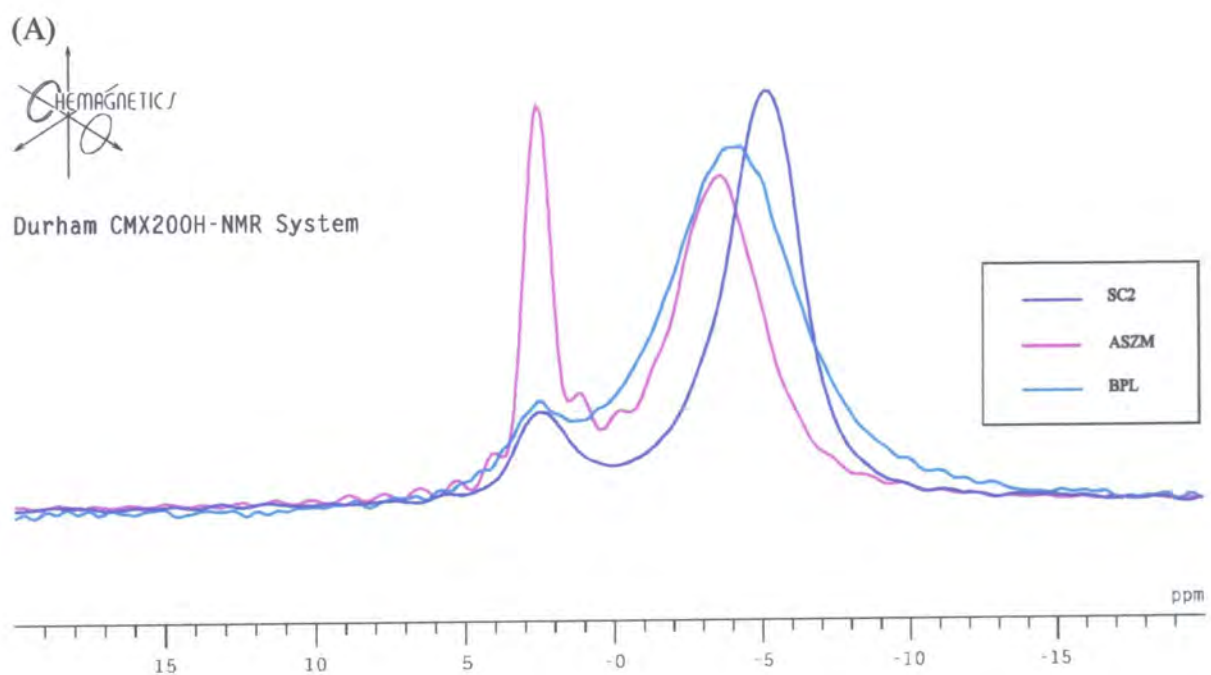


Figure 4.20.  $^{31}\text{P}$  NMR spectra of the three carbon substrates with (A) 60% w/w load of TMP and (B) 60% w/w load of TEP adsorbed.

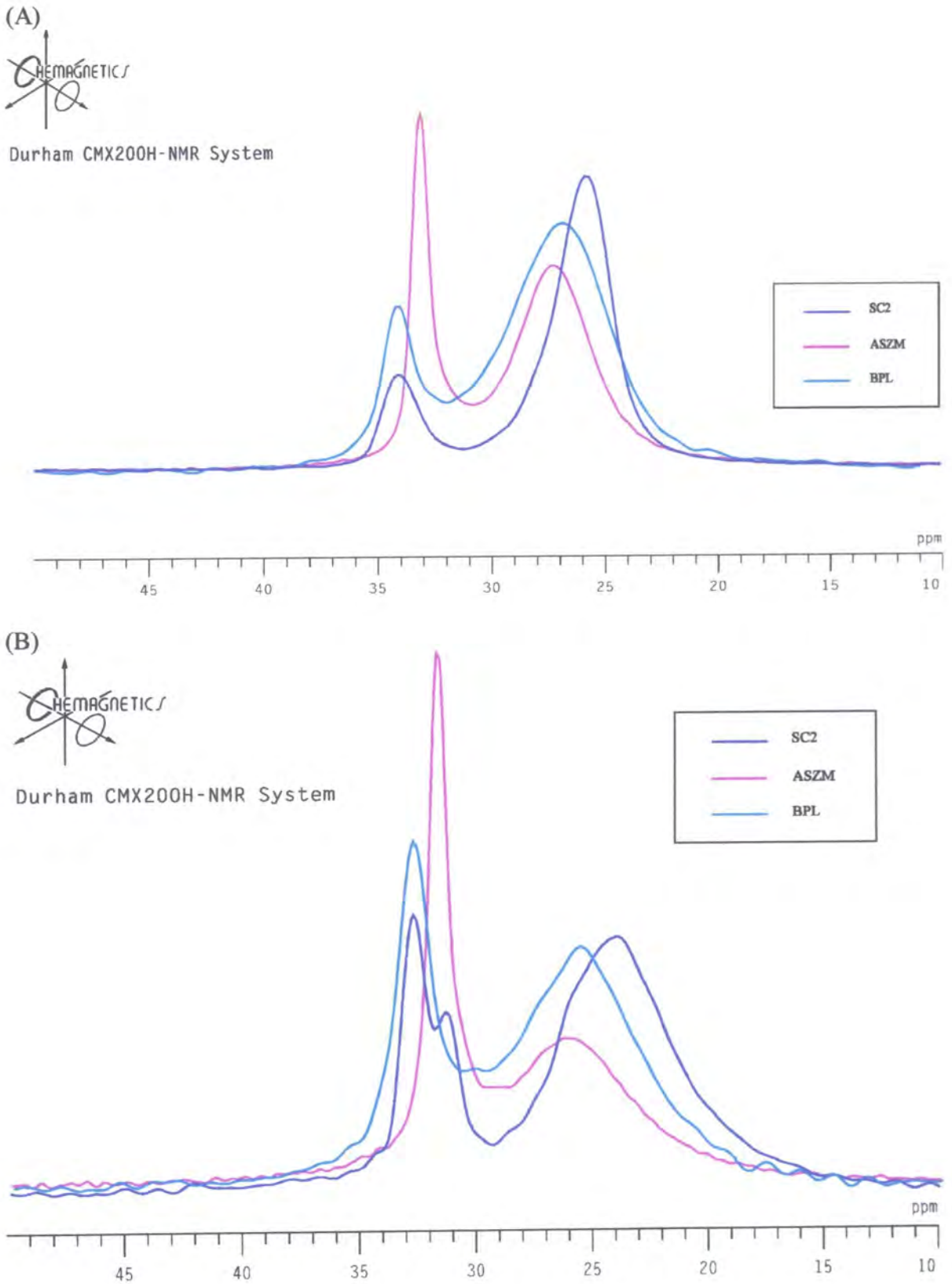


Figure 4.21.  $^{31}\text{P}$  NMR spectra of the three carbon substrates with (A) 60% w/w load of DMMP and (B) 60% w/w load of PP adsorbed.

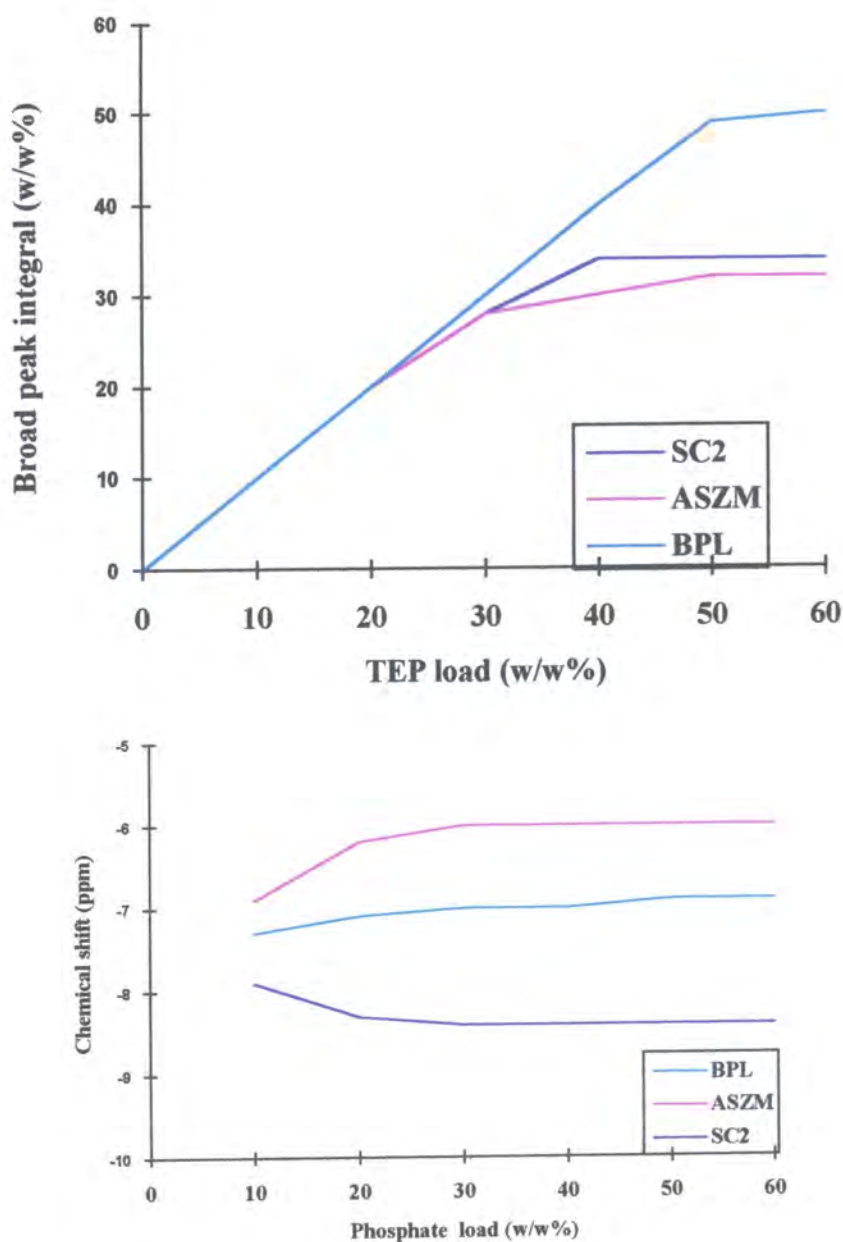


Figure 4.22. Plots of the broad peak integral and chemical shift for the TEP loading experiment on the three carbon types.

The results show that the integrals give a similar loading pattern for each carbon substrate. The BPL has the largest broad peak area available to TEP and ASZM has the smallest. The chemical shift data are very different with the SC2 carbon moving to lower frequency and the BPL and ASZM moving to higher frequency as the TEP load increases.

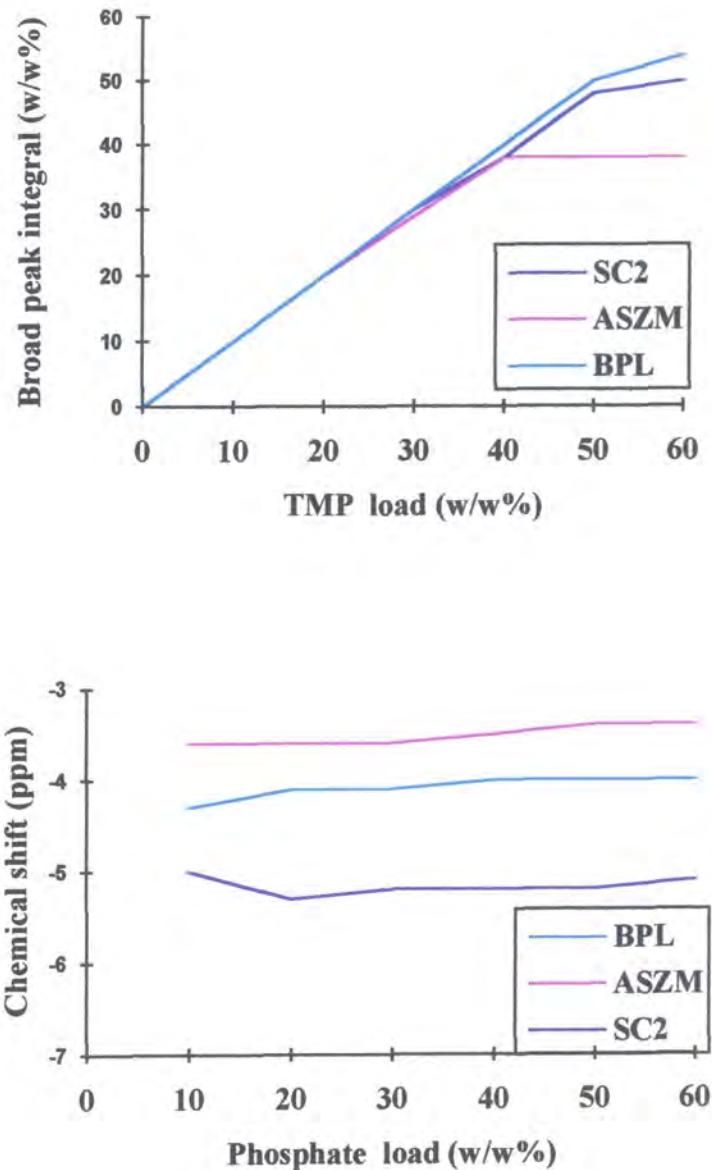


Figure 4.23. Plots of the broad peak integral and chemical shift for the TMP loading experiment on the three carbon types.

The results show that the integrals give a similar loading pattern for each carbon substrate. The BPL has the largest broad peak area available to TMP and ASZM the smallest. The chemical shift data are very different, with the SC2 carbon moving to lower frequency and the BPL and ASZM moving to higher frequency as the TEP load increases. The results are similar to the TEP data.

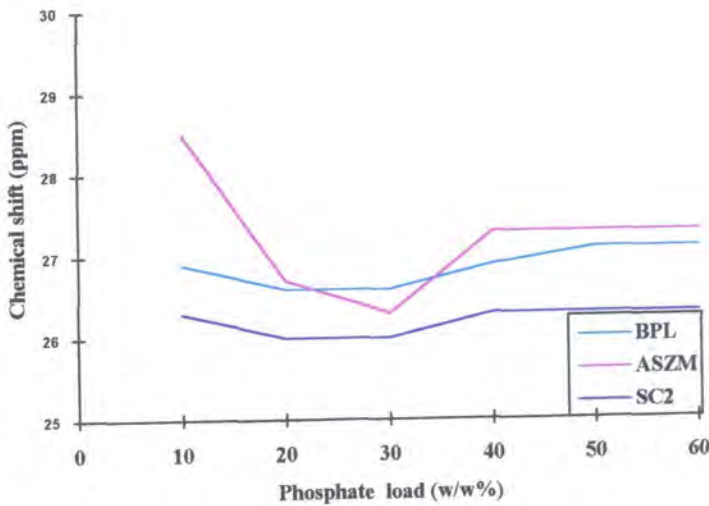
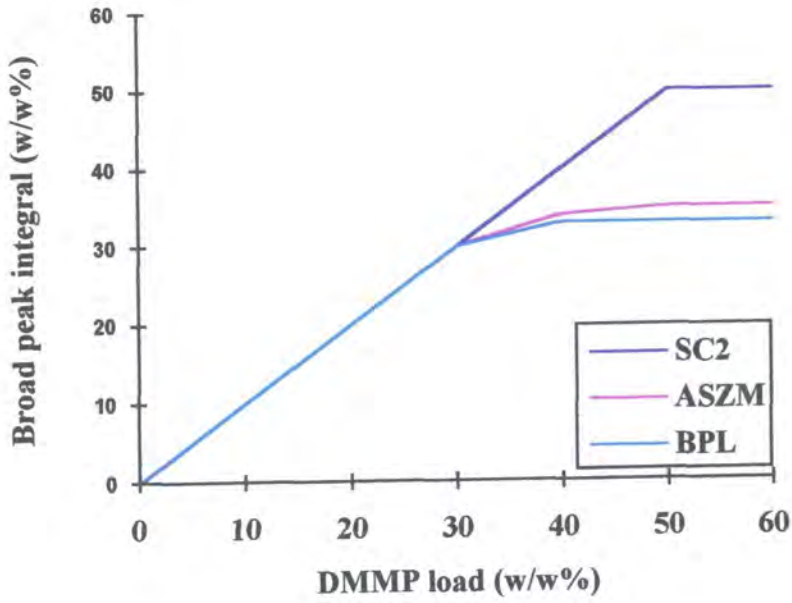


Figure 4.24. Plots of the broad peak integral and chemical shift for the DMMP loading experiment on the three carbon types.

The results show that the integrals give a similar loading pattern for the BPL and ASZM carbon substrates. The loading onto the SC2 carbon shows a very much larger broad peak area available for the DMMP. The chemical shift data are very similar with the broad peak for each carbon moving to lower frequency and then to higher frequency as the DMMP load increases.

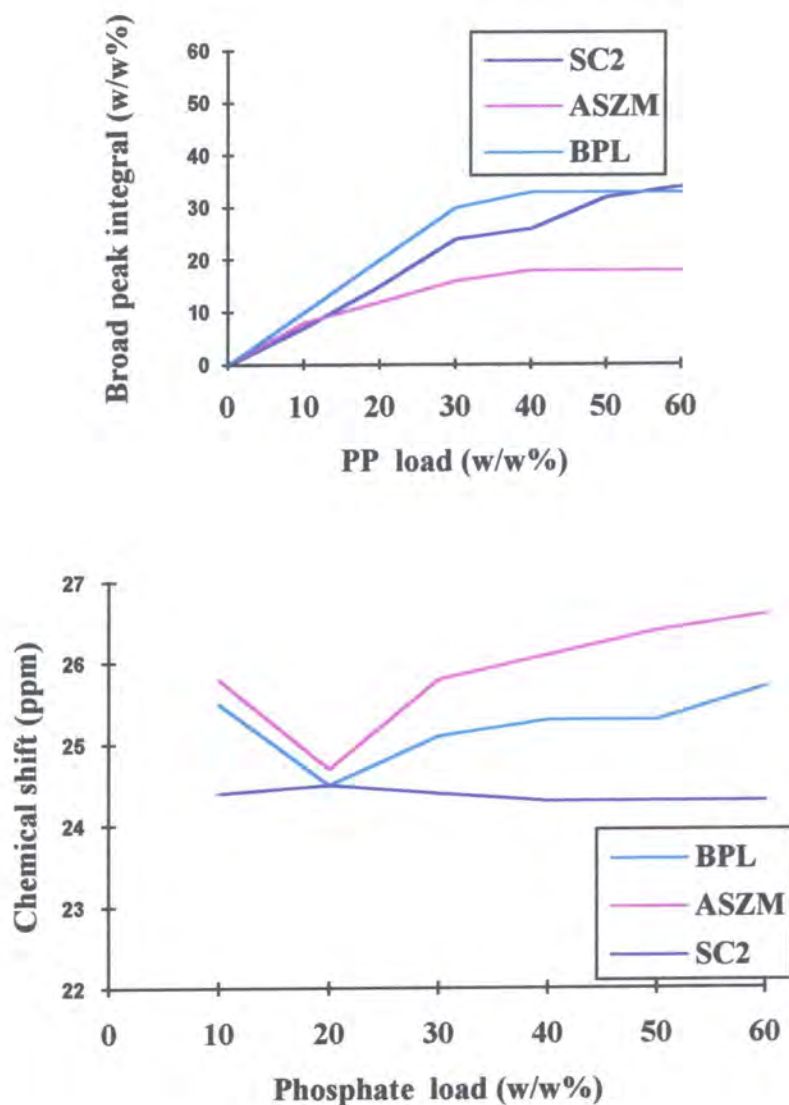


Figure 4.25. Plots of the broad peak integral and chemical shift for the PP loading experiment on the three carbon types.

The results show that the integrals give a differing loading pattern for the carbon substrates. The loading onto the SC2 carbon shows a larger broad peak area available for the PP but the broad peak develops slowly. The ASZM carbon has a very small broad peak area which fills slowly. The BPL carbon has a larger broad peak area available and fills quicker than the SC2 carbon. The chemical shift data are very similar for the BPL and ASZM carbons, with the broad peak for each carbon moving to lower frequency and then to higher frequency as the DMMP load increases. The reverse is true of the SC2 carbon.

#### 4.1.3. Long term ageing effects

The final section in the  $^{31}\text{P}$  experiments is concerned with long term ageing effects in the samples. The same sample was re-run under identical conditions over a thirty-three day period to see if the spectrum changed over time. Figure 4.26 shows the spectrum after one hour, ten days and thirty-three days. The intensity of the narrow peak falls off during the period and a corresponding increase in the broad peak area is observed.

#### 4.1.4. Discussion

##### 4.1.4.1. The effects of adsorption on the pure liquid

High-resolution  $^{31}\text{P}$  NMR spectra of the pure liquid adsorbates were obtained with a single-pulse regime and no magic-angle spinning. The rapid molecular motion in the liquid averages the orientation-dependent SA and dipolar interactions to zero so the linewidths are small (ca 50Hz for TEP and 75 Hz for PP). The molecular motion for PP is restricted since the molecules are large and the liquid is quite viscous, so this causes the linewidth to be slightly larger than the TEP.

When the 10% load of phosphates is adsorbed onto the activated carbon then the linewidth increases to 220-250 Hz. High-resolution spectra are obtained using a single-pulse regime with magic-angle spinning at 3.0 kHz to remove SA broadening effects. This broad peak is shifted some 7-8 ppm to low frequency as the adsorbate is adsorbed. The results are similar to those for  $^2\text{H}_2\text{O}$  adsorption described in chapter 3. The adsorbed molecules are held between graphitic sheets in the micropores, and the de-localised electron cloud creates extra shielding of the phosphorus nuclei. This extra shielding causes the chemical shift  $^{31}\text{P}$  to move to low frequency. The increased linewidth indicates a restriction in molecular motion caused by the adsorption process. The molecular motion is probably rapid but anisotropic, in contrast to the rapid isotropic motion of the liquid adsorbate. This restriction in motion scales the dipolar interaction and SA but does not remove it completely. The residual dipolar and SA interactions broaden the peak. The broad peak may also be composed of a number of lines with

## Ageing of the adsorbed Phosphate

~~HEMAGNETICS~~

Durham CMX200H-NMR System

Durham Initial Settings  
single pulse Bloch Decay  
pofn=1pulse  
cd1r=31Psc2wtmod  
cfn=51193sp.7  
cfd=0  
sf1=81.019167 MHz  
sw=50 KHz  
ad=15 usec  
al=2k cd1x  
aqt=40.961 msec  
dw=20 usec  
extm=2.041 sec  
p=157 deg  
pd=2 sec  
pw=4 usec  
rd=15 usec  
ac=64 scns

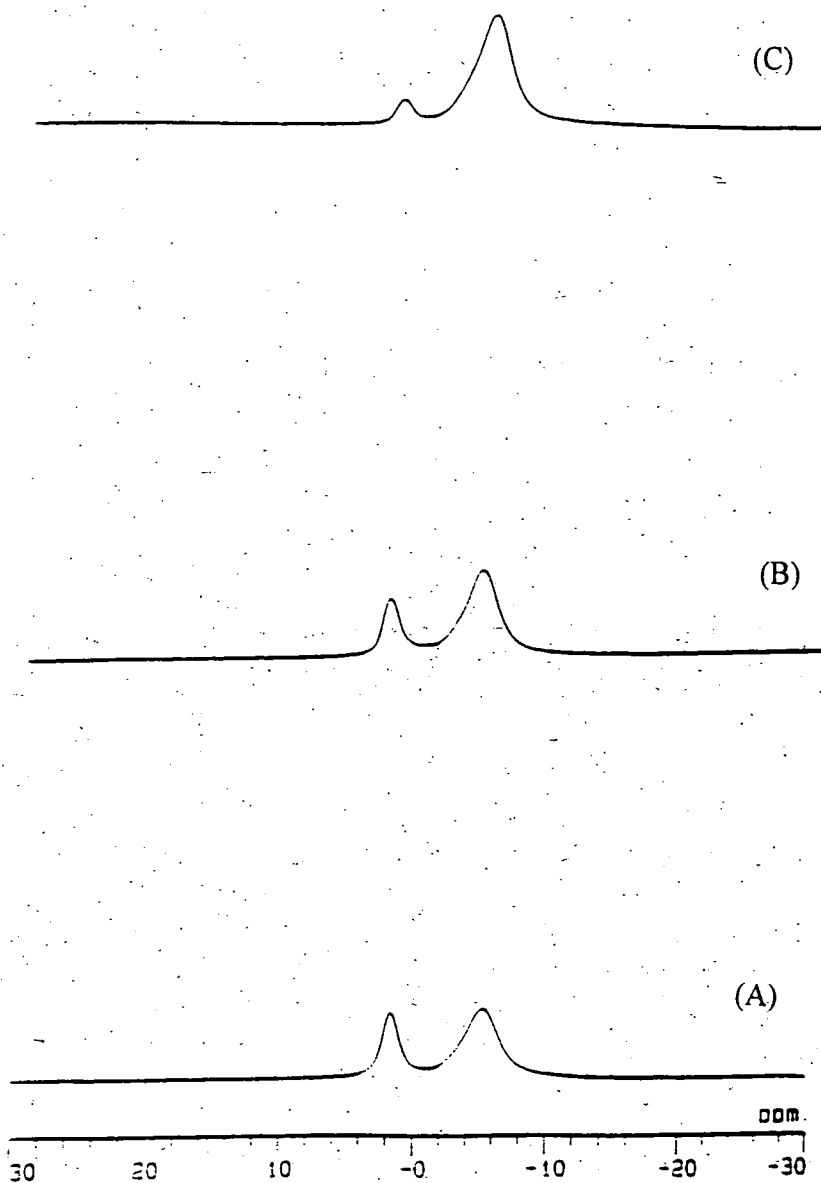


Figure 4.26.  $^{31}\text{P}$  NMR spectra of the SC2 carbon long-term ageing experiment with a 60% w/w TMP loading. Spectrum (A) was taken after 1 hour, (B) after 10 days, and (C) after 33 days.

similar shift which overlap. This means that the observed peak width increases as the various adsorbate environments are populated. The observed peak width is caused by a mixture of broadening from anisotropic motion and peak overlap.

The spectra of the SC2 with 60% w/w loading of each phosphate show that a similar loading pattern is seen in the  $^{31}\text{P}$  NMR of the phosphates, to that observed by  $^2\text{H}$  NMR of  $^2\text{H}_2\text{O}$  loading on SC2 activated carbon. The broad peak fills at high loads and a second narrow peak develops at a chemical shift close to the pure liquid adsorbate. The second peak is 100-140 Hz wide and therefore of intermediate width between the liquid adsorbate and the adsorbate held in the micropores. The second peak is attributed to molecules adsorbed on the carbon external surface or in the macropores. The result of the PP adsorption at 60% w/w on SC2 is obviously abnormal, with two narrow peaks, and will be discussed later.

#### 4.1.4.2. Typical loading characteristics

The results then concentrate on each of the carbon substrates, looking at the peak areas as a function of the adsorbate load. Figure 4.4 and 4.5 show a typical set of spectra following the loading increase of the TMP phosphate on the SC2 carbon. The results are again very similar to the previous  $^2\text{H}_2\text{O}$  loading experiment. The broad peak develops initially as the phosphate is adsorbed into the micropores. A second, narrower, peak develops at 30% w/w loading. The narrow peak increases in intensity as the phosphate load increases.

#### 4.1.4.3. Maximum available micropore volume

The analysis of relative peak areas enables the NMR data to provide information about the amount of phosphate adsorbed in each environment. The plots of the broad peak area, as a function of phosphate, give values of the maximum amount of phosphate which can be adsorbed into the micropores. When the data for the narrow peak are included then a complete picture of the adsorption of phosphates can be built up.

The SC2 carbon has the largest micropore availability for the DMMP and TMP adsorbates. The amount of TEP that can be adsorbed is only 65% of that amount and even less PP can be adsorbed. The PP loading shows a completely different broad peak loading profile and will be discussed separately.

The ASZM carbon has a maximum accessibility for the TMP molecule in the micropores. The DMMP micropore adsorption limit is slightly reduced, and the TEP adsorption in the micropores is a little lower than that. The PP adsorption has a strange profile. The broad peak does not fill to a maximum area until the load is 50% w/w PP, even though the maximum area available in the micropores corresponds to less than a 20% w/w load of PP. The PP molecule is very large and the adsorption is probably diffusion controlled with the molecules not filling the available micropores quickly.

The BPL carbon has the largest maximum micropore accessibility for TMP then TEP and thirdly DMMP. The amount of these three phosphates adsorbed into the micropores is generally larger for the BPL carbon than the SC2 and ASZM. The PP loading seems to have a standard profile but the large molecular size means that the peak area is only 60% the size of the TMP peak. The fact that the large PP molecules are adsorbed at the same rate as the other phosphates suggests that the BPL micropores are easier to access than for the SC2 and ASZM carbons.

The plots of the development for the narrow peak show that it develops slightly before the broad peak fills. This means that some external surface sites are filled preferentially to some micropores. This is especially true for the TMP molecules which develop a small narrow peak well before the micropore reaches its maximum area. The SC2 carbon shows a very different profile for the PP adsorption which is discussed next. The advent of the narrow peak can be used to find the maximum micropore area by extrapolation from the region where the narrow peak takes all the extra load of phosphate.

#### 4.1.4.4. Anomalous loading characteristics

The loading of PP onto the SC2 activated carbon shown in figures 4.12 and 4.13 follows a different pattern. The broad peak associated with PP adsorbed in the micropores builds up throughout the loading experiment and seems to be via a diffusion controlled process. A narrow peak at 31.5 ppm builds up from 10% to a limiting value at 50% w/w loads of PP. A second narrow peak at 32.8 ppm is seen at 40% w/w loads and this gradually increases with the load. The two narrow peaks suggest two separate external surface/macropore environments are available to PP molecules not adsorbed in the micropores. The peaks are broader than the pure liquid PP, with one shifted to low frequency and one to high frequency. The PP is certainly associated with the carbon since the motion is reduced, increasing the linewidth. One site has increased shielding of the phosphorus and the other one shows decreased shielding. The peak moved to low frequency of the liquid PP shift is populated straightaway at low loads but reaches a finite area at 50% w/w loads. The exact nature of these sites is not yet known.

#### 4.1.4.5. External surface adsorption

Table 4.5 shows the position of the narrow peak for each phosphate on the three carbons compared to the pure liquid values. The TMP and TEP adsorbates have narrow peaks shifted to low frequency when adsorbed onto the activated carbon. The DMMP and PP however have shifted to high frequency. As mentioned previously the PP adsorbed onto SC2 has two peaks, one either side of the liquid value. The exact reason for the shielding differences is not yet known.

#### 4.1.4.6. Detailed analysis of the micropore adsorption

The broad peak for the TEP and TMP was analysed in detail over the loading experiment to see if the chemical shift and linewidth varied. The results show that the broad peak associated with molecules adsorbed in the micropores did vary for each carbon type as the load increased. The observed variations in linewidth and chemical

shift were significant but not as dramatic as the differences between micropore and external surface adsorption. This variation in the chemical shift implies that the broad peak is a composite consisting of overlapping lines with similar chemical shifts. The associated linewidth differences suggest that the linewidth is also dependent on the molecular motion and on how rigidly the adsorbate is held in the pores. The results give a complicated picture, with the observed chemical shift being a weighted average of the available sites in the micropores. These systems have never been studied in such detail and therefore no theories to describe the adsorption process have been developed. The NMR results themselves give some evidence about these processes, but the lack of conventional analysis as corroborative evidence means that the conclusions drawn from NMR data can not be considered as conclusive.

The SC2 carbon initially exhibits decreases in chemical shift and increases in linewidth as the adsorbate load increases. This is consistent with extra different micropore sites being available as more phosphate is added to the system. The extra sites are at lower frequency to the ones accepting the first adsorbate molecules. This means that phosphate is preferentially adsorbed in the larger micropores. This suggests that the smaller pores, where the adsorption potential is greatest, are more difficult for the adsorbate to reach. The larger micropores create less shielding of the phosphorus nuclei, giving a peak at a slightly higher frequency.

The increased load of phosphate is then adsorbed in the more abundant smaller micropores with high adsorption potential, and the chemical shift remains constant. The linewidth falls off as the broad peak increases in area. This occurs because the molecules are less rigidly bound as multi-layers develop and the phosphate becomes more liquid like.

At the point that the narrow peak develops the broad peak increases in width and the chemical shift does not move. This is logical as the small amount of micropores at the extremity of possible adsorption size will fill after this point. The broad peak will develop extra area at low and high frequency (very small and very large micropores), increasing the linewidth but not changing the mean peak position.

The ASZM carbon has a different profile, with an initial increase in frequency and decrease in linewidth. The ASZM carbon initially adsorbs the phosphate in the smaller pores and then the larger micropores fill. The linewidth initially is broad as the molecular motion is restricted in the narrow pores but decreases as the larger pores are filled. The transport of the adsorbate to the small pores is better than for the SC2 carbon. The linewidth then falls off as the molecular motion increases with multi-layer build-up.

The BPL carbon does not show much variation in the observed chemical shift, and the linewidth increases consistently as the loading increases. The results suggest that the BPL carbon has a large distribution range of pore sizes available to the phosphate. As the load increases then pores at the small and large end of the distribution are filled and the peak becomes wider, but the average shift will remain constant.

The DMMP and PP molecules showed different characteristics with the variation of chemical shift with loading. The linewidth was difficult to measure accurately so the results just give the chemical shift data. The SC2 carbon shows the same adsorption pattern for DMMP as for TEP and TMP. The PP loading is different as discussed earlier. The ASZM and BPL carbons show large variations in the chemical shift as the load increases. For both the DMMP and PP the shift moves to low frequency as the load increases, but as the broad peak reaches its maximum area, then the chemical shift moves to high frequency. This suggests that these larger molecules adsorb in the larger micropores initially, and then move into the smaller pores with the larger adsorption potential. The final movement back to high frequency shows that the larger micropore sites previously unpopulated are available as the micropores become saturated. The results are opposite to the TEP and TMP results for the ASZM carbon because the transport pores do not seem to be able to move the larger molecules into the micropores as easily.

#### 4.1.4.7. Comparison of the carbon substrates

The carbon substrates can be compared directly by looking at the spectra for each one with the same load of adsorbate. The best way to compare the carbon substrate is to saturate the load so that all the available pores are full. Figures 4.20 and 4.21 show this scenario. The phosphate spectra basically show similar characteristics with two distinct adsorption environments. The SC2 and ASZM carbons have similar linewidths for the broad peak, but the BPL carbon is visibly broader. This suggests that the BPL carbon has a larger distribution of micropore size, with more overlapping lines creating the extra linewidth. The micropore peak for the SC2 is shifted to lower frequency for each adsorbate. This may be caused by a greater shielding effect from the graphitic carbon  $\pi$ -electron cloud. The SC2 carbon is derived from coconut shells and the BPL and ASZM from coal and the carbon structure is thought to be much better defined than the coal based carbons, with a smaller pore-size distribution.

The broad peak especially for the SC2 carbon is not symmetric, with extra area developing on the high frequency side. This phenomenon was discussed for the deuterium results. The SC2 carbon has a quite small pore-size distribution and gives a quite narrow peak. However as the carbon is saturated the sites with lower adsorption potential will be populated. Micropores at the small end of the distribution will not fill because the phosphate molecule can not fit into the pore. However the larger micropores can be accessed and give rise to peaks at the high-frequency edge of the broad peak.

The narrow peak seems to develop in quite similar positions for the TEP and TMP adsorbates. However, the DMMP and PP adsorbates have very different narrow peak positions. The ASZM carbon has the external adsorption shifted to low frequency compared to the BPL carbon. The SC2 carbon has adsorption at high frequency similar to the BPL for DMMP. However, the two narrow peaks for the PP adsorbate give one to low and one to high frequency. Obviously the carbons adsorb the DMMP and PP in different environments but the exact nature of the sites is not yet known.

When the carbon is saturated it gives information about the complete range of pores available, but an investigation of the NMR data as the load increases shows how the phosphate is adsorbed. The plots of the broad peak integral and the corresponding chemical shift data help to suggest which pores are filled preferentially for each carbon type.

The largest amount of TMP and TEP adsorbed into the micropores is by the BPL carbon, and the least by the ASZM. The chemical shift data show that the adsorption process is very different for the ASZM and BPL compared to the SC2 carbon, as discussed previously. The SC2 carbon adsorbs initially into the large micropores whereas the ASZM and BPL adsorb into smaller micropores and then the larger ones. The differences probably lie in the ease of access to the small micropores.

The DMMP has a maximum adsorption in the micropores from the SC2 carbon, with the BPL and ASZM very similar in area available. The mechanism for adsorption is very similar, with the phosphate going into the larger micropores prior to the larger ones. The transport to the small micropores is not as effective for DMMP in the ASZM and BPL carbons.

The PP adsorption is complicated because the molecule is very bulky and the broad peak filling is diffusion controlled. The ASZM and BPL carbons have similar loading profiles and chemical shift patterns. The phosphate data give accessibility information for specific molecules: the ASZM will not adsorb very much PP in total, so the micropores are either too small or the entrances get blocked up. The SC2 carbon once again is very different in the way it adsorbs the PP molecules. The broad peak fills slowly but eventually adsorbs more than the BPL, suggesting the SC2 has pores the correct size for the PP but the transport to the micropores limits the adsorption.

#### 4.1.4.8. Long-term ageing effects

The long-term ageing experiment is very interesting. The spectrum changes over time, with the TMP adsorbed on the external surface moving into the micropore peak. The thirty-three day period sees the narrow peak lose 75% of its intensity. The

long-term ageing is probably a mixture of two effects. The molecules in the micropores can re-arrange over time, unblocking some pores so that more of the micropore volume is available. The gravimetric data from water adsorption suggest that equilibrium is reached in a few hours, but this can not detect any movement between adsorption sites. There is also evidence from carbon chemists, discussed in the introduction, that the phosphates cause the pore system to change. Successive adsorption of TEP molecules mutates the micropore surface, including hetero atoms into the graphitic planes thus widening the pores. The widening of the pores would take some time and would increase the accessible micropore area.

#### 4.1.5. Conclusions

Phosphorus NMR can be used to follow the adsorption of phosphates onto the activated carbon samples. The effect of the adsorption on the pure liquid can be observed, initially with a broad peak shifted to low frequency associated with the adsorption of the phosphates in the micropores. At higher loads a narrow peak is observed which is attributed to phosphate adsorbed on the external surface. This standard loading pattern is followed by each system except PP adsorbed onto SC2 carbon. This anomalous experiment gives two narrow peaks associated with external surface sites.

The peak integration data give information about the maximum micropore accessibility for each phosphate-carbon system. More detailed analysis of the chemical shift and linewidth data for the micropore adsorption gives some extra information about the loading process. The results show that analysis of the carbon substrates as a group, with similar adsorbate loads, gives valuable information about the carbon and how it adsorbs each phosphate. The spectra with each carbon saturated with phosphate yields information about the type of pores accessible in each carbon substrate.

The long-term ageing experiment shows that NMR is useful because it can distinguish adsorbate movement between various sites within the carbon. This is a major advantage over the more conventional gravimetric analysis.

## Chapter 5 Competition reactions

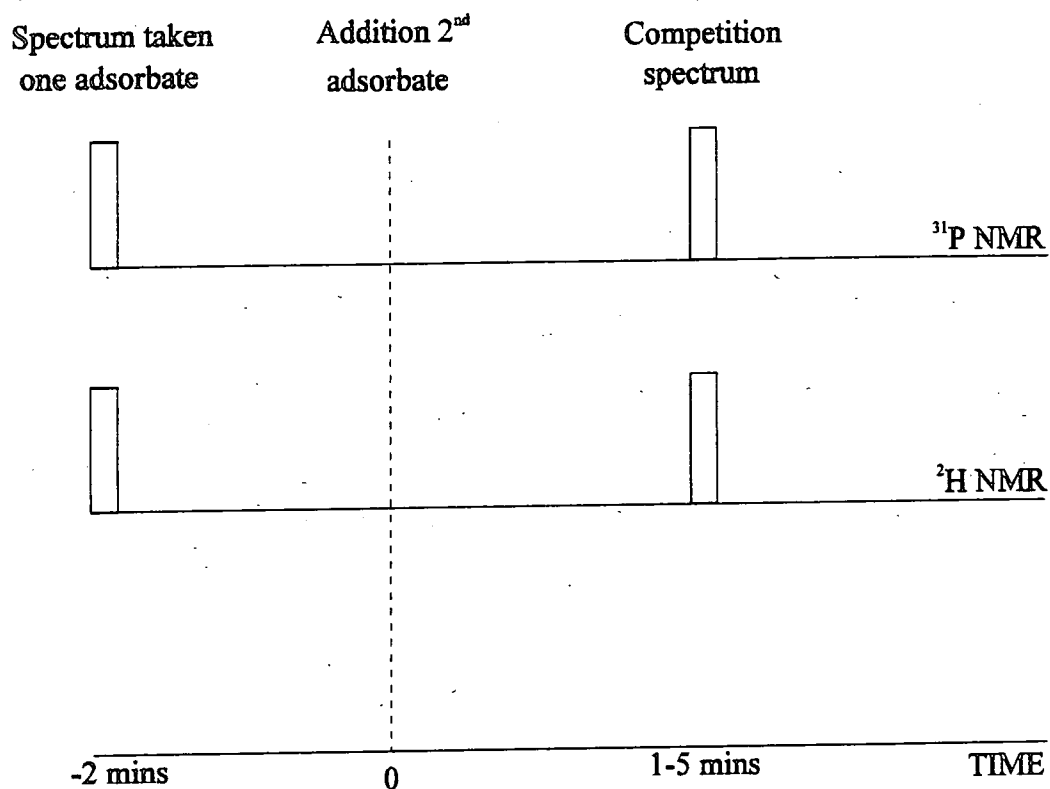
### 5.1 Introduction

It is possible to use solid-state NMR to follow competition between adsorbates for activated carbon systems. The major system of interest for the project was competition between deuterated water and organophosphates. These systems simulate a possible environment in which the carbons would be used in the battle field. NMR data were taken under identical conditions at regular intervals to study the kinetics of the adsorption competition.

The adsorbates used in these experiments were 99.99% enriched  $^2\text{H}_2\text{O}$  from Aldrich, triethyl phosphate (TEP) and cyclohexyl methyl methyl phosphonate (PP). These were adsorbed onto the dry SC2 nutshell carbon and the dry ASZM coal carbon provided by the C.B.D.E. The samples were prepared by adsorbing a known amount of one adsorbate via pipette onto the carbon. This was left for one hour to reach equilibrium, then the second adsorbate was added via pipette to the sample. The sample was transferred to a teflon insert with a thumb-tight lid and then analysed by NMR as quickly as possible.

The NMR spectra were run on the CMX 200 using a MAS probe with a 7.5 mm pencil rotor containing the air-tight teflon insert, which avoided any evaporation into the atmosphere. High-resolution spectra were obtained for the  $^2\text{H}$  and  $^{31}\text{P}$  nuclei using a single-pulse regime with no proton decoupling. The pulse delay was 1-2s to allow complete relaxation between pulses. The number of transients taken varied between 4 and 64 so each spectra took between 4s and 2 minutes to acquire. All the competition spectra were acquired using the CMXW macro Delay. This macro allowed the spectrum to be re-run under identical conditions. The number of spectra to be run and the delay period between spectra can be set by the experimentalist to follow the competition as required. The experiments varied from spectra run every hour for 24 hours, to spectra every minute for 2 hours.

The time plotted for each experiment needs to be examined carefully to avoid confusion. I have set the time of addition of the second adsorbate as time zero in each case. This is explained below:



The experiments that were run on the competition reactions fell into two groups. The first section involved  $^2\text{H}_2\text{O}$  pre-adsorbed onto the carbon and then the phosphate was added. The competition was followed by  $^2\text{H}$  and  $^{31}\text{P}$  NMR. The second section concerned TEP pre-adsorbed onto the carbon and then  $^2\text{H}_2\text{O}$  was added, this was also studied using  $^2\text{H}$  and  $^{31}\text{P}$  NMR.

## 5.2 Results

The results have been included as a series of selected stacked spectra because there were too many spectra taken to show them all. There are also several graphs showing the salient peak heights as a function of time. These show the general trends observed in the  $^2\text{H}$  and  $^{31}\text{P}$  NMR spectra.

### 5.2.1 Pre-adsorbed $^2\text{H}_2\text{O}$ .

The first experiment used the SC2 dry carbon with 35% w/w  $^2\text{H}_2\text{O}$  adsorbed. The sample was left to equilibrate for one hour, and then the  $^2\text{H}$  spectra were taken. The sample then had 35% w/w TEP added, followed by transfer to the NMR insert. The  $^2\text{H}$  spectra were run 1 minute after the addition of the second adsorbate. Each spectrum had 64 transients with a pulse delay of 2s, the  $^2\text{H}$  spectra were run once every hour for the next 24 hours. The  $^{31}\text{P}$  NMR spectra were taken in a subsequent experiment using a sample prepared in the same manner. The  $^{31}\text{P}$  spectra were run using 64 transients and a 2 s pulse delay. Once again a spectrum was run one minute after the addition of the second adsorbate and every hour subsequently for 24 hours. The stacked plots for the  $^{31}\text{P}$  and  $^2\text{H}$  NMR are shown in figure 5.1. The time since the addition of the second adsorbate is indicated on the figure.

Figure 5.2 shows the  $^2\text{H}$  spectrum before the addition of the second adsorbate compared to the first spectra taken after 2 minutes in the competition reaction. The spectra show that when there is only  $^2\text{H}_2\text{O}$  adsorbed on the carbon then the broad peak at -8.5 ppm is very large. However just two minutes after the addition of the TEP the spectrum changes dramatically, with the narrow peak at 0 ppm becoming a lot larger than the broad peak. The spectra are on the same scales and the total area under the peaks in each, remains the same. This means that the  $^2\text{H}_2\text{O}$  is re-distributed within the carbon and not lost to the atmosphere.

Figure 5.3 is a graph of the peak intensities for the competition reaction as a function of time. The  $^{31}\text{P}$  and  $^2\text{H}$  NMR data are included on the same graph to compare the two adsorbates behaviour. The  $^{31}\text{P}$  data show that the narrow peak at -1 ppm decreases in intensity exponentially as a function of time. The time constant for this exponential decay is 6.5 hours. The broad peak increases in intensity over the same period of time. The  $^2\text{H}$  NMR data show the narrow peak at 0 ppm increasing dramatically as the second adsorbate is added to the system. The narrow peak then increases in intensity at a slower rate over the next 24 hours.

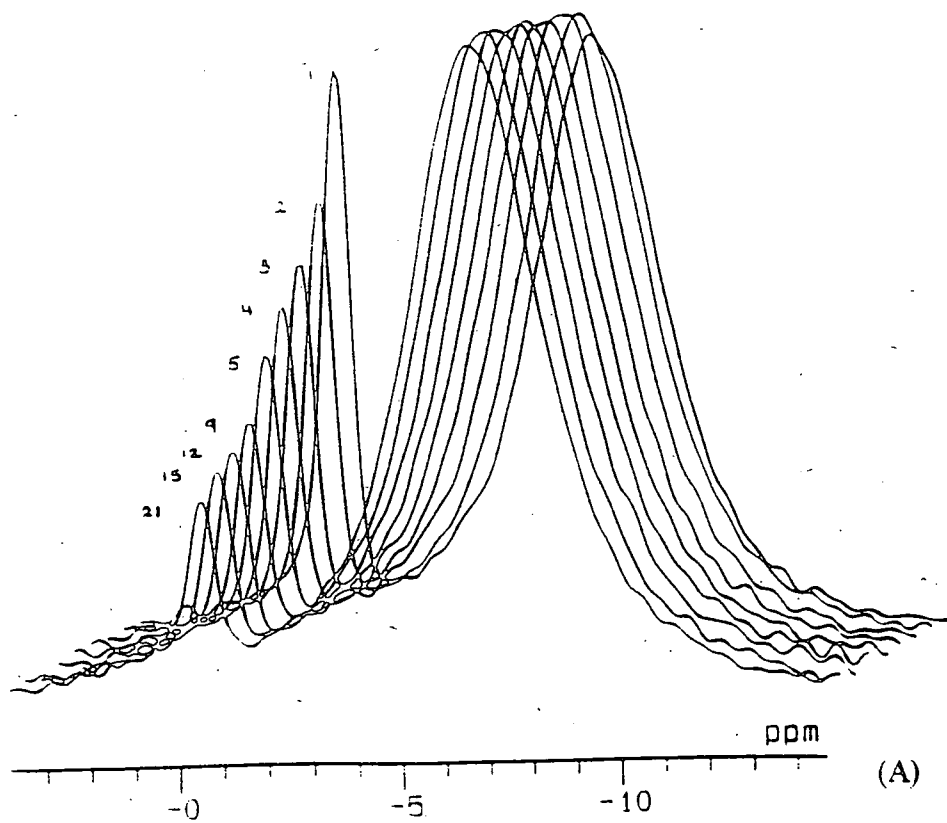
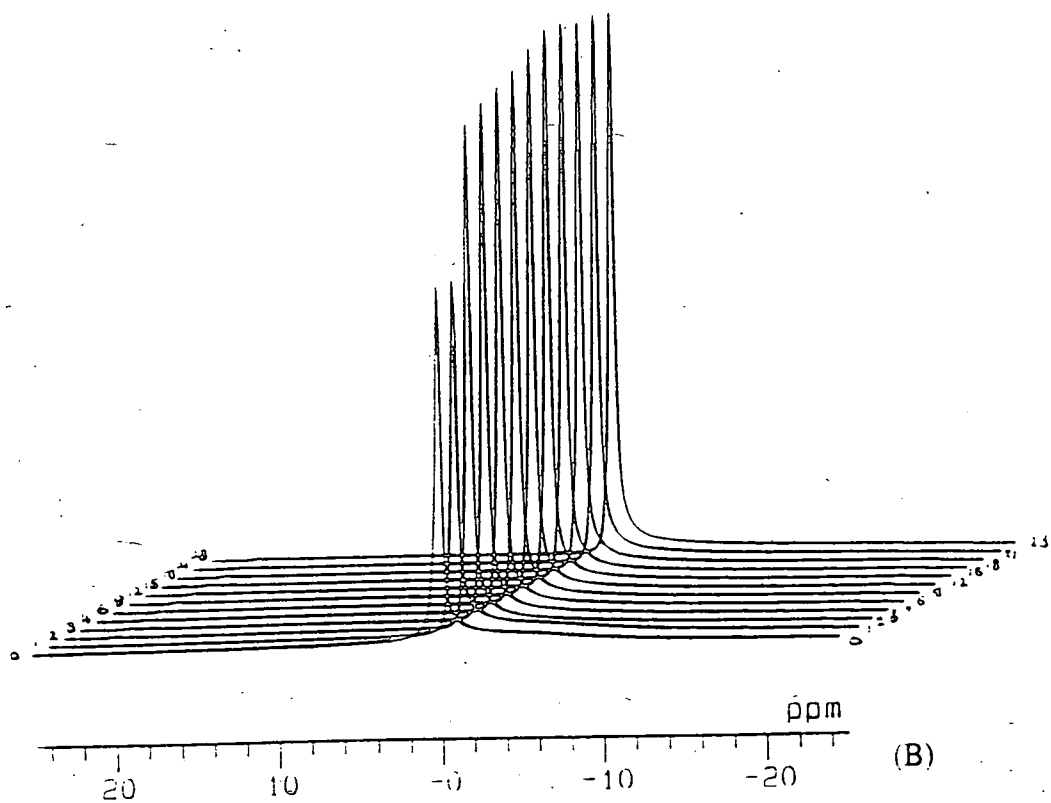


Figure 5.1. Stacked spectra following the adsorbate competition between 35% w/w TEP, added to a sample of SC2 with 35%  $^2\text{H}_2\text{O}$  pre-adsorbed, for 24 hours. Spectra (A) shows  $^{31}\text{P}$  NMR of TEP. Spectra (B) shows  $^2\text{H}$  NMR of the  $^2\text{H}_2\text{O}$ . Time indicated in hours.



### Durham CMX200H-NMR System

Durham Initial Settings  
single pulse Bloch Decay

ppfn=1pulse  
cdir=react10  
cfn=t1m  
cfd=0  
sf1=30.72201 MHz  
sw=50 KHZ  
ad=15 usec  
al=2k colx  
aqt=40.961 msec  
dw=20 usec  
extm=1.041 sec  
p=157 deg  
pd=1 sec  
pw=6 usec  
rd=15 usec  
ac=4 scns

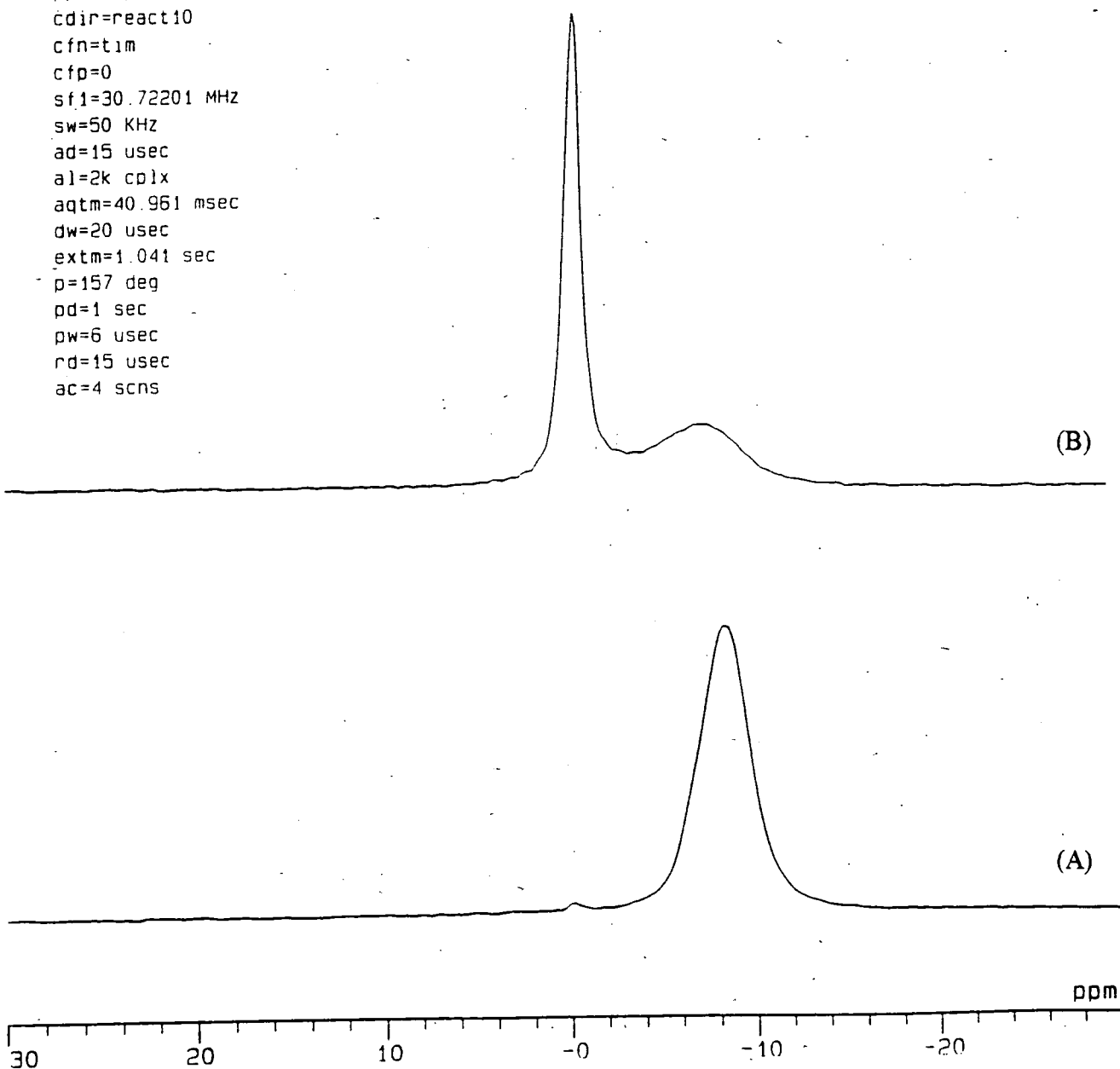


Figure 5.2.  $^2\text{H}$  spectra of (A) SC2 with just 35%  $^2\text{H}_2\text{O}$  adsorbed and (B) 1 minute after 35% TEP was added to the sample.

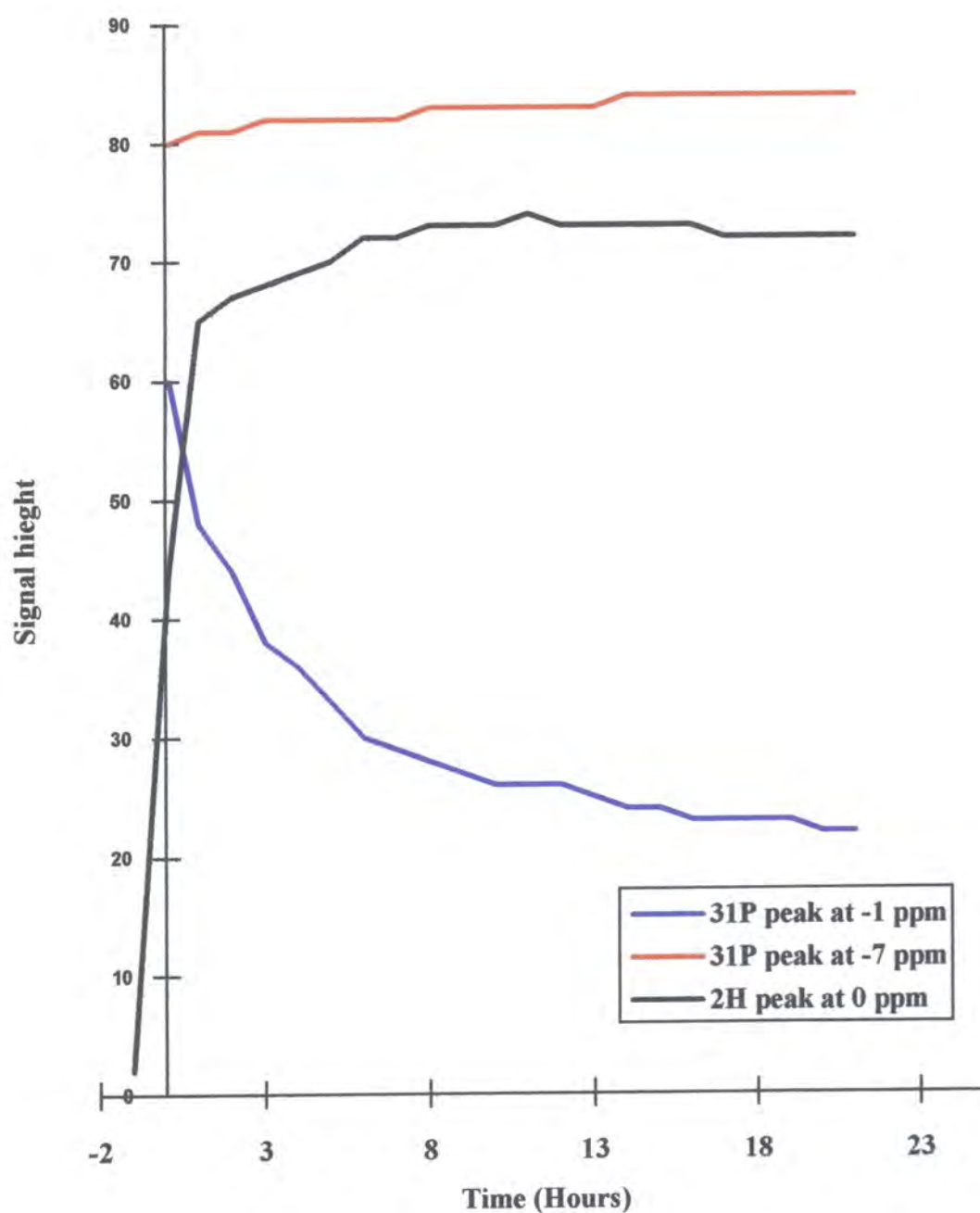


Figure 5.3. Graph showing the relative  $^{31}\text{P}$  and  $^2\text{H}$  NMR peak heights for 24 hours after the addition of 35% TEP to the SC2 carbon with 35%  $^2\text{H}_2\text{O}$  pre-adsorbed.

The next experiment was set up to compare the results using a different carbon and a larger phosphate. The experiment used the ASZM dry carbon with 35% w/w  $^2\text{H}_2\text{O}$  pre-adsorbed onto it. The system was allowed to equilibrate for one hour and

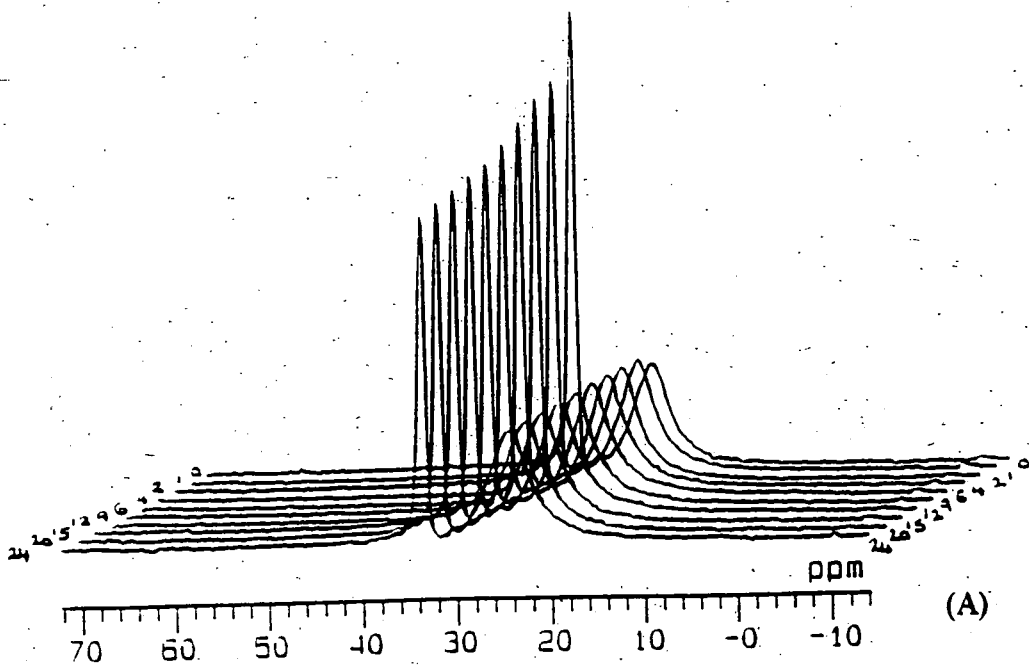
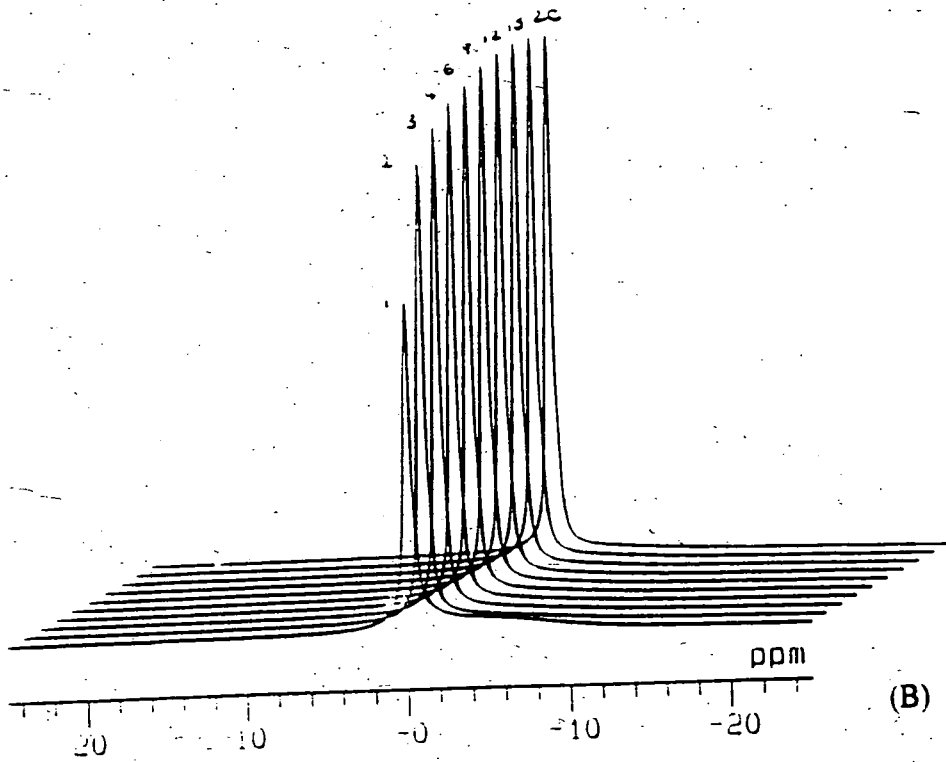


Figure 5.4. Stacked spectra following the adsorbate competition between 35% w/w PP, added to a sample of ASZM with 35%  $^2\text{H}_2\text{O}$  pre-adsorbed, for 24 hours. Spectra (A) show  $^{31}\text{P}$  NMR of pp. Spectra (B) show  $^2\text{H}$  NMR of the  $^2\text{H}_2\text{O}$ . Time indicated in hours.

then 35% w/w of PP was added to the sample. The sample was transferred to the NMR insert and the NMR analysis started as soon as possible. The first  $^2\text{H}$  spectrum was run 1 minute after the addition of the second adsorbate. Each spectrum had 64 transients with a pulse delay of 2 s, and the  $^2\text{H}$  spectra were run once every hour for the next 24 hours. The  $^{31}\text{P}$  NMR spectra were taken in a subsequent experiment using a sample prepared in the same manner. The  $^{31}\text{P}$  spectra were run using 64 transients and a 2 s pulse delay. Once again the spectrum was run one minute after the addition of the second adsorbate and every hour subsequently for 24 hours.

The stacked plots for the  $^{31}\text{P}$  and  $^2\text{H}$  NMR are shown in figure 5.4. The time since the addition of the second adsorbate is indicated on the figure. The general trend of the  $^{31}\text{P}$  stacked plot is the same for the two phosphate molecules, except that the decrease in intensity of the narrow peak is less dramatic for the larger P.P molecule. Once again the major increase in the  $^{31}\text{P}$  broad peak occurs over the first hour. These results were very consistent and repeatable.

Figure 5.5 is a graph of the peak intensities for the competition reaction as a function of time. The  $^{31}\text{P}$  and  $^2\text{H}$  NMR data are included on the same graph to compare the behaviour of the two adsorbates. The  $^{31}\text{P}$  data show that the narrow peak at 34 ppm decreases in intensity as a function of time. The initial decrease over the first 2 hours is more pronounced than the decrease over the next 22 hours. The broad peak at 24 ppm increases in intensity over the same period of time. The  $^2\text{H}$  NMR data show the narrow peak at 0 ppm increases in intensity over the 24 hours. Once again the initial increase is gradually reduced in rate over the 24 hour period.

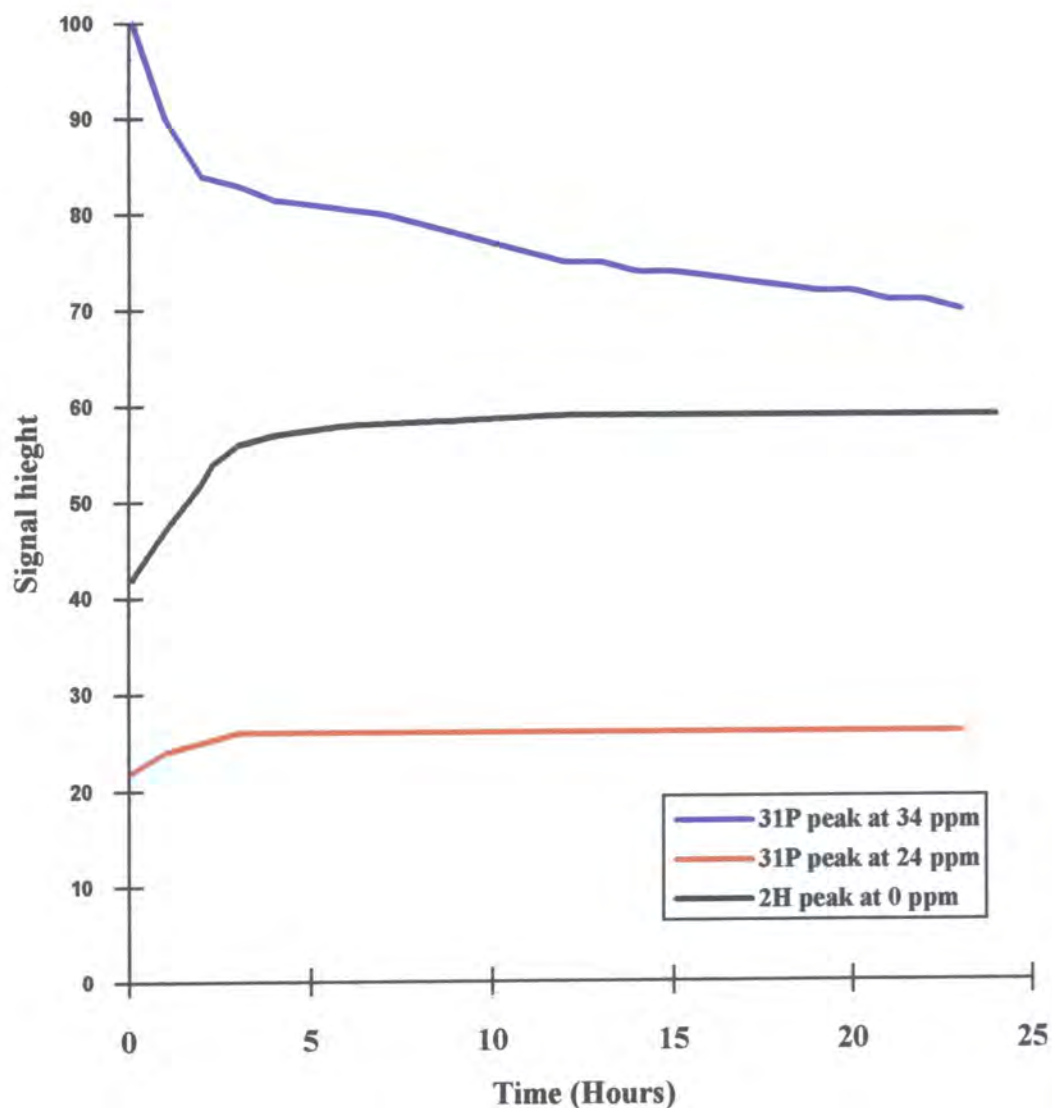


Figure 5.5. Graph showing the relative  $^{31}\text{P}$  and  $^2\text{H}$  NMR peak heights for 24 hours after the addition of 35% PP to the ASZM carbon with 35%  $^2\text{H}_2\text{O}$  pre-adsorbed.

The third set of experiments was set up to see if the choice of carbon substrate made any difference to the results. The first experiment used the SC2 dry carbon with 40% w/w  $^2\text{H}_2\text{O}$  adsorbed. The second experiment had 40% w/w  $^2\text{H}_2\text{O}$  adsorbed onto the ASZM carbon. The samples were left to equilibrate for one hour then had 40% w/w TEP added. Each sample was transferred to the NMR insert and the  $^{31}\text{P}$  spectra were run using 16 transients and a 2 s pulse delay. Once again the spectrum was run one minute after the addition of the second adsorbate and every hour subsequently for 18

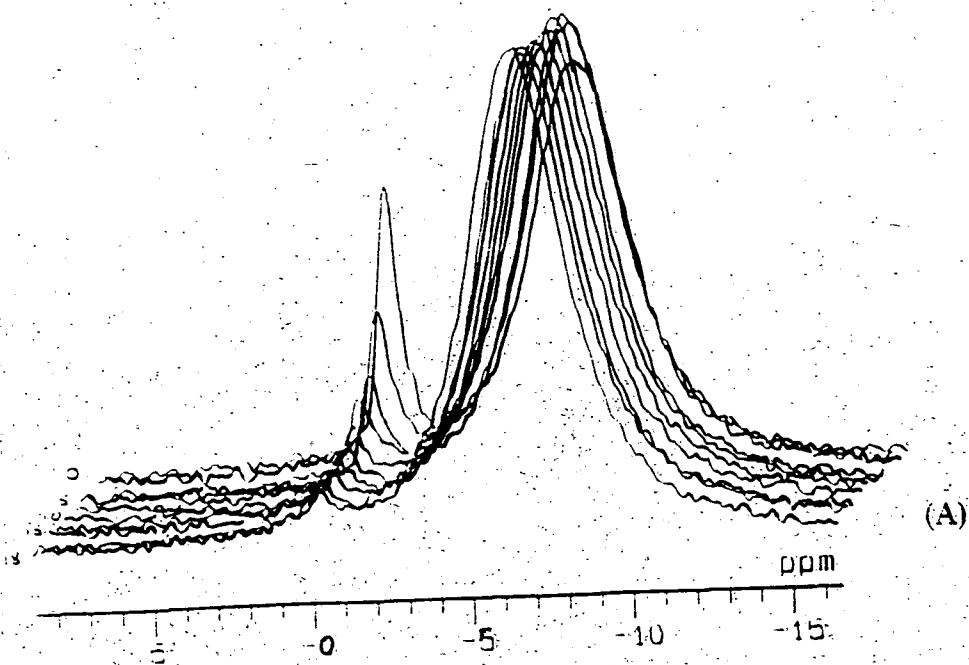
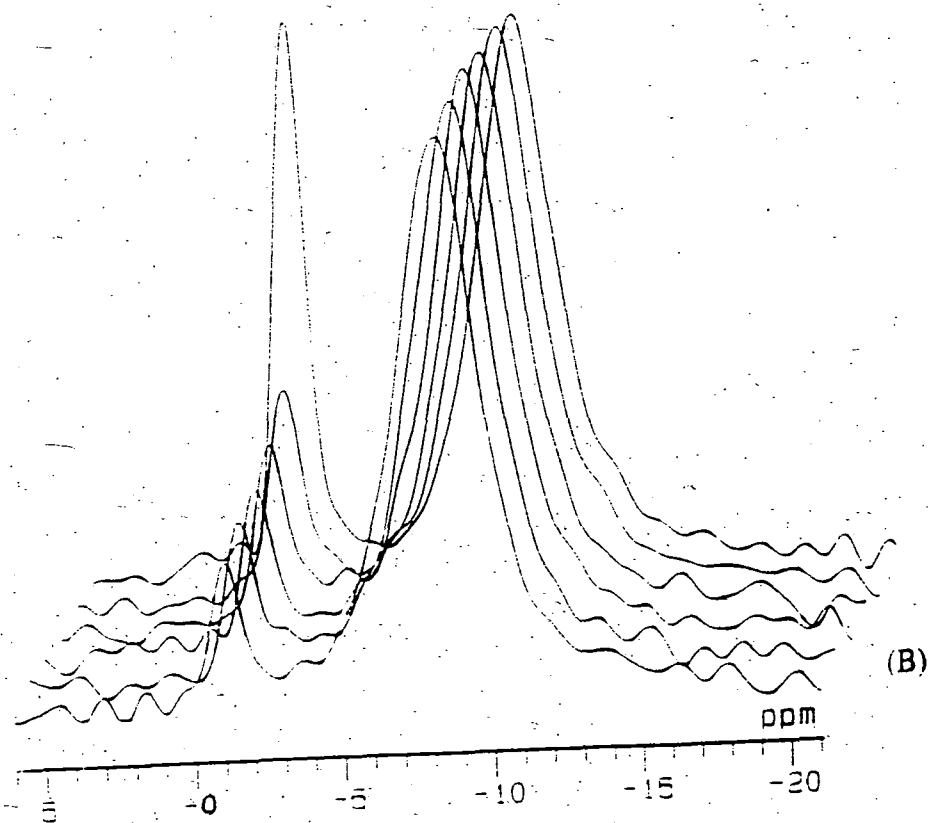


Figure 5.6: Stacked spectra from  $^{31}\text{P}$  NMR of TEP following the adsorbate competition for 18 hours as 40% w/w TEP is added to a carbon substrate with 40%  $^2\text{H}_2\text{O}$  pre-adsorbed. Spectra (A) shows the ASZM carbon, and spectra (B) shows the SC2 carbon. Time indicated in hours.

hours. The stacked plots for the  $^{31}\text{P}$  NMR data for each carbon are shown in figure 5.6. The time since the addition of the second adsorbate is indicated on the figure.

Figure 5.7 is a graph of the peak intensities for the competition reaction as a function of time for the ASZM carbon. The  $^{31}\text{P}$  NMR data are included on the same graph to compare the adsorbate's behaviour with the graph in figure 5.3, showing the corresponding data for the SC2 carbon. The  $^{31}\text{P}$  data show that the narrow peak at -1 ppm decreases in intensity exponentially as a function of time. The broad peak increases in intensity over the same period of time. This pattern applies for both types of carbon.

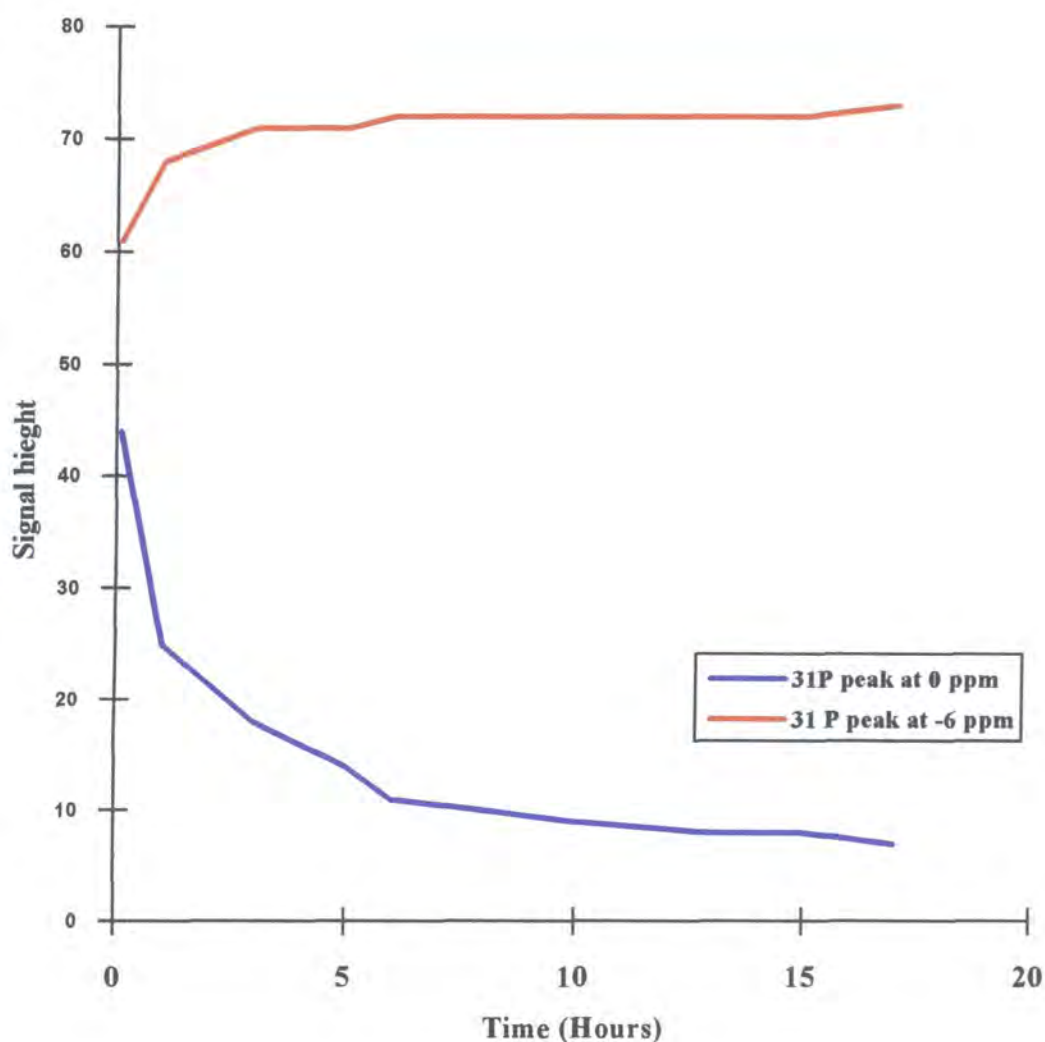


Figure 5.7. Graph showing the relative  $^{31}\text{P}$  NMR peak heights for 18 hours after the addition of 40% w/w TEP to the ASZM carbon with 40% w/w  $^2\text{H}_2\text{O}$  pre-adsorbed.

### 5.2.2 Pre-adsorbed TEP

The second section describes experiments using samples with 60% TEP pre-adsorbed onto the SC2 dry carbon substrate. The sample was left to equilibrate for one hour, and then the  $^{31}\text{P}$  spectra were run. The sample then had 40% w/w  $^2\text{H}_2\text{O}$  added, after which it was transferred to the NMR insert. The first competition spectrum was run 1 minute after the addition of the second adsorbate. Each  $^{31}\text{P}$  spectrum had 16 transients with a pulse delay of 1 s. The spectra were run once every minute for the next 2 hours. The  $^2\text{H}$  NMR spectra were taken in a subsequent experiment using a sample prepared in the same manner. The  $^2\text{H}$  spectra were run using 4 transients and a 1 s pulse delay. Once again the spectrum was run one minute after the addition of the second adsorbate and every minute subsequently for 2 hours.

Figure 5.8 shows the  $^{31}\text{P}$  spectrum before the addition of the second adsorbate compared to the first spectrum taken after 2 minutes in the competition reaction. The spectra show that when there is only TEP adsorbed on the carbon then the narrow peak at -8 ppm is larger than the broad peak at -1 ppm. However just two minutes after the addition of the  $^2\text{H}_2\text{O}$  then the spectrum changes, with the narrow peak at -1 ppm becoming the same height as the broad peak. The spectra are on the same scale and the total area under the peaks in each remains the same. This means that the TEP is re-distributed within the carbon and not lost to the atmosphere.

Figure 5.9 is a graph of the peak intensities for the competition reaction as a function of time. The  $^{31}\text{P}$  and  $^2\text{H}$  NMR data are included on the same graph to compare the behaviour of the two adsorbates. The  $^{31}\text{P}$  data show that the narrow peak at -1 ppm decreases in intensity as a function of time. The broad peak increases in intensity over the same period of time. The  $^2\text{H}$  NMR data show the narrow peak at 0 ppm decreasing in intensity over the 2 hours, and the broad peak also becoming smaller. This suggests that some  $^2\text{H}_2\text{O}$  is lost in the experiment, but that is not the case because the broad peak becomes wider. The height decreases but the area under the peak actually increases.



### Durham CMX200H-NMR System

60% TEP on SC2 carbon spectrum run 5 mins after 40% D2O was added  
single pulse Bloch Decay

ppfn=1pulse  
cdir=react8  
cfn=tepd2osc2  
cfd=0  
sf1=81.019167 MHz  
sw=50 KHZ  
ad=15 usec  
a1=512 cplx  
aqt=10.241 msec  
dw=20 usec  
extm=1.0103 sec  
p=157 deg  
pd=1 sec  
pw=8 usec  
rd=15 usec  
ac=16 scns

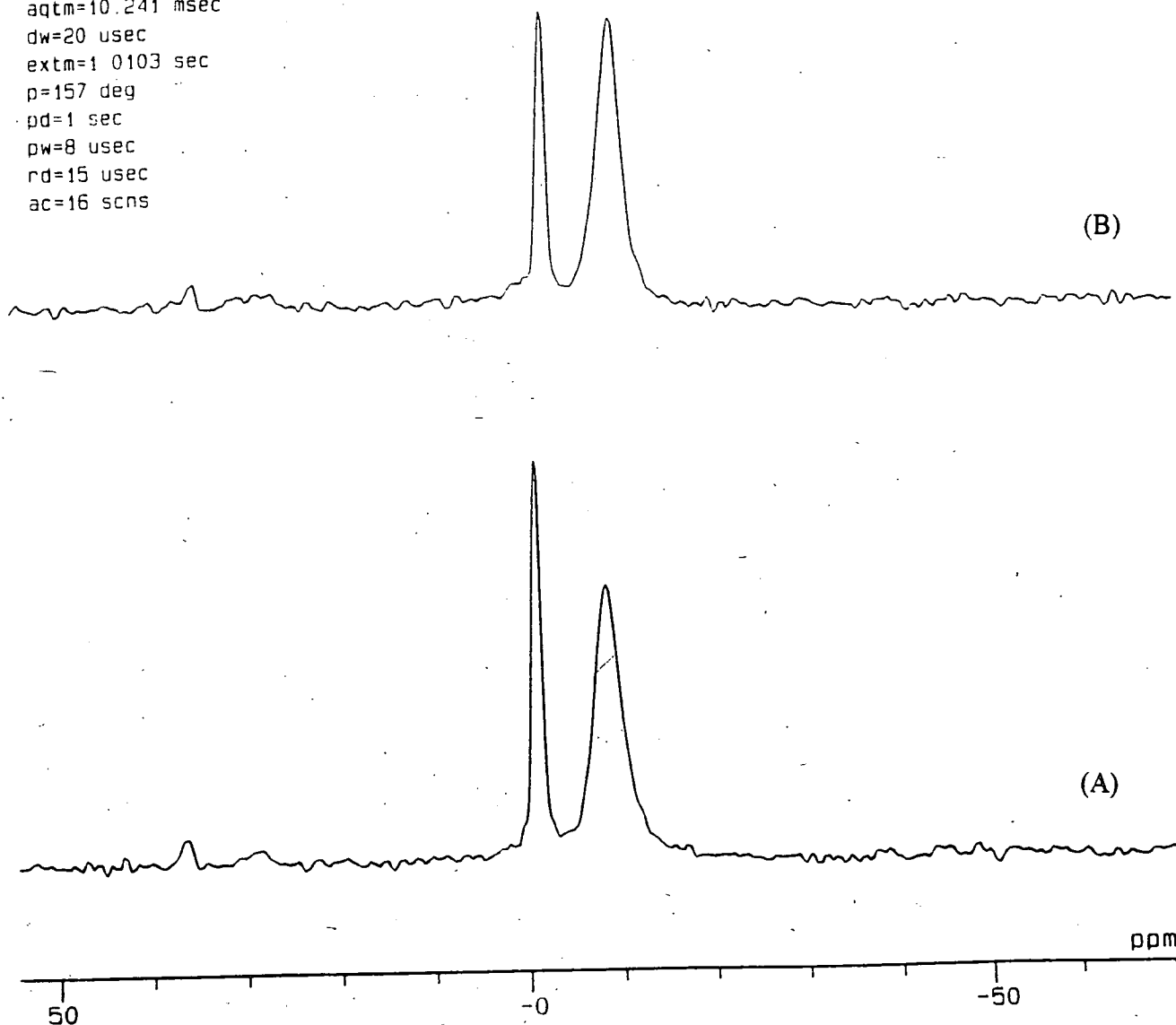


Figure 5.8.  $^{31}\text{P}$  spectra of (A) SC2 with just 60% w/w TEP adsorbed and (B) 2 minutes after 40% w/w  $^2\text{H}_2\text{O}$  was added to the sample.

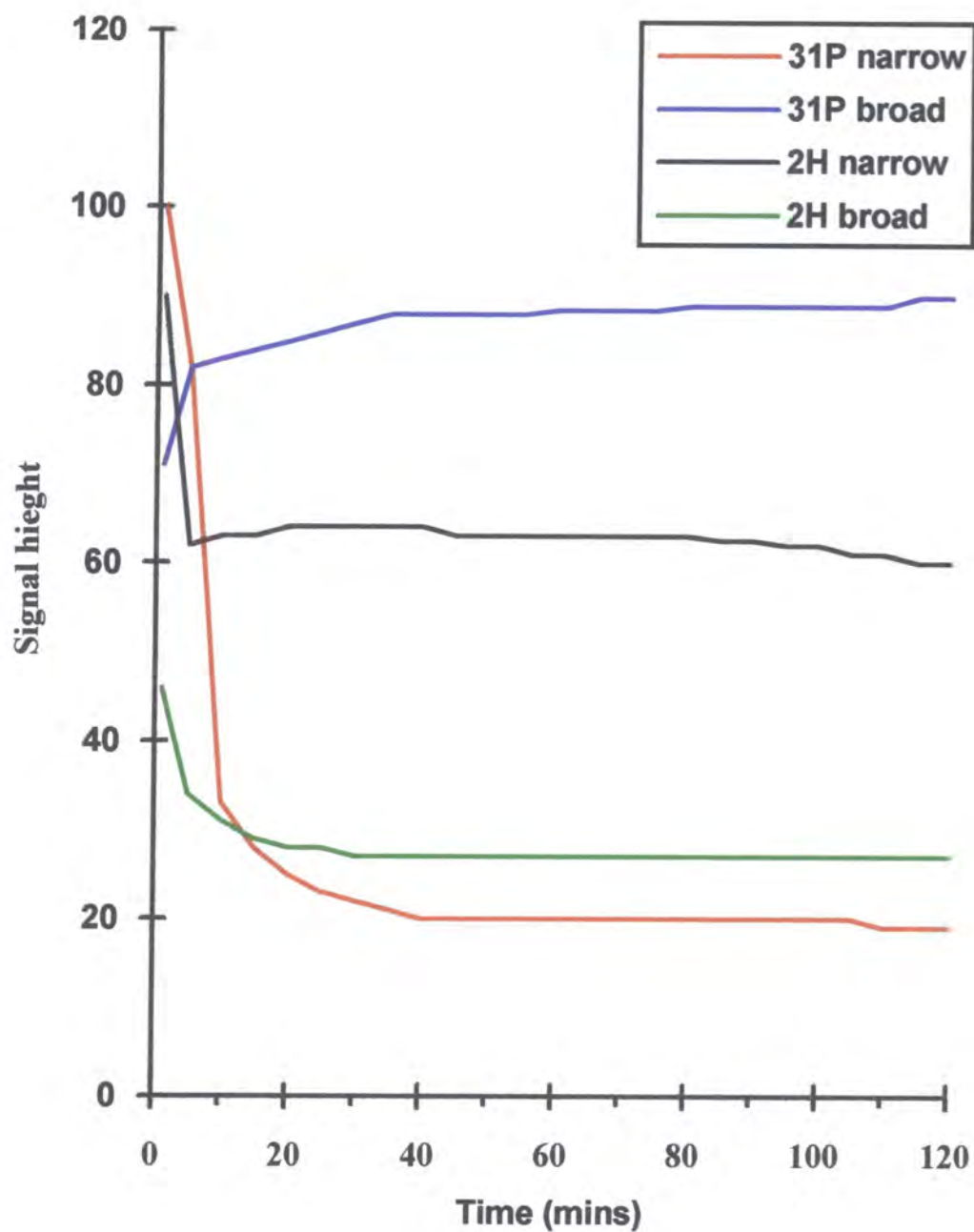


Figure 5.9. Graph showing the relative  $^{31}\text{P}$  and  $^2\text{H}$  NMR peak heights for 2 hours after the addition of 40% w/w  $^2\text{H}_2\text{O}$  to the SC2 carbon, with 60% w/w TEP pre-adsorbed.

The second part to the pre-adsorbed TEP section describes experiments using samples with 60% TEP pre-adsorbed onto the SC2 dry carbon substrate. The sample was left to equilibrate for one hour, and then the  $^{31}\text{P}$  spectra were run. The sample then had 40% w/w  $^2\text{H}_2\text{O}$  added, after which it was transferred to the NMR insert. The first competition spectrum was run 1 minute after the addition of the second adsorbate. Each  $^{31}\text{P}$  spectra had 16 transients with a pulse delay of 1 s. The spectra were run once every minute for the next 21 hours. The  $^2\text{H}$  NMR spectra were taken in a subsequent experiment using a sample prepared in the same manner. The  $^2\text{H}$  spectra were run using 16 transients and a 1 s pulse delay. Once again the spectrum was run one minute after the addition of the second adsorbate and every minute subsequently for 21 hours. This experiment was used to see if there were any changes in the spectra over a longer time period.

Figure 5.10 is a graph of the peak intensities for the competition reaction as a function of time. The  $^{31}\text{P}$  NMR data are plotted on the same graph to show the behaviour of the TEP over the 21-hour period. The  $^{31}\text{P}$  data show that the narrow peak at -1 ppm decreases in intensity as a function of time. The broad peak increases in intensity over the same period of time. There seems to be little variation in the narrow peak intensity after 2 hours, but the broad peak height continues to increase over the 21 hour period.

Figure 5.11 shows the stacked plot of the  $^2\text{H}$  NMR data for the 21 hour experiment. The time after the addition of the second adsorbate is indicated in hours on the figure. The narrow peak at 0 ppm decreases in intensity quickly over the first 20 minutes and then decreases more slowly for the next 21 hours. The broad peak at -8 ppm is quite small in comparison to the narrow peak, and the intensity appears to decrease over the 21 hour competition period.

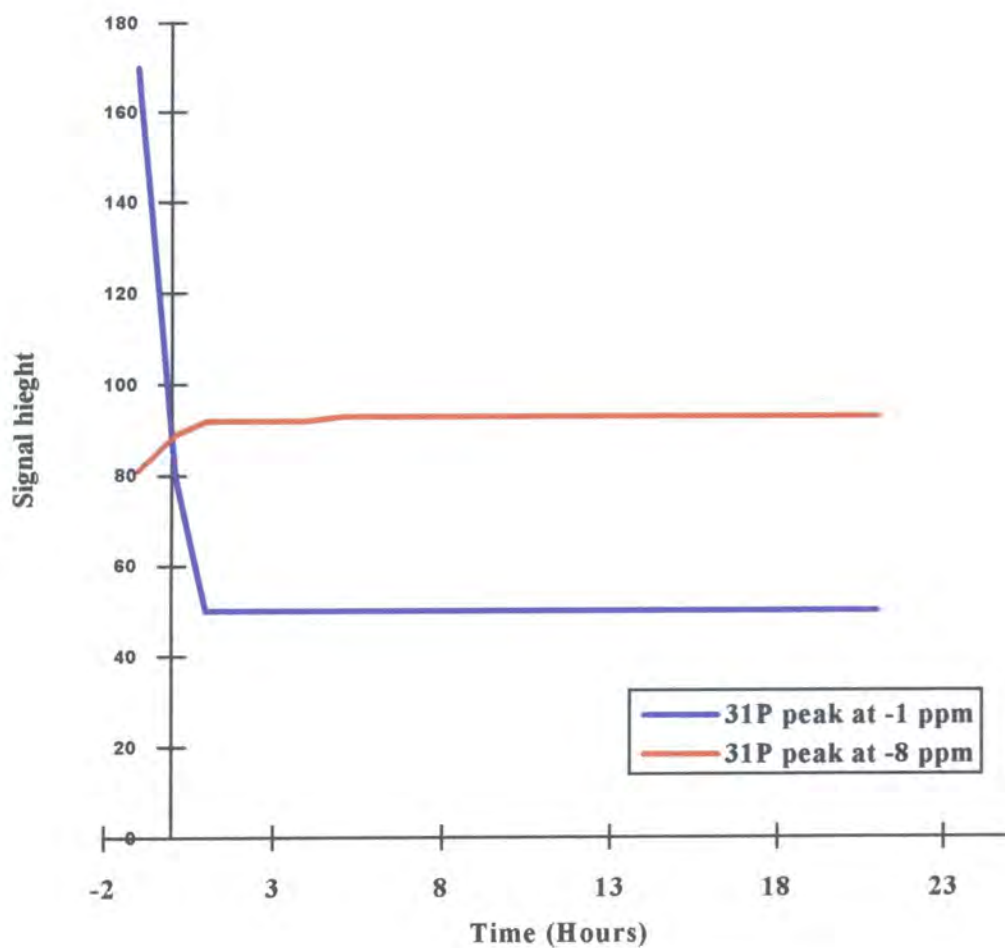
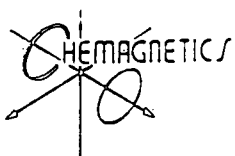


Figure 5.10. Graph showing the relative  $^{31}\text{P}$  NMR peak heights for 21 hours after the addition of 40% w/w  $^2\text{H}_2\text{O}$  to the SC2 carbon with 60% w/w TEP pre-adsorbed



# Durham CMX200H-NMR System

TEP and D2O competition reaction sampled every 5 minutes

single pulse Bloch Decay

ppfn=1pulse

cdir=react9c

cfm=1

cfp=0

sf1=30.72201 MHz

sw=50 KHz

ad=15 usec

al=8k cplx

aqtm=163.84 msec

dw=20 usec

extm=1.1639 sec

p=157 deg

pd=1 sec

pw=6 usec

rd=15 usec

ac=16 scns

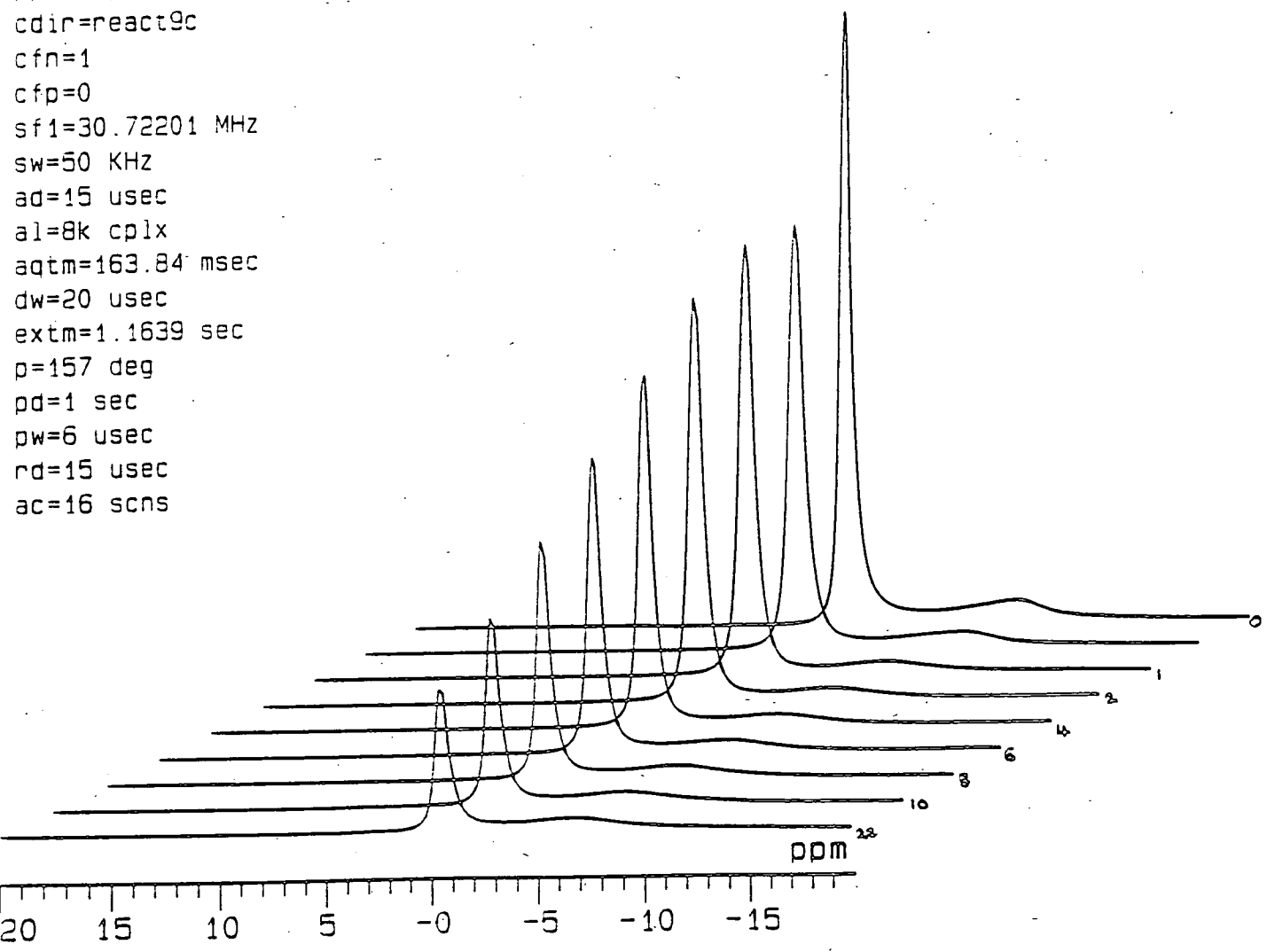


Figure 5.11. Stacked spectra from <sup>2</sup>H NMR of <sup>2</sup>H<sub>2</sub>O following the adsorbate competition for 24 hours as 40% w/w <sup>2</sup>H<sub>2</sub>O is added to SC2 carbon with 60% w/w TEP pre-adsorbed. Time indicated in hours.

Figure 5.12. shows a graph of the peak heights for the  $^2\text{H}$  NMR data over the 21-hour period of the competition reaction.

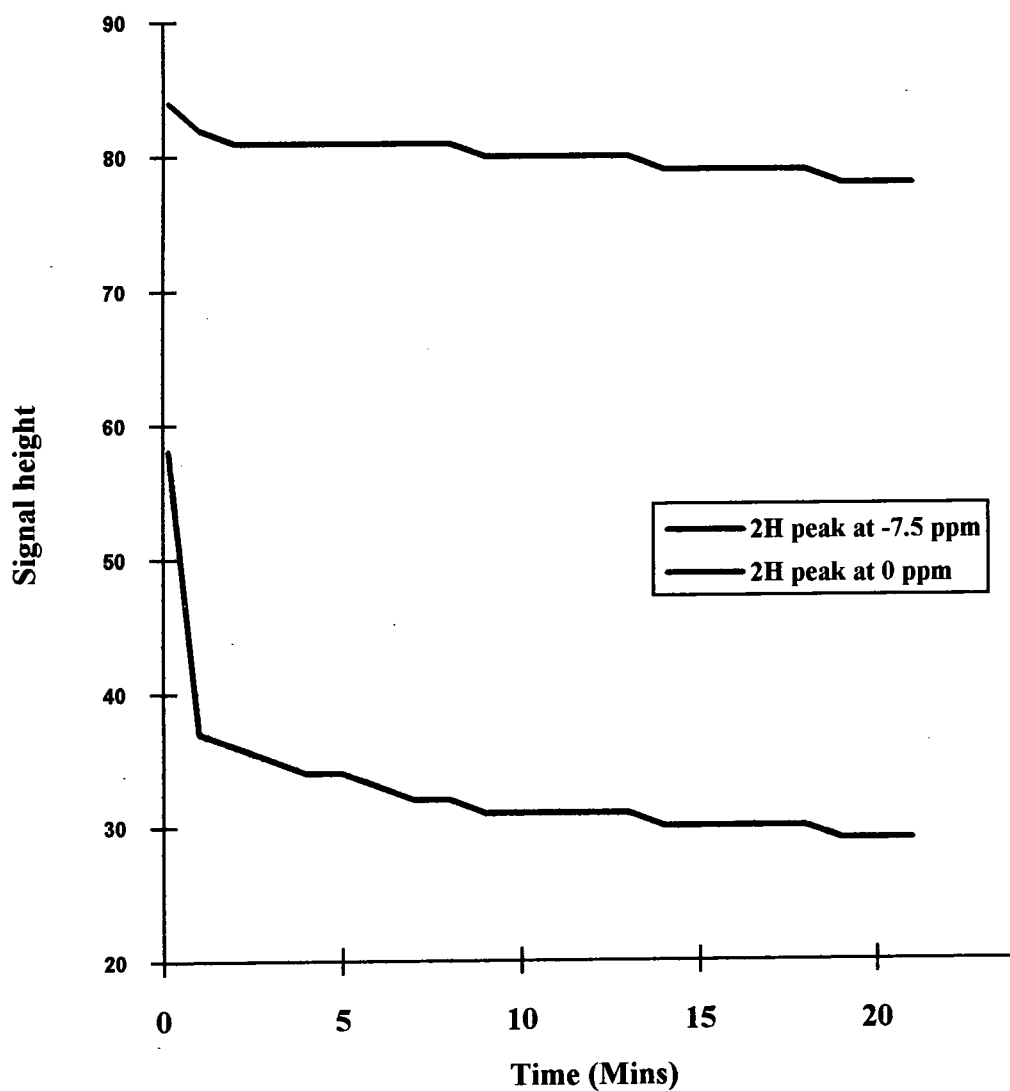


Figure 5.12. Graph showing the relative  $^2\text{H}$  NMR peak heights for 24 hours after the addition of 40% w/w  $^2\text{H}_2\text{O}$  to the SC2 carbon with 60% w/w TEP pre-adsorbed

The analysis of the broad  $^2\text{H}$  NMR peak at  $-7.5$  ppm needs to be very carefully carried out. The peak height seems to decrease, but the area under the line actually increases. Figure 5.13 also shows that the chemical shift of the  $^2\text{H}$  NMR broad peak changes dramatically through the experiment. The chemical shift changes from  $-8.5$  ppm to  $-6.5$  ppm over the 21 hours. This may provide further information about the competition between the two adsorbates.

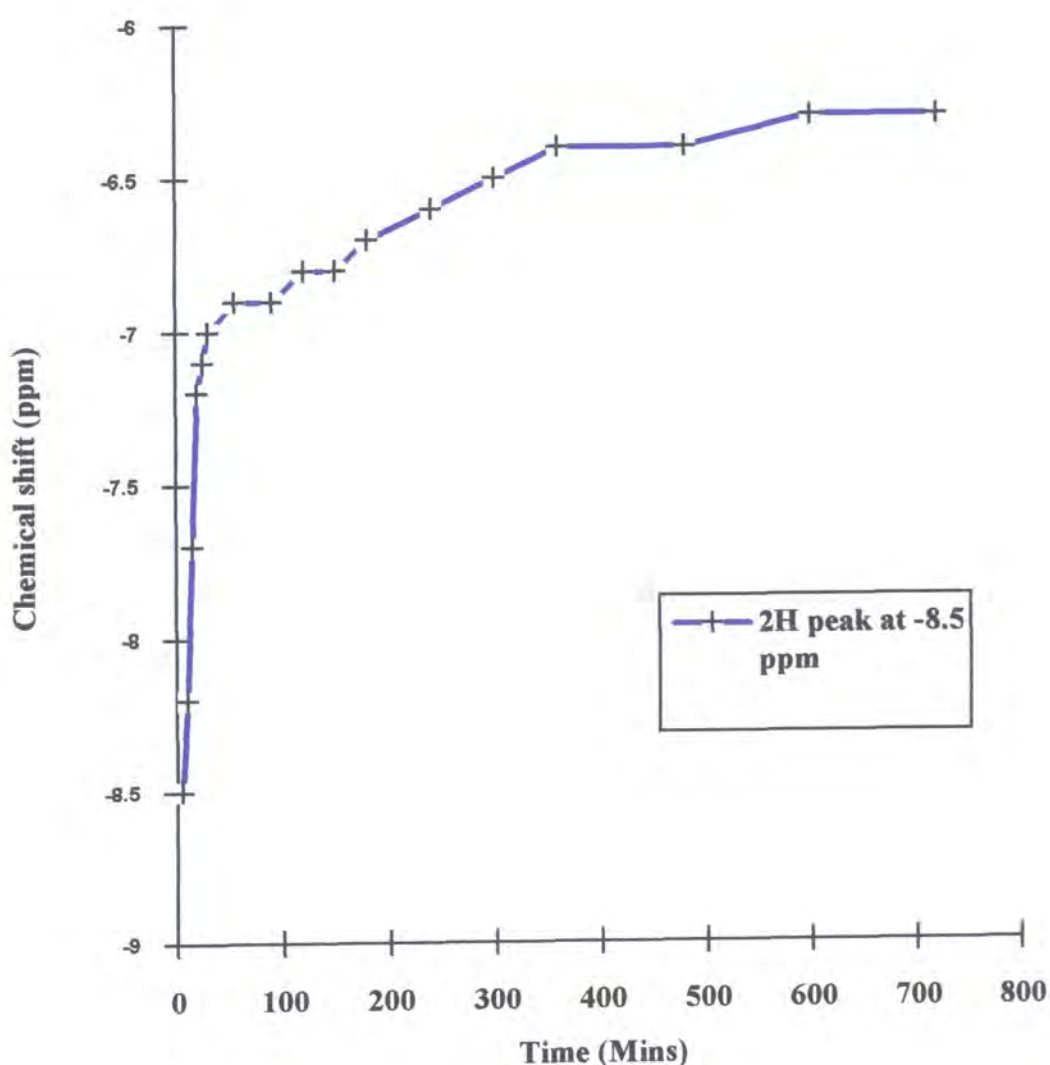


Figure 5.13. Graph showing the  $^2\text{H}$  NMR chemical shift of the broad peak, associated with  $^2\text{H}_2\text{O}$  adsorbed in the micropores, for 24 hours after the addition of 40% w/w  $^2\text{H}_2\text{O}$  to the SC2 carbon with 60% w/w TEP pre-adsorbed

### 5.3 Discussion

The phosphate competition experiments with pre-adsorbed  $^2\text{H}_2\text{O}$  on the activated carbon substrate give a good simulation of respirator canister use in an atmosphere challenged with a nerve agent. Figure 5.2 shows that in the initial 2 minutes of the adsorption of the phosphate, the adsorbed  $^2\text{H}_2\text{O}$  changes environment drastically. The  $^2\text{H}$  NMR spectra show that the  $^2\text{H}_2\text{O}$  will adsorb into the micropores of the carbon ( $\delta_{2\text{H}}$  -8 ppm) when there is no adsorption competition. When the TEP is introduced then the  $^2\text{H}_2\text{O}$  very quickly moves into the macropore/external surface environment, giving a peak at 0 ppm. Some of the  $^2\text{H}_2\text{O}$  stays in the broad peak associated with the micropores. This could compromise molecules adsorbed in pores too small for the TEP molecules to exchange with the  $^2\text{H}_2\text{O}$ , together with  $^2\text{H}_2\text{O}$  trapped in pores by adsorbed TEP.

The stacked plot for the competition reaction shown in figure 5.1 shows more information about the adsorbate competition. The  $^{31}\text{P}$  NMR data show evidence of a further exchange process taking place over a longer time period. The graph in figure 5.3 gives evidence of the  $^{31}\text{P}$  narrow peak at -1 ppm decreasing in intensity exponentially over the 24 hour experiment time. The exponential time constant shows that half the molecules in the external surface sites, move into the micropores at a half-life constant of 4.5 hours. The phosphate molecules adsorbed in the external surface or macropore environment only move gradually into the micropores via this secondary diffusion controlled process. This evidence is supported by the corresponding increase in the  $^{31}\text{P}$  broad peak at -7 ppm over the same time period. The increase in the height of the broad peak is small compared to the loss of height of the narrow peak, which is expected as the total area for both peaks has to remain constant in a sealed system. The  $^2\text{H}$  NMR data over the same period show that after the initial large increase in the narrow peak there is a second slower increase during the next twenty four hours. This is consistent with more  $^2\text{H}_2\text{O}$  moving out of the micropores to the macropore/ external surface environment.

The NMR data following the two adsorbates for the 24-hour experiment give mutually supportive evidence. The vast majority of the adsorbed water which is initially in the micropores moves into the macropore environment during the first two minutes of the addition of the TEP. Over the next twenty-four hours more  $^2\text{H}_2\text{O}$  moves slowly from the micropores into the mesopores. This process is probably diffusion-controlled. The corresponding  $^{31}\text{P}$  data from the TEP molecules show TEP preferentially adsorbed in the micropores, and the majority are adsorbed there after two minutes of competition. The TEP adsorbed in the macropores or on the external surface gradually moves into the micropores over the twenty four hours via the diffusion-controlled process exchanging with the  $^2\text{H}_2\text{O}$  adsorbed there.

The experiment using ASZM carbon and the larger PP phosphate gave very similar results to the TEP phosphate and SC2 carbon. The larger phosphate has fewer molecules adsorbed in the micropores because the molecules will not fit into the smaller micropores. The second, slower exchange process occurs at a slower rate than for the TEP and has not finished after 24 hours. This is expected as the larger molecules will take longer in a diffusion controlled process.

The experiment comparing the competition with TEP on the SC2 and ASZM carbons gives exactly the same results for both carbon types. The carbons are similar in structure and both have a large micropore and mesopore volume, and should not provide any conflicting competition evidence.

The experiments with pre-adsorbed TEP gave some further evidence about the competition for adsorption sites within the carbon samples. Surprisingly, the addition of  $^2\text{H}_2\text{O}$  to the system does affect the adsorbed TEP. Figure 5.8 shows that the 60% w/w TEP adsorbed on its own shows two peaks with the narrow peak at -1 ppm larger than the broad peak at -8 ppm. After the addition of 40%  $^2\text{H}_2\text{O}$  the two peaks have the same peak height. This suggests that some TEP molecules, originally adsorbed in the macropores, move into micropores that previously were not able to adsorb them.

Figure 5.9 shows that over the first two hours the  $^{31}\text{P}$  NMR broad peak increases in intensity quickly for the initial 10 minutes and then more slowly for the rest of the two-hour period. The narrow peak at -1 ppm decreases in intensity accordingly. This suggests that more of the TEP can be adsorbed in the micropores when  $^2\text{H}_2\text{O}$  is present.

The  $^2\text{H}$  NMR shows that the narrow peak at 0 ppm decreases in intensity initially then increases from 10 minutes to 50 minutes and then falls away again. The broad peak seems to decrease in intensity over the first 40 minutes of the competition reaction. There is, however, no loss of  $^2\text{H}_2\text{O}$  because the broad peak becomes wider, so that the total area under the two peaks remains constant. The results are complicated, and the  $^2\text{H}_2\text{O}$  seems to be influenced by a cooperative process. Initially some of the  $^2\text{H}_2\text{O}$  is adsorbed into the micropores that will not accept the TEP. Then some TEP adsorbed in the macropores or on the external surface, seems to be adsorbed into those micropores, exchanging with some of the newly adsorbed  $^2\text{H}_2\text{O}$ . This would cause a rapid decrease in the intensity of the  $^2\text{H}$  NMR narrow peak, followed by a small increase. This is supported by the increase in the amount of TEP adsorbed in the micropores. The ensuing further decrease in the  $^2\text{H}$  NMR narrow peak is caused by a separate process shown in the 24-hour experiment.

Figure 5.11 shows that after the 2 hour period the  $^2\text{H}$  NMR narrow peak decreases in intensity consistently over the next 22 hours. This process is explained by looking at the  $^2\text{H}$  NMR broad peak. The peak height drops but the peak becomes broader. Figure 5.13 plots the chemical shift of the broad peak as a function of time over the competition period. The chemical shift moves from -8.5 ppm to -6.5 ppm. This is consistent with the average size of the occupied pores increasing. The  $^2\text{H}_2\text{O}$  is adsorbed in the large micropores and mesopores in the carbon that will not adsorb TEP. The water molecules initially, over the first 40 minutes, do seem to help adsorb some extra TEP in these pores. The larger pores only adsorb TEP when  $^2\text{H}_2\text{O}$  molecules are present, and the adsorption process is quite slow.

#### 5.4. Conclusions

The experiments show that it is possible to observe some competition among adsorbates for the different adsorption centres in the carbon. Standard approaches such as gravimetric analysis yield no information about competition or adsorbate exchange within a sample. NMR is unique in its capability to directly observe the adsorbates and yield meaningful data about non-equilibrium systems.

The NMR results prove that the TEP is preferentially adsorbed into micropores and displaces  $^2\text{H}_2\text{O}$  in a two step process. NMR can observe this process and follow both adsorbates as they exchange. Furthermore the NMR results suggest that  $^2\text{H}_2\text{O}$  has a role in co-operative adsorption of the TEP into larger micropores and possibly mesopore sites in the carbon. The NMR data could be used to determine some kinetic data and total adsorption volumes for various phosphate molecular sizes.

## Chapter 6 Relaxation results

### 6.1. Hahn-echo experiments

The transverse relaxation time  $T_2$  is a measure of relaxation in the  $xz$ - and  $yz$ -planes. The relaxation arises from direct interactions between the spins of different nuclei without energy transfer to the lattice. The enthalpy of the spin system remains constant, but the entropy increases via the transverse relaxation process. The natural linewidth of a frequency domain signal is related to the decay rate of the transverse magnetization (for a perfectly homogeneous magnetic field). The transverse magnetization is represented by the FID measured in the time domain. The transverse relaxation time in the absence of inhomogeneous line broadening effects is given by equation 6.1.

$$\Delta_{1/2} = 1/(\pi T_2)$$

Equation 6.1.

This section describes an experiment set up to look at the broad peak observed in the  $^2\text{H}$  and  $^{31}\text{P}$  NMR spectra associated with the adsorption in the micropores. The  $T_2$  experiment will differentiate between peaks with different natural linewidths and help to prove whether the broad peak does consist of overlapping peaks.

When a  $90^\circ$  pulse is applied along the  $x$  axis then the entire magnetisation is transferred to the  $y$  axis. The magnetisation can relax because of inhomogeneity in the external field and because of interaction processes in the system. The Hahn-echo experiment refocusses the effect of any inhomogeneity in the external field so that only  $T_2$  relaxation processes can be causing the magnetisation's decay. The interaction processes cause the spins to exchange energy with each other. These interactions in the solid-state could be dipolar coupling between nuclear magnetic moments, magnetic coupling of electrons to the nuclei and quadrupolar coupling. In the solution-state the rapid molecular motion causes local variations in the field about the nucleus, aiding relaxation. Chemical exchange also causes the system to relax because if an atom moves from one chemically distinguishable site to another, carrying with it a nuclear

spin, and is replaced with an atom with a similar spin, the new precession phase is random and will not be refocused.

Spins in different parts of the sample precess at different rates, so individual isochromats spread out in the  $xy$  plane as shown in figure 6.1(B). These can be refocussed, but the true transverse relaxation results in a dephasing of the coherent superposition of the transverse magnetisation with a time function that can be measured.

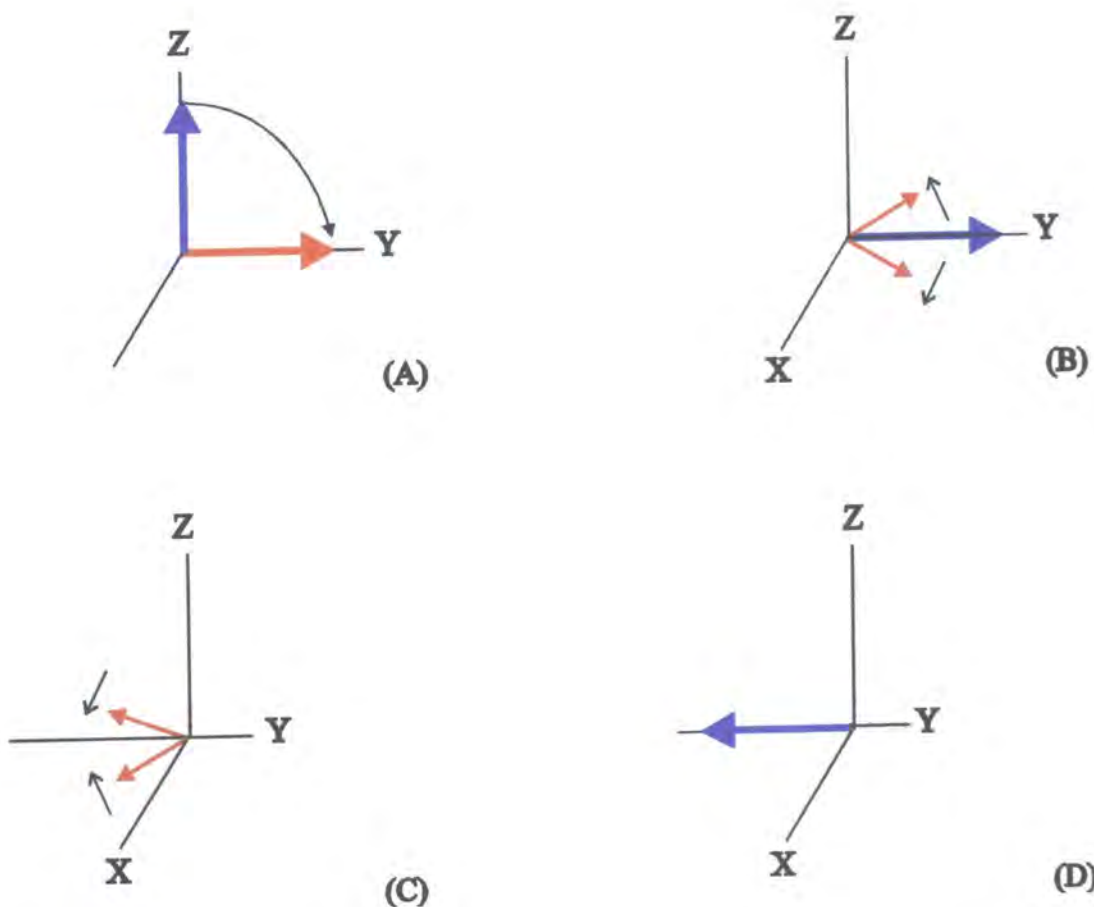


Figure 6.1. Dephasing of transverse magnetisation in the rotating frame. (A) the action of a  $90^\circ$  pulse. (B) behaviour of the different isochromats of transverse magnetisation before and (C) after the  $180^\circ$  pulse. (D) Formation of the spin-echo.

The Hahn spin-echo experiment, shown in figure 6.2, consists of a  $90^\circ$  pulse followed by a variable time period,  $\tau$ , to allow the spins to de-phase. A  $180^\circ$  pulse moves the magnetisation into the  $-zy$  plane, and is then followed by another time

period  $\tau$  allowing the spins to refocus. This re-phasing causes a spin-echo signal shifted in phase to the initial FID by  $180^\circ$ . The spin-echo has a reduced intensity due to transverse relaxation and not due to magnetic field inhomogeneities that typically cause a FID to decay. The magnetic field inhomogeneities are re-focused, so no intensity is lost from them.

The FID is recorded at the end of the second time period  $\tau$ . The amplitudes of the Fourier transformed resonance lines are reduced by a factor of  $\exp(-2\tau/T_2)$ . It is also valid to measure the maximum of the FID as a function of the dephasing time  $\tau$ . The experiment is repeated with various values of  $\tau$ , and the  $T_2$  value calculated by plotting the  $\ln$  signal against  $2\tau$ . The slope of the graph is equal to  $-1/T_2$ .

#### Hahn-echo sequence

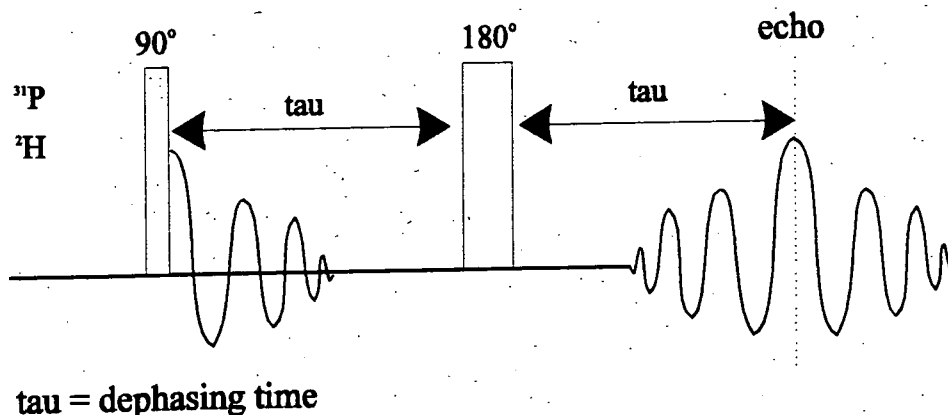


Figure 6.2. Schematic diagram of the Hahn-echo pulse sequence.

#### 6.2. Experimental method

The NMR experiment was run on the CMX 200 spectrometer with the 7.5mm pencil rotor MAS probe. The  $^{31}\text{P}$  and  $^2\text{H}$  NMR experiments were run using the same procedure but at each specific frequency. Initially the single-pulse experiment was set up in the normal manner with close attention to calibrating the  $90^\circ$  pulse duration accurately. This is awkward to do as explained previously so a separate pulse programme called Fullecho was written to help the Hahn-echo experiment. The Fullecho pulse programme records the magnetisation straight after the  $180^\circ$  pulse until

the echo has fully decayed. This enables the experimentalist to observe the build up of the echo and hence accurately determine the maximum echo amplitude. This was necessary because pulse sequence imperfections mean that the echo maximum does not necessarily occur exactly one tau period after the  $180^\circ$  pulse. The Fullecho results were used to obtain maximum echo amplitude values used in the plots for determining  $T_2$  values. The samples were spun at 4.0 kHz, with 256 transients and a pulse delay of 2 seconds. The tau values varied between experiments and are included in the results section.

The 'Hahnecho' pulse-programme was used after the position of the maxima was determined using the Fullecho sequence. The Hahnecho sequence recorded the FID starting at a time tau after the  $180^\circ$  pulse. This FID observed the echo decay, and allowed Fourier transform spectra to be obtained showing how the peaks changed with increasing values of the dephasing time tau.

The phosphate experiments looked at the SC2 carbon with loads of 20%, 40% and 60% w/w of TEP. The deuterium experiment looked at SC2 sample with 40% and 60%w/w of  $^2\text{H}_2\text{O}$ . The results are presented in the following section.

### 6.3. Results

The first experiment looked at the sample of SC2 with 20% w/w TEP adsorbed on it. The 'Fullecho' FID was recorded for tau values between 0.5 ms and 5ms. Figure 6.3 shows the plot of the ln of the maximum echo height against  $2x$  tau. The slope of the line enabled  $T_2$  to be calculated using equation 2.2.

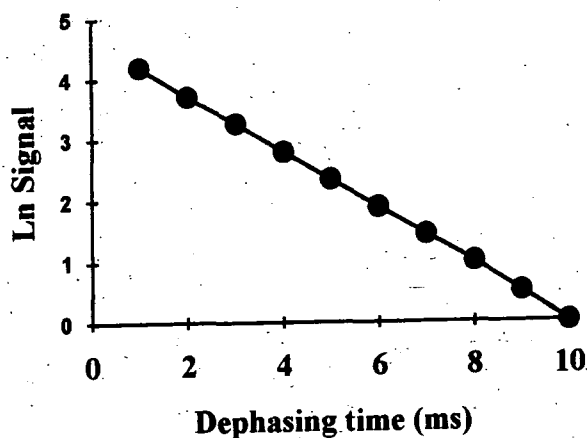


Figure 6.3. Graph of the Ln signal vs dephasing time  $\tau$  for  $^{31}\text{P}$  NMR spectra of SC2 with 20% TEP.

The calculated value of  $T_2$  is  $2.4 \pm 0.1$  ms. The plot of the Ln Signal against dephasing time gives one line suggesting that the broad peak consists of just one peak for the sample with 20% w/w TEP. The natural linewidth calculated using equation 6.1. is 138 Hz.

Figure 6.3.1 shows a plot of the actual linewidth of the Fourier transformed spectra for the same sample as a function of the dephasing time  $2x$  tau.

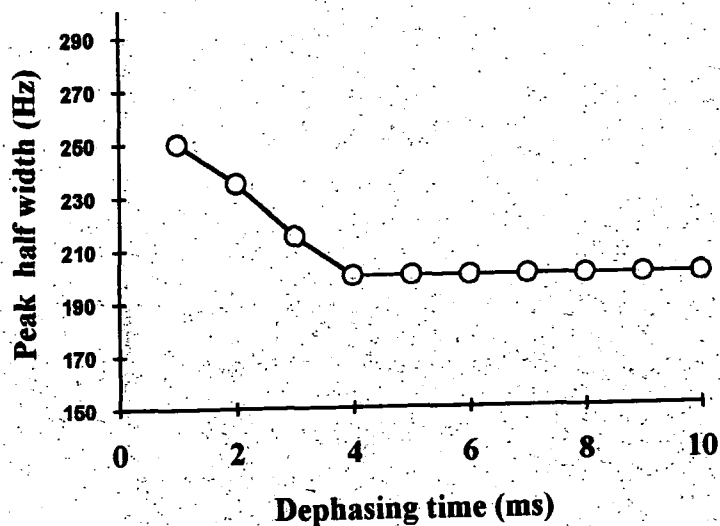


Figure 6.3.1: Graph of the  $^{31}\text{P}$  NMR spectra broad peak width as a function of dephasing time  $2x$  Tau.

The fact that the linewidth reduces as the tau value increases up to 2ms, suggests that some of the line broadening is heterogeneous and therefore not re-focused in the Hahn-echo experiment. This indicates a dispersion of sites with different widths but figure 6.3 does not show any evidence of a multicomponent relaxation. This may be because the tau values used only went up to 10 ms. The extrapolated value of the observed linewidth from figure 6.3.1 gives 198 Hz which is larger than the natural linewidth value of 138 Hz calculated from the T2 of 2.4 ms. The observed linewidth is presumably broadened because of a dispersion of chemical shifts with similar widths.

The second sample to be analysed was the SC2 with 40% w/w TEP adsorbed on to it. Figure 6.4 shows the corresponding plot of the natural log of the maximum echo height against the dephasing time  $2x$  tau. The tau values range from 0.5 ms to 20 ms.

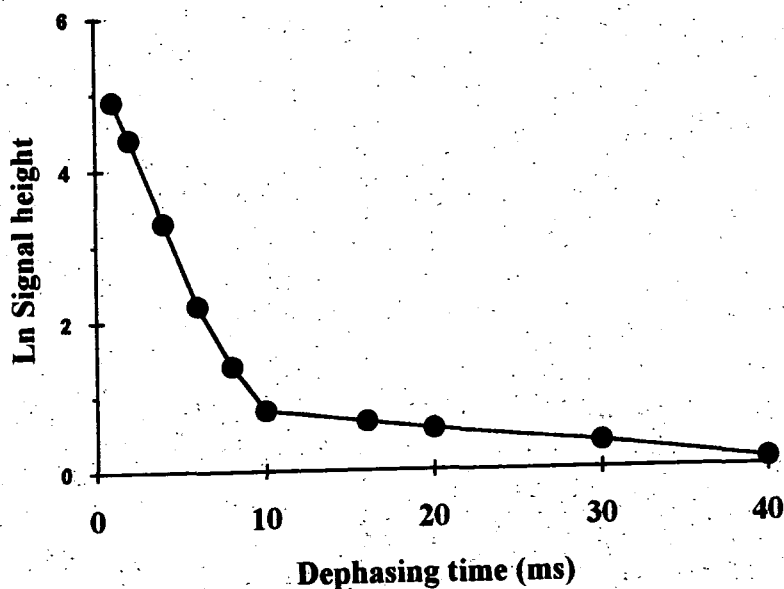


Figure 6.4. Graph of the Ln Signal against dephasing time  $2x$  tau for the  $^{31}\text{P}$  Spectra of SC2 carbon with 40% TEP.



# Durham CMX200H-NMR System

Hahn spin echo experiment  
pprn=Hanneco  
cdir=t2sc2tep  
crn=121194sp.3  
cip=3  
sf1=81.013542 MHz  
sw=50 KHZ  
a1=200  
a1=512 cplx  
aqt=10.241 msec  
dw=20 usec  
extm=1.0263 sec  
p=271 deg  
pd=1 sec  
pw=6 usec  
pw2=12 usec  
rd=15 usec  
tau=8 msec  
ac=256 scns

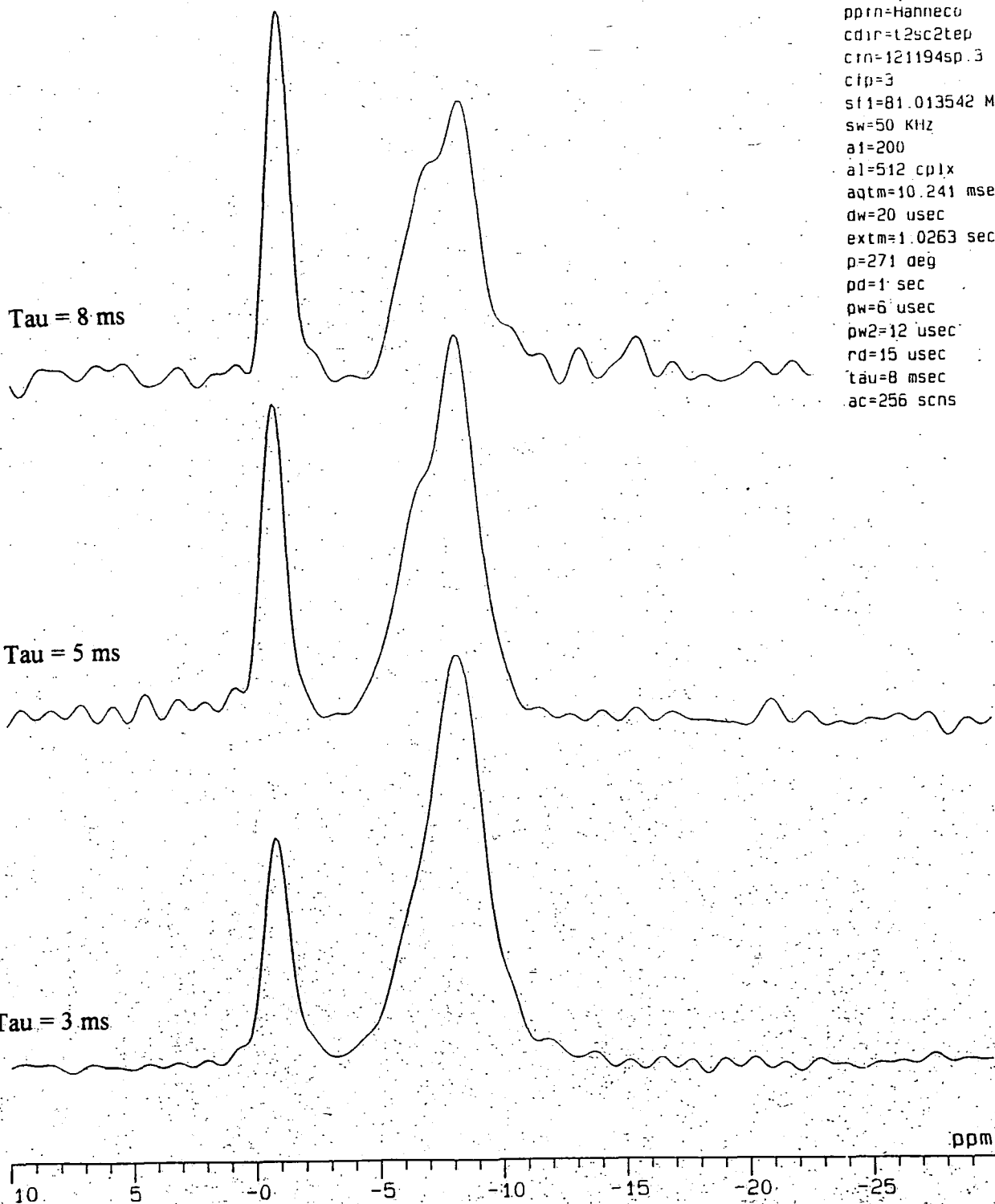


Figure 6.5. Fourier transformed Hahn-echo experiment on SC2 with 60% w/w TEP with the tau values indicated.



Durham CMX200H-NMR System

60% TEP on SC2 dry  
Hahn spin echo experiment

ppin=Hanneco

cdir=t2sc2tep

cfi=121194sp.3

cfp=6

sf1=81.013542 MHz

sw=50 KHz

a1=200

a1=512 cplx

aqtm=10.241 msec

dw=20 usec

extm=1.0503 sec

p=271 deg

pd=1 sec

pw=6 usec

pw2=12 usec

rd=15 usec

tau=20 msec

ac=256 scns

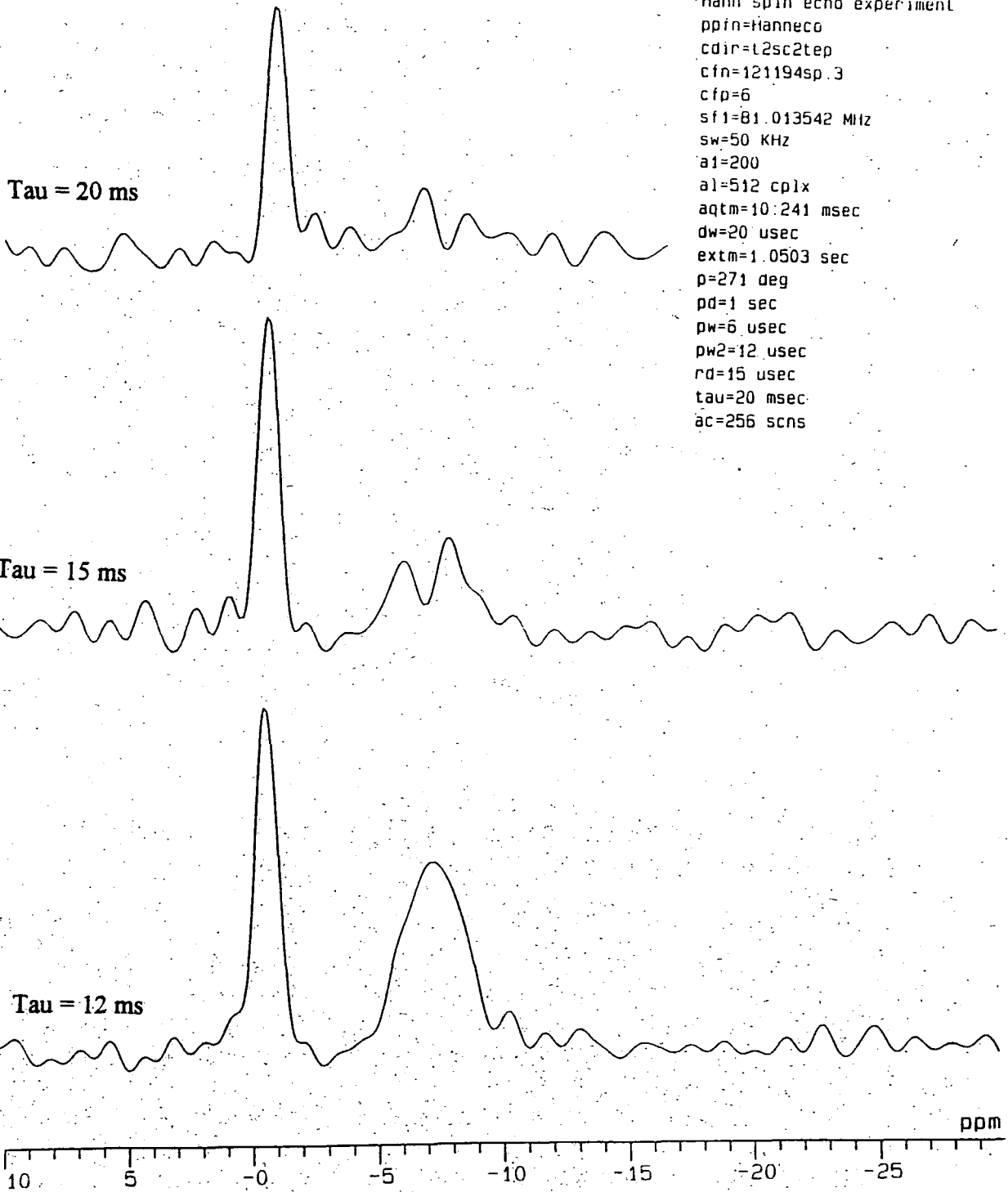


Figure 6.6. Fourier transformed Hahn-echo experiment on SC2 with 60% w/w TEP with the tau values indicated.

The graph of Ln signal versus dephasing time for the 40% loading of TEP on the SC2 carbon shows two distinct parts to the line. These correspond to two peaks with different  $T_2$  values. Analysis of the graph gives one line with a  $T_2$  value of 2.38  $\pm$  0.2 ms (relating to a natural line-width of 134 Hz) and the other has a value of 43.7  $\pm$  0.2 ms (with a natural line-width of 7 Hz). The relative populations are 91% for the broad peak and 9% for the narrow one.

The sample with 60% w/w TEP has a broad peak and a narrow peak. The FID is difficult to analyse because the line contains many components, it is very difficult to separate each component. However the Fourier transform spectra shown in figure 6.5 and 6.6. show some interesting aspects. As the tau value increases the broad peak loses intensity quickly and the narrow peak more slowly. Interestingly the phosphorus spectrum has such a large shift range that the broad peak can be seen to divide into two separate peaks as the tau value increases. This happens because the line-width of the overlapping peaks falls off and the peaks become distinct. This is unequivocal evidence of at least two separate lines within the broad peak, corresponding to two distinct chemical environments for the adsorbed molecules.

The narrow peak associated with TEP adsorbed on the external surface has a  $T_2$  value of 15.2  $\pm$  0.4 ms. This gives a calculated natural linewidth of 20.9 Hz which compares to the observed linewidth of 82 Hz.

The deuterium NMR observed the SC2 sample with 40%  $^2\text{H}_2\text{O}$  adsorbed on the carbon. The plot of the Ln signal against dephasing time is presented in figure 6.7. The tau values used varied from 0.5 ms to 13 ms.

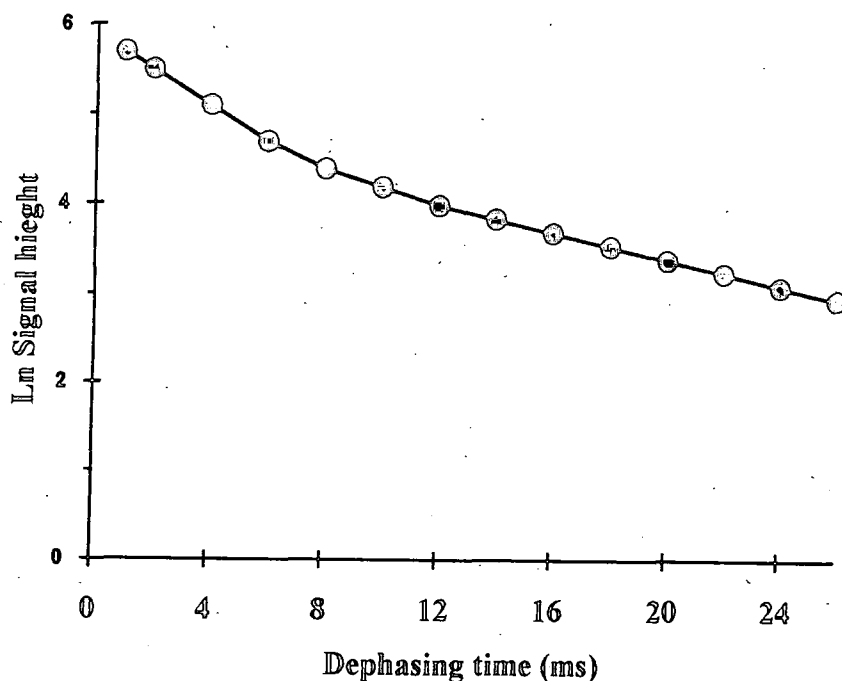


Figure 6.7. Graph of the Ln Signal against dephasing time for  $^2\text{H}$  spectra of SC2 with 40% w/w  $^2\text{H}_2\text{O}$  adsorbed.

The deuterium spectra give some evidence of the two peaks with a plot consisting of two different slopes for the Ln signal versus dephasing time. The two  $T_2$  values calculated are  $T_2 = 13.9 \pm 1.2$  ms and  $T_2 = 7.0 \pm 1.2$  ms. The values relate to natural line-widths of 45 Hz (population 12%) and 22 Hz (population 88%).

The final sample observed the spectra of 60% w/w  $^2\text{H}_2\text{O}$  adsorbed onto the SC2 carbon. The spectrum had a broad and narrow peak so the results have been presented as a stacked plot in figure 6.8. The spectra show that the broad peak does not separate into two separate peaks. This is presumably because the two overlapping peaks are of very similar chemical shift. The broad peak does not decay away as quickly as the  $^{31}\text{P}$  NMR following the TEP adsorption does.

The narrow peak associated with  $^2\text{H}_2\text{O}$  adsorbed on the external surface has a  $T_2$  value of  $17.7 \pm 0.3$  ms. This gives a calculated natural linewidth of 18.0 Hz which compares to the observed linewidth of 42 Hz.

Sample on SC2	Peak	Observed $\Delta_{1/2}$ (Hz)	Minimum $\Delta_{1/2}$ (Hz)	T2 value (ms)	Natural $\Delta_{1/2}$ (Hz)	Relative populations
20% TEP	Broad	250	198	$2.4 \pm 0.1$	138	
40% TEP	Broad	260		$2.38 \pm 0.2$	134	91%
	Broad	260		$43.7 \pm 0.2$	7	9%
60% TEP	Broad	260				
	Narrow	72		$15.2 \pm 0.4$	7	
40% $^2\text{H}_2\text{O}$	Broad	140		$13.9 \pm 1.2$	22	88%
	Broad	140		$7.0 \pm 1.2$	45	12%
60% $^2\text{H}_2\text{O}$	Broad	140				
	Narrow	40		$17.7 \pm 0.3$	18	

Table 6.1 Summary table of the  $^{31}\text{P}$  and  $^2\text{H}$  NMR Hahn-echo experiment results.

#### 6.4. Discussion

The Hahn-echo experiment gives good experimental results for adsorbate systems but a careful experimental set-up is necessary. The  $^{31}\text{P}$  NMR results show that the broad micropore peak consists of more than one component as the load builds up. Figures 6.4 and 6.5 show that two peaks are observable as the dephasing time increases. The plot of the linewidth as a function of dephasing time shows a decrease as the tau value increases until a minimum of 198 Hz is achieved. The reduction in linewidth with increasing tau indicates a dispersion of sites with different widths, however the corresponding plot of the signal with dephasing time only shows one component in the T2. Clearly these results are conflicting and more experiments need to be performed to clarify the situation. The smallest observed linewidth of 198 Hz is larger than the calculated natural linewidth of 134 Hz. This suggests that there is a dispersion of chemical shifts with similar linewidths. Increasing the load to 40% gives the same broad peak plus an extra narrow peak (7Hz) at a similar shift. The 60%

spectra in figures 6.5 and 6.6 show evidence of these two distinct sites within the broad peak.

The deuterium results also show a multi-component system, with two distinct values of  $T_2$  calculated for the broad peak for the 40% w/w sample. The deuterium micropore peak has a larger  $T_2$  value than the phosphorus adsorbate, and the spectra in figure 6.8. show that some components of the broad peak are refocussed even at tau values of 20 ms. This deviation from the  $^{31}\text{P}$  results suggests that the observed deuterium line is broadened even more compared to the calculated natural linewidth. This broadening arises from a dispersion of chemical shifts with similar linewidths. The results for the narrow peaks shows that these also appear much broader than the calculated natural linewidth.

#### 6.5 Conclusion

The relaxation results show that the broad micropore peak shifted to low frequency, is broadened by a dispersion of chemical shifts with similar linewidths, but there is also a dispersion of linewidths. The results suggest that the peak consists of overlapping lines with similar chemical shifts. This is reasonable because the pores are not of a uniform size so the adsorbate will experience a dispersion of similar environments.

The narrow external surface peak, is also broadened by a dispersion of chemical shifts with similar linewidths. The results suggest that this peak consists of overlapping lines with similar chemical shifts. This is reasonable because the external surface will have variations so the adsorbate will experience a dispersion of similar environments.

## Chapter 7 Conclusions

This was a study of adsorption on three activated carbon substrates using solid-state NMR. The adsorbates used as probe molecules included a range of phosphates, phosphonates and deuterated water. High-resolution  $^{31}\text{P}$  and  $^2\text{H}$  NMR spectra were obtained using magic-angle spinning and a single-pulse regime.

The deuterium results included the generation of an adsorption isotherm. The traditional gravimetric analysis and NMR experiments were run concurrently. These results showed that the NMR technique was qualitatively and quantitatively accurate, while the proven adsorption isotherm theory could be applied to the NMR results. The additional information given by the  $^2\text{H}$  NMR results showed evidence of two distinct adsorption sites. Initial adsorption in the micropores gives a peak shifted by 6 ppm to low frequency of the liquid  $^2\text{H}_2\text{O}$  line. This peak was broadened due to restricted motion in the micropores. The second peak was observed at high relative humidities, and was attributed to adsorption on the external surface or in macropores. The chemical shift was similar to that of the pure liquid. Deuterium NMR was used to look at carbon substrates with different degrees of activation. The chemical shift results showed that the largest shift to low frequency occurred with low burn-off levels. As the burnoff increased the chemical shift of the micropore adsorption moved to high frequency. This shift was attributed to the pore size increasing, with a corresponding reduction in shielding of the adsorbed molecule.

The  $^{31}\text{P}$  NMR results were used to directly observe the adsorption of phosphates with a range of molecular sizes. The effect on the pure liquid phosphates of adsorption onto the activated carbon was analysed. The adsorption into the micropores once again gave a broad peak shifted to low frequency. At high phosphate loads, a

second narrow peak developed, close to the pure liquid line. The NMR data were used to calculate the micropore accessibility for each phosphate. Differences in the adsorption mechanism were recorded, and direct comparison of each carbon gave some structural information. The long-term ageing of the sample was observed, with phosphate molecules moving from the external surface sites into the micropores over a thirty-three day period.

It was possible to follow competition reactions over time periods of 1 min to 24 hours. A battlefield simulation was studied, with  $^2\text{H}_2\text{O}$  and a phosphate competing for the adsorption sites. The NMR results showed that the phosphate was preferentially adsorbed into the micropores, displacing the  $^2\text{H}_2\text{O}$ . However, the addition of  $^2\text{H}_2\text{O}$  to a carbon saturated with a phosphate enabled more phosphate to be adsorbed into the micropores via a cooperative mechanism.

Measurements of the transverse relaxation for adsorbed molecules suggested that the broad micropore signal consists of some overlapping peaks. The peaks with similar chemical shift are attributed to adsorption in pores with differing dimensions. The natural linewidth involves broadening caused by restricted anisotropic motion within the micropores.

This report clearly shows that solid-state NMR is a very versatile tool that can be used to look at adsorption onto activated carbon. The direct observation of the adsorbate molecules gives valuable information about the adsorption process and the nature of the activated carbon itself. The adsorption information and battlefield simulations provide new insights into the way respirator cannisters perform. The knowledge should enable the military carbons to be tailored to specific adsorption tasks with increasing performance. Increased performance would reduce the carbon

bed-depth required to meet breakthrough criteria. This would make the respirator system easier to use, with greater airflow for personnel exposed to an agent threat.

Future experiments using solid-state NMR are required to fully explore the adsorption process and analyse the carbon substrates. There is a huge scope for research in the adsorption area, with many applications benefitting by improved efficiency and cost reduction via an increased understanding of adsorption onto activated carbon. The adsorption isotherm needs to be run on each substrate so that the additional NMR information can be compared directly. The range of adsorbates can be increased to include different phosphates, and perhaps some fluorine containing molecules. The adsorption studies with varying molecular size and precoverage could be run concurrently with immersion calorimetry, to help in the understanding of the adsorption potentials. The standard adsorption isotherms with nitrogen and carbon dioxide gas need to be investigated using NMR of isotopically labelled gases. The adsorption kinetics of the competition reactions also need to be studied in greater depth, to see what characteristics of the activated carbon improve the speed of adsorption.

## Papers Presented and Research Conferences Attended

### Oral Presentations

Advances in adsorption studies using solid-state NMR. CBDE Porton Down, Salisbury. November 1993.

Solid-state NMR studies of adsorption. Durham University Third Year Graduate Colloquia, 10 May 1995.

### Posters Presented

Solid-state NMR studies of adsorption onto activated carbon substrates, 36th Experimental Nuclear Magnetic Resonance Conference, Marriott Copley Place, Boston MA (USA) 26-30 March 1995.

Advances in adsorption studies by NMR, ICI Poster Competition, University of Durham, December 1993.

### Publications

High-resolution  $^2\text{H}$  NMR of  $^2\text{H}_2\text{O}$  adsorbed onto activated carbon.  
R. K. Harris and T. V. Thompson, *J. Chem. Soc. Faraday trans.*, 1995, 91(12), 1795.

## Colloquia, Seminars and Lectures Given by Invited Speakers

An asterisk denotes attendance.

1992

- October 15 Dr. M. Glazer, Oxford University, & Dr. S. Tarling, Birkbeck College, London  
It Pays To Be British! The Chemists Role as an Expert Witness in Patent Litigation.
- October 20 Dr. H.E. Bryndza, Du Pont Central Research  
Syntheses, Reactions and Thermochemistry of Metal (Alkyl) Cyanide Complexes and Their impact on Olefin Hydrocyanation Catalysis
- October 22 Prof. A. Davies, University College London  
The Ingold-Albert Lecture. The Behaviour of Hydrogen as a Pseudometal\*
- October 28 Dr. J. K. Cockcroft, University of Durham  
Recent Developments in Powder Diffraction\*
- October 29 Dr. J. Emsley, Imperial College London  
the Shocking History of Phosphorus\*
- November 4 Dr. T. P. Kee, University of Leeds  
Synthesis and Co-ordination Chemistry of Silylated Phosphites
- November 5 Dr. C. J. Ludman, University of Durham  
Explosions, A Demonstration Lecture\*
- November 11 Prof. D. Robins, Glasgow University  
Pyrrolizidine Alkaloids: Biological Activity, Biosynthesis and Benefits
- November 12 Prof. M. R. Truter, University college, London  
Luck and Logic in Host-Guest Chemistry\*
- November 18 Dr. R Nix, Queen Mary College, London  
Characterisation of Heterogeneous Catalysts
- November 25 Prof. Y. Vallee, University of Caen  
Reactive thiocarbonyl Compounds
- November 25 Prof. L. D. Quin, University of Massachusetts, Amherst  
Fragmentation of Phosphorus Heterocycles as a Route to Phosphoryl Species with Uncommon Bonding
- November 26 Dr. D. Humber, Glaxo Greenford  
AIDS- The Development of a Novel Series of Inhibitors of HIV

- December 2 Prof. A. F. Hegarty, University College Dublin  
Highly Reactive Enols Stabilised by Steric Protection
- December 2 Dr. R. A. Aitken, University of St. Andrews  
The Versatile Cycloaddition of  $\text{Bu}_3\text{P}\cdot\text{CS}_2$
- December 3 Prof. P Edwards, Birmingham University  
The SCI Lecture: What is Metal?\*
- December 9 Dr. A. N. Burgess, ICI Runcorn  
The structure of Perfluorinated Ionomer Membranes
- 1993
- January 20 Dr. D. C. Clary, University of Cambridge  
Energy Flow in Chemical Reactions\*
- January 21 Prof. L. Hall, Cambridge  
NMR- Window to the Human Body
- January 27 Dr. W. Kerr, University of Strathclyde  
Development of the Pauson-Khand Annulation Reaction:  
Organocobalt Mediated Synthesis of Natural and Unnatural Products
- January 28 Prof. J. Mann, University of Reading  
Murder, Magic and Medicine\*
- February 3 Prof. M. S. Roberts, University of Exeter  
Enzymes in Organic Synthesis
- February 10 Dr. D. Gillies, University of Surrey  
NMR and Molecular Motion in Solution
- February 11 Prof. S. Knox, Bristol University  
The Tiden Lecture: Organic Chemistry at Polynuclear Metal Centres\*
- February 17 Dr. W. R. Kemmitt, University of Leicester  
Oxatrimethylenemethane Metal Complexes
- February 18 Dr. I. Fraser, ICI Wilton  
Reactive Processing of Composite Materials
- February 22 Prof. D. M. Grant, University of Utah  
Single Crystals, Molecular Structure and Chemical-Shift Anisotropy
- February 24 Prof. C. J. M. Stirling, University of Sheffield  
Chemistry on the Flat Reactivity of Ordered Systems\*

- March 10 Dr. P. K. Baker, University College of North Wales, Bangor  
'Chemistry of Highly Versatile 7-Coordinate Complexes
- March 11 Dr. R. A. Y. Jones, University of East Anglia  
The Chemistry of Wine Making
- March 17 Dr. R. J. K. Taylor, University of East Anglia  
Adventures in Natural Product Synthesis
- March 24 Prof. I. O. Sutherland, University of Liverpool  
Chromogenic Reagents for Cations
- May 13 Prof. J. A. Pople, Carnegie-Mellon University, Pittsburgh, USA  
The Boys-Rahman Lecture: Applications of Molecular Orbital Theory\*
- May 21 Prof. L. Weber, University of Bielefeld  
Metallo-phospha Alkenes as Synthons in Organometallic Chemistry
- June 1 Prof. J. P. Konopelski, University of California Santa Cruz  
Synthetic Adventures with Enantiomerically Pure Acetals
- June 2 Prof. F. Ciardelli, University of Pisa  
Chiral Discrimination in the Stereospecific Polymerisation of Alpha Olefins
- June 7 Prof. R. S. Stein, University of Massachusetts  
Scattering Studies of Crystalline and Liquid Crystalline Polymers
- June 16 Prof. A. K. Covington, University of Newcastle  
Use of Ion Selective Electrodes as Detectors in Ion Chromatography
- June 17 Prof. O. F. Nielsen, H. C. Ørsted Institute, University of Copenhagen  
Low-Frequency IR- and Raman Studies of Hydrogen Bonded Liquids
- September 13 Dr. A. D. Schluter, Freie Universitat, Berlin, Germany  
Synthesis and Characterisation of Molecular Rods and Ribbons
- September 13 Dr. K. J. Wynne, Office of Naval Research, Washington, USA  
Polymer Surface Design for Minimal Adhesion
- September 14 Prof. J. M. DeSimone, University of North Carolina, Chapel Hill, USA  
Homogeneous and Heterogeneous Polymerisations in Environmentally Responsible Carbon Dioxide
- September 28 Prof. H. Ila, North Eastern Hill University, India  
Synthetic Strategies for Cyclopentanoids via Oxoketene Dithioacetals
- October 4 Prof. F. J. Feher, University of California, Irvine, USA  
Bridging the Gap Between Surfaces and Solution with Sessilquioxanes\*

- October 14 Dr. P. Hubberstey, University of Nottingham  
Alkali Metals: Alchemist's Nightmare, Biochemist's Puzzle and  
Technologist's Dream
- October 20 Dr. P. Quayle, University of Manchester  
Aspects of aqueous ROMP Chemistry\*
- October 23 Prof. R. Adams, University of South Carolina, USA  
Chemistry of Metal Carbonyl Cluster Complexes: Development of  
Cluster Based Alkyne Hydrogenation Catalysts\*
- October 27 Dr. R. A. L. Jones, Cavendish Laboratory, Cambridge  
Perambulating Polymers\*
- November 10 Prof. M. N. R. Ashfold, University of Bristol  
High Resolution Photofragment Translational Spectroscopy: A New  
Way to Watch Photodissociation
- November 17 Dr. A. Parker, Rutherford Appleton Laboratory, Didcot  
Applications of Time Resolved Resonance Raman Spectroscopy to  
Chemical and Biochemical Problems\*
- November 24 Dr P. G. Bruce, University of St. Andrews  
Structure and Properties of Inorganic Solids and Polymers
- November 25 Dr. R. P. Wayne, University of Oxford  
The Origin and Evolution of the Atmosphere
- December 1 Prof. M. A. McKervey, Queen's University, Belfast  
Synthesis and Applications of Chemically Modified Calixarenes
- December 8 Prof. O. Meth-Cohn, University of Sunderland  
Friedel's Folly Revisited- A Super Way to Fused Pyridines
- December 16 Prof. R. F. Hudson, University of Kent  
Close Encounters of the Second Kind
- 1994
- January 26 Prof. J. Evans, University of Southampton  
Shining Light on Catalysts\*
- February 2 Dr. A. Masters, University of Manchester  
Modelling Water Without Using Pair Potentials\*
- February 9 Prof. D. Young, University of Sussex  
Chemical and Biological Studies on the Coenzyme Tetrahydrofolic  
Acid

- February 16 Prof. K. P. Theopold, University of Delaware, USA  
Paramagnetic Chromium Alkyls: Synthesis and Reactivity
- February 23 Prof. P. M. Maitlis, University of Sheffield  
Across the Border: From Homogeneous to Heterogeneous Catalysis\*
- March 2 Dr. C. Hunter, University of Sheffield  
Noncovalent Interaction between Aromatic Molecules\*
- March 9 Prof. R. Wilkinson, Loughborough University of Technology  
Nanosecond and Picosecond Laser Flash Photolysis
- March 10 Prof. S. V. Ley, University of Cambridge  
New Methods for Organic Synthesis
- March 25 Dr. J. Dilworth, University of Essex  
Technetium and Rhenium Compounds with Applications as Imaging Agents
- April 28 Prof. R. J. Gillespie, McMaster University, Canada  
The Molecular Structure of some Metal Fluorides and Oxofluorides:  
Apparent Exceptions to the VSEPR Model
- May 12 Prof. D. A. Humphreys, McMaster University, Canada  
Bringing Knowledge to Life
- October 5 Prof. N. L. Owen, Brigham Young University, Utah, USA  
Determining Molecular Structure-The INADEQUATE NMR Way\*
- October 19 Professor N. Bartlett, University of California  
Some Aspects of (AgII) and (AgIII) Chemistry.\*
- October 26 Dr. G. Rumbles, Imperial College  
Real or Imaginary 3rd Order Non-Linear Optical Materials.\*
- November 2 Dr. P. G. Edwards, University of Wales, Cardiff  
The Manipulation of Electronic and Structural Diversity in Metal  
Complexes - New Ligands for New Properties.\*
- November 9 Dr. G. Hogarth, University College, London  
New Vistas in Metal Imido Chemistry.\*
- November 16 Professor M. Page, University of Huddersfield  
Four Membered Rings and B-Lactamase.
- November 23 Dr. J. Williams, University of Loughborough  
New Approaches to Asymmetric Catalysis.

- November 30 Professor P. Parsons, University of Reading  
Applications of Tandem Reactions in Organic Synthesis.
- December 7 Professor D. Briggs, ICI and University of Durham  
Surface Mass Spectrometry.\*
- 1995
- January 25 Dr. D. A. Roberts, Zeneca Pharmaceuticals  
The Design and Synthesis of Inhibitors of the Renin-Angiotensin System.
- February 1 Dr. T. Cosgrove, Bristol University  
Polymers do it at Interfaces.
- February 8 Dr. D. O'Hare, Oxford University  
Synthesis and Solid State Properties of Poly- Oligo- and Multidecker Metallocenes.
- February 15 Professor W. Motherwell, University College, London  
New Reactions for Organic Synthesis.
- February 22 Professor E. Schaumann, University of Clausthal  
Silicon- and Sulphur-mediated Ring-opening Reactions of Epoxide.
- March 1 Dr. M. Rosseinsky, Oxford University  
Fullerene Intercalation Chemistry.\*
- April 26 Dr. M. Schroder, University of Edinburgh  
Redox Active Macrocyclic Complexes: Rings, Stacks and Liquid Crystals.
- May 3 Professor E. W. Randall, Queen Mary and Westfield College  
New Perspectives in NMR imaging.\*
- May 24 Dr. P. Beer, Oxford University  
Anion Complexation Chemistry.